THE ORIGIN, COMPOSITION, AND EVOLUTION OF THE KIMBERLEY KIMBERLITES (SOUTH AFRICA)

Ashton Soltys – 391550

Thesis submitted in total fulfilment of the requirements of the degree of Doctor of Philosophy (Earth Science), The University of Melbourne

Submitted November 2019

ABSTRACT

Kimberlites are deeply derived (i.e., >150 km), small-volume igneous bodies that have been emplaced on all continents throughout the last 2.8 billion years. The typical volcanic expression of kimberlites is a deep irregular root zone and/or feeder dyke system connected to a regular steeply dipping and outwardly tapering pipe-like diatreme, which may be overlain by a crater and extrusive material (when not removed by erosion). The crater and diatreme facies contain pyroclastic rocks, which transition into coherent (sub-volcanic) rocks in the root zone.

Kimberlites are of economic value as the major host of gem quality diamonds at the Earth's surface. They also hold great scientific significance, as the deepest derived melts to reach the surface, with entrained mantle material that provides some of our best information on the structure, composition, and evolution of the sub-continental lithospheric mantle. However, despite over a century of dedicated research, numerous aspects of kimberlite petrogenesis remain poorly understood and contentious. One central issue that this project has addressed is the composition and evolution of kimberlite melts. The composition of kimberlite melts remain poorly constrained because: (1) rocks emplaced near the surface are prone to deuteric and hydrothermal alteration; (2) they have been contaminated by the physical incorporation of xenocrystic and xenolithic material; (3) their parental magmas have been modified by interaction with and partial assimilation of mantle and crustal material; and (4) they undergo syn-emplacement differentiation. Therefore, in this study exceptionaly 'fresh' rocks from the well studied kimbeley cluster (the type locality) were examined to gain further insights into kimberlite melt compositions. Better constraints on kimberlite melt compositions are pivotal if we are to move toward a comprehensive understanding of the petrogenesis of these enigmatic rocks.

The studied samples derive from the Kimberley cluster (South Africa), which lies within the Western terrane of the Kaapvaal carton. This cluster constitutes the type locality of kimberlites, containing five major kimberlite pipes (The Kimberley mine, De Beers, Dutoitspan, Wesselton, and Bultfontein), numerous smaller pipes, and abundant dyke/sill complexes (e.g., Benfontein, Wesselton Floors, Wesselton Water Tunnels). The Kimberley cluster has been dated by various geochronological techniques yielding emplacement ages of ~80-90 Ma.

To provide new insights into the composition and evolution of kimberlite melts, a detailed petrographic study of sub-volcanic (hypabyssal) coherent kimberlites was conducted. This included the investigation of mineralogy, mineral zonation, inclusion populations (mineral, melt, and fluid), and textural relationships between phases, utilizing a range of microscopy techniques. This petrographic data formed the basis of targeted geochemical analysis by electron microprobe.

A study of olivine compositions across multiple intrusions of the Kimberley cluster shows that olivine, more than any other mineral, provides the most complete record of kimberlite evolution. This study showed that pre-ascent metasomatism of the lithosphere by kimberlite melts is wide-spread, and that so-called ‘xenocrystic’ olivine is not directly representative of the wider lithosphere due to metasomatism of the conduit by previous pulses of kimberlite magmatism. The composition of kimberlitic liquidus olivine overlaps that of olivine from other mantle-derived carbonate-bearing magmas (orangeites, ultramafic lamprophyres, melilitites), with low Mn/Fe and Ca/Fe, and moderate Ni/Mg ratios. It is suggested that these compositions are typical of olivine in equilibrium with melts derived from carbonate-rich peridotite sources. Compositional zonation patterns indicte that olivine crystallises throughout magma ascent and that its crystallisation continues after emplacement into the upper crust. Magmatic olivine (i.e. crystallised from the kimbelrite magma) displays

distinct generations of crystallisation, with increasing Mg, Ca, and Mn contents interpreted as the result of fractional crystallisation and increasing oxygen fugacity (fO_2). The stability of olivine at sub-solidus conditions implies that secondary melt inclusions cannot trap primitive melts, but rather evolved residual fluids.

Although olivine provides a wealth of information on early kimberlite melt evolution and metasomatism of the surrounding lithosphere, details about the later stages of kimberlite melt evolution are evident in other magmatic groundmass phases. Therefore, detailed petrographic and mineral chemical studies were undertaken on all mineral consistents from a suite of samples from the exceptionally fresh De Beers dyke to determine the crystallisation sequence. In turn, this data yielded insights into melt evolution from the perspective of multiple different magmatic phases. The early stages of kimberlite crystallisation (i.e., olivine, Cr-spinel, Mg-Ilmenite, rutile) are defined by decreasing Mg/Fe ratios. This subsequently reverses (i.e., increasing Mg/Fe) during later groundmass crystallisation, which is attributed to increasing fO_2. Comparison with published data shows that the melt parental to early crystallising phases in this dyke are indistinguishable from those in the root-zone intrusions of the Kimberley cluster, meaning that not all dykes are the crystalisation product of magmas that underwent pre-emplacement fractionation.

To gain additional insights into the very late stages of kimberlite melt evolution further detailed petrographic and mineral chemical studies were conducted on late-stage groundmass phases (i.e., apatite and mica) from samples of different root zone intrusions and dyke/sill complexes in the Kimberley area. Despite the early crystallising phases (i.e., olivine, Cr-spinel, Mg-ilmenite) being compositional indistinguishable in dykes/sills and root zone kimberlites, the compositions of apatite appear to be controlled by the style of magma emplacement. Apatite from dykes/sills is Si-rich and Sr-poor, whereas apatite in root zone intrusions show the opposite features. The high Si content of apatite in dykes/sills is attributed to the coupled

incorporation of silica and a carbonate ion for phosphorus, reflecting higher CO_2 contents in the melts parental to dykes/sills. The high Sr content of apatite in root zone intrusions likely requires crystallisation from, or overprinting by, hydrous fluids. These features indicate that dyke/sill kimberlites have higher CO_2/H_2O ratios than the magma that produced root zone intrusions. This is consistent with petrographic observations, whereby dykes/sills are enriched in carbonates, may contain dolomite, and have lower abundances of serpentine, mica, and monticellite than root-zone kimberlites. These differences in CO_2/H_2O ratios of the crystallised melt are attributed to differences in emplacement style, whereby a rapid decrease in pressure in root zone kimberlites leads to exsolution of a (CO_2-rich) fluid phase, possibly caused by breakthrough to the surface.

The knowledge gained through detailed petrographic and mineral chemical studies led to the development a new quantitative method for reconstructing the composition of kimberlite melts. This model allowed for constraints to be placed on the composition of primitive kimberlite melts and their evolution, as they incorporate and assimilate xenocrystic material, undergo fractional crystallisation, and post emplacement alteration. The results of this modelling indicate that the melt parental to the Bultfontein kimberlite was transitional between silicate and carbonate. This composition is consistent with experimental constraints on the amount of CO_2 that can be dissolved into kimberlite melts in the upper crust. The reconstructed primitive melt composition is in equilibrium with asthenospheric source rocks. Based on constraints from experimental studies, Kimberley kimberlites could have been produced by ~0.5% melting of carbonated lherzolite in the upper asthenosphere (i.e., 6.0-8.6 GPa and ~1400-1500°C).

ACKNOWLEDGEMENTS

This thesis was made possible by the financial support provided by the Melbourne Research Scholarship, and the Baragwanath fund which facilitated attendance of the 11th International Kimberlite Conference. Equally important, the time, expertise, and unwavering support provided by my supervisors Andrea Giuliani and David Phillips. Hopefully this is not the end of out work together.

I would also like to thank the technical staff for their tireless assistance, Alan Greig (LA-ICP-MS), Karsten Geomann (FE-SEM and EPMA), and especially Graham Hutchinson (SEM, EPMA). Various academics and organisations kindly provided samples, and/or permission to collect samples used in this project, including: Petra Diamonds, De Beers Group, Dr. Simon Shee, Dr. Stephen Sparks, and Dr. Philip Janney (John Gurney Mantle room collection).

Many thanks go to my fellow students and friends at the University of Melbourne for their support, stimulating discussions, and company during various forms of beverage consumption. In no specific order, Michael Heath, Hayden Dalton, Angus Fitzpayne, Madeline Tovey, Henrietta Farr, and Emily Lim.

Constructive and comprehensive reviews of the chapters contained in this thesis were provided by Yves Moussallam, Maya Kopylova, Matt Gaudet, Bruce Kjarsgaard, Sonja Aulbach, Andy Moore, Nick Arndt, Sally Gibson, and two anonymous reviewers. This constructive feedback greatly improved the content of these chapters.

Finally, and most importantly a heartfelt thank you to my Mum, Dad, partner Cheyne, and two dogs, Spud and Fig. Your support and encouragement throughout my many years of study has played a pivotal in maintaining my sanity and happiness.

DECLARATION

This is to certify that:

1) This thesis comprises of only my original work towards the PhD

2) Acknowledgment has been made within the text to all other material used

3) This thesis is less than 100,000 words in length, excluding tables, references, and appendices

PREFACE

The data and ideas presented in this thesis are my own [AS]. However, this work was undertaken in collaboration with academics from the University of Melbourne (Dr. A. Giuliani [AG], Prof. D. Phillips [DP]) and the University of Tasmania (Prof. V.S. Kamenetsky [VK]). The project was conceived by AG, DP, and AS. Most of the samples studied here were collected by AS and AG during field work at the Kimberley mines in July 2015. Additional samples that could not be directly collected (i.e., due to mine closure or flooding – Kimberley and De Beers mines, Wesselton water tunnel sills), were loaned from the John Gurney Mantle Room collection at the University of Cape Town, The Kimberley Mine Museum, or the private collections of individuals (Prof R. Mitchell; Prof. S. Sparks). The first author (AS) designed and co-ordinated this study with input from AG and DP. The analysis, modelling, development of concepts, and writing of these chapters was primarily the work or AS. Some assistance (e.g., with interpretation, comments on written work) and financial support was provided by AG, DP, and VK.

The first two chapters of this thesis introduce and provide background information on kimberlite magmatism. This includes an overview of kimberlite classification, distribution, morphology, and petrology, followed by specific information on the local geology, internal pipe geology, the lithospheric mantle beneath the Kimberley kimberlites, including the effects of kimberlite metasomatism on mantle wall rocks. The main outcomes of this research project are reported in chapters three to six, with additional supplementary material provided in Appendix S1. These chapters consist both of published journal articles (chapters four and six) and manuscripts submitted for publication (chapters three and five). Due to the policies of the journals, chapters four and six can only be reproduced here as the "author accepted manuscript versions," i.e., without the journals formatting. In all chapters the appendices have not been

reproduced in hard copy, primarily due to exceptionally large quantity of data contained therein, and the difficulty in presenting this material (e.g., geochemical modelling spreadsheets) in a paper format. The appendices that accompany these published manuscripts are provided in the accompanying electronic files or can be downloaded from the publisher's websites. Because the results of this research project have been published (or have been accepted for publication pending minor revisions) the introduction, background, analytical methods, results, discussion, conclusion, and reference sections are self-contained within each chapter. Therefore, chapters one and two only provide a general summary of the literature on kimberlite petrology, and chapter seven provides a short summary of the overarching conclusions. The results of this study are organised to provide a bottom up account of kimberlite crystallisation and evolution (Chapters 3-5). This provides the necessary context for quantitative modelling of kimberlite melt compositions through the application of a new reconstruction framework (Chapter 6).

Chapter three has been submitted to the *Journal of Petrology* and has been accepted for publication pending revision. This chapter provides a detailed petrographic and geochemical study of olivine from twelve of the freshest units of the Kimberley kimberlite cluster. Based on a comprehensive examination of the different compositional zones present within kimberlitic olivine, we show that olivine preserves a much longer crystallisation and re-equilibration history in kimberlites than previously assumed. Therefore, olivine, more than any other mineral, is an excellent monitor of kimberlite melt evolution. These results highlight the abundance of mantle-derived olivine that experienced metasomatism by early pulses of kimberlite melt (i.e., derived from megacrysts and sheared peridotites). In addition, we show that olivine is stable until the very late stages of kimberlite consolidation (i.e., after emplacement in the upper crust), which has implications for the composition of kimberlite melts as inferred from secondary melt inclusions in some previous studies. Finally, the composition of liquidus olivine in kimberlites is remarkably similar to olivine from other mantle derived carbonate-rich magmas (e.g.,

orangeites, melilitites, aillikites). This allows for the definition of the composition of olivine in equilibrium with melts derived from carbonate-rich peridotite sources and crystallised at relatively high pressure-temperature conditions.

Chapter four has been published in the journal *Mineralogy and Petrology* – Proceedings of the 11th International Kimberlite Conference. This manuscript describes a detailed petrographic and mineral chemical study of all phases contained in a suite of fresh samples from the De Beers dyke. This exceptionally fresh mineralogy allowed for an assessment of the origin of all contained mineral phases and their zones, as well as the reconstruction of the crystallisation sequence of the dyke. In turn this permited an evaluation of kimberlite melt evolution from the perspective of multiple mineral constituents. The indistinguishable compositions of olivine, spinel, and ilmenite in dykes/sills and root-zone kimberlites from the De Beers pipe implies that the same or similar magmas are parental to different varieties of coherent kimberlite (i.e., root zone intrusions *vs.* dyke/sills). The supplementary material accompanying this publication is avilable via the following link:

https://link.springer.com/article/10.1007/s00710-018-0588-5

Chapter five has been accepted for publication in *Contributions to Mineralogy and Petrology*. Here we report the petrography of late stage groundmass and mesostasis phases, as well as the mineral chemistry of mica and apatite across multiple samples of the Kimberley kimberlites. The aim of this study was to determine the late stages of kimberlite evolution and any relation to the different emplacement mechanisms of coherent kimberlites. In contrast to earlier olivine and oxide mineral phases, which have indistinguishable compositions between different samples, the later crystallised apatite shows systematic differences between kimberlites with different emplacement modes. Apatite from dyke/sill kimberlites are Si-rich and Sr-poor, whereas those from root zone kimberlites are Si-poor and Sr-rich. These differences are attributed to different melt evolution trajectories, particularly with respect to

CO_2/H_2O ratios and volatile contents, which are linked to the emplacement mechanism. In root-zone kimberlites, surface breakthrough causes a decrease in pressure and is linked to exsolution of a CO_2-rich fluid. In contrast, in dykes/sills, surface breakthrough does not occur and higher confining pressure results in retention of more CO_2.

Chapter six has been published in the journal *Lithos* (i.e., Soltys et al., 2018a). This study presents data on a sample of coherent hypabyssal kimberlite from the Bultfontein mine. The sample was selected for its well characterised petrography, superior freshness, and bulk rock chemistry which does not show significant olivine accumulation or fractionation. Numerical modelling was employed to determine the potential compositions of kimberlite magmas and melts through different stages of their evolution (i.e., on emplacement in the upper crust, and primitive kimberlite melts), after making assumptions about the origin of serpentine, assimilation of mantle material and volatile degassing. This modelling allowed constraints to be placed on kimberlite source compositions and locations. The supplementary material accompanying this publication is avilable via the following link:

https://www.sciencedirect.com/science/article/pii/S0024493718300379

LIST OF PUBLICATIONS

CHAPTER 3

Soltys, A., Giuliani, A., Phillips, D., Kamenetsky, V. (2019). Kimberlite metasomatism of the lithosphere and the evolution of olivine in carbonate-rich melts – evidence from the kimberley kimberlites (south africa). *The Journal of Petrology* (submitted).

CHAPTER 4

Soltys, A., Giuliani, A. & Phillips, D. (2018b). Crystallisation sequence and magma evolution of the De Beers dyke (Kimberley, South Africa). *Mineralogy and Petrology* **112**, 503-518.

CHAPTER 5

Soltys, A., Giuliani, A. & Phillips, D. (2019). Apatite compositions record divergent melt evolution trajectories in coherent kimberlites caused by differing emplacement mechanisms. *Contributions to Mineralogy and Petrology* (accepted)

CHAPTER 6

Soltys, A., Giuliani, A. & Phillips, D. (2018a). A new approach to reconstructing the composition and evolution of kimberlite melts: A case study of the archetypal Bultfontein kimberlite (Kimberley, South Africa). *Lithos* **304**, 1-15.

LIST OF FIGURES & TABLES

The figure and table captions reported below are summarised versions. The full figure and table captions, inclusive of references and legend explanations can be found accompanying the relevant figure or table in the main body of the thesis.

CHAPTER 2 – Kimberlite Background

Figure 2-1. Representative rimward geochemical evolution of spinel and mica in kimberlitic and other 'similar' rock types (e.g., orangeites, lamproites, carbonatites, UML).

Figure 2-2. The bulk-rock composition of kimberlites worldwide compared with other similar rock types plotted in bivariate charts of SiO_2 *vs*. TiO_2; MgO; K_2O; and Al_2O_3.

Figure 2-3. The isotopic composition of kimberlites compared with orangeites and aillikites in εNd(i) *vs*. $^{87}Sr/^{86}Sr_{(i)}$; and $\varepsilon Hf_{(i)}$ *vs*. $\varepsilon Nd_{(i)}$ space.

Figure 2-4. Global distribution of kimberlite magmatism from Tappe et al., (2018)

Figure 2-5. Distribution and representative ages of kimberlite clusters and other alkaline volcanism in southern Africa from Moore et al., (2008).

Figure2-6. Histogram showing the frequency distribution of global kimberlite occurrences (modified from Tappe et al., 2018).

Figure 2-7. The intrusion morphology of the different types of kimberlite pipes from Scott Smith, (2013).

Figure 2-8. The surface expression and vertical cross-sections through the main pipes of the Kimberley cluster shown alongside the local stratigraphy.

Figure 2-9. Internal structure of the Dutoitspan pipe.

Figure 2-10. Internal structure of the Wesselton pipe.

Figure 2-11. Chemical tomography of the lithospheric mantle sampled by the Kimberley kimberlites based on the composition of garnet xenocrysts; calculated Mg# of olivine; calculated shear-wave velocities.

CHAPTER 3

Figure 3-1. Schematic diagrams to illustrate the compositional zonation of an idealised olivine grain from the Kimberley kimberlites.

Figure 3-2. A map showing the main structural units of the Kaapvaal craton and a map of the known kimberlite intrusions in the Kimberley area.

Figure 3-3. The composition of olivine cores plotted in Mg# *vs.* NiO; MnO; and CaO space.

Figure 3-4. Kernel density estimate plots of the distribution of Mg# and CaO wt.% contents in olivine cores from the Kimberley kimberlites

Figure 3-5. Back-scattered electron images of olivine grains from the Kimberley kimberlites.

Figure 3-6. The compositions of the different olivine zones plotted in bivariate charts of Mg# *vs.* NiO; Mg# *vs*. MnO; and Mg# *vs.* CaO.

Figure 3-7. A bar chart of the average Mg# of olivine rims and internal zone (II) from different intrusions of the Kimberley cluster compared with previous studies of the Benfontein Sills and Wesselton kimberlite.

Figure 3-8. Back-scattered electron images show grains which contain rinds (a-c).

Figure 3-9. Back-scattered electron images showing the petrographic features of olivine grains from the Wesselton water tunnel sills complex.

Figure 3-10. Representative electron probe micro-analyser traverses across a normal zoned grain from the Bultfontein kimberlite.

Figure 3-11. Representative electron probe micro-analyser traverses across a reverse zoned grain from the Bultfontein kimberlite.

Figure 3-12. All electron probe micro-analyser traverses across olivine grain from the Bultfontein kimberlite plotted in bivariate charts of Mg# *vs.* NiO; Mg# *vs*. MnO; and Mg# *vs.* CaO.

Figure 3-13. The compositions of internal olivine zones (II) (Mg# *vs.* (100×) Mn/Fe; Mg# *vs*. (100×) Ca/Fe; and Mg# *vs.* (100×) Ni/Mg) compared with olivine in mantle rocks, magmatic rocks (bassalts, aillikites, melilitites, orangites) and experimental studies.

Table 3-1. Summarised petrographic features of the studied samples

Table 3-2. The compositions of different olivine zones in the Kimberley kimberlites.

CHAPTER 4

Figure 4-1. Map showing the location of the Kimberley cluster and the local intrusions, as well as detailes of the De Beers pipe internal geology.

Figure 4-2. Photomicrographs of the samples studied from the De Beers dyke, showing the porphyritic texture of olivine, magnesian ilmenite, macrocrystic phlogopite, and calcite laths set in a fine-grained mesostasis

Figure 4-3. Representative back scattered electron images and photomicrographs of olivine, phlogopite and magnesian ilmenite in the studied samples of the De Beers dyke.

Figure 4-4. Representative back scattered electron images and photomicrographs of magnesian ilmenite, spinel, calcite laths, and the replacement of olivine and monticellite in the studied samples of the De Beers dyke.

Figure 4-5. (A, B) Different olivine zones illustrated in plots of Fo mol. *vs.* NiO, and MnO. Compositions of phlogopite macrocryst cores and rims plotted in Cr_2O_3 *vs*. TiO_2 space. Compositions of rutile (I) plotted in Nb_2O_5 *vs*. Cr_2O_3 space.

Figure 4-6. Compositions of magnesian ilmenite plotted in (A) Cr_2O_3 vs. MgO, and (B) Cr_2O_3 *vs.* $Mg/(Mg + Fe^{2+})$ space. The composition of spinel plotted in $Fe^{3+}/(Fe^{3+}+Al + Cr)$ *vs.* $Fe^{2+}/(Fe^{2+}+ Mg)$, and TiO_2 *vs.* $Mg/(Mg + Fe^{2+})$ space.

Figure 4-7. Crystallisation sequence of the De Beers dyke. The inclusions in any given phase are demarcated by the accompanying italicised green text.

Table 4-1. Average major element compositions of phases contained in the De Beers dyke reported as wt.%

CHAPTER 5

Figure 5-1. Representative images showing the different petrographic features of coherent kimberlite from dykes/sills and root zone intrusions.

Figure 5-2. Back-scattered electron images showing the two textural types of apatite (Ap) in the Kimberley kimberlites. Textural generation (I): discrete euhedral grains; textural generation (II): radiating acicular aggregates.

Figure 5-3. Back-scattered electron images showing the textural relationships between apatite (Ap) and other groundmass phases in the Kimberley kimberlites.

Figure 5-4. Back-scattered electron images showing the textural relationships between apatite (Ap) and other groundmass phases in the Wesselton Water Tunnel sills.

Figure 5-5. SiO_2 wt.% *vs*. SrO wt.%, and $La_2O_3 + Ce_2O_3$ wt.% charts showing the compositions of apatite from the Kimberley kimberlites.

Figure 5-6. P *vs.* Si (a.p.f.u.), and S + LREE *vs*. Si (a.p.f.u) charts showing the compositions of apatite from the Kimberley kimberlites.

Figure 5-7. NiO (wt.%) *vs.* Mg# [Mg/(Mg+Fe) × 100] chart showing the composition of olivine in dyke/sill and root zone kimberlites from the Kimberley area. $Fe^{3+}/(Fe^{3+}+Al+Cr)$ *vs.* $Fe^{2+}/(Fe^{2+}+Mg)$ chart showing the compositions of spinel from dyke/sill and root zone kimberlites from the Kimberley area.

Figure 5-8. SiO_2 *vs*. SrO, F *vs.* P_2O_5, and $La_2O_3 + Ce_2O_3$ *vs*. CaO charts showing the composition of apatite from the Kimberley kimberlites. This data is compared with apatite from other kimberlites worldwide, and apatite from aillikites, carbonatites, and orangeites/lamproites.

Table 5-1. Summarised petrographic features of the studied samples

Table 5-2. Average major element composition of groundmass apatite in the studied samples

CHAPTER 6

Figure 6-1. A map showing the location of the major kimberlite mines in southern Africa, and the main kimberlite mines, kimberlite pipes, as well as dykes and sills in the Kimberley area.

Figure 6-2. Back-scattered electron image of the area of sample BK-1 used for reconstruction of the whole-rock composition.

Figure 6-3. The range of reconstructed and measured whole-rock compositions of sample BK-1 plotted in (A) FeO *vs* MgO, (B) SiO_2 *vs* MgO, and (C)Ni *vs* Mg# space.

Figure 6-4. The range of reconstructed whole-rock and melt compositions from Models I and IV plotted in MgO/CaO *vs* SiO_2/MgO space.

Figure 6-5. The range of reconstructed melt compositions from Step 4 of Models I and IV (Table 4), plotted against CO_2 solubility as a function of SiO_2+Al_2O_3 content.

Figure 6-6. MgO/CaO vs SiO_2/Al_2O_3 plot comparing the range of reconstructed whole-rock and melt compositions from this study (Table 2), and the compositions of experimentally produced melts in the peridotite+CO_2 and CAMS-CO_2 systems.

Table 6-1. Measured modal mineral abundances and the proportions of xenocrystic and magmatic components in olivine of sample BK-1.

Table 6-2. Measured whole-rock, and reconstructed whole-rock and melt compositions for Models I and IV.

Table 6-3. Reconstructed melt compositions parental to sample BK-1 on emplacement in the upper crust, compared with previously reconstructed compositions tested in experimental studies.

Table 6-4. Reconstructed whole-rock composition of sample BK-1 compared with worldwide whole-rock hypabyssal kimberlite data.

Table 6-5. Reconstructed primitive melt compositions parental to sample BK compared with previously estimates of primitive kimberlite melt/magma compositions.

TABLE OF CONTENTS

ABSTRACT ..... **II**

ACKNOWLEDGEMENTS ..... **VI**

DECLARATION ..... **VII**

PREFACE ..... **VIII**

LIST OF PUBLICATIONS ..... **XII**

LIST OF FIGURES & TABLES ..... **XIII**

TABLE OF CONTENTS ..... **XVII**

CHAPTER 1: INTRODUCTION **1**

RESEARCH AIMS 4

CHAPTER 2: KIMBERLITE BACKGROUND **7**

CLASSIFICATION AND COMPARISON WITH 'SIMILAR' ROCK TYPES 7

SPATIAL AND TEMPORAL DISTRIBUTION 12

INTRUSION MORPHOLOGY 13

KIMBERLITE ROCK TYPES 15

A PETROGRAPHIC OVERVIEW OF COHERENT KIMBERLITES 17

THE KIMBERLEY KIMBERLITE CLUSTER 21

PREVIOUS STUDIES OF THE KIMBERLEY KIMBERLITES 22

FIGURES 32

CHAPTER 3: KIMBERLITE METASOMATISM OF THE LITHOSPHERE AND THE EVOLUTION OF OLIVINE IN CARBONATE-RICH MELTS – EVIDENCE FROM THE KIMBERLEY KIMBERLITES (SOUTH AFRICA) **40**

ABSTRACT 41

INTRODUCTION 43

GEOLOGICAL SETTING, PREVIOUS WORK, AND SAMPLES 45

ANALYTICAL METHODS 47

PETROGRAPHY AND MINERAL CHEMISTRY 49

DISCUSSION 62

Conclusions 84
Acknowledgements 87
Figures 87
Tables 100

CHAPTER 4: CRYSTALLISATION SEQUENCE AND MAGMA EVOLUTION OF THE DE BEERS DYKE (KIMBERLEY, SOUTH AFRICA) 102

Abstract 103
Introduction 104
Geological setting and previous work 105
Samples and Methods 106
Petrography and mineral compositions 108
Discussion 117
Conclusions 122
Acknowledgements 125
Figures 126
Tables 133

CHAPTER 5: APATITE COMPOSITIONS AND GROUNDMASS MINERALOGY RECORD DIVERGENT MELT/FLUID EVOLUTION TRAJECTORIES IN COHERENT KIMBERLITES CAUSED BY DIFFERING EMPLACEMENT MECHANISMS 135

Abstract 136
Introduction 138
Kimberlite mineralogy 139
Geological setting, sample selection, and methods 141
Kimberlite petrography 142
Apatite petrography 144
Apatite composition 147
Discussion 148
Conclusions 161
ACKNOWLEDGMENTS 164

Figures 165

Tables 172

CHAPTER 6: A NEW APPROACH TO RECONSTRUCTING THE COMPOSITION AND EVOLUTION OF KIMBERLITE MELTS: A CASE STUDY OF THE ARCHETYPAL BULTFONTEIN KIMBERLITE (KIMBERLEY, SOUTH AFRICA) 176

Abstract 177

Introduction 178

Background 180

Geological Setting and Sample Description 183

Whole-rock and Melt Reconstruction Methodology 185

Results 189

Discussion 195

Conclusions 205

Acknowledgments 206

Figures 208

Tables 213

CHAPTER 7: CONCLUSIONS 219

REFERENCES 225

APPENDIX 1 – SUPPLEMENTARY MATERIAL TO CHAPTER 3 256

A1-1: Supplementary Figures (S1-S16) 257

A1-2: Supplementary Tables (S1-S6) 258

APPENDIX 2 – SUPPLEMENTARY MATERIAL TO CHAPTER 4 273

A2-1: Supplementary Figures (S1-S13) 274

A2-2: Supplementary Tables (S1-S5) 275

APPENDIX 3 – SUPPLEMENTARY MATERIAL TO CHAPTER 5 280

A3-1: Supplementary Figures (S1-S24) 281

A3-2: Supplementary Tables (S1-S2) 282

APPENDIX 4 – SUPPLEMENTARY MATERIAL TO CHAPTER 6 294

A4-1: Analytical methods 295

A4-2: Estimation of the amount of orthopyroxene, clinopyroxene and garnet available for assimilation. 297

A4-3: Calculation of melt fraction and CO_2 loss 297

A4-4: Whole-rock and Melt reconstruction template. 299

A4-5: Supplementary Figures (S1-S5) 300

A4-6: Supplementary Tables (S1-S3) 301

CHAPTER 1: INTRODUCTION

Kimberlites are igneous, holocrystalline, and often inequgranular rocks that crystallise from volatile-rich (i.e., CO_2 + H_2O), silica-undersaturated magmas. They commonly occur as regular steeply-dipping and partially eroded pipe-like diatremes associated with extensive sill and dyke complexes. The diatremes may transition into irregular root zone intrusions, or directly into feeder dykes. Kimberlite intrusions are volumetrically small and relatively rare (i.e., ~5,600 known intrusions worldwide – Tappe et al., 2018, and references therein). However, despite their rarity and volumetric insignificance, kimberlites occur on all continents (e.g. Jelsma et al., 2009; Yaxley et al., 2013) and have been emplaced throughout most of earth's history (i.e., from ~2.85 Ga to ~12 Ka – Henning et al., 2003; and Brown et al., 2012, respectively).

Kimberlite magmas originate from exceptionally deep within the Earth's mantle (i.e. >150 km, and potentially >600 km – e.g., Haggerty, 1994, Ringwood et al., 1992;). During their rapid ascent, kimberlite magmas entrain fragments of mantle and crustal wall-rock lithologies. Therefore, kimberlites entrained xenocrystic and xenolithic cargo provide a unique opportunity to study the structure, composition, and evolution of the sub-continental mantle. Moreover, kimberlite melts themselves can provide important constraints on melting processes, mantle dynamics, and the volatile budget of the deep Earth. In addition, the xenocrystic material entrained by kimberlites includes diamonds, and kimberlites host the largest volume of gem quality diamonds at the Earth's surface, making them the most common type of diamond mine. Due to the combination of these unique features, kimberlites have attracted extensive exploratory, economic, and scientific interest.

Despite the geological and economic importance of kimberlites and decades of dedicated research, there remain numerous unresolved issues that are integral to a comprehensive understanding of kimberlite petrogenesis and evolution. These include:

(1) The location of kimberlite source region(s), which may be within the lithosphere (e.g., Becker and le Roex, 2006; Gaffney et al., 2007; le Roex et al., 2003; Tainton and McKenzie, 1992); the shallow asthenosphere (e.g., Bailey, 1980, 1993; Moore et al., 2008; Tappe et al., 2013, 2017); the mantle transition zone (e.g., Ringwood et al., 1992); or as deep as the core-mantle boundary (Haggerty, 1994; Torsvik et al., 2010).

(2) The composition and mineralogy of the source region(s). This has been described as garnet lherzolite (e.g., Becker and le Roex, 2006; le Roex et al., 2003; Price et al., 2000; Stamm and Schmidt, 2017); garnet harzburgite (Girnis et al. 2011); garnet wehrlite (Sokol et al., 2013); majorite + wadsleyite (i.e., transition zone lithologies – Ringwood et al., 1992); garnetite (i.e., garnet + clinopyroxene ± olivine – Edgar and Charbonneau, 1993); or [carbonate] veined lherzolite or harzburgite (Mitchell, 2004). Most of these studies argue that the source region has been recently metasomatised and contains a carbonate component (i.e., dolomite or magnesite – e.g., Mitchell, 1995; and references therein), or, that melting occurs in presence of fluids enriched in $CO_2 \pm H_2O$ (e.g., Foley et al., 2013; Wiley, 1980).

(3) The composition of primitive kimberlite melts. These have been described as occurring anywhere in a spectrum from volatile-rich ($CO_2 + H_2O$) ultramafic silicate melts (e.g., Kopylova et al., 2007; le Roex et al., 2003; Price et al., 2000); through transitional silicate-carbonate melts (e.g., Brooker et al., 2011; Nielsen and Sand, 2008); to silica-poor or silica-free "carbonatitic" melts (e.g., Brett et al., 2015; Pilbeam et al., 2013; Russell et al., 2012). Alternatively, some authors advocate that primitive kimberlite melts have an alkali-chloride carbonatitic composition

(Kamenetsky et al., 2004; 2014), although this latter model remains controversial (e.g., see Kopylova et al., 2016).

(4) The extent to which kimberlite melts are effected by mantle contamination and assimilation. For instance, some authors argue that kimberlites are formed as 'carbonatitic' melts and obtain their 'kimberlitic' character (i.e., enrichment in Si and Mg) through the extensive assimilation of lithospheric mantle material (e.g., Brett et al., 2015; Dawson and Hawthorne, 1973; Howarth and Taylor, 2016; Kamenetsky et al., 2008; 2014; Kamenetsky and Yaxley, 2015; Russel et al., 2012). In contrast, other authors argue that extensive assimilation of mantle material is not feasible, and that the starting composition of kimberlites is essentially fixed (e.g., Tappe et al., 2013). In addition, it is uncertain when and where assimilation of mantle material occurs. Some authors suggest assimilation occurs prior to the initiation of ascent near the lithosphere-asthenosphere boundary (e.g., Arndt et al., 2010; Cordier et al., 2015; Howarth and Taylor, 2016), whereas others argue for assimilation during the last ~100 km of ascent (e.g., Stone and Luth, 2016).

(5) The origin of phases contained in kimberlite rocks. This concerns most mineral constituents (i.e., olivine, phlogopite, ilmenite, spinel, carbonates, and serpentine). Importantly, these phases (particularly olivine, carbonates, and serpentine) constitute a large volume of kimberlitic rocks, and therefore impart a strong control on their bulk composition. Kimberlites may contain phases of xenocrystic, antecrystic, magmatic, hydrothermal, mixed origins (e.g., Giuliani et al., 2016; Giuliani et al., 2017; Kamenetsky et al, 2008; Schultze, 2001).

(6) Controls on the mechanism(s) of emplacement of kimberlite magmas. Kimberlite intrusions may contain a variety of textural rock types (i.e., coherent and pyroclastic). In addition, there exist different modes of coherent kimberlite (i.e., planar dykes and sills *vs*. irregular root zone intrusions). The factors controlling emplacement styles may include variable amounts of degassing, country rock compositions, or external ground water availability (e.g., Lorenz, 1986; Sparks, 2013).

A significant problem in kimberlite research is that these issues are intrinsically linked. For example, the uncertainties surrounding the origin of mineral phases (and their contained zones) means that it is challenging to determine the composition of kimberlite magmas and melts. Without this knowledge, it is not possible to accurately constrain the location or composition of the kimberlite source region. Moreover, some of the issues raised above have only come to light relatively recently with the widespread application of modern analytical and imaging techniques (e.g., FE-SEM and LA-ICP-MS). For example, Fedortchouk & Canil, (2004) and Kamenetsky et al. (2008) recognised olivine grains contain a larger proportion of xenocrystic components than previoutly excepted (cf. Mitchell, 1986). In the decade since these observations, there have been a plethora of studies on kimberlitic olivine (reviewed in Giuliani, 2018), which have modified long-held views of kimberlite genesis, such as the proposed ultramafic composition of kimberlite melts. Therefore, despite decades of dedicated studies, there is still much to be learned about the petrography and petrogenesis of kimberlites.

Research aims

The principal aim of this thesis is to provide new constraints on the composition and evolution of kimberlites. To achieve this objective, I have undertaken a comprehensive petrographic and mineral chemical investigation of fresh coherent kimberlite samples from the Kimberley cluster

(South Africa). This study utilised a variety of microscopy instrumentation (i.e., transmitted and reflected optical light microscopy, conventional and field-emission scanning electron microscopy, and cold cathode luminescence microscopy). The petrographic studies included all mineral constituents, and provides details of mineral abundances, zonation, textural relationships, and inclusion populations (particularly mineral, but also fluid/melt). This petrographic data provides the necessary context for targeted geochemical analyses (by Electron Probe Micro-Analyser (EPMA)) of specific phases, and/or individual zones within these phases. These new results are combined with the abundant published data from the Kimberley kimberlites to reevaluate their petrogenesis.

The current study utilises kimberlite samples derived from multiple pipes of the Kimberley kimberlite cluster (South Africa), namely the Kimberley mine, Wesselton, Dutoitspan, De Beers, Bultfontein, the Wesselton Water Tunnel Sills [WWTS], and the De Beers dyke. Specific petrographic details and geochemical information is reported in the relevant chapters. The Kimberley cluster was chosen for this study for the two main reasons outlined below.

The Kimberley kimberlites constitute the type locality of archetypal kimberlites and have been the site of almost continuous mining for over a century. The result is that there exists a large amount of published data on the Kimberley kimberlites (e.g., Clement, 1982; Giuliani et al., 2017; Pasteris, 1980; Shee, 1985; Wagner, 1914; White et al., 2012; Williams, 1932) as well as their entrained xenoliths (e.g., Aoki ,1974; Bishop et al. 1975; Dawson & Smith 1977; Erlank et al. 1982, 1987; Gregoire et al. 2002, 2003; Giuliani et al., 2013; 2014; Hawkesworth et al. 1990; Jones et al. 1982; Konzett et al. 1998; Kramers et al. 1983; Lawless et al., 1979). The extensive base of knowledge provided by previous studies provides an excellent platform to address the outstanding issues in kimberlite petrology.

Secondly, some of the Kimberley kimberlites (i.e., Wesselton, Bultfontein, and Dutoitspan) are still active mines, and represent some of the deepest operational kimberlite mines on Earth (i.e., 995 m below the present-day surface; ~1.8 km below the surface at the time of emplacement). In addition, the Kimberley kimberlites are relatively young (i.e., ~82-93 Ma; e.g., Allsopp and Barrett 1975; Batumike et al. 2008; Fitch and Miller 1983; Li et al. 2010). The combination of these factors allowed for sampling of exceptionally fresh kimberlite. Such fresh samples are limited to a few localities worldwide (e.g., some Russian, Canadian and Greenland kimberlites), and are exceedingly rare from arid regions such as southern Africa.

CHAPTER 2: KIMBERLITE BACKGROUND

Classification and Comparison with 'Similar' Rock Types

Throughout this thesis, the term 'kimberlite' is used strictly in reference to archetypal kimberlites, which have previously been termed Group I or basaltic kimberlites (e.g., Smith, 1983; Wagner, 1914). Orangeites (previously termed Group II or micaceous kimberlites) have historically been considered part of a 'kimberlite clan'. In addition, the origins of kimberlites, olivine lamproites, and ultramafic lamprophyres (UML) have often been described and interpreted together, as if they are related (e.g., Dalton & Presnall, 1998; Dawson, 1971). However, the petrographic and geochemical differences between these rock types (summarised below) provides strong evidence that they should be considered as separate entities (Mitchell, 1995). Archetypal kimberlites form a distinct and discrete rock type which can be effectively distinguished from the other rock types mentioned above, based on a combined assessment of texture, mineralogy, as well as mineral and whole-rock geochemistry. This thesis is only concerned with coherent kimberlites, hence the term "kimberlite" is used to refer strictly to coherent varities and the conclusions reached can not nessisarily be applied to volcanoclastic rocks.

Texture, Mineralogy, & Mineral Chemistry

Kimberlites [as well as orangeites] are hybrid rocks that contain a complex mixture of xenolithic, xenocrystic, antecrystic, magmatic, and secondary components (Fedortchouk & Canil, 2004; Giuliani, 2018; Kamenetsky et al., 2008; Mitchell, 2008; Schultze, 2001). This results in their distinctive inequgranular texture, where discrete components (i.e., excluding xenoliths) may range in size from >10 cm to <1 μm. Kimberlites contain a predominantly magmatic groundmass assemblage that may consist of olivine, spinel group minerals, ilmenite,

perovskite, phlogopite-kinoshitalite mica, apatite, monticellite, sulfides/sulfates and calcite [phenocrysts]. These groundmass phases are set in a cryptocrystalline mesostasis which consists of a mixture of serpentine and calcite ± dolomite (e.g., Mitchell, 1986).

In contrast, orangeites may contain magmatic phases not observed in kimberlites (e.g., diopside-aegirine, Ba-K titanates, sanidine, zirconium silicates, K-richterite, and leucite), whereas monticellite is not present in orangeites (except as reaction phases surrounding entrained dolomitic xenoliths). In addition to the typical kimberlitic phases, aillikites (i.e., the UML type with the most similarities to kimberlites) may contain primary magmatic clinopyroxene and Ti-rich garnets (e.g., schorlomite, kimzeyite). In addition to mineralogical differences there are also general differences in the modal mineral abundances, where kimberlites are relatively enriched in olivine and primary calcite, but contain less phlogopite than orangeites. These textural and mineralogical features have been used to define kimberlites (e.g., Woolley et al., 1996). However, caution should be applied when using a textural and mineralogical classification alone, because some unevolved orangeites and aillikites (i.e., those lacking clinopyroxene, Ti-rich garnets, and other exotic minerals) may be mineralogically similar to kimberlites (e.g., Tappe et al., 2005). In these instances, further mineral chemical or whole-rock data is required for classification.

There are substantial differences in the compositions of groundmass minerals between these rock types (e.g., Fig. 2-1). Kimberlites display spinel evolution from TIMAC [titanian magnesian aluminous chromite] to MUM [solid solution between magnesian-ulvöspinel, ulvöspinel, and magnetite] (e.g., Mitchell 1986; Roeder & Schultze, 2008), mica evolution from phlogopite toward kinoshitalite (e.g., Mitchell 1986), and olivine rims with constant Mg# [Mg/(Mg+Fe) × 100] and decreasing NiO contents (e.g., Brett et al., 2009; Bussweiler et al., 2015; Giuliani, 2018; Kamenetsky et al., 2008). In contrast, orangeites display spinel evolution from Mg-chromite to Ti-magnetite (Mitchell, 1995), mica evolution toward tetraferriphlogopite

(Mitchell, 1995), and olivine rims with increasing Mg# at decreasing NiO contents (Howarth, 2018; supplementary material). Likewise, aillikite spinels evolve toward Ti-magnetite (but at a lower Cr# [Cr/(Cr+Al)] than orangeites), micas evolve toward tetraferriphlogopite (but at higher Al concentrations than orangeites), and olivine displays decreasing Mg# and NiO contents (Veter et al. 2017).

Whole-rock Chemistry

Determining the geochemical characteristics of kimberlites is complicated because their primary composition is obscured by alteration, incorporation and assimilation of mantle and crustal material, degassing, and differentiation (see chapter 6). For these reasons the whole-rock compositions of kimberlites do not represent magma or melt compositions (e.g., Mitchell, 2008).

Schemes have been devised to assess the extent of crustal contamination on whole-rock samples (e.g., Clement's contamination index – Clement 1982). However, these screening measures do not account for the other processes listed above. In some instances, these problems can be avoided by analysing minerals which have an entirely magmatic origin (e.g., perovskite for Sr-isotopes and trace element abundances). The drawback of such an approach is that it can only provide very specific constraints (i.e., certain isotope systematics), or relies on appropriate distribution coefficients (which are often not available) for inferences to be made about the kimberlite melt. To determine, the major element composition of primitive kimberlite melts various reconstruction techniques have been employed (see chapter 6 for further details). Previous kimberlite melt reconstructions can be placed into one of three categories: (1) whole-rock analyses of aphanitic kimberlites (e.g., Kopylova et al., 2007; Price et al., 2000; Shee, 1985); (2) subtraction of the xenocrystic components from whole-rock compositions (e.g., Kjarsgaard et al., 2009; Nielsen and Sand, 2008); and (3) projections in geochemical plots using

large whole-rock datasets from a single locality (e.g., Becker and le Roex, 2006; le Roex et al., 2003;).

Despite the fact that whole-rock compositions do not reflect melt/magma compositions, samples of kimberlites deemed to be fresh, uncontaminated, and free of large xenocrystic components define a sufficiently narrow range to be useful in distinguishing kimberlites from other similar rock types (Fig. 2-2). It is stressed here that these compositional ranges simply represent the variations in modal mineralogy between different samples, a statement which is equally true for the other similar rock types (e.g., orangites). Samples of 'fresh' kimberlite contain low SiO_2 and high MgO (~18-35 wt.%), moderate CaO and FeO_t (~6-15 wt.%), coupled with low Al_2O_3 (<2.6 wt.%), TiO_2 (<4.5 wt.%), Na_2O (<0.3 wt.%), and K_2O contents (<1.5 wt.%) (e.g., Becker and le Roex, 2006; Kjarsgaard et al., 2009; le Roex et al., 2003; Mitchell, 1986). The volatile contents of kimberlites are highly variable (i.e., ~2-14 wt.% H_2O and ~1-15 wt.% CO_2) and there remains much debate as to their origin (i.e., primary *vs*. secondary). However, most kimberlites contain $CO_2 > H_2O$ (Mitchell, 1986). In contrast, orangeites commonly contain higher K_2O (up to ~7 wt.%), Al_2O_3 (~2-6 wt.%), and SiO_2 contents (~35-40 wt.%). Moreover, most orangeites contain $CO_2 < H_2O$. These compositional differences reflect their different mineralogy and modal mineral abundances, i.e., orangeites are enriched in phlogopite, contain primary clinopyroxene and K-richterite, yet are generally poor in olivine and primary calcite (e.g., Mitchell, 1995). Aillikites display more subtle differences in whole-rock chemistry when compared with kimberlites, i.e. higher TiO_2 (2.5-3.8 wt.%), CaO (13-25 wt.%), CO_2 (10-20 wt.%) and Al_2O_3 (i.e., up to 3.5 wt.%), and lower MgO (~15-20 wt.%), with broadly similar SiO_2 contents (17-29 wt.%) (e.g., Tappe et al., 2006; Rock, 1991). The main difference is the Mg# of aillikites (i.e., 60-77; Tappe et al., 2006), which is generally lower than kimberlites (i.e., 74-89; le Roex et al., 2003).

Kimberlites are characterised by extreme enrichment in incompatible and light rare earth elements (LREE), and moderate depletion in heavy rare earth elements (HREE). Therefore, kimberlites have relatively simple and linear REE patterns (normalised to chondrite). Most kimberlite samples have LREE to HREE ratios (i.e., La/Yb_N) in the range of 80 to 200 (e.g., le Roex et al., 2003; Mitchell, 1986).

Kimberlites, orangeites, and aillikites all have similar REE patterns (Mitchell, 1995), although aillikites are slightly more enriched in HREEs (i.e., La/Yb_N = 70-140). Several trace element ratios have been used to discriminate kimberlites from orangeites. For example, kimberlites have higher Ce/Pb ratios (>22), and lower Th/Nb (<1.1), La/Nb (<1.1), and Ba/Nb (<12) ratios when compared with orangeites (Becker and le Roex, 2006; Mitchell, 1986).

Kimberlites are defined by low initial $^{87}Sr/^{86}Sr$ (~0.703-0.705), and Nd and Hf isotopes which range from slightly enriched to slightly depleted relative to the chondritic uniform reservoir, i.e., ε_{Hf} of -10 to +10, and ε_{Nd} of -5 to +6 (Becker and le Roux, 2006; Griffin et al., 2014; Nowell et al., 2004; Smith, 1983; Tappe et al., 2017; Woodhead et al., 2009; Fig. 2-3). In addition, southern African kimberlites (including the Kimberley kimberlites) have radiogenic yet variable $^{206}Pb/^{204}Pb$ (18.45-20.05) and $^{207}Pb/^{204}Pb$ (15.52-15.72). These isotope ratios overlap modern ocean island basalt (OIB) which provide evidence that kimberlites originate from the convecting asthenosphere. In contrast, orangeites display significantly higher $^{87}Sr/^{86}Sr$ values (i.e., ~0.707-0.712 – Mitchell, 1995; Smith, 1983), coupled with more enriched Nd and Hf isotopes (ε_{Hf} of -25 to -3, and ε_{Nd} of -15 to -5 – Nowell et al., 2004), which are interpreted to represent derivation from metasomatised lithosphere. In contrast, aillikites, and more broadly UML's, exhibit Nd and Sr isotope compositions that overlap those of kimberlites (e.g., Tappe et al., 2006), and likewise are interpreted to have significant input from the asthenosphere.

Spatial and Temporal Distribution

Kimberlites occur on all continents of Earth (e.g. Jelsma et al., 2009; Yaxley et al., 2013 – Fig. 2-4) in spatially restricted clusters of up to 20 intrusions (i.e., excluding dykes and sills) spaced <1 km apart from one another. There is usually a spacing >2 km between clusters (Mitchell, 1986 and references therein). Multiple kimberlite clusters define a field (containing in the order of 100 individual intrusions), and numerous kimberlite fields may form part of a larger kimberlite province (e.g., the southern African kimberlite province – Fig. 2-5).

Individual kimberlites as well as entire kimberlite clusters are commonly emplaced along, or roughly follow, pre-existing lithospheric-scale structures (e.g., terrane boundaries, large dyke swarms, fracture systems, incipient rifts – Jelsma et al., 2009). These structural features are thought to provide pathways of least resistance and therefore facilitate kimberlite intrusion at or close to surface (e.g., Jelsma et al., 2009; Mitchell, 1986). It is common for multiple periods of kimberlite magmatism to exploit the same lithospheric pathways.

The southern African kimberlite province (which includes the Kimberley kimberlites) hosts at least eight distinct periods of magmatism, where several clusters may form during each period (e.g., Mitchell, 1986; Moore et al., 2008). Kimberlite activity across the southern Africa province extends from the Precambrian (i.e., ~1.6-1.8 Ga; Kuruman province – Donnelley et al., 2012) to the late Cretaceous (i.e., ~71.5 Ma; Gibeon province – Davies et al., 2001). The mid Cretaceous (i.e., 80-90 Ma) saw the highest abundance of kimberlite intrusions and was widespread across southern Africa (as well as Brazil – e.g., Jelsma et al., 2009). The Kimberley cluster, as well as the Orapa, and Northern Lesotho clusters were all emplaced during this mid-Cretaceous period (Allsopp & Barrett, 1975; Davis, 1977; Kramers & Smith, 1983; Mitchell, 1986; Moore et al., 2008;).

This temporal clustering of kimberlite emplacement ages in southern African is replicated globally. Tappe et al., (2018) recently compiled worldwide kimberlite emplacement

ages, which show periods of enhanced magmatic activity at ~1200-1075 Ma, 600-500 Ma, 400-350 Ma, and 250-50 Ma (Fig. 2-6). These authors note that the above listed periods of magmatism account for ~84% of known kimberlite intrusions.

Intrusion Morphology

The morphology of kimberlite pipe was first accurately described in the seminal work of Hawthorne, (1975). Since this early work the morphology of kimberlite intrusions has been based on generalized models (e.g., Field and Scott Smith, 1999; Scott Smith et al., 2013). The shape of a kimberlite pipe is thought to be strongly influenced by country rock competency, and therefore kimberlite occurrences worldwide display different shapes (Fig. 2-7). Most Cretaceous-aged southern African kimberlites form "Type 1" pipes (Field and Scott Smith, 1999). This is a result of their intrusion through the consistent and laterally extensive sedimentary rocks of the Karoo Supergroup. However, older kimberlites such as Permian-aged Jwaneng pipe pre-dates the Stromberg lavas and has different pipe infill structures (Field and Scott Smith, 1999)

The description below of the morphology of a typical type 1 kimberlite pipe uses non-genetic terms; therefore, the morphological zones described are not related to emplacement mechanisms (e.g., both pyroclastic and coherent rocks may occur in the diatreme zone).

Type 1 kimberlite pipes form deep intrusions (i.e., ~2-2.5 km from surface to their feeder dyke; data from Clement, 1982; and Hanson et al., 2009). A crater zone may be present at the highest stratigraphic position, although this zone is commonly removed by erosion (including in the Kimberley kimberlites). The original presence of this zone is inferred by its rare preservation in some (usually younger) kimberlite occurrences (e.g., Igwisi hills [Tanzania] – Brown et al., 2012; Fort à la Corne [Canada] – Leckie et al.,1997; Orapa [Botswana] – Field et al., 1997; Pimento Bueno [Brazil] – Masun & Scott Smith, 2008).

The crater zone overlies the diatreme zone, which usually constitutes most of the kimberlite intrusion by volume (i.e., vertical extensions of up to ~1000m – Field and Scott Smith, 1999). This diatreme is usually regular and conical in shape, distinguished by its steeply dipping almost vertical contacts with the host rock (i.e., 75-85 degrees) that taper inward with depth (e.g., Fig. 2-7 – Field & Scott Smith 1999; Hawthorne, 1975; Scott Smith et al., 2013).

The diatreme zone may transition into a complex and irregular root zone at depth, although the depth of this transition is highly variable between pipes. The root-zone may contain numerous discrete 'pillars', which coalesce at a higher stratigraphic position, as well as so called "blind" intrusions that do not reach the surface (Fig. 2-7; Clement, 1982). The root zone of a kimberlite pipe may contain contact breccias and, in most cases, these breccias show little or no evidence of movement, i.e. they were probably formed by explosive release of volatiles *in situ.* In addition, contact breccias may also be located at higher startgaraphic positions such as within the crater facies (e.g., Fig. 3 of Field et al., 2008).

The diatreme and root zones (and probably the crater zone) of an individual kimberlite pipe commonly contain multiple discrete intrusions, termed units. The number of units in a pipe is highly variable within a kimberlite cluster. For example, in the Kimberley cluster the Dutoitspan pipe contains at least 18 units, the Wesselton pipe at least 10 units, whereas the Bultfontein pipe contains only three known units (Clement, 1982). Individual units may have distinct xenolith and diamond populations, as well as diamond grades, which can vary by as much as a factor of 10 (Clement, 1982). Contacts between units are sharp and often have a welded appearance with prominent slickensides (Clement, 1982). Pasteris, (1980) reported discernible variations in groundmass spinel chemistry between units of the De Beers pipe, which have also been observed elsewhere (e.g., Koffiefontein – Nadioo et al, 2004). However, these variations are not apparent in the different units of the Wesselton pipe (Shee, 1985; this study). The above observations led to the conclusion that each unit represents a discrete batch

of magma (e.g., Clement, 1982; Naidoo et al., 2004; Pasteris, 1983; Shee, 1985) and it is evident from field relationships that previous intrusions must have completely solidified before the intrusion of subsequent magma batches. More recently, high precision geochronology has revealed that different units of the Renard 2 kimberlite (Canada) were emplaced over a period of ~20 Ma (Ranger et al., 2018). However, it is unclear if this protracted emplacement history is applicable to the Kimberley kimberlites.

Finally, kimberlite pipes are generally associated with extensive dyke and less common sill complexes. Dykes and sills that are associated with a kimberlite pipe may intrude pre-, syn-, or post-emplacement of the pipe. In addition, there exist multiple examples of sills and dykes with no obvious association with a kimberlite pipe (e.g., Benfontein – Dawson and Hawthorne, 1975). Dykes and sills are commonly <1 meter in width, although some sills may be slightly thicker (i.e., ~2 meters at Mayeng – 70 km north of Kimberley; Apter et al., 1984). These intrusions are planar and have sharp contacts with host-rocks where the latter show little evidence of thermal metamorphism, thus indicating a relatively low temperature of emplacement for kimberlite magmas.

Kimberlite Rock Types

The rocks that infill a kimberlite pipe can be divided into two textural types: coherent kimberlite (CK) and volcaniclastic kimberlite (VK). This division is based purely on textural grounds (Scott Smith et al., 2013). However, there are also mineralogical differences in that only VK contains clinopyroxene, as well as a higher abundance of serpentine at the expense of carbonates and monticellite (e.g., Skinner and Marsh, 2004).

Volcaniclastic kimberlites show evidence of fragmentation (e.g., pyroclasts, magmaclasts, autoclasts), interpreted to represent formation following fluidisation and degassing. Volcaniclastic rocks are most commonly found within the crater and upper diatreme

zones and can be further divided into three sub-categories: pyroclastic, re-sedimented volcanoclastic, and epiclastic volcanic. Because this thesis is concerned only with CK (see the next paragraph) VK rock types are not discussed further. The interested reader is referred to Scott Smith et al., (2013) for a comprehensive guide to the textural classification and nomenclature of kimberlite rock types.

Coherent kimberlites exhibit primary and homogeneous magmatic features, with little or no evidence of fragmentation (Nowicki et al., 2008; Skinner and Marsh, 2004; Scott Smith et al., 2013; van Straaten et al., 2011). Coherent kimberlites crystallise from kimberlitic magmas before degassing or fluidisation (e.g., Clement and Skinner 1985). Coherent kimberlite is usually (but not always) an intrusive rock (i.e., hypabyssal kimberlite [HK]), where it commonly occurs within the root zone, in the dyke and sill systems which accompany kimberlite pipes, and rarely in the lower diatreme zone. In addition, there rare extrusive coherent kimberlite lavas exist, which are only preserved in the crater zone (i.e., Igwisi hills [Tanzania] – Brown et al., 2012; Central Angola – Jelsma et al., 2013; Tokapal [India] – Mainkar et al., 2004).

Although the magmatic nature of dyke/sill kimberlites is not debated, direct magmatic crystallisation of root zone CK is not accepted by all authors. Sparks et al., (2006) note that it remains unclear from a volcanological standpoint why intrusive CK forms different intrusion morphologies, i.e., irregular root zones *vs.* planar dykes and sills. Sparks et al. (2006) alternatively suggests that root zone CK represents intensely welded pyroclastic kimberlite (Brown et al., 2008; Sparks et al., 2006). It is noteworthy that CK may show transitional textures to VK (e.g., Gaudet et al., 2018; Hetman et al., 2004; Mitchell et al., 2009; Skinner & Marsh, 2004). The explanation for these textures highlights the difference in these two models (i.e., magmatic *vs*. pyroclastic) for formation of root zone CK:

1. The “freezing” of a fluid segregation front fuelled by exsolving volatiles, which cause disruption and increasingly explosive emplacement (e.g., Hetman et al. 2004; Muntener & Scott Smith 2013; Skinner & Marsh, 2004). This is interpreted to represent magma degassing in response to decompression (i.e., surface breakthrough).
2. Pyroclastic material which has been variably welded in a fluidised system (Brown et al., 2008; Sparks et al., 2006; Stripp et al., 2006). Similar processes have been invoked to explain the formation of pipe filling coherent kimberlites (e.g., Nowicki et al. 2008).

A Petrographic Overview of Coherent Kimberlites

Coherent kimberlites do not appear to have undergone fluidization, fragmentation, abundant incorporation of crustal material, or major degassing (see the previous section). The resultant relatively low porosity and their deep stratigraphic position makes CK generally less susceptible to secondary alteration. The combination of these factors means that CK is closer (relative to VK) to representing a kimberlite magma composition. Hence, CK is often used in detailed petrographic studies. Nevertheless, all CK still contains xenocrystic mantle fragments and has been subjected to at least some alteration (i.e., deuteric, hydrothermal, or both). Therefore, no CK can directly represent a melt composition (see Chapter 6).

Coherent kimberlite is a holocrystalline and typically inequgranular textured rock, which ranges from aphanitic to macrocrystic. The discrete components contained in kimberlites (i.e., excluding xenoliths) are often classified based on their size and shape, as megacrysts (1-20 cm, rounded), macrocrysts (0.5-10 mm, rounded), (micro-)phenocrysts (≤0.5 mm, subhedral-euhedral), and groundmass phase (generally ≤0.05 mm, subhedral-euhedral) (e.g.,

Mitchell, 1986). It is this hybrid nature which plays a major contributing role to the heterogeneous composition and texture of kimberlites.

The megacryst assemblage contained by kimberlites is unique (i.e., the same assemblages do not occur in other 'similar' rock types). Megacrysts fall into one of two chemical classifications - Cr-rich or Cr-poor (e.g., Eggler et al. 1979; Moore & Belousova, 2005), with the Cr-poor suite being more abundant. The megacryst suite includes orthopyroxene, clinopyroxene, garnet, olivine, ilmenite, phlogopite, and zircon. These minerals commonly occur as discrete phases, although rarely as intergrowths, or inclusions in other members of the megacryst suite.

The macrocryst assemblage consists of olivine, phlogopite, garnet, clinopyroxene, ilmenite, spinel, and lesser orthopyroxene (i.e., typical mantle phases, and/or members of the megacryst suite). Some of these phases (particularly pyroxenes and garnet) show evidence of reaction with the host kimberlite melt and contain inclusions of other typical mantle minerals (e.g., pyroxenes and garnet included in olivine macrocryst cores – see chapter 3).

Phenocrysts and micro-phenocrysts are predominantly olivine and phlogopite, but some intrusions may also contain calcite and ilmenite. The groundmass phases include olivine, phlogopite-kinoshitalite mica, apatite, spinel group minerals, perovskite, monticellite, ilmenite, and accessory phases (e.g., barite, sulfides, baddeleyite).

The aforementioned components are set in a cryptocrystalline mesostasis, which consists of variable proportions of serpentine and calcite, although some intrusions may also contain dolomite. Minor amounts of chlorite, smectite, and brucite may also be present. In addition, the mesostasis phases (as well as other secondary phases) may replace pre-existing components.

Whilst the descriptive textural terms outlined above are useful, they provide no information as to the origin of these phases. It has been demonstrated that many phases in

kimberlites have multiple paragenesis (e.g., ilmenite may be a xenocryst, a magmatic phase, and a hydrothermal alteration product – Mitchell, 1986). More recently it has been shown that individual grains may contain zones with different origins including magmatic and xenocrystic (e.g., olivine, phlogopite, spinel – Fedortchouk & Canil, 2004; Giuliani et al., 2016; Giuliani, 2018; Kamenetsky et al., 2008; Schultze, 2001; Shee, 1985). Importantly, grains that contain zones of distinct origins may fall into any of the above listed size/shape classifications (i.e., megacrysts, macrocrysts, and phenocrysts).

Additional genetic classification of these phases (or zones therein) is possible only if additional information is available (i.e., mineral chemistry and SEM-based petrography). The benefit of a genetic classification scheme is that it allows for identification of only the magmatic components, which is vital to accurately define any rock type and assess its variability (see Woolley et al., 1996). In this thesis, components are classified as: (1) xenocrysts; (2) kimberlite-metasomatised material; (3) kimberlite antecrysts; (4) magmatic kimberlite phases; or (5) secondary phases.

The xenocrystic components of kimberlites are derived from the disaggregation of mantle wall rocks. These predominantly include material derived from mantle peridotites, with a lesser contribution from other subordinate mantle and crustal lithologies (e.g., eclogites, pyroxenites, MARID [Mica-Amphibole-Rutile-Ilmenite-Diopside], granulites). The major phases that have a xenocrystic origin in kimberlites are olivine, orthopyroxene, clinopyroxene, garnet, phlogopite, ilmenite, K-richterite, zircon, and diamond.

Kimberlite metasomatised material includes mantle phases which have undergone metasomatic enrichment that can be directly linked to kimberlite activity (see also chapter 3 and 4). This classification may include (but may not be limited to) minerals of the megacryst suite (e.g., Kargin et al., 2017; Kopylova et al., 2009; Pivin et al., 2009) and sheared peridotites (e.g., Ionov et al., 2010, 2017; Kargin et al., 2017; Katayama et al., 2009). In addition,

clinopyroxene and garnet that appear to have formed during kimberlite-metasomatism of some peridotites are included here (e.g., Aulbach et al., 2013; Fitzpayne et al., 2018b; Grégoire et al., 2003; Kargin et al., 2016; Simon et al., 2003).

Antecrysts are the direct crystallisation product of a previous pulse of genetically related (i.e., kimberlitic) magma. However, the distinction between kimberlitic antecrysts and kimberlite metasomatised material may be somewhat blurred in cases such as megacrysts, where their mode of formation is debated (e.g., cognate/antecrystic – Moore & Loch, 2001; *vs*. metasomatic – Kopylova et al., 2009). Kimberlite antecrysts have only recently been described - Giuliani et al. (2016) attributed high Cr-Ti phlogopite compositions to crystallisation from a previous pulse of kimberlite melt (see also chapter 4). In addition, matrix phases in polymict breccia xenoliths should also be considered antecrystic components (Giuliani et al., 2013).

The common magmatic components in kimberlites include: olivine, spinel group minerals, magnesian ilmenite, perovskite, apatite, phlogopite-kinoshitalite, monticellite and calcite (e.g., Mitchell, 1986). Accessory phases may include rutile, Ni-sulfides, sulfates (e.g., barite), baddeleyite, Ba-Sr carbonates and native copper.

The origin of the late stage mesostasis (i.e., calcite, and sometimes lesser dolomite) is contentious. Carbonate phases have been argued to be of mixed (i.e., magmatic, hydrothermal, secondary) origin (e.g., Giuliani et al., 2018; Soltys et al., 2018). The origin of serpentine is less clear. Some authors argue for a purely magmatic origin for serpentine (e.g., Mitchell, 1986, 2008, 2013), whereas others suggest an entirely secondary external origin (e.g., Afanasyev et al., 2014; Brooker et al., 2011; Sparks et al., 2006, 2009; Stripp et al., 2006). Some recent studies have advocated that these mesostasis phases crystallised from fluids of mixed origin (i.e., deuteric and crustal – e.g., Giuliani et al., 2014, 2017). In addition, to their occurrence as interstitial phases, these mesostasis phases may replace pre-existing minerals (i.e., olivine and monticellite – see chapter 4).

Finally, there are unambiguously secondary phases such as bultfonteinite and pectolite and certain generations of serpentine (see Mitchell, 2008). These phases are commonly attributed to crystallisation from external fluids and/or local contamination of the kimberlite magma by their crustal host rocks.

The Kimberley Kimberlite Cluster

The Kimberley cluster is located in the approximate centre of the Western terrane of the Kaapvaal craton (see Fig. 3-2a). The Kimberley kimberlite cluster contains five main pipes (i.e., The Kimberley mine [also known as "The Big Hole"], De Beers, Dutoitspan, Bultfontein, and Wesselton – e.g., Fig. 3-2b), numerous smaller pipes (e.g., Kamfersdam, Otto's Kopje, and St. Augustine's), as well as extensive dyke and sill complexes (e.g., Wesselton water tunnel sills, Wesselton floors sill complex, and the Benfontein sills). In addition, there exist some 30 known kimberlite pipes within a 10 km radius of Kimberley, although these intrusions are not considered in this study due to poor exposure. Together these intrusions represent the type-locality of kimberlites. Most of the pipes in Kimberley and the surrounding area have been mined to some extent, although many by artisanal miners.

The surface areas at the time of emplacement was estimated by Clement (1982) based on projections from current exposure based on the estimated amount of erosion. However, these may represent overestimates, because the extent of erosion has since been revised downwards. Nevertheless, the main pipes have modelled surface areas as follows: Bultfontein = 9.7 ha, Dutoitspan = 10.8 ha, Wesselton = 8.7 ha, De Beers = 5.1 ha, and Kimberley mine = 3.7 ha. The size of the Kimberley pipes makes them typical of kimberlite intrusions worldwide emplaced in the last 250 Ma (mean = 10.1 ha; median = 2.7 ha – Tappe et al., 2018)

Local Geology

The Kimberley kimberlites, as well as the nearby Koffiefontein cluster and the Jagersfontein pipe are all emplaced along a NW-SE trending lineament (Jelsma et al., 2004). This lineament parallels a major system of fractures in the local area (Mitchell, 1986, and references therein). It was suggested by Mitchell (1986) that the dykes that feed these pipes all exploit the same zone of weakness, and hence the kimberlite pipes all show the same alignment. Examples of such aligned feeder dykes are exposed at depth in the Kamsferdam and Bultfontein pipes of the Kimberley cluster.

The Kimberley kimberlites are hosted by a package of sedimentary and volcanic rocks, which overlie Archean basement (e.g., Fig. 2-8). From the present day surface the upper ~100 meters of the stratigraphic column contain rocks of the Dwyka formation (part of the Karoo sequence). This formation predominantly consists of shales, with minor interbedded sandstones and siltstones. These sedimentary units were intruded by thick (i.e., 30-40 meters) Karoo dolerite sills at ~180-190 Ma (e.g., Jourdan et al., 2007). These dolerite sills commonly form a physical barrier to kimberlite intrusion (e.g., the Benfontein sills – Dawson and Hawthorne, 1973). The Karoo sequence overlies andesitic-basaltic lavas of the Ventersdorp supergroup (~2.7 Ga – Poujol et al., 2003), which locally contain thick units of quartzite (i.e., up to 250 meters), and a minor conglomerate unit at the base (i.e., up to 25 meters thick). The Karoo and Ventersdorp sequences unconformably overlie Archean basement rocks, which comprise granitic and amphibolite gneisses, with local development of talc schists (Clement, 1982).

The Kimberley pipes contain upper crustal xenoliths that derive from stratigraphic units which are no longer present in the local area (but do occur elsewhere), which indicates that since the time of kimberlite emplacement (~80-93 Ma) the Kimberley area has undergone ~850 meters of erosion (Hanson et al., 2009).

Previous Studies of the Kimberley kimberlites

Mapping and Structure

The main pipes of the Kimberley cluster were mapped in detail by Clement (1982). Examples of internal structures from Wesselton and Dutoitspan pipes are shown in Figs. 2-9 and 2-10, and the De Beers pipe in Fig. 4-1. In many instances, underground mapping has allowed for the determination of a relative emplacement sequence of the different units within an individual pipe. The general structure and morphology of the main pipes is typical of class one pipes (see the previous section).

The Wesselton Water Tunnel Sills (WWTS) were initially mapped by Hill (1977), and in more detail by White et al. (2012). The latter authors also reported field relations and structural data. This sill complex intrudes the contact between a Karoo dolerite sill and Dwyka shales and covers an area of over 70 ha (Shee et al., 1991). This sill complex is probably fed by pre-emplacement dykes, which are associated with the main Wesselton pipe, and this sill complex is crosscut by the main pipe. White et al. (2012) identified three separate units in this sill complex.

The Benfontein sills were mapped by Dawson and Hawthorn, (1975) and contain three discreet sills (the upper, middle, and lower sills). The entire complex was argued to have formed by multiple (i.e., more than three) injections of small volumes of melt that then underwent *in situ* differentiation. There is no clear feeder system to this sill complex, and it is not associated with any known pipes.

Whilst the Kimberley kimberlites have been the subject of extensive studies (see below) a limitation of this locality is that new exposures are rare, and hence there must be a reliance on previous mapping studies (e.g., Clement, 1982)

Petrology

Coherent kimberlites from the Kimberley area have mineralogical and petrographic features typical of kimberlites worldwide (see the previous section "*A petrographic overview of coherent kimberlites*"; Clement, 1982; Shee, 1985) and will therefore not be repeated here in detail. This section summarises the coverage of different pipes and emplacement styles of CK in previous studies of the Kimberley cluster.

The most detailed study of root zone CK from the Kimberley kimberlites is that of Shee (1985). This author found that the macrocryst-rich samples from the Wesselton kimberlite have broadly similar petrography, whole-rock compositions, and mineral chemistry. In contrast, the sill complex studied by this author (i.e., the WWTS) exhibit distinct petrography, modal mineral abundances, whole-rock compositions, and mineral chemistry. This led to the conclusion that macrocryst-rich samples had not undergone significant pre-emplacement fractionation, in contrast to the sills and dykes. The notion that sills/dykes are the products of fractionated magmas appears to be true for the samples studied by Shee (1985), but it remains unclear if this is applicable to all dykes and sills. Not stressed by Shee (1985) is the extensive mantle contamination that effected macrocryst-rich HK material in the WWTS (e.g., le Roex et al., 2003).

The carbonate-rich sill and dyke complexes of the Kimberley cluster have attracted significant attention. This is because they are well exposed, either at the present-day surface (e.g., Benfontein Sills) or by deep mining activity, and they are often exceptionally fresh (e.g., Chapter 4). Examples from well-studied complexes, highlighting the diverse nature of these intrusions, are listed below.

Petrographic descriptions and/or mineral chemistry of the Benfontein Sills have been reported by Boctor and Boyd (1981), Gaspar and Wyllie (1984), Howarth and Taylor (2016), McMahon and Haggerty (1984), and Mitchel (1994). Some samples contain minerals (i.e., olivine, spinel) with compositions indistinguishable from the main kimberlite pipes. In contrast,

other samples appear to have undergone early crystal fractionation (i.e., prior to olivine/spinel crystallisation). This is exemplified by the chemistry of olivine, where Arndt et al., (2010) reported olivine rims with compositions typical of the Kimberley kimberlites (i.e., Mg# = 88), whereas Howarth and Taylor (2016) report two populations in the same sample (i.e., Mg# ~87 and ~89). The presence of multiple olivine rim populations in a single sample may indicate syn- or post-emplacement magma mixing or crystallization from multiple injections of variably differentiated magma.

The Wesselton Water tunnel sills have been studied by Hill (1977), Mitchell (1991), Shee (1985), Shee et al. (1991), White et al. (2012), and. Unlike the variably fractionated magmas parental to the Benfontein sills complex, it has been argued that the WWTS have undergone significant pre-emplacement fractionation (e.g., Shee et al., 1991). This is based on the Mg- and Cr-depleted mineral chemistry of spinel, ilmenite, and phlogopite, which is unlike any other intrusions of the Kimberley cluster. In addition, these sills contain distinct xenolith populations and heavy mineral concentrations (i.e., lacking garnet facies material and diamond).

The only major dyke in the Kimberley area to have been the subject of detailed studies is the De Beers dyke (also known as the Eyebrow dyke). This dyke was investigated by Donaldson & Reid (1982) as well as Exley & Jones, (1983). Using field relationships (i.e., sharp unit contacts, flow alignment parallel to contacts), Donaldson & Reid (1982) showed that this dyke formed from multiple injections of magma. Based on variations in whole-rock compositions and modal mineral abundances between different units of this dyke, Donaldson & Reid (1982) argued that the dyke had undergone variable degrees of pre-emplacement fractionation of olivine, ilmenite, spinel, phlogopite, and serpentine. However, it is possible that these differences in modal abundance, and therefore whole-rock chemistry, simply reflect syn-emplacement differentiation by flow processes (see chapter 4 for further details).

In summary, various dykes and sills in the Kimberley area show some evidence of pre-emplacement fractionation. It appears that the WWTS represents an endmember of extreme pre-emplacement fractionation. The Benfontein sills may represent a mixture of fractionated and unfractionated magmas. In contrast, the data for the De Beers dyke is inconclusive. Therefore, it appears that some, but not all, dyke/sills were potentially produced by fractionated magmas. In contrast, there is yet to be any evidence that root zone HK formed from fractionated magmas.

Isotopes and Geochronology

The archetypal classification of the Kimberley kimberlites based on their petrographic features, mineralogy, and mineral compositions (e.g., Clement, 1982; Shee, 1985) is corroborated by their Sr-Nd-Hf-Pb isotope systematics (Becker and le Roux, 2006; le Roux et al., 2003; Nowell et al., 2004; Smith, 1983; Woodhead et al., 2009). These isotope systematics, as well as those of kimberlites worldwide, have been interpreted as indicating derivation from a sub-lithospheric source region. It has been argued that the Pb and Nd-Hf isotopic signature of the southern African Cretaceous kimberlites (i.e., elevated $^{206}Pb/^{204}Pb$, and Nd-Hf isotope compositions which extend below the mantle array) represents input from ancient subducted oceanic crust (Nowell et al., 2004; Tappe et al., 2013). However, recent oxygen isotope data for olivine from the Kimberley kimberlites, and other kimberlites worldwide, argues against a large subducted component in the source of these kimberlites (Giuliani et al., 2019).

The emplacement age of the Kimberley cluster has been determined by multiple geochronological studies, including U-Pb and fission track studies of zircon, U-Pb of perovskite, as well as Rb-Sr and $^{40}Ar/^{39}Ar$ of phlogopite (Allsopp and Barrett, 1975; Batumike et al., 2008; Davis, 1977; Fitch and Miller, 1983; Green, 1985; Kramers et al., 1983; Smith et al., 1985, 1989). These studies yield variable emplacement ages, ranging from 80 to 93 Ma. It

appears that all the Kimberley kimberlites were emplaced in the same interval, although this is uncertain due to the low precision of these ages.

The Lithospheric Mantle Sampled by the Kimberley Kimberlites

The sub-continental mantle sampled by the Kimberley kimberlites is one of the most studied sections of continental lithosphere anywhere in the world. This is a direct result of: (1) the large volume of material excavated from the Kimberley kimberlites; (2) the exceptional preservation of many xenoliths, due to deep mining and the relatively young age of these kimberlites; (3) early mining techniques which did not involve the crushing of all material (i.e., large xenoliths were left intact); and (4) access to mine dumps over numerous decades, combined with the preservation and storage of these xenoliths in various collections (e.g., the John J. Gurney Upper Mantle collection).

The Kaapvaal carton, like all cratons, formed in the Archean by the accretion of smaller continental blocks (e.g., Schmitz et al., 2004). The long-term stability and preservation of cratons is attributed to their thick, rigid, and buoyant nature which prevents their subduction. The sub-continental lithospheric mantle (SCLM) is thought to have been produced by major (i.e., 30-50%) melting of fertile lherzolite (e.g., Bernstein et al., 2007; Herzberg, 2004; Pearson and Wittig, 2008). Based on Re-Os dating it is estimated that most of this melting occurred prior to ~2.7 Ga (e.g., Pearson and Wittig, 2008; Simon et al., 2007). The resulting residue of this melting is thought to be refractory dunite and/or orthopyroxene-poor peridotite (e.g., Banas et al., 2009). Most authors agree that melting took place at relatively shallow depths i.e., within the spinel stability field (e.g., Pearson & Wittig, 2008; Simon et al., 2007).

Since melt extraction and craton formation, the SCLM has undergone episodic re-fertilisation; i.e. metasomatism by melts of variable composition (see below). Metasomatism can be defined as a process whereby the composition of a rock is altered due to interaction with

a fluid (e.g., Erlank et al., 1987; Lloyd & Bailey, 1973;). This may manifest in two different ways, modal and cryptic metasomatism. Modal metasomatism is defined as the addition of new phases (e.g., phlogopite, K-richterite, zircon – Harte, 1983). A subset of modal metasomatism has been termed "stealth" metasomatism (O'Reilly & Griffin, 2013), where the phases added to the peridotite are the same as those which are normally found in peridotites (e.g., orthopyroxene, clinopyroxene, garnet). Cryptic metasomatism is where no new phases are added to the rock, but the composition of pre-existing phases is modified (e.g., Dawson, 1984). It was studies of xenoliths derived from the Kimberley kimberlites that highlighted the importance and widespread occurrence of mantle metasomatism (Erlank et al., 1987). Indeed, the SCLM sampled by the Kimberley kimberlites is well known for its heterogeneity, and most xenoliths entrained by the Kimberley kimberlites display some evidence of metasomatism (e.g., Boyd, 1989; Dawson, 1984; Grégoire et al., 2002; O'Reilly & Griffin, 2013; Rehfeldt et al., 2008)

One such craton wide metasomatic event is the re-addition of orthopyroxene. This metasomatic introduction of orthopyroxene was particularly prominent in the Kaapvaal SCLM relative to other cratons (e.g., Boyd, 1989). The later metasomatic addition of orthopyroxene is a good example of stealth metasomatism. This orthopyroxene is argued to have been introduced by the percolation of Si-rich fluids released by subducting slabs, potentially during craton accretion (e.g., Bell et al., 2005; Simon et al., 2007).

In addition to the (potentially) craton-wide orthopyroxene introduction, there are a wide range of other (more localised?) metasomatic events recorded in xenoliths entrained by the Kimberley kimberlites, including:

i. MARID [Mica-Amphibole-Rutile-Ilmenite-Diopside] rocks, which are inferred to represent metasomatism by, or crystallisation from, hydrous alkaline melts (potentially related to Karoo magmatism? – e.g., Dawson and

Smith, 1977; Fitzpayne et al., 2018; Grégoire et al., 2002). These rocks may form the endmember of the GP-PKP series (see below).

ii. PIC [phlogopite-ilmenite-clinopyroxene] rocks are inferred to represent intense metasomatism by kimberlite related melts (Fitzpayne et al., 2018; Grégoire et al., 2002; see also Chapter 5).

iii. The garnet peridotite (GP) – garnet phlogopite peridotite (GPP) – phlogopite peridotite (PP) – phlogopite potassium-richterite peridotite (PKP) series (e.g., Erlank et al., 1987; Rehfeldt et al., 2008). These rocks are also inferred to be the product of hydrous alkaline melt metasomatism. It is noteworthy that phlogopite metasomatism is widespread in xenoliths from the Kimberley cluster and may manifest in rocks of all mantle lithologies (i.e., peridotites – Erlank et al., 1987; eclogites – Jacob et al., 2009; pyroxenites – Rehfeldt et al., 2008).

The "chemical tomography" of the SW Kaapvaal craton (including samples from the Kimberley cluster) has been examined using garnet xenocrysts (e.g., Gaul, 2010; O'Reilly & Griffin, 2006). These studies indicate that the upper ~110 km of the Kaapvaal SCLM is dominated by fertile lherzolite, whereas the abundance of melt metasomatised material (i.e., addition of clinopyroxene and phlogopite) increases below this depth, and dramatically so below ~150km (Griffin et al. 2003; Griffin & O'Reilly, 2007).

Kimberlite-Related Metasomatism

Various exotic and disparate metasomatic assemblages in peridotites have been temporally linked to kimberlite magmatism, based on compositional heterogeneity, disequilibrium with the host rock, and diffusion modelling. This includes carbonate-rich assemblages (e.g., Araujo et

al., 2009; Bussweiler et al., 2016; Dawson et al., 2001; Soltys et al., 2016; van Achterbergh et al., 2002), carbonate-bearing Ni-rich mineralisation (Giuliani et al., 2013a), and sulfate veins (Giuliani et al., 2013b). However, these are clearly not kimberlitic in composition. The activity of such a wide variety of melt/fluid compositions may be due to the thermal anomaly of kimberlite magmatism (Giuliani and Foley, 2016), and/or metasomatism by highly evolved, modified, and fractionated kimberlite melts (e.g., Soltys et al., 2016).

In addition to these obvious examples of modal metasomatism and veined peridotites, there are other examples of metasomatism/crystallisation that have been interpreted to be related to kimberlite activity. These include the formation of: (i) megacrysts (e.g., Kopylova et al., 2009; Moore & Belousova, 2005); (ii) sheared peridotites (Ionov et al., 2010, 2017; Kargin et al., 2017; Katayama et al., 2009); (iii) mantle polymict peridotites (Giuliani et al., 2014; Lawless et al., 1979); and (iv) PIC rocks (Fitzpayne et al., 2018). The link between these lithologies and kimberlites has been inferred based on: (1) broad isotopic similarity with their host kimberlite (e.g., Nowell et al., 2004), and the production of sheared peridotites immediately preceding kimberlite magmatism. Moreover, many of these 'kimberlite-metasomatised' rocks have been genetically linked to one another; for instance, polymict breccias and megacrysts (Giuliani et al., 2014), sheared peridotites and megacrysts (Moore and Loch, 2001).

Additionally, it has been suggested that clinopyroxene and garnet in some granular mantle peridotites formed by kimberlitic stealth metasomatism (e.g., Aulbach et al., 2013; Bussweiler et al., 2018; Fitzpayne et al., 2018b; Grégoire et al., 2003; Jackson and Gibson, 2018; Kargin et al., 2016; Pearson et al., 2002; Simon et al., 2003, 2007). The kimberlitic affinity of the melt that formed this clinopyroxene and garnet is based on isotopic and trace element evidence. Such a scenario is supported by experimental studies, which indicate that clinopyroxene and garnet are stable in melts with "kimberlite-like" compositions at lithospheric

mantle pressures (e.g., Edgar et al. 1988; Girnis et al. 1995; Stone and Luth, 2016). In this respect, it is noteworthy that the major and trace element, as well as Sr-isotope compositions of lherzolitic clinopyroxene from Lac de Gras, overlap those of clinopyroxene megacrysts from the same locality. Bussweiler et al., (2018) explained this relationship by percolation and fractional crystallisation of a failed kimberlite intrusion, where polymict peridotites and Cr-rich megacrysts form near (or within) a failed intrusion, Cr-rich megacrysts form more distal, and finally metasomatic clinopyroxene and garnet is introduced even further away from the failed intrusion.

It remains unknown to what extent the xenocrystic cargo of kimberlite magmas has been metasomatised by previous pulses of kimberlite magma, and if there are any links between the extent of pre-ascent kimberlite metasomatism and the composition or intrusion mechanism (i.e., root zone *vs.* dykes/sills) of kimberlites.

Figures

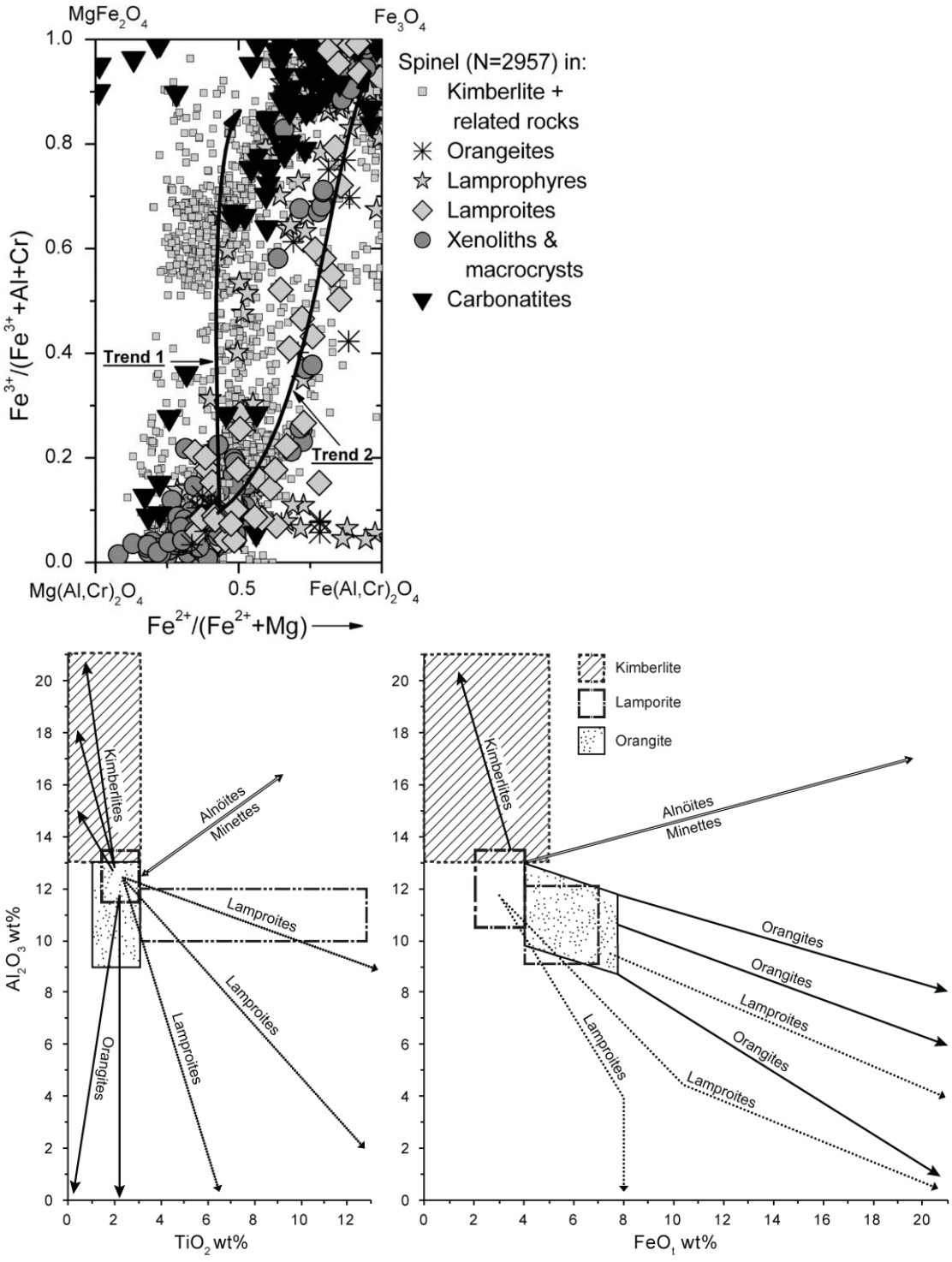

Figure 2-1. Representative rimward geochemical evolution of spinel (after Roeder and Schultze, 2008) and mica (after Mitchell, 1986) in kimberlitic and other 'similar' rock types (e.g., orangeites, lamproites, carbonatites, UML).

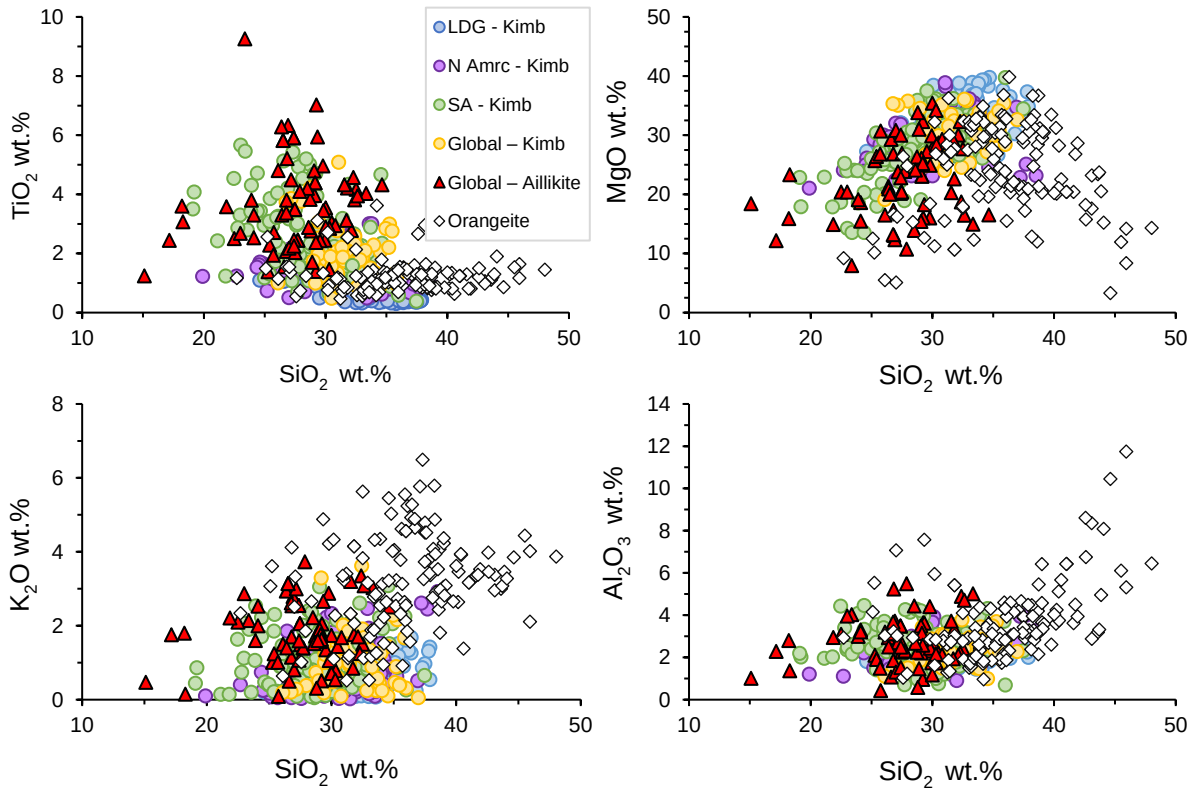

Figure 2-2. The bulk-rock composition of kimberlites worldwide compared with other similar rock types plotted in bivariate charts of SiO_2 (wt.%) vs. TiO_2 (a), MgO (b), K_2O (c), Al_2O_3 (d). The kimberlite data is from Kjarsgaard et al., (2009) and references therein, orangeite data is from (Becker and le Roex, 2006; Coe, 2004; Coetzee, 2004; Fraser, 1987; Howarth et al., 2011; Rowlands, 2008; Tainton, 1992), and Aillikite data is from (Donnelly et al. 2011; Kargin et al. 2016; Nielsen et al. 2009; Tappe et al. 2004, 2006, 2008, 2011;).

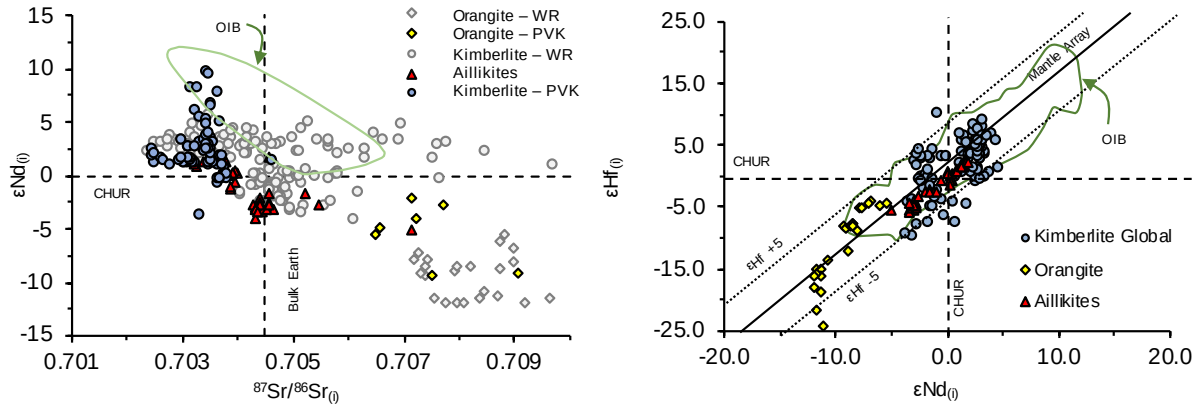

Figure 2-3. The isotopic composition of kimberlites (perovskite and whole-rock – data from: Carlson et al., 2006; Kopylova et al., 2009; Nowell et al., 2004; Paton et al., 2009; Tappe et al., 2011; Tappe et al., 2013; Tappe et al., 2014; Tappe et al., 2017; Yang et al., 2009) plotted in (a) $\varepsilon Nd_{(i)}$ *vs.* $^{87}Sr/^{86}Sr_{(i)}$, and (b) $\varepsilon Hf_{(i)}$ *vs.* εNd space. Shown for comparison are the isotopic compositions of orangeites (perovskite and whole-rock – data from: Coe et al., 2008; Griffin et al., 2014; Nowell et al. ,2004), and Aillikites (whole-rock – data from: Tappe et al., 2007, 2008).

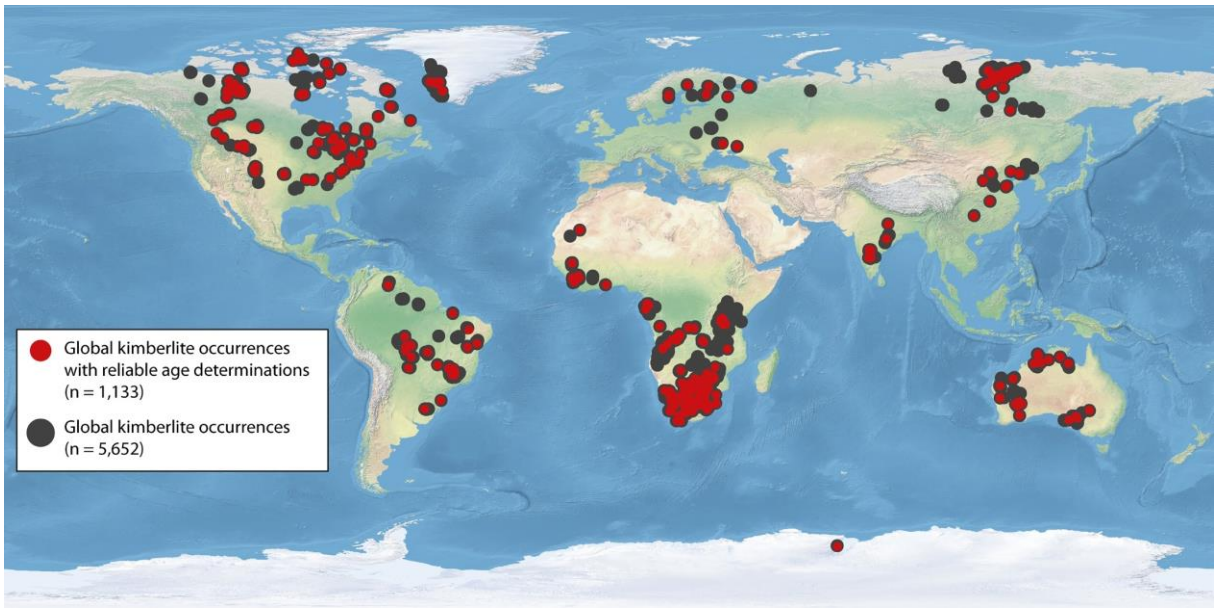

Figure 2-4. Global distribution of kimberlite magmatism from Tappe et al., (2018)

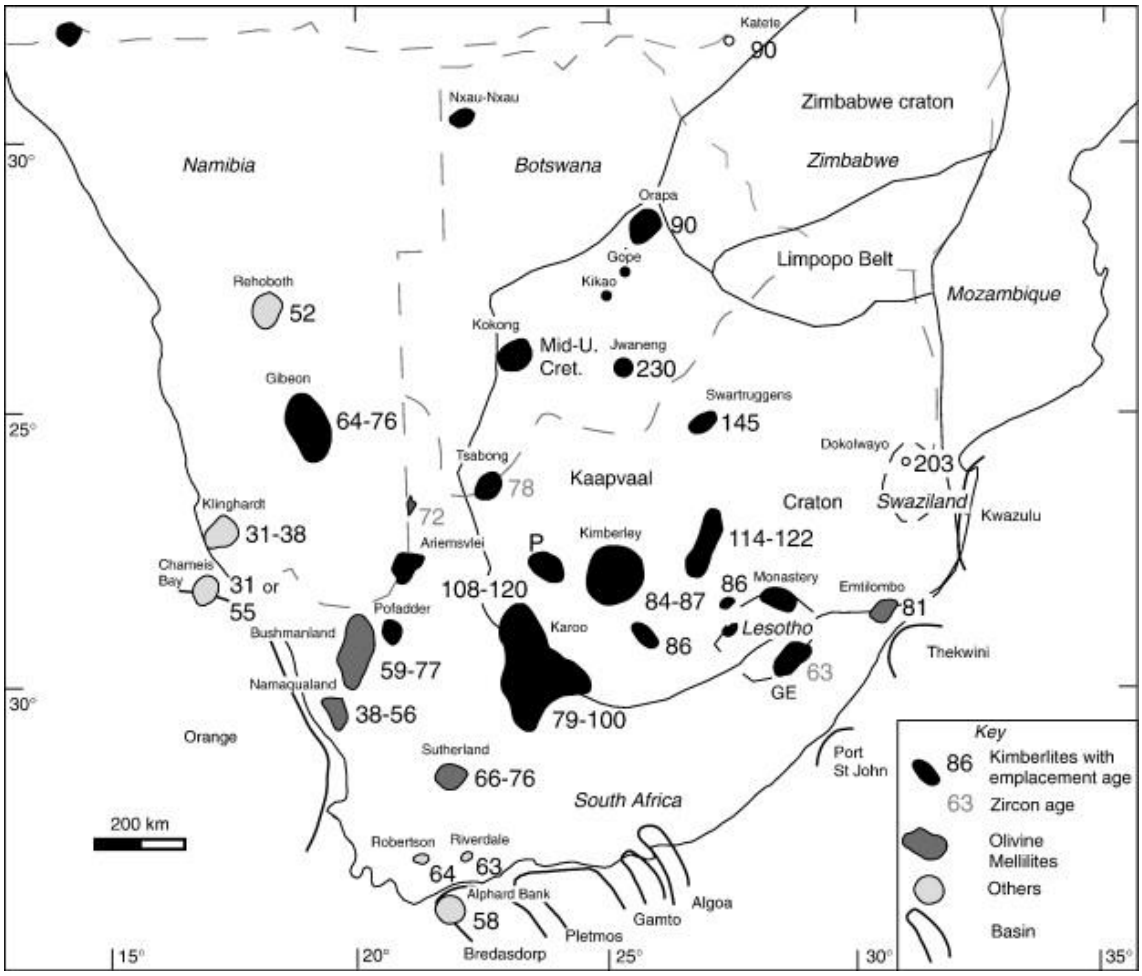

Figure 2-5. Distribution and representative ages of Kimberlite clusters and other alkaline volcanism in southern Africa from Moore et al., (2008).

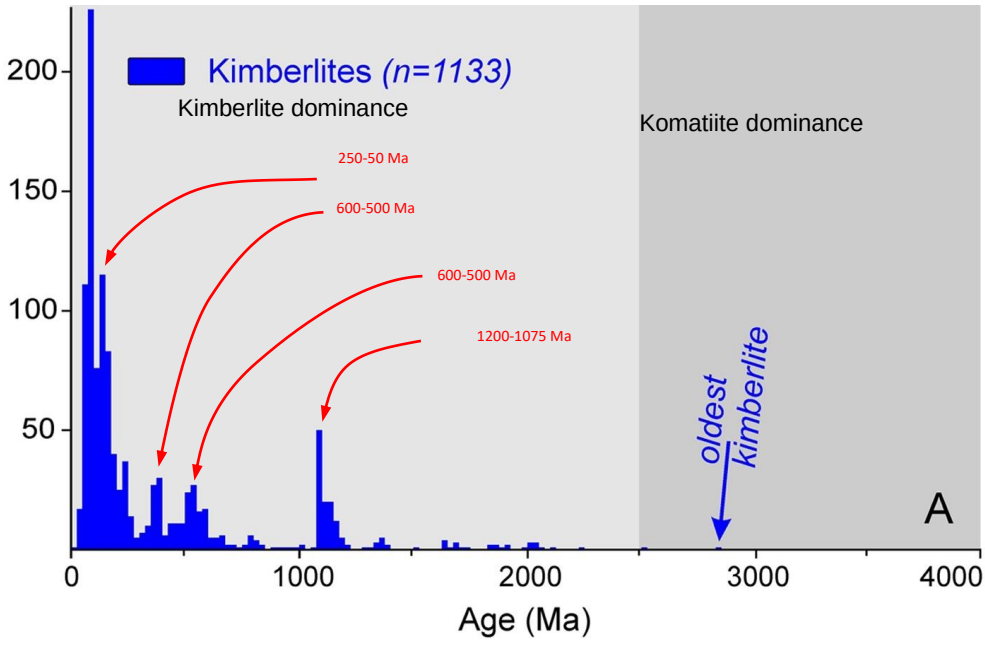

Figure 2-6. Histogram showing the frequency distribution of global kimberlite magmatism (modified from Tappe et al., 2018).

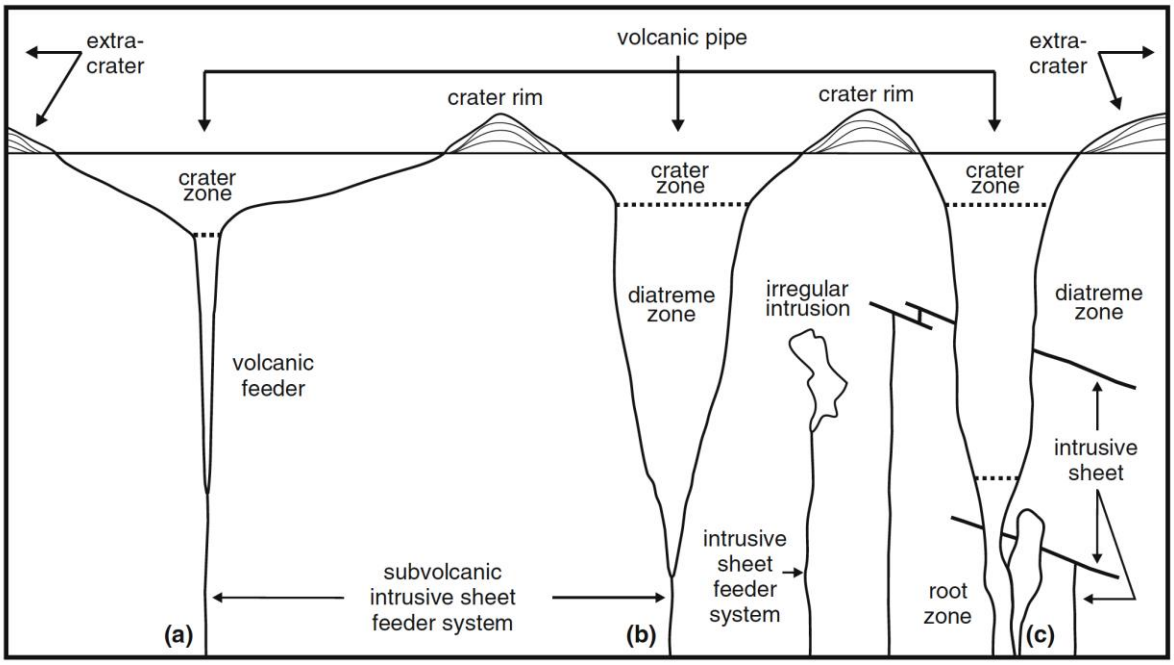

Figure 2-7. The intrusion morphology of the different classes of kimberlite pipes from Scott Smith, (2013)

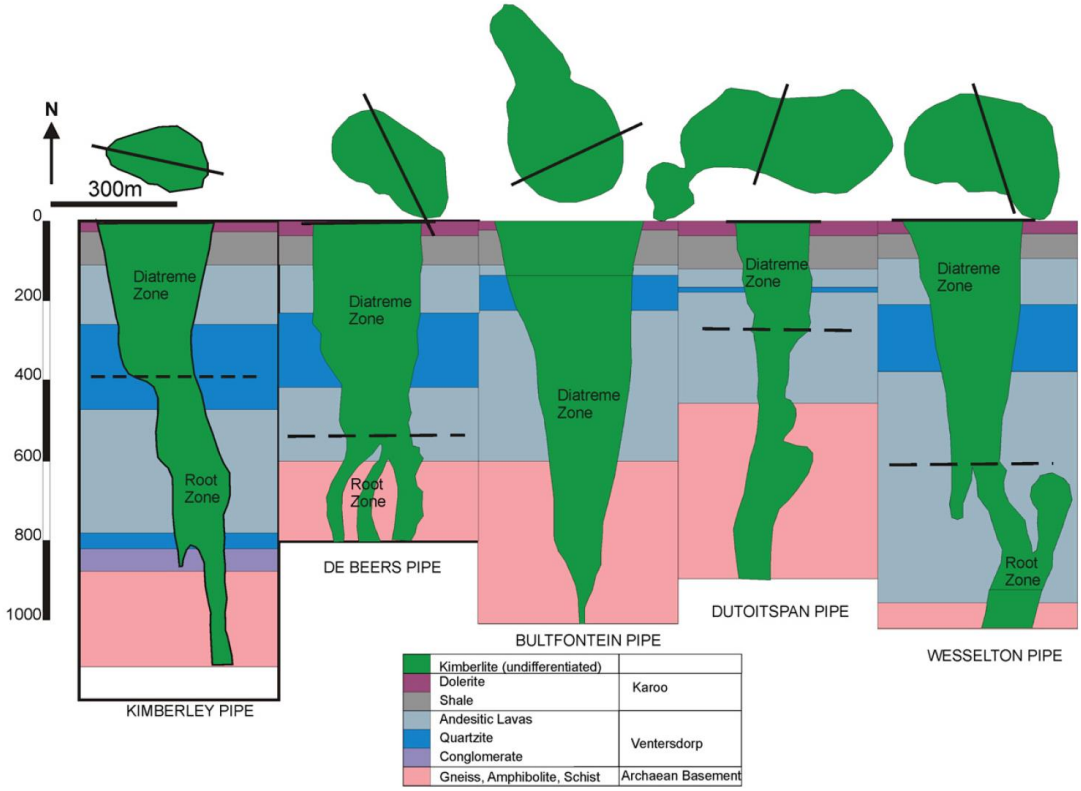

Figure 2-8 The surface expression and vertical cross-sections through the main pipes of the Kimberley cluster shown alongside the local stratigraphy (taken from Field et al., 2008; modified from Clement, 1982).

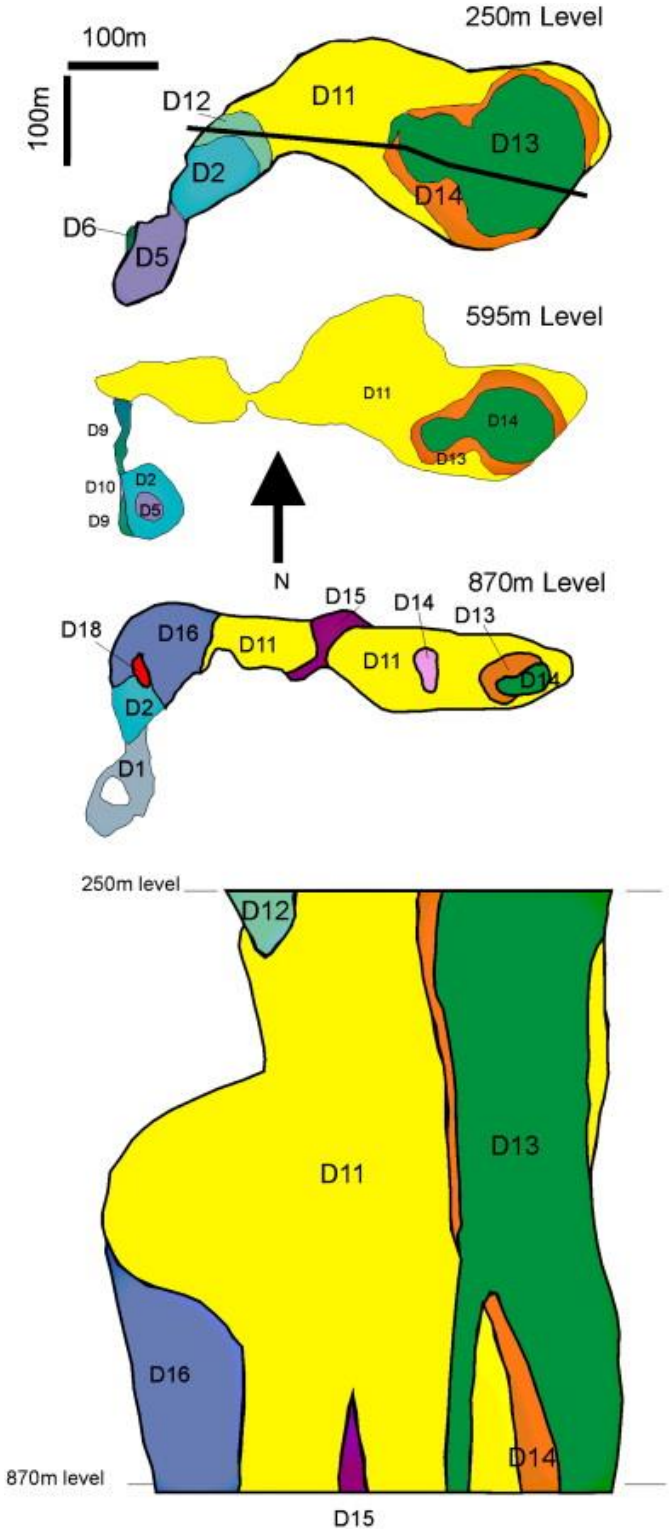

Figiure 2-9. Internal structure of the Dutoitspan pipe (taken from Field et al., 2008; modified from Clement, 1982).

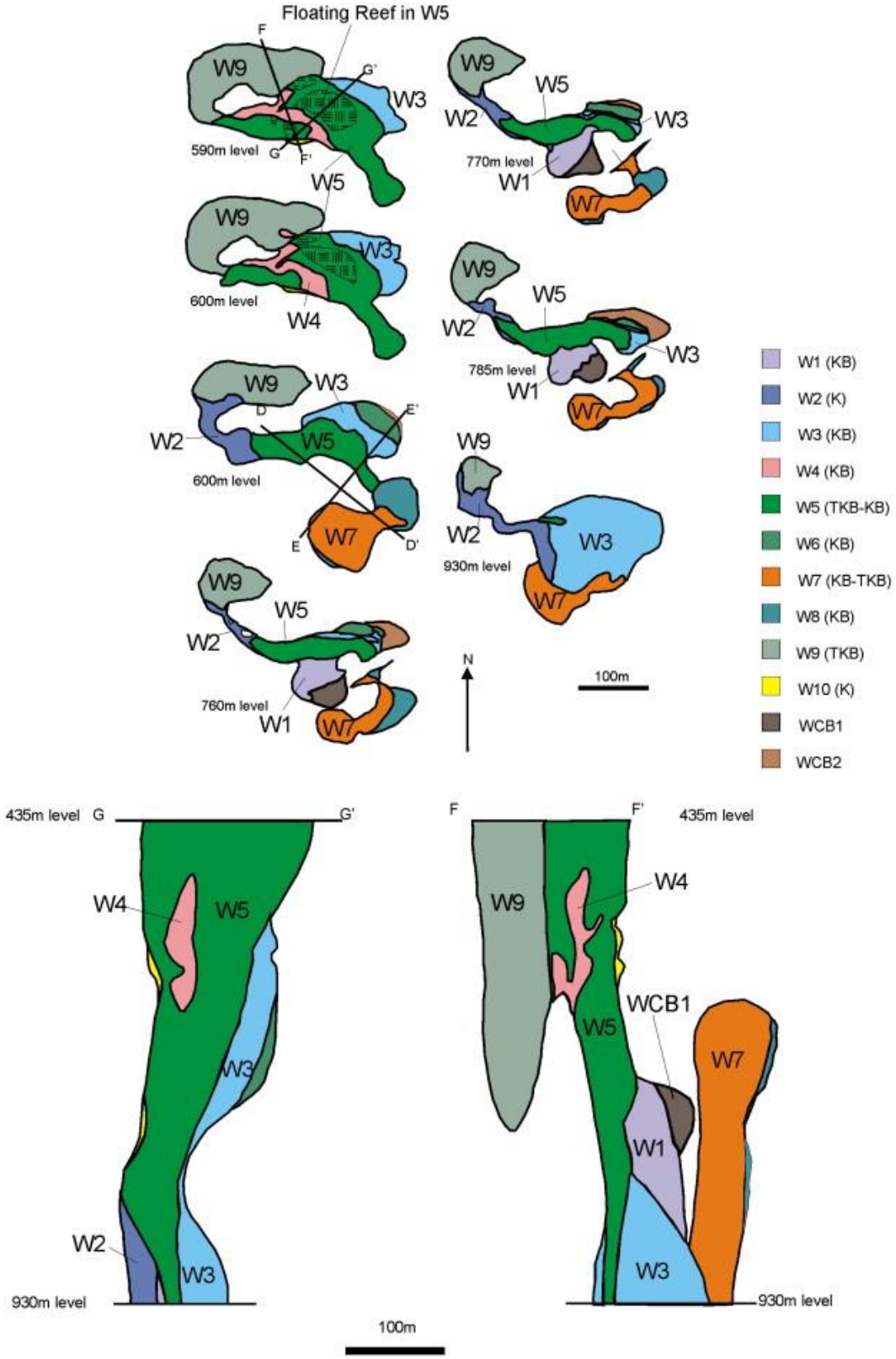

Figure 2-10. Internal structure of the Wesselton pipe (taken from Field et al., 2008; modified from Clement, 1982)

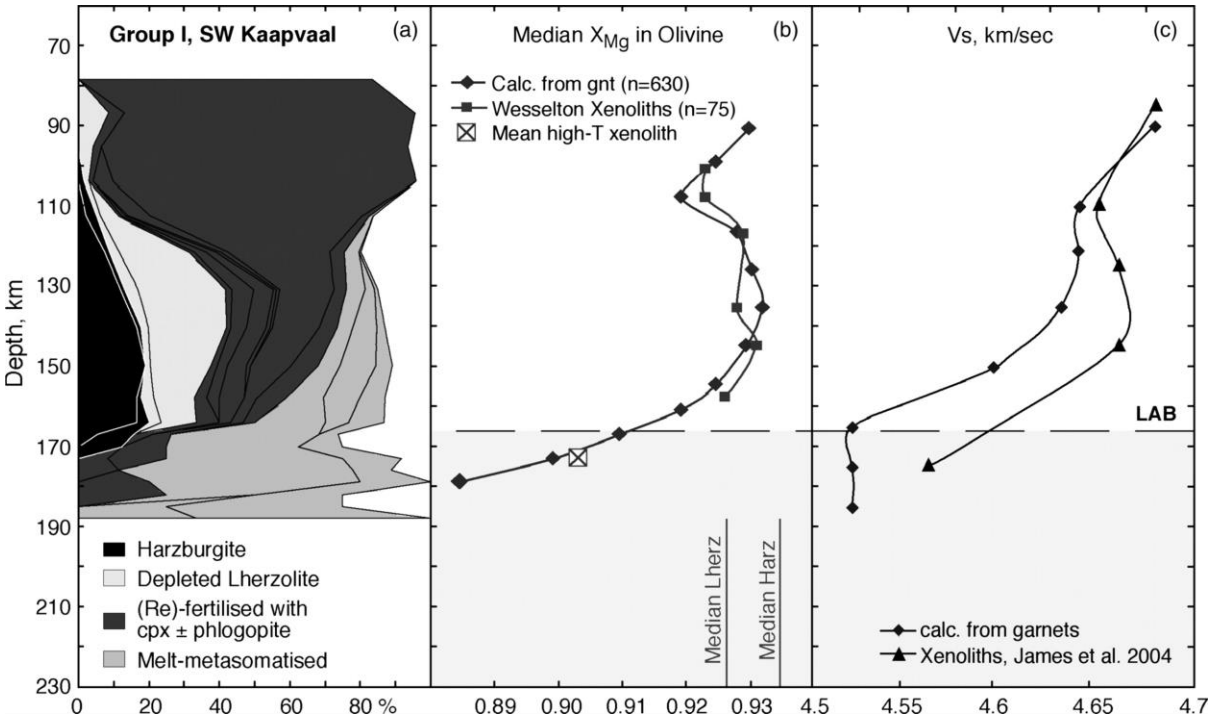

Figure 2-11. (a) Chemical tomography of the lithospheric mantle sampled by the Kimberley kimberlites based on the composition of garnet xenocrysts; (b) the calculated Mg# of olivine based on garnet xenocrysts and garnet bearing peridotites; and (c) calculated shear-wave velocities based on based on garnet xenocrysts and garnet bearing peridotites (taken from Griffin et al., 2009).

CHAPTER 3: KIMBERLITE METASOMATISM OF THE LITHOSPHERE AND THE EVOLUTION OF OLIVINE IN CARBONATE-RICH MELTS – EVIDENCE FROM THE KIMBERLEY KIMBERLITES (SOUTH AFRICA)

Ashton Soltys[a*], Andrea Giuliani[a,b], David Phillips[a], Vadim S. Kamenetsky[c,d]

[a] KiDs (Kimberlites and Diamonds), School of Earth Sciences, The University of Melbourne, Parkville, 3010 Victoria, Australia

[b] ARC Centre of Excellence for Core to Crust Fluid Systems and GEMOC, Department of Earth and Planetary Sciences, Macquarie University, North Ryde, 2019 NSW, Australia

[c] School of Natural Sciences, University of Tasmania, Hobart, 7001, Tasmania, Australia

[d] Institute of Experimental Mineralogy RAS, Chernogolovka 142432, Russia

Abstract

Olivine is the most abundant phase in kimberlites and is stable throughout most of the magma's crystallisation sequence, thus providing an extensive record of kimberlite petrogenesis. To better constrain the composition, evolution, and source of kimberlites we present a detailed petrographic and geochemical study of olivine from multiple dyke, sill, and root zone kimberlites in the Kimberley cluster (South Africa). Olivine grains in these kimberlites are zoned, with a central core, a rim overgrowth, and occasionally an external rind. Additional 'internal' and 'transitional' zones may occur between the core and rim, and some samples of root zone kimberlites contain a late generation of high-Mg olivine in cross-cutting veins.

Olivine records widespread pre-ascent (proto-)kimberlite metasomatism in the mantle including: (a) Relatively Fe-rich (Mg# <89) olivine cores interpreted to derive from the disaggregation of kimberlite-related megacrysts (20% of cores); (b) Mg-Ca-rich olivine cores (Mg# >89; >0.05 wt.% CaO) suggested to be sourced from neoblasts in sheared peridotites (25% of cores); (c) transitional zones between cores and rims probably formed by partial re-equilibration of xenocrysts (now cores) with a previous pulse of kimberlite melt (i.e., compositionally heterogeneous xenocrysts); and (d) olivine from the Wesselton water tunnel sills, internal zones (I), and low-Mg# rims, that crystallised from a kimberlite melt that underwent olivine fractionation within the shallow lithospheric mantle.

Magmatic crystallisation begins with internal olivine zones (II); which are common but not ubiquitous in the Kimberley olivine. These zones are euhedral, contain rare inclusions of Cr-spinel, and have a higher Mg# (90.0 ± 0.5), NiO, and Cr_2O_3 contents, but are depleted in CaO compared to the rims. Internal olivine zones (II) are interpreted to crystallise from a primitive kimberlite melt during its ascent and transport of olivine toward the surface. Their compositions suggest assimilation of peridotitic material (particularly orthopyroxene) and potentially sulfide minerals prior to or during crystallisation. Comparison of internal zones (II)

with liquidus olivine from other mantle-derived carbonate-bearing magmas (i.e., orangeites, ultramafic lamprophyres, melilitites) show that low Mn/Fe, very low Ca/Fe, and moderate Ni/Mg ratios appear to be the hallmarks of olivine in melts derived from carbonate-bearing garnet-peridotite sources.

Olivine rims display features indicative of magmatic crystallisation, which are typical of olivine rims in other studied kimberlites – i.e. primary inclusions of Cr-spinel, Mg-ilmenite and rutile, homogeneous Mg# (88.8 ± 0.3), decreasing Ni and Cr, increasing Ca and Mn. Rinds and high-Mg olivine are characterised by extreme Mg-Ca-Mn enrichment and Ni depletion, and textural relationships indicate these zones represent replacement of pre-existing olivine, with some new crystallisation of rinds. These zones likely precipitated from evolved, oxidised, and relatively low temperature kimberlite fluids after crustal emplacement. In summary, this study demonstrates the utility of combined petrography and olivine geochemistry to trace the evolution of kimberlite magmatic systems from early metasomatism of the lithospheric mantle by (proto-)kimberlite melts, to crystallisation at different depths *en route* to surface, and finally late-stage deuteric/hydrothermal fluid alteration processes after crustal emplacement.

Introduction

Fresh coherent kimberlites are usually dominated by olivine, which commonly comprises 20-60 vol.% (e.g., Dawson, 1980; Mitchell, 2008; Moss et al., 2010; Soltys et al., 2018a). Kimberlitic olivine grains may contain both xenocrystic and magmatic components (e.g., Arndt et al., 2010; Brett et al., 2009; Bussweiler et al., 2015; Kamenetsky et al., 2008; Nielson & Sand, 2008) and have a protracted crystallisation period, as olivine is one of the earliest crystallising phases (e.g., Fedortchouk & Canil, 2004; Mitchell, 1986), and also forms part of the late-stage groundmass crystallisation (e.g., Nielson & Sand, 2008; Lim et al., 2018; Soltys et al., 2018b). As a result, the crystallisation and re-equilibration of olivine provides an almost complete record of the petrogenesis and evolution of kimberlite magmas. Detailed studies of olivine therefore have the potential to aid our understanding of the pre-ascent metasomatic activity of proto-kimberlite melts, as well as the earliest and latest stages of kimberlite crystallisation; which remain some of the more poorly understood aspects of kimberlite petrogenesis and evolution. In this contribution we focus particularly on features of olivine zonation that have been poorly documented previously, such as internal zonation (i.e., olivine which forms before voluminous rim crystallisation) and late forming olivine zones (e.g., rinds that crystallise after or replace the rims).

Historically discrete olivine grains in kimberlites have been described as macrocrystic or phenocrystic, based on a visual assessment of their shape and size (e.g., Clement, 1982; Clement & Skinner, 1979; Shee, 1985). The term macrocryst is used here and by previous studies in a non-genetic sense to describes large (i.e., >0.5 mm), rounded-anhedral grains (or polygranular clusters of grains – e.g., Arndt et al., 2010), which commonly show evidence of strain (e.g., undulose extinction) and fractures that are attributed to rapid decompression. In contrast, (micro-)phenocrysts are smaller (typically <1 mm), euhedral-subhedral grains, that usually lack evidence of strain or decompression. Modern analytical and imaging techniques

have produced a plethora of new petrographic and compositional data on kimberlitic olivine (see the review of Giuliani, 2018 and references therein). Arguably the most important finding is that kimberlitic olivine is commonly complexly zoned, contains a higher proportion of xenocrystic components than suggested by early studies (e.g., Mitchell, 1973, 1986), and xenocrystic cores can occur in olivine regardless of grain size or shape (e.g., Brett et al., 2009; Bussweiler at al., 2015; Kamenetsky et al., 2008; Pilbeam et al., 2013). In addition, the size of olivine grains has been shown to form a complete continuum (Moore, 1988; Moss et al., 2010). Therefore, it seems likely that kimberlitic olivine represents a single population, formed by a universal process, rather than the mixing of two distinct populations (i.e., xenocrysts and phenocrysts, or different phenocryst populations).

Most olivine grains contain a core of uniform composition, but their compositions vary widely from grain to grain. These cores are overgrown by one or more concentric zones of relatively restricted composition(s) (Fig. 3-1). However, the terminology used to describe these zones is not consistent between studies. Here we adopt the classification of Lim et al. (2018) and Giuliani (2018) as standard terminology. Most olivine grains contain a ***core*** that may be overgrown by ***internal zones*** (i.e., the "transitional olivine" of Howarth & Taylor, 2016). Cores or internal zones are overgrown by ***rims*** (i.e., the "margins" or "melt trend" of Bussweiler et al., 2015; and Howarth & Taylor, 2016), which are ubiquitous and recognised in early studies (e.g., Boyd & Clement, 1977; Mitchell, 1973). Diffuse zones termed ***transitional zones*** have been observed between the cores and rims of some olivine grains in kimberlites worldwide (Cordier et al., 2015; Howarth & Taylor, 2016; Lim et al., 2018; Pilbeam et al., 2013). In this study, transitional zones are observed between the core and rim, as well as between the core and internal zones. In fresh kimberlites, rims may be overgrown by ***rinds*** (i.e., the "rims" of Nielson & Sand, 2008). Finally, we report an additional late-stage ***high-Mg*** generation of olivine developed along fractures that crosscut all previous olivine zones.

Recently Giuliani (2018) reviewed the zonation patterns observed in kimberlitic olivine from numerous global localities, with emplacement ages spanning 50 to 640 Ma. This allowed for assessment of the variability of olivine core and rim compositions and discussion of the processes that formed these two volumetrically major zones. In the current study we provide a more detailed grain-scale account of the complexity of olivine zonation in the Kimberley kimberlites (South Africa) – the type-locality for kimberlites (Dawson, 1980). The current study is the first to include samples from multiple pipes, multiple units of the same pipe (Wesselton), as well as the different emplacement modes of coherent kimberlite (i.e., planar dykes/sills and irregular root-zone kimberlites) within the same cluster. We also focus on features that have not been documented previously, or described in brief (i.e., transitional and internal olivine zones, as well as late-stage rinds and high-Mg olivine). The formation of these uncommon zones has important implications for pre-ascent (proto-)kimberlite metasomatism of the lithospheric mantle, early kimberlite crystallisation, the nature of the kimberlite source, and the composition and evolution of late-stage kimberlite melts after emplacement into the upper crust. These results are compared with data reported in all previous studies of the Kimberley kimberlites and their entrained xenoliths and xenocrysts. This combined data set is employed to provide an updated assessment of the chemical variation of olivine in the Kimberley kimberlites, with application to the petrogenesis of kimberlites worldwide.

Geological setting, previous work, and samples

The Kimberley cluster is located in the western terrane of the Kaapvaal craton in southern Africa (Fig. 3-2a), and contains five main kimberlite pipes (i.e., Kimberley – "The Big Hole", De Beers, Wesselton, Bultfontein, and Dutoitspan; Fig. 3-2b), numerous smaller pipes (e.g., St Augustine's, Kamfersdam, and Otto's Kopje), as well as extensive dyke and sill systems (e.g., Benfontein sills, Wesselton floors' sill, and Wesselton water tunnel sills [WWTS]). Several

intrusions of the Kimberley cluster have been dated by different geochronological techniques (e.g., $^{40}Ar/^{39}Ar$ phlogopite, U-Pb perovskite), yielding emplacement ages spanning 80 to 93 Ma (e.g., Allsopp & Barrett 1975; Batumike et al., 2008; Fitch & Miller, 1983; Li et al., 2010).

The Kimberley cluster was the focus of the first modern petrographic and geochemical studies on kimberlites (e.g., Clement, 1982; Dawson and Hawthorn, 1973; Mitchell, 1973; Pasteris, 1980; Shee, 1985), and remains one of the most studied and arguably best understood kimberlite localities in the world. Since these early investigations, there have been numerous additional studies of the cluster, including whole-rock and isotopic analyses (le Roex et al., 2003; Nowell et al., 2004; Woodhead et al., 2009), and examinations of the mineral chemistry of single intrusions and/or phases (e.g., Howarth & Taylor, 2016; Giuliani et al., 2017; Ogilvie-Harris et al., 2009; Soltys et al., 2018b; White et al., 2012).

The Kimberley kimberlites contain macrocrysts of dominant olivine, together with ilmenite, phlogopite, garnet, clinopyroxene, spinel, and lesser orthopyroxene. The magmatic assemblage may include abundant olivine, phlogopite, and, rarely, ilmenite, in a groundmass of olivine, spinel, perovskite, ilmenite, apatite, and in some intrusions monticellite. These phases are set in an interstitial mesostasis consisting of variable proportions of serpentine and carbonates (calcite, and in some intrusions lesser dolomite).

In this contribution, we report petrographic and major element compositional data for olivine from 12 units of coherent kimberlite (Table 3-1). The studied samples range in texture from macrocryst-free aphanitic, to highly macrocrystic (i.e., ≥30 vol.% olivine macrocrysts), and are derived from root-zone, dyke, and sill kimberlites. The main petrographic features of the studied samples are summarised in Table 3-1.

Olivine is generally better preserved in carbonate-rich kimberlites, which often correspond to samples from dykes or sills. These samples of dykes and sills commonly contain groundmass dolomite, whereas phlogopite-kinoshitalite (micro-)phenocrysts are less abundant

relative to samples of root zone kimberlites. In addition, in dyke and sill samples that contain fresh olivine, monticellite is commonly replaced by serpentine ± dolomite/calcite. In contrast, many root zone kimberlites contain more serpentine and phlogopite-kinoshitalite; in these cases, olivine is commonly incipiently altered, or almost completely replaced, whereas monticellite often remains unaltered. The general petrographic correrlations observed in the studied samples are consistent with the style of alteration reported in the De Beers dyke (Kimberley – Soltys et al., 2018b), and other kimberlite dykes and sills worldwide (e.g., Armstrong et al., 2004). Nevertheless, despite widespread alteration of olivine in many root zone kimberlites, the outermost zones (i.e., rims and rinds) can often still be observed and sometimes analysed due to the erratic nature of alteration (Supp. Fig. S1).

Analytical Methods

Field-emission and Conventional Scanning Electron Microscopy

Investigation of micro-textures and mineral inclusions was performed at the University of Melbourne, using a Philips (FEI) XL30 scanning electron microscope (SEM), equipped with an OXFORD INCA energy dispersive X-ray spectrometer (EDS). Further investigation of the petrographic features which were not resolvable using a conventional SEM, was performed at the Central Science Laboratory, University of Tasmania, using a Hitachi SU-70 field emission scanning electron microscope (FE-SEM) equipped with an OXFORD INCA-XMax80 EDS. Back-scattered electron (BSE) images and semi-quantitative chemical spot analysis were obtained using a beam acceleration of 15 kV.

Electron Probe Micro-Analysis

Analytical point selection was performed under high-contrast conditions using a SEM. Major element oxide composition of olivine were determined using a Cameca SX-50 Electron Probe Micro-analyser (EPMA), equipped with four vertical wavelength dispersive spectrometers, located at the University of Melbourne. Analytical conditions were as follows: beam acceleration voltage of 15 keV, beam current of 35 nA, and beam diameter of 2 μm; counting times per analysis of 20 s on peak positions and 10 s on two background positions located on either side of the peak position. The elemental standards analysed for calibration purposes consisted of natural and synthetic materials, including: Wollastonite (Si-Kα, Ca-Kα), Hematite (Fe-Kα), Metallic Manganese (Mn-Kα), Magnesium oxide (Mg-Kα), and Metallic Nickel (Ni-Kα). Data reduction was performed using the PAP matrix correction software program (Pouchou & Pichoir, 1984). The concentrations of all oxides were above EPMA detection limits, except for some analyses of olivine cores which contain CaO concentrations at or below the limits of detection (i.e., <0.02 wt.%). EPMA elemental detection limits are analogous to those reported for routine olivine analyses in the literature.

Additional major element oxide concentrations of olivine (predominantly line traverses) were determined using a Cameca SX-100 EPMA, equipped with 5 tuneable wavelength dispersive spectrometers, located in the Central Science Laboratory, University of Tasmania. Analytical conditions were as follows: beam energy of 15 keV, beam current 30 nA, and beam diameter of 2 μm; counting times varied between 20 and 60 seconds on peak positions and between 4 and 120 seconds on background positions. The elemental standards analysed for calibration purposes consisted of natural and synthetic materials, including: spectrosil (Si-Kα), Delegate clinopyroxene or Wollastonite (Ca-Kα), Minas Gerais magnetite, (Fe-Kα), bustamite or rhodonite (Mn-Kα), magnesium oxide or periclase (Mg-Kα), nickel silicide or nickel oxide (Ni-Kα), and eskolaite (Cr-Kα). Data reduction was performed using ZAF or Phi-Rho-Z calculations (Armstrong, 1988). During all analytical sessions San Carlos olivine was analysed

as a reference material, and the resultant compositions were within uncertainty of accepted values (e.g., Jarosewich et al., 1980).

Petrography and Mineral Chemistry

The petrographic features and mineral chemistry of olivine were determined on 12 samples from 12 separate units (Table 3-1). Average values, standard deviations, and compositional ranges of the different olivine zones are reported in Table 3-2. The full data set is reported in Supplementary Tables S1-2. The dataset discussed in this section consists of new EPMA spot analyses (n = 320) covering all samples. These new data are supplemented by published analysis from previous studies on the De Beers dyke (n = 26; Soltys et al., 2018b) and the Bultfontein kimberlite (n = 54; Giuliani et al., 2017), and analyses (i.e., n = 86) recently reported alongside oxygen isotopes in a subset of the current samples by Giuliani et al. (2019).

Most olivine grains in the Kimberley kimberlite samples are concentrically zoned and share a 'common' core-margin zonation pattern, irrespective of their size or shape (Fig. 3-1). However, not all zones shown in Figure 3-1 are present in all grains. One exception is olivine from the WWTS, which contains olivine with distinct petrographic and compositional features (see below).

In many samples small (i.e., <100-75 μm), euhedral olivine grains that lack a core component occur throughout the groundmass (Supp. Fig. S2). These grains are more common in macrocryst-poor or aphanitic samples (e.g., WESK-3A; DB-D; Supp. Fig. S1) than in macrocryst-rich samples (e.g., WESK-7; WESK-8; BHK-1; Supp. Fig S1). These grains appear unzoned in BSE images, except where overgrown by rinds (e.g., Supp. Fig. S2f, i), and are often replaced by serpentine. The olivine grains analysed in this study span a wide range of grain sizes and shapes, from small (i.e., <50 μm) euhedral groundmass grains through to large (> 1cm) rounded-ovoid macrocrysts.

Olivine Cores

Most olivine cores are rounded to ovoid, but more angular shapes were also observed. Cores with a higher Mg# tend to be larger and more angular (i.e., predominantly macrocrysts), consistent with the observations of Moore (1988). Cores with a 'euhedral' shape (i.e., with straight, regular borders corresponding to crystallographic directions) are exceptionally rare (i.e., <0.1% of grains). The core shapes observed in the current samples are consistent with those reported previously (e.g., Bussweiler et al., 2015; Cordier et al., 2015; Kamenetsky et al., 2008). In addition, some cores, particularly those of macrocrysts, display undulose extinction, consistent with deformation prior to entrainment into the host kimberlite (see also Arndt et al., 2010).

Individual olivine cores are compositionally homogeneous, but significant inter-grain variation is observed (Fig. 3-3; Table 3-2). Their Mg# ranges from 82.7 to 94.9, with a mean ($\overline{x}$) of 91.0 ± 2.6 (1σ; *n* = 176); NiO contents range from 0.06 to 0.56 wt.%, but are generally high ($\overline{x}$ = 0.37 ± 0.08); MnO contents are <0.27 wt.% ($\overline{x}$ = 0.11 ± 0.03); and CaO contents are generally low (<0.11 wt.%; $\overline{x}$ = 0.06 ± 0.03). These compositions overlap previously reported analyses of olivine cores from the Kimberley kimberlites (Supp. Fig. S3; Arndt et al., 2010; Boctor & Boyd, 1981; Howarth & Taylor, 2016; Moore, 1988).

Most olivine cores analysed in this study (~80%) have an Mg# ≥89, and are termed "Mg-rich" (Figs. 3-3, 3-4; see also Giuliani, 2018; Lim et al., 2018). The Mg# of these cores shows no statistically significant correlation with NiO or MnO contents, but a weak negative correlation with CaO (R^2 = 0.43; Supp. Fig. S4). A subordinate population of olivine cores (~20%) have an Mg# <89, and are termed "Fe-rich" (Figs. 3-3, 3-4). These Fe-rich cores show a positive correlation between Mg# and NiO (R^2 = 0.76) and, to a lesser extent, CaO (R^2 = 0.44), but an inverse correlation with MnO (R^2 =0.50) (Supp. Fig. S4).

Mineral inclusions in olivine cores are rare, and only observed in the Mg-rich population, where they include clinopyroxene, orthopyroxene, phlogopite, garnet, and chromite (e.g., Supp. Fig. S5). These inclusions are generally monomineralic, anhedral-rounded, and <100 μm in size (rarely up to 500 μm – Supp. Fig. S5c). In one rare instance, multiple (clino- and ortho-)pyroxene inclusions were observed within a single core (e.g., Supp. Fig. S5d-f). Where clinopyroxene inclusions (the most abundant inclusion type) were exposed to the kimberlite groundmass (i.e., due to fracturing of the olivine host), they are resorbed and partially replaced by fine scale intergrowths that may consist of MÜM spinel (solid solution between magnesian-ulvöspinel, ulvöspinel, and magnetite; Mitchell 1986), monticellite, phlogopite, and other accessory phases (Supp. Fig. S5g-j; see also Kamenetsky et al., 2009).

A large Cr-diopside inclusion in an olivine core from sample WA-1 (Supp. Fig. S5c) is relatively homogeneous (e.g., Mg# = 93, Cr_2O_3 = 3.4 ± 0.1 wt.%, Al_2O_3= 2.6 ± 0.1 wt.%, CaO = 17.5 ± 0.1 wt.%, Na_2O = 2.9 ± 0.2 wt.% – Supp. Table S3). Application of the Nimis & Taylor, (2000) single clinopyroxene thermobarometer yields average pressure-temperature conditions of 1005 °C and 43.5 Kbar (i.e., ~145 km depth), consistent with the geotherm derived by Mather et al. (2011) using mantle xenoliths and clinopyroxene xenocrysts from the Bultfontein kimberlite. In contrast, a Cr-diopside inclusion in an olivine core from sample WESK-8 (Supp. Fig. S5d-f) has a more heterogeneous composition (e.g., Mg# = 90, Cr_2O_3 = 1.5 ± 0.1 wt.%, Al_2O_3 = 1.5 ± 0.6 wt.%, CaO = 20.8 ± 1.2 wt.%, Na_2O = 1.7 ± 0.5 wt.% – Supp. Table S3). The compositional variability of this inclusion in terms of Al, Ca, and Na contents is similar to, but less pronounced than the variations reported by Kamenetsky et al. (2009) and Sobolev et al. (2015) for clinopyroxene inclusions in olivine cores from the Udachnaya-East kimberlite (Russia). Despite this compositional heterogeneity, these Cr-diopside inclusions (i.e., from both samples) are within the range defined by clinopyroxene in mantle-derived

granular peridotite xenoliths entrained by southern African kimberlites (e.g., Supp. Fig. S6a, c, e, g).

Three separate enstatite inclusions in a single olivine core from sample WESK-8 (Supp. Fig. S5d-f) are homogeneous and their compositions are within error of one another (e.g., Mg# = 91 Al_2O_3 = 0.49 ± 0.02 wt.%, CaO = 0.53 ± 0.03 wt.%, Cr_2O_3 0.18 ± 0.02 wt.% – Supp. Table S3). These compositions are also within the range defined by orthopyroxene in granular peridotites entrained by southern African kimberlites (e.g., Rehfeldt et al., 2008; Simon et al., 2003 –Supp. Fig. S6b, d, f).

Internal olivine zones

Internal zones occur between the core and rim of some olivine grains. Two distinct types of internal zonation were observed, termed (I) and (II) with distinct petrographic and compositional features.

Internal zones (I)

Internal zone (I) was observed in olivine from four samples of the Wesselton kimberlite (i.e., WESK-3A, WESK-3M, WESK-8, and WESK-7 – Table 3-1). These zones are common (i.e., observed in ~5-10 % of grains) in sample WESK-3A, an aphanitic late-stage dyke that cross-cuts the main Wesselton pipe. Fewer grains from the remaining Wesselton samples contain this internal zone.

Internal zone (I) is up to 50 μm in width, but commonly <20 μm, devoid of mineral inclusions, with an anhedral shape and pronounced embayments, and a lighter BSE response than the succeeding rim (Fig. 3-5a, b; Supp. Fig. S7). The contact between internal zone (I) and the core is relatively sharp and only occasionally marked by a thin diffuse region (~10-20 μm thick), whereas the contact with the rim is sharp (Fig. 3-5a, b; Supp. Fig. S7). Cores are

commonly embayed where in contact with this internal zone. Petrographically similar internal zones have been reported in other kimberlites worldwide, but, with the exception of Tres Ranchos-04 (Brazil), are generally rare (Cordier et al., 2015 [their M1 zone]; Lim et al., 2018). A single olivine core with a composition analogous to internal zone (I) was identified in sample WESK-3A

Internal olivine zones (I) (including a core of similar composition) have Mg# ranging from 86.5 to 87.8 ($\bar{x}$ = 87.0 ± 0.5; *n* = 6), coupled with low CaO (<0.05 wt.% – Fig. 3-6e; Table 3-2). The MnO and NiO contents are variable (i.e., 0.13-0.21 and 0.09-0.29 wt.%, respectively; Fig. 3-6a, c). The trends defined by internal zone (I) in MnO and NiO *vs.* Mg# space resemble the core-margin zonation trend of rims (Fig. 3-6). Similar internal olivine zones in kimberlites worldwide exhibit comparable compositional features (e.g., Fig. 3 of Lim et al., 2018), although the Mg# varies between localities (e.g., ~87 – This study; ~87-88 (Tres Ranchos-04, Brazil) and ~90 (Grizzly, Canada) – Lim et al., 2018).

Internal zones (II)

Internal zones (II) were observed in ~20-40% of olivine grains in most of the current samples (except the WWTS, and sample BHK-3 from the Kimberley mine). The internal olivine zones (II) may exhibit a moderately heterogeneous BSE response (e.g., Fig. 3-5c-f), which is most obvious in grains with high Mg# core (e.g., Fig. 3-5c, d). Internal zones (II) are usually ~20-70 μm thick (up to 100 μm) and exhibit diffuse contacts with the preceding core, but sharp contacts with the rims (Fig. 3-5c-f). These internal zones display ‘euhedral’ forms (i.e., with straight, regular borders corresponding to crystallographic directions) when overgrowing relatively small cores and irrespective of core shape (i.e., Fig. 3-5d-f, 3-8b; Supp. Fig. S2).

In three samples (DB-D, WFSC-5, WESK-8), the outer regions of the internal zones (II) contain rare monomineralic inclusions of TIMAC spinel (titanian magnesian aluminous

chromite; Mitchell, 1986; Supp. Fig. S8). Petrographically similar internal zones have been described in other intrusions of the Kimberley cluster (e.g., see Fig. 4-6 of Howarth & Taylor, 2016; and Fig. 3a of Soltys et al., 2018b), as well as other kimberlites worldwide (e.g., see Fig. 11-12 of Sobolev et al., 2015).

Internal olivine zone (II) has a restricted Mg# (89.0-91.1; $\bar{x}$ = 90.0 ± 0.5, *n* = 56) and NiO contents (0.36-0.49 wt.%; $\bar{x}$ = 0.41 ± 0.03) that are higher than rims (Fig. 3-6a). CaO and MnO contents are low (≤0.1 wt.%; $\bar{x}$ = 0.06 ± 0.02, and 0.06-0.15 wt.%; $\bar{x}$ = 0.11 ± 0.02, respectively). These compositions are consistent with similar internal zones in olivine from the Benfontein sills (Howarth & Taylor, 2016).

Olivine Rims

Olivine rims were observed in all the studied samples and form a single and homogeneous zone in BSE images (Fig. 3-5, 3-8), consistent with rims in kimberlites worldwide (e.g., Bussweiler et al., 2015; Brett et al., 2009; Pilbeam et al., 2013; Nielson & Sand, 2008; Sazonova et al., 2015; Shaikh et al., 2018), including other samples from the Kimberley kimberlites (Giuliani et al., 2017; Soltys et al., 2018b).

In the studied samples, rims are generally <200 μm wide, but may be up to 350 μm thick (e.g., Fig. 3-5, 3-7). The maximum rim thickness reported here is substantially greater than that reported by Brett et al. (2009) in samples from Lac de Gras (Canada – i.e., <120 μm). However, our results are generally consistent with rim thicknesses reported by Arndt et al. (2010) in kimberlites from Greenland and southern Africa (i.e., exceeding 200 μm). Where rims directly overgrow olivine cores (i.e., internal zones are absent), the core-rim contact is usually sharp, and some rare cores show embayments (Supp. Fig. S9).

Olivine rims host a primary mineral inclusion assemblage that may include TIMAC-MÜM spinel, Mg-ilmenite, and rutile. These inclusions are almost always monomineralic and

generally 5-10 μm in size (occasionally up to 30-40 μm). This inclusion assemblage has been reported in olivine rims from other samples of the Kimberley kimberlites (i.e., Pasteris, 1980; Shee, 1985), as well as in many other kimberlites worldwide (e.g., Fedortchouk & Canil, 2004; Kamenetsky et al., 2008; Nielson & Sand, 2008).

Finally, olivine with a BSE response (and composition) identical to that of the rims occasionally lines decompression fractures that crosscut olivine grains (Supp. Fig. S10), as well as grain boundaries of polygranular macrocrysts (i.e., the 'nodules' described by Arndt et al., 2010; e.g., Supp. Fig. S10f), which are occasionally observed in the Kimberley kimberlites. This olivine is devoid of mineral inclusions and generally has a diffuse contact with the adjacent core. Occasionally these fractures may also contain carbonates and oxide minerals (e.g., Supp. Fig. S10d; see also Brett et al., 2015).

Olivine rims have a restricted Mg# (i.e., 87.9-89.3; $\overline{x}$ = 88.8 ± 0.3, *n* = 153 – Figs. 3-6, 3-7; Table 3-2). NiO contents decrease toward grain margins (0.39 to 0.06 wt.%), whereas CaO and MnO concentrations increase (0.01 to 0.32 wt.% and 0.08 to 0.28 wt.%, respectively). The compositions of these rims overlap those from other samples of the Kimberley cluster, e.g., Wesselton (Mg# ~89 – Shee 1985) and De Beers (Mg# ~88-89 – Boyd & Clement 1977; Moore 1988; Fig. 3-7).

Rims from sample BHK-3 have a systematically lower Mg# (86.8-87.8; $\overline{x}$ = 87.2 ± 0.3, *n* = 21) with similar decreases in NiO (i.e., 0.45 to 0.07 wt.%), and increases in MnO contents (0.07 to 0.24 wt.%). However, the CaO contents of rims in sample BHK-3 are low and relatively constant (<0.1 wt.%; Fig. 3-6e). These compositional features are indistinguishable from internal olivine zones (I), and very similar to those of olivine cores from the WWTS (albeit at a marginally higher Mg# – Fig. 3-6, see below). We note that the cores in sample BHK-3 are resorbed at a higher frequency than cores from other samples of the Kimberley kimberlites, with Fe-rich cores being absent.

Despite their apparent homogeneity in BSE images, the small (i.e., <100 μm) groundmass grains, which are common in aphanitic samples and lack typical core components, are zoned. These grains contain central region with compositions analogous to internal zone (II) (i.e., Mg# ~89-90, ~0.4-0.5 wt.% NiO), a rim with compositions indistinguishable from the rims of larger grains (i.e., Mg# ~89, NiO <0.4 wt.%, CaO >0.1 wt.%; Fig. 3-6), and occasionally a rind (Supp. Fig. S2).

Olivine Rinds

Olivine rinds were analysed in three samples (DB-D, WESK-3A, WESK-3M). Rinds also occur in samples BK-1 and WA1 but were either too thin or too altered to be analysed. Olivine rinds may be up to 50 μm thick, but are commonly <20 μm wide, and only preserved in unaltered samples. In BSE images olivine rinds appear homogeneous (Fig. 3-8), as is typical of most kimberlites worldwide (e.g., Bussweiler et al., 2015; Nielson & Sand, 2008). The contacts between olivine rinds and adjacent rims are generally sharp, with only thin (i.e., up to 10 μm) diffuse regions between the two zones in some grains (Fig. 3-8a). Where rinds are present, the rims may retain a euhedral shape (e.g., Fig. 3-5a), but more commonly exhibit embayments or partial replacement by rinds (Fig. 3-8c; Supp. Fig. S2). The rinds contain primary monomineralic inclusions of groundmass phases (i.e., Ti-rich MÜM spinel, perovskite, apatite and baddeleyite – e.g., Fig. 3-8a; Supp. Fig. S2i; see also Soltys et al., 2018b).

Olivine rinds have similar compositions in all analysed samples, with a high Mg# (92.0-92.9; $\bar{x}$ = 92.5 ± 0.3, *n* = 11), and low NiO (0.02-0.10 wt.%; $\bar{x}$ = 0.05 ± 0.02). The CaO (0.29-0.78 wt.%; $\bar{x}$ = 0.49 ± 0.15) and MnO (0.19-0.36 wt.%; $\bar{x}$ = 0.28 ± 0.05) contents increase toward grain margins (Fig. 3-6). One of the two outer zones (i.e. “Rim 1”) recognised by Howarth & Taylor (2016) in the Benfontein sills has a composition broadly similar to olivine rinds in the current study. Olivine rinds in kimberlites from Greenland, Canada, and Russia also

exhibit restricted and high Mg# values, low NiO, and increasing CaO and MnO concentrations toward grain margins, although the Mg# varies between intrusions (e.g., ~94 - Greenland – Nielsen and Sand, 2008; ~96-98 - Lac da Gras – Bussweiler et al., 2015; ~96 - Udachnaya-East – Kamenetsky et al., 2008).

High-Mg olivine

High-Mg olivine (i.e., Mg# > 96) occurs in samples WESK-7 and WESK-8. High-Mg olivine does not form concentric overgrowths, but occurs along grain margins, adjacent to fractures that cross-cut earlier olivine zones, and along trails of secondary inclusions (Fig. 3-8d-f; Supp. Fig. S5g-j). In contrast to the rim-like olivine that lines some fractures, high-Mg olivine is distinguished by its dark BSE response and sharp (rather than diffuse) contact with the adjacent olivine, which is usually strongly embayed (Fig. 3-8d-f, Supp. Fig. S11). The high-Mg regions may be up to ~60 μm thick, but are commonly <10 μm, and may contain relic inclusions of the adjacent olivine (i.e., the core or rim – Fig. 3-4e). High-Mg olivine is sometimes associated with olivine that has a BSE response intermediate between that of high-Mg olivine and adjacent olivine (Fig. 3-8f; Supp. Fig. S11). High-Mg olivine is texturally associated with magnetite, monticellite, and serpentine (and, in rare cases, phlogopite, pectolite, apatite, and sulfide minerals; Supp. Fig. S11a-d). Magnetite and monticellite occur as inclusions or intergrowths with high-Mg olivine (Fig. 3-8d, e; Supp. Fig. S11d), and together with serpentine and minor carbonates fill the fractures lined by high-Mg olivine. It is noteworthy that rinds and high-Mg olivine do not co-exist in the same sample, and that high-Mg olivine was only observed in samples of root zone kimberlites. Olivine with petrographic features similar to high-Mg olivine has been reported in the Pipe 1 kimberlite, Finland (see Fig. 1e of Abersteiner et al., 2018a), and surround secondary fluid inclusions in olivine from the Udachnaya-East kimberlite, Russia (see Fig. 11 of Abersteiner et al., 2018b).

High-Mg olivine has compositions approaching pure forsterite (up to Mg# = 97.6), coupled with high CaO and MnO (up to 0.76 and 0.22 wt.%, respectively), and low NiO contents (<0.05 wt.%). Many analyses of this zone have compositions intermediate between the adjacent zone and that of high-Mg crosscutting olivine (Fig. 3-6a, c, e), consistent with the observed variation in BSE response (e.g., Fig. 3-8f; Supp. Fig. S11). In the Pipe 1 kimberlite (Finland) this olivine has a similarly high Mg# (98.3-98.9), MnO and CaO contents between 0.19-0.23 and 0.21-0.30 wt.%, respectively (Abersteiner et al., 2018a).

Olivine from the Wesselton Water Tunnel Sills

Olivine from the WWTS sample has petrographic and compositional features that are distinct from olivine in other intrusions of the Kimberley kimberlites. In the WWTS most olivine grains are euhedral-subhedral and 0.5-1.0 mm in size, but occasionally up to 3 mm (Fig. 3-9). In BSE images these grains are (relatively) homogeneous, except for a thin (i.e., 20-50 μm) diffuse rim. These grains are all reversely zoned (i.e., cores have a lower Mg# then rims; Fig. 3-9; Supp. Fig. S12). The cores of these grains contain inclusions (~50 μm in size) of euhedral-subhedral TIMAC spinel, and less commonly Mg-ilmenite (e.g., Fig. 3-9; Supp. Fig. S12c, f). These inclusions are exceptionally abundant in some cores (Fig. 3-9b).

These low-Mg# cores have similar compositions, with an average Mg# of 86.2 ± 0.4 (*n* = 19), relatively high NiO (0.33 ± 0.05 wt.%), low CaO (0.08 ± 0.01 wt.%), and moderate MnO contents (0.16 ± 0.03 wt.%) (Table 3-2; Fig. 3-6b, d, f). These cores are compositionally distinct from those in olivine grains from other intrusions of the Kimberley cluster in that they do not exhibit the same variation in Mg# (typically ~6 units), and contain slightly higher NiO contents at comparable Mg# (Fig. 3-6b). The low-Mg# cores are compositional similar to internal olivine zone (I), and the low Mg# rims in sample BHK-3 of the Kimberley mine (Fig. 3-6).

The diffuse rims of olivine grains in the WWTS range from compositions similar to the low-Mg# cores, towards higher Mg# (i.e., 86.7-90.5), CaO (0.11-0.65 wt.%), and MnO contents (0.12-0.33 wt.%), but lower NiO contents (0.28-0.02 wt.%; Fig. 3-6b, d, f). This trend is distinct from the (relatively) constant Mg# of rims from other intrusions in the Kimberley cluster. The composition of olivine rims from the WWTS show limited variation between grains or across different samples (cf. Shee et al., 1994, and White et al., 2012 in Fig. 3-6b, d, f).

Rare larger and anhedral olivine grains from the WWTS contain high-Mg# cores, which are indistinguishable from those in the other Kimberley kimberlites (Fig. 3-6b, d, f; Table 3-2). These cores are overgrown by olivine that has features similar to the reversely zoned olivine described above (Fig. 3-9c; Supp. Fig. S12e). The contact between these high-Mg# cores and the overgrowths are sharp, and internal and transitional olivine zones are absent. These high-Mg# cores have a relatively restricted Mg# range (92.0-93.2; $\overline{x} = 92.8 \pm 0.4$, $n = 19$), and overlap those from previously studied samples of the WWTS (Fig. 3-6b, d; Shee et al., 1994; White et al., 2012).

Inclusions in low-Mg# olivine cores from the Wesselton Water Tunnel Sills

Spinel included in the low-Mg# olivine cores from the WWTS (e.g., Fig. 3-9b; Supp. Fig. S12) have homogeneous compositions within and between olivine grains (Supp. Table S4). These spinel inclusions are enriched in TiO_2 and depleted in Cr_2O_3 relative to early crystallised TIMAC spinel from other intrusions of the Kimberley kimberlites (e.g., Shee, 1985; Pasteris, 1983), but are consistent with the cores of groundmass spinel in the WWTS (Supp. Fig. S13; Shee et al., 1994; White et al., 2012). Despite these differences, the spinel compositions lie broadly along the same evolutionary trend as spinel from other intrusions of the Kimberley kimberlites (Supp. Fig. S13).

Application of the spinel-olivine Fe-Mg exchange thermometer ($T_{Ol\text{-}Sp}$) of Ballhaus et al. (1991), using the compositions of low-Mg# olivine cores and their spinel inclusions, yields average equilibration temperatures of 1116, 1127, and 1153 °C (±18 °C), at 0.1, 1.0, and 3.0 GPa, respectively. These temperatures are within the range calculated for spinel-olivine rim pairs in the Lac de Gras kimberlites (Canada) at the same pressure (i.e., 1170 ± 50 °C – Fedortchouk & Canil, 2004).

Compositional Variations Within Individual Olivine Grains

To resolve fine scale compositional variations within and between individual olivine zones, EPMA traverses (5 μm spacing) were undertaken on fresh olivine grains from the Bultfontein kimberlite (Fig. 3-10, 3-11; Supp. Fig. S14-S16). The results of these transects are consistent with EPMA spot analyses and the full data set is reported in Supp. Table S6.

Olivine cores exhibit homogeneous major element compositions (Fig. 3-10, 3-11), but diffuse transitional zones occur between the core and internal zone (II), as well as between the core and rim (i.e., where internal zones are absent). As similar core-rim transitional zones have been described in detail for kimberlitic olivine from Greenland, Canada, Brazil, and Southern Africa (Cordier et al., 2015; Howarth & Taylor, 2016; Lim et al., 2018; Pilbeam et al., 2013), we only present data for the transitional zones that occur between the core and internal zone (II); these zones are also far more abundant in the current samples. The compositions of these transitional zones are dependent on the core compositions; hence we describe the variations across transitional zones with respect to normal (high-Mg-Cr cores) and reverse (high-Fe-Mn cores) zonation patterns.

The transitional zones surrounding the cores of most normal zoned grains show a decrease in Mg# and Cr_2O_3 contents, whereas MnO contents increase with increasing distance from the core (e.g., Fig. 3-10, 3-12; Supp. Fig. S14, S15). In contrast, the transitional zones of

most reverse zoned grains show an increase in Mg# and Cr_2O_3 contents, whereas MnO contents are unchanged (e.g., Fig. 3-11, 3-12; Supp. Fig. S16). The CaO contents of the transitional zone increase across all measured grains. The variations in the transitional zones of normal zoned grains are consistent with the data reported by Cordier et al. (2015).

Variations in NiO contents across the transitional zones are non-systematic. Cordier et al. (2015) reported that variations in NiO contents across the transitional zones in their samples of kimberlites from Greenland were decoupled from variations in Mg#, and NiO concentrations remained similar to those of the adjacent core (see Fig. 1 of Cordier et al., 2015). Some grains from the current study display such features (Fig. 3-11, 3-12; Supp. Fig. S14), whereas other grains exhibit a minor decrease in NiO contents, linked to changes in Mg# (e.g., Fig. 3-10, 3-12). Interestingly there is no correlation between the NiO content of the core, and the variations in NiO content across the transitional zone (Fig. 3-12).

Regardless of the absolute composition of the transitional zones (which are dependent on core compositions), the trend is toward a relatively constant composition (except for NiO – see above), i.e., Mg# ~89-90, ~0.03-0.05 wt.% Cr_2O_3, and ~0.11-0.12 wt.% MnO. The contents of CaO increase across the transitional zone of all grains, and may reach values of up to 0.1 wt.%. These compositions are broadly consistent with the compositions of olivine rims (Fig. 3-12). However, whilst transitional zones in different grains show broadly similar compositional trends between grains, these zones never reach a homogeneous or consistent composition.

At the boundary between the transitional zones and the internal olivine zones (II), NiO contents begin to increase in both normally and reversely zoned grains, whereas Mg#, CaO and Cr_2O_3 contents may decrease or increase depending on their concentrations in the adjacent transitional zone (Fig. 3-10, 3-11, 3-12). The concentrations of MnO typically increase, but remain unchanged in some reverse zoned grains that have cores with MnO concentrations comparable to those of internal zone (II) (e.g., Fig. 3-11).

The absolute composition of internal zone (II) is dependent on the orientation of individual olivine crystals. When transects are measured parallel to the long axis (c or c') the Mg# (~90), NiO (~0.45 wt.%), Cr_2O_3 (~0.07 wt.%) and MnO (~0.12 wt.%) contents show homogeneous contents over a "plateau" of ~20 μm (e.g., Fig. 3-10 d, f). This plateaux corresponds to the outermost region (i.e., euhedral, dark BSE response) of internal zone (II) (Fig. 3-5c, d). In contrast, in transects measured parallel to the short axis (a or a') the Mg#, NiO, Cr_2O_3, and MnO contents of internal zone (II) increase towards values similar to the plateaux, before increasing/decreasing toward values typical of the rims (Fig. 3-10e, g).

The transition from internal zones (II) to olivine rims is marked by a decrease in Mg#, before stabilising at values typical of rims (~89). The NiO and Cr_2O_3 contents show a continuous decrease from internal zones (II) toward grain margins, whereas CaO and MnO contents increase (Fig. 3-10, 3-11, 3-12).

Discussion

Origin of Homogeneous Mg-rich Olivine Cores

The composition of olivine cores with Mg# >89 and CaO <0.05 wt.% (i.e., ~55% of cores analysed) have compositions that overlap olivine in granular peridotite xenoliths entrained by the Kimberley kimberlites (e.g., Fig. 3-3, 3-4). A xenocrystic origin of such cores is supported by: (1) inclusion of mantle phases (e.g., Cr-diopside, enstatite), with compositions typical of those in granular peridotites (i.e., high Ca# [100 × Ca/(Ca + Mg)] and Na_2O in Cr-diopside; low CaO and Al_2O_3 in enstatite – e.g., Moore and Lock, 2001; Gibson et al., 2008); (2) thermobarometric calculations indicating equilibration of Cr-diopside inclusions within the SCLM (i.e., ~145 km depth); and (3) solid-state deformation of olivine grains before entrainment into the host kimberlite (see also Arndt et al., 2010; Cordier et al., 2015). The Na-Al enrichment of the margins of some clinopyroxene inclusions probably represents slight

modification by kimberlitic fluids that infiltrated along fractures (see also Kamenetsky et al., 2009). An origin of such cores as xenocrysts from the disagregation of mantle peridotites is consistent interpretations by multiple previous studies (e.g. Boyd and Clement, 1977; Mitchell, 1973, 1986)

Origin of Homogeneous Mg-Ca-rich Olivine Cores

Olivine in most (~98%) coarse-grained granular peridotite xenoliths from Kimberley have CaO contents ≤0.05 wt.% ($\overline{x}$ = 0.02 ± 0.01 wt.%, *n* = 167 – Fig. 3-4d). However, the CaO contents of some Mg-rich (Mg# >89) 'peridotitic' cores are marginally higher than 0.05 wt.% (up to 0.11 wt.% CaO; Fig. 3-3c, 3-4b), with 25% of cores being Mg-Ca-rich (Fig. 3-4b). Olivine cores anomalously enriched in Ca have been reported in other kimberlites worldwide (e.g., Sobolev et al., 2015; Sazonova et al., 2015), including other studies of the Kimberley cluster (Supp. Fig. S3; Arndt et al., 2010; Howarth & Taylor, 2016; Moore, 1988). In addition, similar Ca-rich cores have recently been reported in olivine lamproites (Shaikh et al., 2019). The Ca-enrichment of the olivine cores in the current samples is similar to the compositions of olivine in sheared peridotite xenoliths from southern African kimberlites (i.e., $\overline{x}$ = 0.07 ± 0.03, *n* = 192; Fig. 3-3, 3-4; see literature compilation in Supp. Table S5). Derivation of the Mg-Ca-rich olivine cores from sheared peridotites is supported by the fact that these Mg-Ca-rich cores have an average Mg# of 91.0 ± 1.3, which is identical to that of sheared peridotites (91.0 ± 1.2), but slightly lower than olivine in granular peridotites (i.e., 92.3 ± 1.4; Fig. 3-4).

In previous studies, the Ca enrichment of these cores was coupled with enrichment in Ti (Sobolev et al., 2015), and other trace elements (e.g., Co, Al, V, Cu, and Na – Howarth & Taylor, 2016). The limited trace element data available for olivine in sheared peridotites indicates similar trace element enrichment (i.e., Al, Na, Ti – Hervig et al., 1986). Finally, these Mg-Ca-rich cores occur exclusively within the smaller (i.e., <500 μm) euhedral groundmass

grains. This observation may be explained by derivation of these cores from the neoblastic olivine grains that represent a major and often dominant component in sheared peridotites.

It is noteworthy that the formation of sheared peridotites is commonly attributed to deformation during the influx of Fe-Ti-Ca-(H_2O)-rich (proto-)kimberlite melts (e.g., Ionov et al., 2017; Kargin et al., 2017; Katayama et al., 2011). Micro-textural (e.g., Mercier, 1979) and geochemical (e.g., Griffin et al., 1999; Jollands et al., 2018) studies indicate that sheared peridotites formed immediately preceding kimberlite magmatism. If Mg-Ca-rich olivine cores are sourced from neoblasts in sheared peridotites as proposed in this study, they must have formed immediately prior to entrainment by the host kimberlite.

Origin of Homogeneous Fe-rich Olivine Cores

The compositions of the subordinate population (~20%) of Fe-rich (i.e., Mg# <89; Figs. 3-3, 3-4) olivine cores are inconsistent with derivation from the disaggregation of typical granular or sheared peridotites. These Fe-rich cores have similar compositions to olivine in cumulate Fe-rich dunite xenoliths from Kimberley (Rehfeldt et al., 2007; Dawson et al., 1981), and olivine megacrysts from some southern African kimberlites (literature compilation in Supp. Table S5). An origin of these Fe-rich cores from the disaggregation of megacrystic/dunitic lithologies is consistent with observations made in previous studies (e.g. Boyd and Clement, 1977; Giuliani, 2018; Lim et al., 2018; Moore & Costin, 2016; Shaikh et al., 2018). As with sheared peridotites, megacrysts are widely considered to have formed during (proto-)kimberlite crystallisation or metasomatism at lithospheric mantle depths (e.g., Giuliani et al., 2014; Kopylova et al., 2009; Lawless et al., 1979; Moore & Belousova, 2005).

Formation of Transitional Olivine Zones (Heterogeneous Xenocrystic Cores)

Transitional zones with diffuse contacts occur between the core and internal zone (II), as well as between the core and rim of some olivine grains in the Kimberley kimberlites (e.g., Fig. 3-10). Regardless of the position of the transitional zone within an individual grain, the compositional trends are the same and therefore the mechanism of formation is inferred to be similar. Previous studies attributed these zones to diffusional re-equilibration of the core with the ascending kimberlite melt before olivine saturation was achieved and the rims crystallised (Lim et al., 2018; Howarth & Taylor, 2016), or alternatively to diffusive exchange between the core and rim after crystallisation of the latter (Pilbeam et al., 2013).

In contrast, Cordier et al. (2015) proposed that these zones form during fluid assisted recrystallization of the deep lithosphere. In this scenario orthopyroxene (as well as clinopyroxene and garnet) is consumed producing dunite lithologies in a metasomatic aureole surrounding a kimberlite fluid pocket (e.g., see Fig. 15 of Arndt et al., 2010). This process is considered to precede entrainment of dunitic material by the host kimberlite. However, this mechanism has been debated – see comments by Moore (2017), and Giuliani & Foley (2016), and the reply by Cordier et al. (2016).

The diffuse contacts between the core and transitional zone, and compositional trends within the transitional zone that are dependent on the core composition, support the formation of the transitional zone by diffusive re-equilibration (see also Lim et al., 2018; Howarth & Taylor, 2016). The peculiarity of the transitional zone is that the melt with which they equilibrated was evidently not the same as that responsible for crystallisation of the succeeding internal zones (II) (e.g., Fig. 3-10, 3-12). This is because the (latter) melt that formed internal zone (II) was relatively enriched in NiO, but depleted in CaO compared to the melt which formed the transitional zone (Fig. 3-12). For the same reasons (compositional differences), the melt which formed the transitional zone could not have been that which was parental to megacryst suite or internal zones (I). The most suitable candidate for the formation of the

transitional zones is a melt with a composition similar to that responsible for crystallisation of the rims (e.g., Fig. 3-12), i.e., a melt compositionally similar to the ascending kimberlite. However, the location of the transitional zones within many olivine grains in this study (i.e., preceding internal zones (II) rather than the rims) presents a contradictory temporal relationship. In other words, the cores appear to have interacted with a melt compositionally similar to that involved in formation of the rims, before crystallisation of the internal zones (II). One explanation is that the melt that formed the transitional zones was an earlier pulse of kimberlite magma which intruded into lithospheric peridotite. In this respect we agree with the conclusions of Cordier et al., (2015), that these zones formed by metasomatism of the deep lithospheric mantle. This explanation accords with other evidence of kimberlite-related metasomatism immediately preceding kimberlite magmatism (see below; and Arndt et al., 2010; Cordier et al., 2015; Jackson & Gibson, 2018).

Not all grains show a decrease in NiO contents across the transitional zones (i.e., they remain similar to the adjacent homogeneous core – see also Cordier et al. 2015), which is in contrast to the systematic variations in Mg#, MnO, and CaO contents (e.g., Fig. 3-11; Supp. Fig. S15). Given that above we advocate that transitional zones formed by diffusive exchange between the core and a previous pulse of kimberlite melt, the lack of decrease in NiO contents of some transitional zones (including those adjacent to high NiO cores) requires explanation. The variable behaviour of NiO across the transitional zones suggests the melt responsible for the generation of the transitional zone evolved (by olivine fractionation) over time; alternatively, the transitional zones of different grains formed during different metasomatic events. The subsequent removal of the outer regions of the transitional zone due to partial assimilation of olivine xenocrysts by the host kimberlite melt (see previous section; Supp. Fig. S9) and/or attrition may explain why the transitional zones do not fully equilibrate with the same melt composition (i.e., they do not reach homogeneous compositions).

Formation of internal olivine zones (I)

Internal olivine zones (I) have an Mg# ranging of 87.0 ± 0.5 (n = 6), very low CaO (<0.05 wt.% – Fig. 3-6e; Table 3-2), and variable MnO and NiO concentrations (i.e., similar to rims - 0.13-0.21 and 0.09-0.29 wt.%, respectively; Fig. 3-6a, c). Internal zones (I) are generally rare in kimberlitic olivine, but their occurrence in kimberlites from multiple cratons (i.e., Greenland, Canada, Brazil, southern Africa – Cordier et al., 2015; Lim et al., 2018; This study) precludes serendipitous formation. At the same time, the rarity of this zone suggests it did not directly crystalised from the ascending host kimberlite melt, else like rims it would likely be more abundant. The relatively sharp contacts between cores and internal zones (I) (Fig 3-5a, b; Supp. Fig. S7; see also Fig. 4e, f of Cordier et al., 2015 [their "M1" zone]) indicate that these zones are not the product of diffusive re-equilibration, but rather crystallisation from a melt. The presence of embayments where internal zones (I) are overgrown by rims (Fig. 3-5a, b; see also Cordier et al., 2015; Lim et al., 2018) indicates resorption by the host kimberlite melt before olivine saturation was reached, or resorption by an unrelated melt prior to entrainment by the host kimberlite. This implies internal olivine zones (I) did not crystallise from the host kimberlite melt. The rarity of internal zone (I) may be partially due to this resorption and/or abrasion, combined with an originally limited thickness.

It was assumed by previous studies that such internal olivine zones crystallised within the lithospheric mantle (e.g., Lim et al., 2018, Cordier et al., 2015). This interpretation was based on the fact that these internal zones formed before rims, which likely crystallised during ascent through the lithospheric mantle, but before emplacement into the upper crust (see below). In addition, these zones are compositionally similar to magmatic olivine from WWTS, which

may have formed from a stalled kimberlite melt that underwent olivine fractionation in the shallow lithospheric mantle (see discussion below).

Lim et al. (2018) suggested that olivine internal zones (I) represent crystallisation from an earlier pulse of 'evolved' kimberlite melt. The Fe enrichment of internal olivine zones (I) relative to the rims, but similar variable NiO and MnO contents (see Fig. 3-7, 3-8 of Lim et al., 2018), was attributed to crystallisation from a kimberlite melt that had experienced olivine fractionation, whereas the low CaO concentrations were ascribed to co-crystallisation of clinopyroxene. Alternatively, Cordier et al. (2015) suggested that these internal zones crystallised from a basaltic melt and also argued for co-crystallisation of clinopyroxene to explain the low CaO contents. However, the presence of this zone in kimberlites worldwide, as well as the connection between this zone and olivine from the WWTS (see below) strongly indicates a genetic association with kimberlite rather than basaltic magmatism.

Experimental data indicates that clinopyroxene is stable in kimberlitic melts at mantle pressures (e.g., Edgar et al., 1988; Stone & Luth, 2016). In addition, the composition and isotope systematics of clinopyroxene in some mantle xenoliths are interpreted to reflect formation during kimberlite metasomatism (Aulbach et al., 2013; Simon et al., 2003; Grégoire et al., 2003; Kargin et al., 2016; Fitzpayne et al., 2018b; Jackson & Gibson, 2018). However, the internal olivine zones (I) appear to be devoid of clinopyroxene inclusions; therefore, it is plausible that the melt parental to internal zones (I) previously crystallised clinopyroxene, lowering the melt CaO content.

An additional factor may also influence the Ca content of internal olivine zones (I). For example, the low Ca contents of kimberlitic olivine megacrysts (which are similar to internal zones (I), and olivine from the WWTS and low Mg# rims from sample BHK-3) were interpreted to reflect crystallisation from a H_2O rich melt (Howarth, 2018). However, the dependence of Ca distribution between olivine and liquid ($D_{Ca}^{Ol/L}$) on H_2O contents was described for basaltic

arc magmas (e.g., Frieg et al., 2006), and it is unclear whether these effects are applicable to kimberlitic magmas, which are considered to be transitional silicate-carbonate melts (e.g., Brooker et al., 2011; Nielsen & Sand, 2008; Soltys et al., 2018a).

In summary, we suggest that internal olivine zone (I) crystallised within the lithospheric mantle from of an earlier pulse of kimberlite melt that had undergone olivine fractionation. The low Ca contents could be attributed to crystallisation from a H_2O-rich melt that previously crystallised clinopyroxene. If this interpretation is correct, then these zones have an 'antecrystic' origin (i.e., crystallised from a previous pulse of related magma). In this case, olivine internal zones (I) may form part of the antecrystic assemblage present in the Kimberley kimberlites, alongside high Ti-Cr phlogopite zones (Giuliani et al., 2016; Soltys et al., 2018b). An antecrystic origin for the internal zones (I) is consistent with the highest abundance of internal olivine zones (I) in sample WESK-3A, which represents a late-stage cross-cutting dyke from the root zone of the Wesselton kimberlite. The abundance of internal olivine zones (I) in this sample is attributed to late-stage sampling of a lithospheric column that had been extensively metasomatised by previous pulses of kimberlite melt (e.g., that which formed the WWTS – see below).

Formation of Olivine in the Wesselton Water Tunnel Sills (WWTS)

The high-Mg# (i.e., ~92.0-93.2), anhedral to angular cores of some large olivine grains from different samples of the WWTS probably represent mantle-derived xenocrysts, akin to those in other samples of the Kimberley kimberlites (Fig. 3-9c, 6b, d, f; See et al., 1994; White et al., 2012). However, xenocrystic cores from the WWTS are rare, and have a restricted compositional range compared to xenocrystic cores from the other intrusions of the Kimberley cluster (i.e., Mg# typically spans ~6 units). The composition of these high-Mg# cores may suggest derivation from a relatively depleted mantle lithology. This could represent sampling

of the shallow depleted lithospheric material which dominates the upper ~120 km below Kimberley (e.g., Fig. 3-11 of O'Reilly & Griffin, 2006).

On the other hand, the petrographic and compositional features of low-Mg# olivine cores from the WWTS are atypical of the xenocrystic olivine cores that are common to other intrusions of the Kimberley cluster. The inclusion of groundmass minerals (i.e., spinel and Mg-ilmenite), a subhedral-euhedral shape, relatively homogeneous Mg#, and variable NiO contents suggests these low-Mg# cores crystallised from the host kimberlite melt. Similar low-Mg# olivine cores may also be (rarely) recorded in other kimberlites worldwide. For example Cordier et al., (2015) and Pilbeam et al., (2013) reported a relatively rare population of low-Mg# cores (i.e., ~85 and ~87) which appear to show decreases in Ni, increasing Mn, and low Ca contents (see Fig. 1 and 3 of Cordier et al., 2015). These localities also notably host olivine with internal zone (I).

The absence of early crystallised TIMAC spinel (i.e., Cr_2O_3 >47 wt.% – Shee et al., 1985), olivine internal zone (II) and rims (as well as Mg-ilmenite and rutile) may be due to fractionation of the kimberlite melt *en route* to the surface. This assumes the primitive melt parental to the WWTS was similar in composition to the other intrusions of the Kimberley cluster and therefore underwent a comparable crystallisation sequence. The removal of these early crystallised Mg-rich phases could explain the relatively Fe-rich compositions of later olivine, spinel, and ilmenite as argued by Shee et al. (1994). Fractionation could occur if the kimberlite melt temporarily stalled (or almost-stalled) at lithospheric mantle depths. The residual melt may have recommenced ascent by mixing with a more primitive magma, or due to CO_2 exsolution triggered by crystallisation of carbonate-free phases. The WWTS magma may have stalled due to ascent through a lithospheric column which had not yet been preconditioned by extensive kimberlite-metasomatism (see Giuliani et al., 2016). This would be consistent with the fact that the WWTS predate intrusion of the main Wesselton pipe (Shee

et al., 1994). In turn, we envisage that magmas such as that parental to the WWTS pre-conditioned the conduit for subsequent magma batches to reach the surface without prohibitive amounts of mantle assimilation. Based on the xenolith constraints (see Shee et al., 1994) we suggest magma stalling occurred after ascent through garnet facies mantle (i.e., above ~90-100 km depth), but before the crust-mantle transition (i.e., ~40 km; Globig et al., 2016). Such low-Mg# olivine crystallising from the WWTS magma, as well as the olivine xenocrysts overgrown by low-Mg# internal zones (I), were then sampled by later-stage dykes (e.g., WESK-3A) which cross-cut the main Wesselton pipe. Based on compositional and petrographic similarities we infer a linked genesis of internal olivine zone (I), low-Mg# cores from the WWTS, and low-Mg# rims from sample BHK-3. The low CaO contents of this olivine is explained by crystallisation from a H_2O rich melt that had previously crystallised clinopyroxene.

The progressive increase in Mg# in the 'rims' (i.e., 86.7-90.5 in the outer ~ 20-50 μm; see Fig. 3-9a; Supp. Fig. S12) of olivine grains from the WWTS was probably caused by increasing fO_2 (Shee et al., 1994) and therefore Fe^{3+}/Fe^{2+} in the melt, with Fe^{3+} having very low compatibility in olivine. Conversely, increasing Mn and Ca, and depletion in Ni toward grain margins is attributed to fractional crystallization of olivine. These 'rims' form a trend between the low-Mg# cores and compositions similar to olivine rinds from other intrusions of the Kimberley cluster (Fig. 3-6). This evidence, combined with the diffuse contact between these 'rims' and low-Mg# cores, suggests that these rims formed by a combination of crystallisation and diffusive re-equilibration with the low-Mg# cores.

The WWTS sills therefore represent a good example of a kimberlite magma that probably stalled within the lithospheric mantle and lost its early crystallised and deep xenolithic/xenocrystic cargo. The fundamental implication is that liquidus olivine and chromite in kimberlites crystallise (or start to crystallise) at depths exceeding the shallow lithospheric mantle (i.e., > 90 km).

Multiple lines of evidence for (proto-)kimberlite metasomatism

A significant proportion of the xenocrystic olivine cores (~45% – i.e., those with Mg# >89 and CaO ≥ 0.05 wt.%; or Mg# < 89) entrained by the Kimberley kimberlites have either undergone pre-entrainment (proto-)kimberlite metasomatism and/or are direct products of (proto-)kimberlite crystallisation (i.e., cores derived from sheared peridotites and megacrysts). However, this is a minimum estimate because: (1) olivine in some rare sheared peridotites have an Mg# >89 and CaO <0.05 wt.% (Fig. 3-3, 3-4); (2) some granular peridotites may have experienced recent kimberlite metasomatism without shearing or a significant decrease in the Mg# and/or increase in CaO contents of olivine (e.g., Simon et al., 2007; Aulbach et al., 2013); and (3) this estimate does not include olivine cores that have a transitional zone (also attributed to proto-kimberlite metasomatism).

Furthermore, olivine from the WWTS has distinct petrographic and compositional features, interpreted to have crystallised from a kimberlite melt that had undergone fractionation of olivine and oxide minerals within the lithospheric mantle. Compositionally similar olivine is also recorded as subordinate populations in the Benfontein sills, late-stage dykes the Wesselton pipe, a sample from the Kimberley mine, and in multiple samples as internal zone (I) overgrowing xenocrystic cores.

The high abundance of kimberlite-metasomatised xenocrysts and kimberlitic antecrysts in the Kimberley kimberlites is consistent with the widespread occurrence of mantle xenoliths that experienced (proto-)kimberlite metasomatism including peridotites, eclogites, and MARID (e.g., Dawson et al., 2001; Soltys et al., 2016; Fitzpayne et al., 2018a; Jollands et al., 2018; Misra et al., 2004; Giuliani et al., 2013a,b). In addition, the recent metasomatic addition of clinopyroxene, garnet, phlogopite, and ilmenite to mantle peridotites from kimberlites worldwide (South Africa, Canada, and Russia) has been attributed to interaction with

kimberlite-related melts, based on geochemical and isotopic constraints (e.g., Aulbach et al., 2013; Fitzpayne et al., 2018b; Grégoire et al., 2003; Jackson & Gibson, 2018; Kargin et al., 2016; Simon et al., 2003). The implication is that the mantle material sampled by kimberlites probably formed within or adjacent to the magmatic conduits and is not necessarily representative of the wider lithospheric mantle. Rather this material was extensively metasomatised by previous pulses of kimberlite magma. This proto-kimberlite metasomatism may be integral to the successful ascent of subsequent magma batches (e.g., Giuliani et al., 2016). Finally, kimberlite metasomatised mantle material may be disproportionately represented by deeply derived xenoliths, as indicated by the Mg# of olivine in spinel peridotites which are systematically higher than olivine in garnet peridotites (e.g., Aulbach et al., 2012).

Olivine formation during kimberlite melt ascent

Internal olivine zones (II)

Internal olivine zone (II) has a restricted Mg# (90.0 ± 0.5, n = 56) and NiO contents (ie., higher than rims - 0.41 ± 0.03; Fig. 3-6a), coupled with low CaO and MnO contents (0.06 ± 0.02, and 0.11 ± 0.02, respectively). Euhedral Mg-Ni-Cr-rich internal zones similar to those described here occur in most intrusions of the Kimberley cluster (Howarth & Taylor, 2016; Soltys et al., 2018b), and in other kimberlites worldwide (Sobolev et al., 2015). Howarth & Taylor (2016) suggested that these zones formed by partial in-situ equilibration of xenocrystic cores with early kimberlitic melts in the deep lithosphere following orthopyroxene assimilation. Whereas, Soltys et al. (2018b) argued that the euhedral shape of internal olivine zones (II) and rare inclusions of TIMAC spinel indicate crystallisation from the host kimberlite magma during ascent through the lithosphere.

Electron microprobe transects show that the Mg#, NiO and Cr_2O_3 contents of the internal zones (II) converge on values of ~90, 0.45 wt.%, and ~0.06-0.07 wt.%, respectively, and are relatively constant in transects parallel to the c/c'-axis (Figs. 3-10d, f). This is interpreted as a growth feature resulting from more rapid and voluminous growth along the c/c' axis.

The elevated Ni contents of internal zones (II) relative to rims (and most cores) may reflect the fact that this olivine is the earliest phase to crystallise in the Kimberley kimberlites. However, the Ni enrichment of internal olivine zones (II) may also be a function of sulfide mineral assimilation, as it has been demonstrated that sulfide minerals are highly soluble in carbonate-rich H_2O-bearing melts such as kimberlites (e.g., Aulbach et al., 2016, 2018, 2019). The combination of high Ni and Cr contents might also indicate assimilation of bulk peridotitic material (including olivine) before olivine saturation was achieved and internal zone (II) crystallised. Early resorption of mantle-derived olivine is supported by petrographic evidence, i.e., embayment of some cores (Supp. Fig. S9). The rarity of TIMAC inclusions in internal olivine zones (II) is consistent with the elevated Cr concentrations of these zones. Low Ca contents relative to the rims, but similar to internal zones (I) may be due to previous crystallisation of clinopyroxene from a melt with high H_2O activity, as outlined in the previous section.

If the onset of olivine crystallisation (i.e., internal zones (II)) is linked to the assimilation of mantle phases (especially orthopyroxene – e.g., Mitchell, 1973; Pilbeam et al., 2013; Buswillier et al., 2015; Brett et al., 2009; Kamenetsky et al., 2008) in an ascending kimberlite melt, then the experiments of Stone & Luth (2016) provide constraints on the depth of olivine crystallisation. This study suggests that orthopyroxene assimilation occurs at 2.5-3.5 GPa (~80-120 km depth). These depths of formation are consistent with the crystallisation of the internal

zones (II), and also rims in the lithospheric mantle, before emplacement into the upper crust (Giuliani, 2018).

Nonetheless, the non-ubiquity of internal zones (II) is difficult to reconcile with magmatic crystallisation, unless these zones formed in the lithospheric mantle before entrainment of xenocrystic cores (i.e., those derived from typical mantle peridotites and megacrysts) derived from the shallow mantle. We therefore also consider a slight variant on the model proposed by Howarth and Taylor, (2016), whereby internal zones (II) formed by crystallisation of (rather than equilibration with) a proto-kimberlite melt rather than the host kimberlite. This model may explain the greater extent of diffusion between internal zones (II) and cores/transitional zones compared to the limited diffusion observed between cores and rims. In conclusion, both crystallisation from the host magma during ascent or crystallisation from earlier pulses of kimberlite melt in the lithospheric mantle are permissible hypotheses based on currently available data, with the former presently favoured.

Olivine rims

Olivine rims have a restricted Mg# (88.8 ± 0.3, n = 153 – Figs. 3-6, 3-7; Table 3-2), NiO contents decrease toward grain margins (0.39 to 0.06 wt.%), whereas CaO and MnO concentrations increase (0.01 to 0.32 wt.% and 0.08 to 0.28 wt.%, respectively). Olivine rims are ubiquitous in fresh coherent and volcaniclastic kimberlites (Boyd and Clement, 1977; Brett et al., 2009; Kopylova et al., 2016; Giuliani, 2018; Lim et al., 2018). Their euhedral shape when overgrowing relatively small cores, consistent geochemical trends between grains, and inclusions of groundmass minerals (i.e., TIMAC spinel, Mg-ilmenite, and rutile) provides strong evidence of a magmatic origin, consistent with previous findings (Giuliani, 2018, and references therein). The composition of rims and internal zones (II) in olivine grains from most intrusions of the Kimberley cluster are indistinguishable (except WWTS samples, sample

BHK-3 from the Kimberley mine, and some samples from the Benfontein Sills; Fig. 3-7), indicating a similar melt composition was parental to most intrusions of the cluster. This implies a similar source composition and is consistent with arguments based on isotope systematics (e.g., Woodhead et al., 2009) and bulk-rock geochemistry (le Roex et al., 2003). The similar rim and internal zone (II) compositions across dyke, sill, and root zone kimberlites supports the conclusion that not all dykes and sills have undergone extensive pre-emplacement fractionation (e.g., Soltys et al., 2018b). However, extensively fractionated magmas appear to preferentially intrude as sills (e.g., WWTS, some units of Benfontein).

Olivine rims are considered to have crystallised on ascent, but before intrusion into the upper crust (Arndt et al., 2010; Mitchell, 2008; Giuliani, 2018; Soltys et al., 2018b). This inference is based on the presence of decompression fractures lined by olivine with rim compositions (Supp. Fig. S10; see also Brett et al., 2015), textural evidence of rim crystallisation before mechanical abrasion in the host kimberlite (Arndt et al., 2010), and homogenous rim compositions in kimberlites within the same cluster despite different emplacement modes (i.e., dykes/sills *vs*. root zone kimberlites – this study; coherent *vs*. volcanoclastic kimberlites – Brett et al., 2009; Giuliani, 2018). Finally, small euhedral groundmass grains (i.e., Mg# = 88-90) that lack a xenocrystic core exhibit compositions consistent with zonation from internal olivine zones (II) to rims and occasionally to rinds (Fig. 3-6; Supp. Fig. S2). This supports previous suggestions that these grains are 'true' phenocrysts (Brett et al., 2009; Bussweiler et al., 2015).

Olivine formation after crustal emplacement

Olivine rinds

Olivine rinds have a high Mg# (92.5 ± 0.3, n = 11), low NiO (0.05 ± 0.02 wt.%). The CaO (0.29-0.78 wt.%; $\bar{x}$ = 0.49 ± 0.15) and MnO (0.19-0.36 wt.%; $\bar{x}$ = 0.28 ± 0.05) contents increase

toward grain margins (Fig. 3-6). The inclusion of groundmass kimberlite phases in olivine rinds (i.e., MÜM spinel, perovskite, apatite, and baddeleyite; Soltys et al., 2018b) indicates crystallisation with or subsequent to these phases. In the Kimberley kimberlites, olivine rinds crystallise before monticellite, kinoshitalite, and mesostasis phases (i.e., calcite, dolomite, and serpentine – Soltys et al., 2018b). Olivine rinds (Mg# = 92.5 ± 0.3) display Mg-enrichment relative to the rims (Mg# = 88.8 ± 0.3), a feature also displayed by other mid-late stage magmatic phases (e.g., spinel, monticellite, and ilmenite; Shee, 1985; Pasteris, 1980; Giuliani et al., 2017; Soltys et al., 2018b). This Mg-enrichment is usually explained by progressive increases in fO_2 of the melt and attendant Fe oxidation to Fe^{3+} during crystallisation (e.g., Bussweiler et al., 2015; Soltys et al., 2018b; Lim et al., 2018). The Ca and Mn enrichment, and Ni depletion of the rinds is best explained by extensive fractional crystallisation of early Ca-Mn-poor, Ni-rich phases (e.g., olivine internal zones (II) and rims, spinel, ilmenite, rutile). Calcium enrichment is also recorded by the replacement of ilmenite with perovskite in the kimberlite groundmass (Pasteris, 1980; Shee, 1985; Soltys et al., 2018b), and culminates with the crystallisation of apatite, monticellite, and eventually carbonates. Therefore, the composition, texture, and inclusion assemblages of these rinds indicate that they crystallised from an evolved and oxidised kimberlite melt, together with other groundmass minerals.

Many rims display embayment features where in contact with rinds (Fig. 3-8a, b), whereas other rims appear to have been directly replaced by rinds (Fig. 3-8c; Supp. Fig. S2). Similar replacement features are evident in the BSE images reported by previous studies (e.g., Fig. 2 of Bussweiler et al., 2015). Therefore, we suggest that olivine rinds formed by a combination of replacement of pre-existing olivine and crystallisation of new olivine. Based on the common assumption that other groundmass phases (i.e., perovskite, apatite, baddeleyite – Mitchell, 2008) crystallise in the upper crust, and the fact that these phases occur included in

the olivine rinds, it is likely that the rinds also formed syn- or post- kimberlite emplacement into the upper crust.

High-Mg cross-cutting olivine

High-Mg olivine exhibits elevated Mg# (up to 97.6), compared to olivine rinds (Mg# ~ 92.5) and rims (Mg# ~ 88.8), coupled with high CaO and MnO (up to 0.76 and 0.22 wt.%, respectively), and low NiO contents (<0.05 wt.%). The textural association between high-Mg olivine, monticellite, magnetite, serpentine, and occasionally pectolite, apatite, phlogopite, and sulfides (Fig. 8d-f; Supp. Fig. S2, S11) indicates formation during the latest stages of groundmass crystallisation in the upper crust. Similar to rinds, the extreme Mg-enrichment of this olivine is best explained by progressively increasing fO_2 in the residual (high Mg/Fe^{2+}) kimberlite fluids. In the case of high-Mg olivine, this enrichment may be exacerbated by the extensive crystallisation of Fe-rich spinel (especially late stage magnetite). Although the rinds and high-Mg olivine were not observed to co-exist in the same sample, high-Mg olivine is inferred to have formed later than rinds based on the included mineral assemblages (i.e. rinds do not host monticellite and magnetite) and their more evolved compositions (i.e., in this case Mg-rich). This evidence, combined with the resorption of olivine adjacent to high-Mg olivine (Fig. 8d-f; Supp. Fig. S2, S5g-j, S11) and the inclusion of relics of the adjacent olivine within high-Mg olivine (Fig. 3-8e), suggests that high-Mg olivine formed by dissolution and reprecipitation (e.g., Putnis & Austrheim, 2013).

The fine scale variations in BSE responses within high-Mg olivine (Fig. 8f; Supp. Fig. S5, 11), and compositions that trend toward the adjacent olivine cores/rims (Fig. 3-6), suggests interaction with pre-existing olivine during high-Mg olivine formation. These fluctuations in high-Mg olivine composition may also represent varying fluid-rock ratios in the waning stages of magmatic/deuteric crystallisation. The sharp contact between high-Mg olivine and the

adjacent olivine indicates that replacement occurred at temperatures low enough to prevent observable diffusion (i.e., <600-700˚C – e.g., Giuliani et al., 2013; Chakraborty, 2010). In contrast, rim-rind contacts may show thin (i.e., 5-10 μm) diffuse regions between these zones (Fig. 3-8a). These features and the textural association with serpentine are consistent with high-Mg olivine formation from hydrous, probably deuteric fluids at relatively low temperature (i.e. in the stability field of serpentine – see below).

Co-precipitation of highly forsteritic olivine (Mg# ~98) and serpentine is not unique to these kimberlites, and has been observed in peridotite massifs (e.g., Majumdar et al., 2016). In these occurrences the Mg-rich olivine was in oxygen isotopic equilibrium with serpentine (lizardite) and magnetite, and isotopic modelling indicates formation at temperatures of ~400-430 °C (Scicchitano et al., 2018). Furthermore, Plechov et al. (2018) recently reviewed occurrences of high-Mg olivine (Mg# >96) in various rock types (e.g., carbonatites, chromitites, skarns, and alkaline ultrabasic lavas) and concluded that such extreme Mg-enrichment only occurs as a result of oxidation and/or low temperature formation (i.e., ~400-650 °C). Therefore, we suggest that high-Mg olivine in the Kimberley kimberlites formed at similarly low temperatures, from highly oxidised fluids in association with serpentinisation (i.e., ~400 °C; Mitchell 2008).

Similar high-Mg olivine in the Pipe 1 kimberlite (Finland) was argued to have formed post-emplacement in the upper crust (Abersteiner et al., 2018a). In addition, high-Mg olivine commonly surrounds secondary fluid inclusions in olivine from the Udachnaya-East (Abersteiner et al., 2018b) and the Kimberley kimberlites (Supp. Fig. S5). However, in the case of the Udachnaya-East kimberlite, Abersteiner et al. (2018b) contrarily propose a high pressure and temperature origin of these inclusions and high-Mg olivine, whereby primitive kimberlite melt existed in fractures and was trapped by olivine [internal zone (II) or rim] crystallisation (see Fig. 16 of Abersteiner et al., 2018b).

Instead, the occurrence of high-Mg olivine in equilibrium with serpentine in the Kimberley kimberlites (this study) and other rock types (Majumdar et al., 2016; Scicchitano et al., 2018) is consistent with these inclusions trapping residual alkali-Cl-rich kimberlite fluids after crustal emplacement and following crystallisation of most groundmass phases (see also Giuliani et al., 2017).

Constraints on the source region of the Kimberley kimberlites

The composition of internal zone (II) represents the most primitive (i.e., the first to appear on the liquidus) olivine composition to crystallise from kimberlite melts. Therefore, this olivine composition may provide important constraints on the composition(s) of primitive kimberlite melt compositions. Here, we employ Fe-Mg distribution coefficients calculated between olivine and carbonate-rich liquids (i.e., K_D = 0.66-0.52 at 2.5 GPa and 1150-1300 °C – Dalton & Wood, 1993), and between olivine and silicate-carbonate 'kimberlitic' liquids (i.e., K_D = 0.45 at 4-5 GPa and 1400-1700 °C; Girnis et al., 2005), to determine the Mg# of the melt that crystallised the internal olivine zones (II) (i.e., Mg# ~90). Assuming that the experimental conditions (i.e., melt fO_2 and volatile contents) approximate those at which internal zones (II) crystallised, than these calculations indicate that the internal zones (II) may have been in equilibrium with a melt with a Mg# of ~85-82 (K_D = 0.66-0.52), or ~79 (K_D = 0.45). These calculated values agree with the Mg# of reconstructed primitive melts parental to the Kimberley kimberlites (i.e., ~86 – Le Roex et al., 2003; 82.5 – Shee, 1985; 83.4-84.4 – Soltys et al., 2018a).

Kimberlite melts likely assimilate mantle material before or during crystallisation of internal olivine zones (II). However, even if we assume complete assimilation of orthopyroxene, clinopyroxene and garnet, based on the abundance of olivine xenocrysts and the ratio of olivine to pyroxenes/garnet in peridotites, the Mg# of the kimberlite melt is unlikely to change significantly (i.e., increases of up to ~1 unit; Soltys et al., 2018a). Therefore, given

the uncertainties in K_D values, assimilation of pyroxenes and garnet has a minimal effect on calculated Mg# values. Moreover, assuming limited change between the pressure, temperature, and composition of melt generation and liquidus crystallisation, the earliest olivine should be similar in composition to that of the source, implying a source with olivine of Mg# ~89-90. Based on the compositions of olivine in the lithospheric mantle (e.g., Gaul et al., 2000; Giuliani, 2018 and references therein) the kimberlite magma source is likely to be sub-lithospheric. This inference is supported by multiple other lines of evidence indicating production of kimberlite melts in the asthenosphere; including radiogenic isotope systematics (Nowell et al., 2004; Woodhead et al., 2009, in press; Tappe et al., 2011), sub-lithospheric xenocrysts and xenoliths (Sautter et al., 1991; Haggerty, 2017), and super deep diamonds (Stachel, 2001; Harte, 2010; Kaminsky, 2012; Pearson et al., 2014; Nestola et al., 2018) in kimberlites worldwide.

Additional constraints on the nature and mineralogy of the source region may be obtained from the minor element composition of magmatic olivine. The ratios of Mn/Fe, Ni/Mg, and Ca/Fe have been used in recent studies to make inferences about the modal mineralogy in the source of a variety of mafic and silica-undersaturated magmas (e.g., Sobolev et al., 2007; Foley et al., 2013; Howarth, 2018; Veter et al., 2017; Weiss et al., 2016; Ammannati et al., 2016; Nosova et al., 2018; Shaikh et al., 2019). It has been argued that melts derived from pyroxenitic (olivine-free) sources generate magmatic olivine with lower Mn/Fe and Ca/Fe, but higher Ni/Mg, than those derived from typical peridotite sources (e.g., Sobolev et al., 2007). Olivine-poor ‘signatures’ may also be related to the presence of metasomatic phases in the source, such as phlogopite, which may produce melts and magmatic olivine with lower Ca/Fe and Mn/Fe than normal peridotitic sources, and Ni/Mg lower than pyroxenitic sources (e.g., Veter et al., 2017; Nosova et al., 2018; Howarth, 2018; Shaikh et al., 2019). In addition, Ammannati et al. (2016) suggested that the high Ca/Fe ratios in olivine reflect clinopyroxene-rich sources produced by carbonate metasomatism. However, authors such as Matzen et al.,

(2017), have argued that low Mn combined with elevated Ni contents at a given olivine Mg# could be due to peridotite melting at higher pressure with limited, if any, pyroxenite contribution. Likewise, the Ca contents of olivine are likely to be influenced by temperature (e.g., De Hoog et al., 2010), and the H_2O content of the melt (Freig et al., 2006).

In Figure 3-13 we compare the composition of internal olivine zones (II) and rims from the Kimberley kimberlites with olivine in polymict breccias from the Bultfontein kimberlite, olivine megacrysts from southern African kimberlites, olivine in other mantle-derived carbonate-bearing magmas (i.e., orangeites, ultramafic lamprophyres, and olivine melilitites; e.g., Brey, 1978), and olivine in equilibrium with carbonate-rich melts in high pressure and temperature experimental studies. The Mn/Fe, Ni/Mg, and Ca/Fe ratios are plotted against Mg# because these ratios are all dependent on the Mg and Fe concentrations, which vary in the various olivine populations compared. Figure 3-13 shows that internal olivine zones (II) as well as the most primitive (Ni-rich) rims plot at the low-Mg# end of a linear trend formed by olivine compositions from partial melting experiments of carbonated peridotites (Brey et al., 2008, 2009; Dalton & Wood, 1993). High-Ni (i.e., the least evolved) olivine in the Finsch orangeite (South Africa; Howarth, 2018), carbonate-rich ultramafic lamprophyres from Aillik Bay (Veter et al., 2017) and, to a lesser extent, Yakutia (Nosova et al., 2018) broadly overlap the field of internal olivine zones (II) (Fig. 3-13). The high-Mg# olivine in southern African melilitites (Day et al., 2014) exhibit considerable scatter but nevertheless overlap the field of internal olivine zones (II) (Fig. 3-13). Moreover, olivine megacrysts from southern African kimberlites, olivine in Fe-rich dunites from Kimberley, and olivine in polymict breccias trend toward the field defined by internal olivine zones (II), with olivine in the highest-Ni-Mg# dunites and polymict breccias showing partial overlap (Fig. 13). The compositional similarities of olivine in mantle-derived and experimental carbonate-rich melts allow us to define a field of liquidus olivine in equilibrium with carbonate-rich melts (thick black dashed lined in Fig. 3-13). This

field includes analyses of olivine internal zones (II) from the Kimberley kimberlites (100×Mn/Fe = 1.15 ± 0.20, 100×Ni/Mg = 1.09 ± 0.08, and 100×Ca/Fe = 0.60 ± 0.16), and the most primitive compositions of olivine in South African orangeites, Canadian and Russian ultramafic lamprophyres, and southern African olivine melilitites.

Veter et al. (2018) argued that the low Mn/Fe (i.e., 0.9-1.5) and Ca/Fe (i.e., 0.7-1.2), coupled with Ni/Mg ratios of ~1 in aillikite olivine reflects their derivation from a phlogopite-carbonate bearing peridotite source. However, melts parental to the Kimberley kimberlites are poor in K_2O (~1 wt.%; le Roex et al., 2003; Soltys et al., 2018a), which makes the occurrence of phlogopite in their source unlikely. This is further supported by Ni/Mg ratios in olivine internal zones (II) which are substantially higher than olivine derived from melts of phlogopite-rich experiments (e.g., Föster et al., 2017 – Fig. 3-13).

The Mn/Fe and Ni/Mg ratios of internal olivine zones (II) (and liquidus olivine from other carbonate-bearing melts) show some overlap with phenocrysts in OIBs and to a lesser extent MORBs, but virtually no overlap with HIMU basalts (Fig. 3-13 – Sobolev et al., 2007 and references therein; Weiss et al., 2016). It has been argued that OIBs and MORBs derived from pyroxenite-bearing sources (e.g., Sobolev et al., 2007). However, the high Ni contents of olivine internal zones (II) may (at least partially) reflect assimilation of peridotite material, particularly sulfide minerals. The similar Mn/Fe ratios may represent derivation of kimberlites from garnet bearing source, as garnet has a strong control on Mn in the mantle (e.g., De Hoog et al., 2010).

The most striking difference between liquidus olivine in kimberlites (and other carbonate-rich magmas) and basaltic olivine, is the lower Ca/Fe ratio of the former (Fig. 3-13). We suggest this low Ca has a strong relationship to the temperature of melting (e.g., De Hoog et al., 2010), where volatile-rich melts such as kimberlites, orangeites, and aillikites form at relatively lower temperatures (~1100 °C – e.g., Fedortchouk and Canil, 2004) compared to

volatile-poor basaltic melts (~1300-1400 °C - Lee et al., 2009. Beyond simply lowering the solidus temperature, increasing H_2O activity also lowers the olivine-melt D_{Ca} value (Freig et al., 2006). In summary, we propose that the low Mn/Fe, moderate-high Ni/Mg, and extremely low Ca/Fe ratios of early crystallised olivine in kimberlites and other carbonate-rich magmas are the hallmarks of olivine crystallising from volatile-rich magmas derived from carbon-bearing mantle sources, potentially combined with some assimilation of peridotitic material (including sulfides).

Conclusions

Olivine zonation patters and compositions are virtually identical across multiple units of coherent kimberlite from root zones, dykes, and sills of the Kimberley kimberlites. Rare high-Mg cross-cutting olivine is restricted to root zone kimberlites. The WWTS contains olivine with distinct petrographic features and evolved compositions, which are also recorded as subordinate populations in the Benfontein sills, late-stage dykes the Wesselton pipe, and a sample from the Kimberley mine. The data presented in this contribution are interpreted to reflect the following stages of kimberlite evolution:

- Pre-entrainment (proto-)kimberlite crystallisation and/or metasomatism of the lithospheric mantle by previous pulses of kimberlite magma, forming: (a) sheared peridotites, where olivine neoblasts are the source of Mg-Ca-rich cores, and megacryst suite olivine which are the source of Fe-rich cores; (b) compositionally heterogenous cores that include a transitional zone formed by diffusive re-equilibration with a melt broadly similar in composition to that which crystallised the olivine rims; and (c) low-Mg# internal olivine zones (I), formed by crystallisation of a kimberlite melt that had previously undergone fractionation of olivine and oxide minerals. These are but a few examples of the widespread metasomatism of the lithospheric conduit preceding successful kimberlite magmatism (e.g., metasomatic

introduction of clinopyroxene and garnet, formation of PIC rocks, and mantle polymict breccias).

- Entrainment of xenocrystic material into the ascending host kimberlite. This includes approximately equal proportions of ‘normal’ mantle material from granular peridotites, and olivine derived from kimberlite metasomatism lithologies (e.g., megacrysts, sheared peridotites, and heterogeneous olivine grains – i.e., those with internal zones (I) and transitional zones).
- Partial assimilation of entrained material (particularly orthopyroxene, but also other peridotitic phases, including sulfides). This is linked to, or followed by, the onset of internal zone (II) ± TIMAC spinel crystallisation, and subsequently crystallisation of olivine rims and other early groundmass phases (i.e., rutile, Mg- ilmenite, and TIMAC-MÜM spinel).We propose that low Mn/Fe, very low Ca/Fe, and moderate Ni/Mg ratios are the hallmarks of olivine in melts derived from carbonate-bearing garnet-peridotite sources. This early magmatic crystallisation occurred during ascent through the lithospheric mantle, but before emplacement into the upper crust. It is following this stage that we speculate the magma parental to the WWTS stalls in the depleted upper mantle and loses its xenocrystic and early magmatic phases due to fractionation.
- Local replacement of olivine rims, and rind crystallisation with relatively late-stage groundmass phases (i.e., evolved MÜM spinel, perovskite, baddeleyite, apatite), likely after emplacement into the upper crust. The composition of olivine rinds reflects increasing fO_2 and, therefore, Fe^{3+}/Fe^{2+} in the residual melt.
- Late-stage formation of high-Mg olivine in some root zone kimberlites, probably via dissolution-reprecipitation triggered by hydrous deuteric fluids. The inclusion of monticellite and magnetite and textural association with serpentine indicates that this event occurred after emplacement into the upper crust at relatively low temperatures (i.e., <600-700 to ~400 °C).

Acknowledgements

We are indebted to Graham Hutchinson for his assistance during SEM and EPMA analysis at the University of Melbourne. We also thank Karsten Goemann for assistance with the FE-SEM and EPMA analysis undertaken at the University of Tasmania. Geoffrey Howarth, Stephen Sparks, and Andy Moore kindly provided access to their full datasets, for which we are grateful. Additionally, Geoffrey Howarth is thanked for providing access to otherwise inaccessible data sets stored at the University of Cape Town. We are grateful to Phillip Janney for facilitating access to the John J. Gurney Upper Mantle Room Collection (University of Cape Town), from which samples of the De Beers dyke were obtained, and to the De Beers Group for providing additional samples from De Beers and Bultfontein. We thank Petra diamonds for providing access to the Wesselton mine for sample collection as well as permission to publish the data from this study. Jock Robey organised access to various sites in the Kimberley area and provided expert field assistance and hospitality during field work, for which we are exceptionally appreciative. We also thank Stephen Sparks for supplying samples of the Wesselton water tunnel sills. AG acknowledges funding from the Australian Research Council through a Discovery Early Career Research Award (DECRA, grant n. DE-150100009). DK acknowledges financial support provided by the Australian Research Council (Discovery Grant DP130100257, 2013–2015) and Russian Science Foundation (grant #16-17-10145). This contribution benefited from detailed and constructive reviews by Sally Gibson, Sonja Aulbach, Andy Moore, and Nick Arndt, and the efficient editorial handling of Marjorie Wilson.

Figures

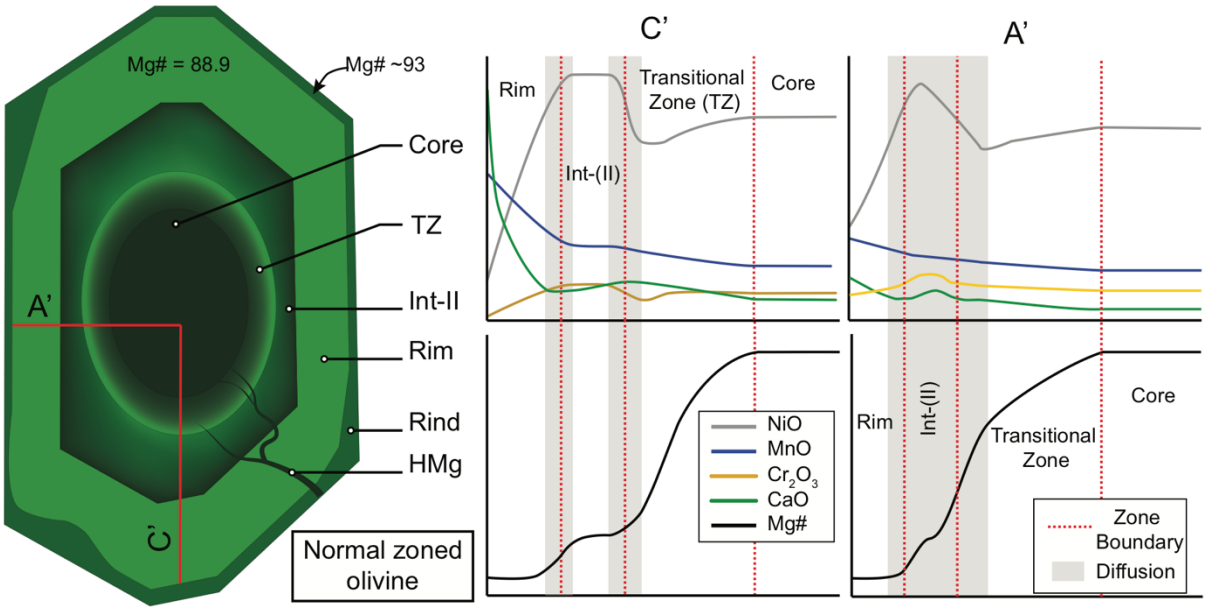

Figure. 3-1. Schematic diagrams to illustrate the compositional zonation of an idealised olivine grain from the Kimberley kimberlites. Note the difference between compositional profiles parallel to the slow diffusion a' axis labelled (A) and the faster diffusion c' axis (C). This grain represents a 'normal zoned olivine' where the core has an Mg# higher than that of the rim.

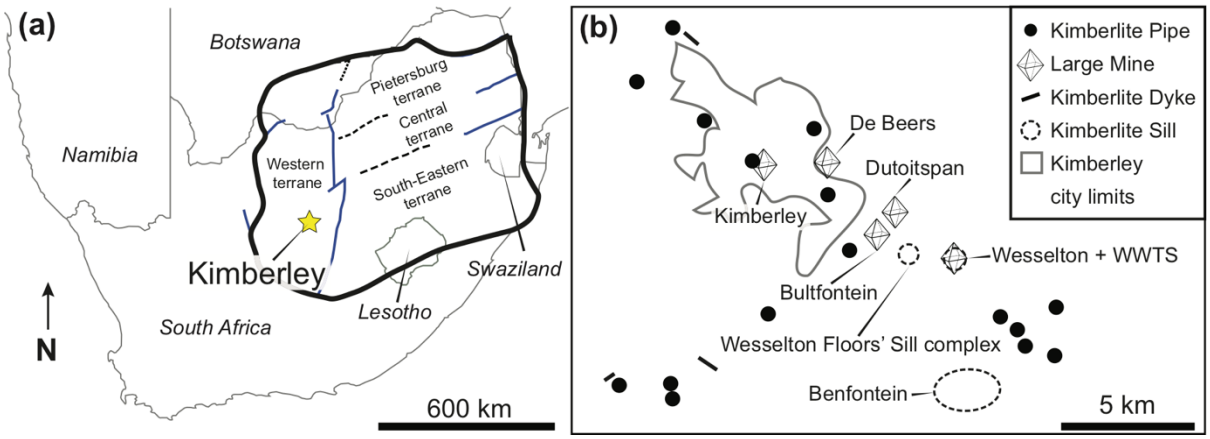

Figure 3-2. A map showing the main structural units of the Kaapvaal craton (modified from Field et al., 2008). The location of the Kimberley kimberlite cluster is indicated by a yellow star. The thick black line represents the inferred craton boundary, the solid blue and black dashed lines represent terrane boundaries and inferred boundaries, respectively. (b) A map of the known kimberlite intrusions in the Kimberley area (modified from Clement, 1982).

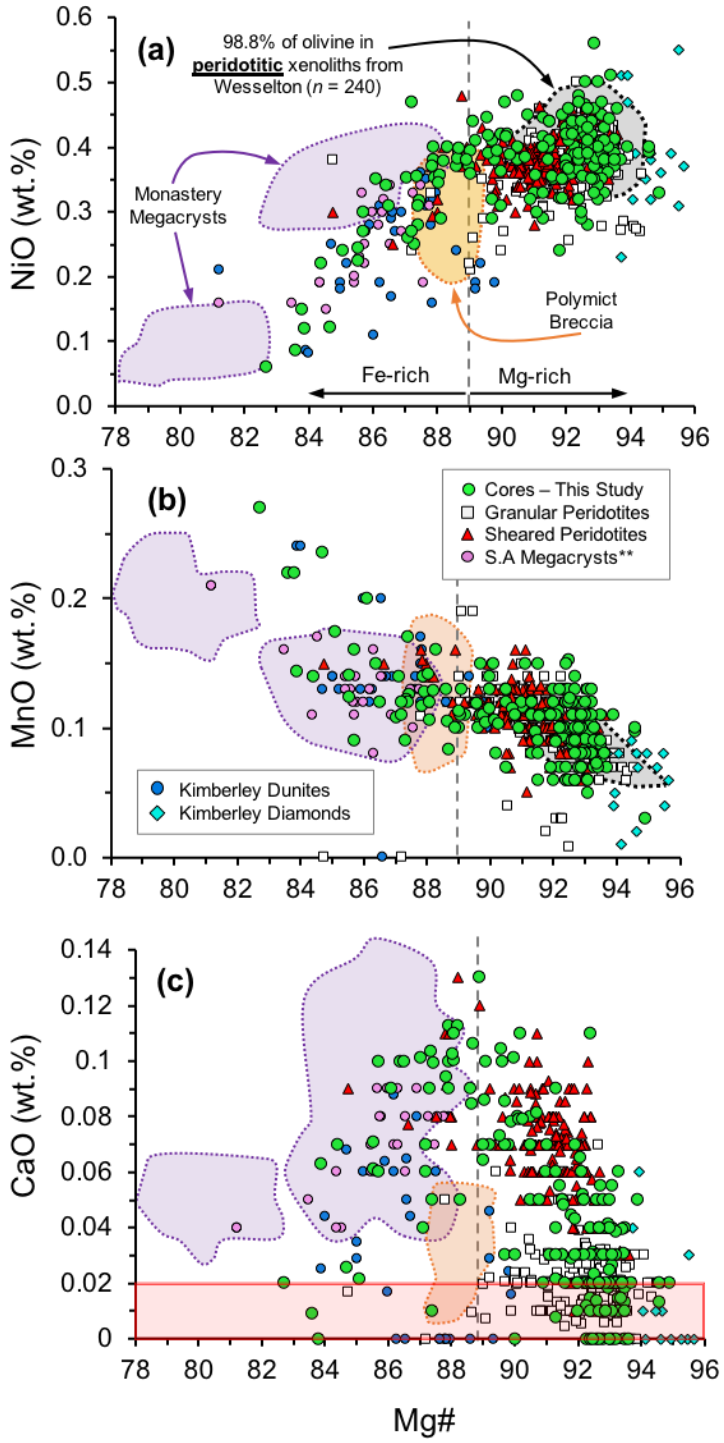

Figure 3-3. The composition of olivine cores (this study) plotted in bivariate charts of: Mg# vs. NiO (wt.%) in panel (a); Mg# vs. MnO (wt.%) in panel (b); and Mg# vs. CaO (wt.%) in panel (c). Shown for comparison are the compositions of: (1) olivine in coarse-grained granular peridotite xenoliths entrained by the Kimberley kimberlites; (2) southern Africa olivine megacrysts (excluding those from the Monastery Kimberlite); (3) cumulate Fe-rich dunite xenoliths from the Kimberley kimberlites; (4) olivine included in diamonds entrained by the Kimberley kimberlites; (5) magmatic olivine in polymict breccia xenoliths from the Kimberley kimberlites; and (6) olivine in sheared peridotite xenoliths from southern African kimberlites. The compositional data of these six olivine parageneses used for comparison were compiled from the literature and are reported in Supp. Table. S4. In addition, the composition field defined by olivine in 240 peridotite xenoliths from the Wesselton kimberlite (Shee, 1985) is shown by a black dashed line in panels (a) and (b). The grey dashed line at Mg# = 89 in all panels represents the distinction between Mg-rich (i.e., peridotitic mantle olivine) and Fe-rich (i.e., metasomatised

olivine) cores (see also Supp. Fig. S4). The red semi-transparent area in panel (c) denotes the EPMA detection limit for CaO (see text for details).

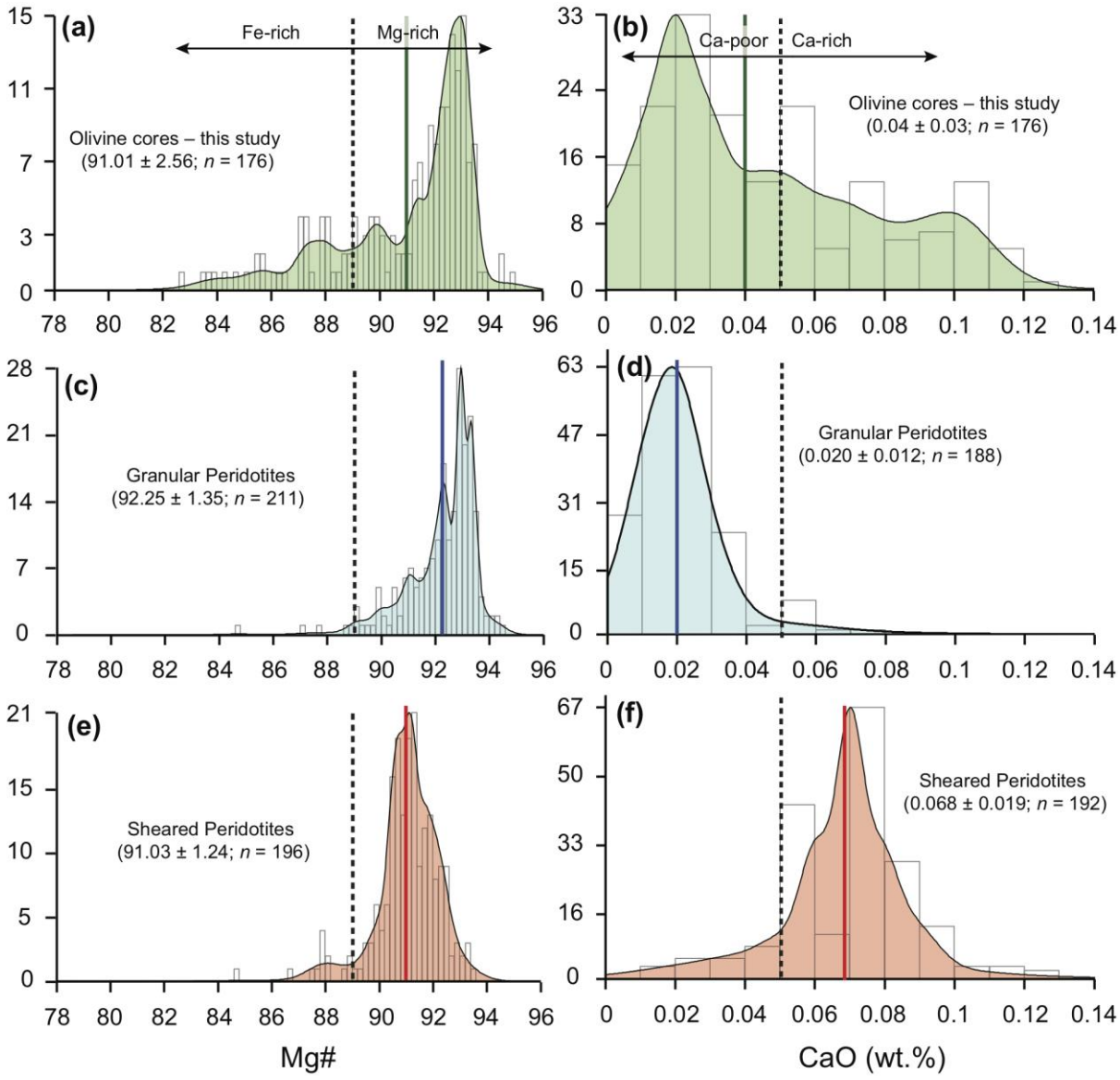

Figure 3-4 Kernel density estimate plots of the distribution of Mg# and CaO wt.% contents in olivine cores from the Kimberley kimberlites (panels (a) and (b); this study; Giuliani et al., 2017; Soltys et al., 2018b), olivine in granular peridotite xenoliths from the Kimberley kimberlites (panels (c) and (d); literature compilation – Supp. Table S5), olivine in sheared peridotites from southern African kimberlites (panels (e) and (f); literature compilation – Supp. Table S5).

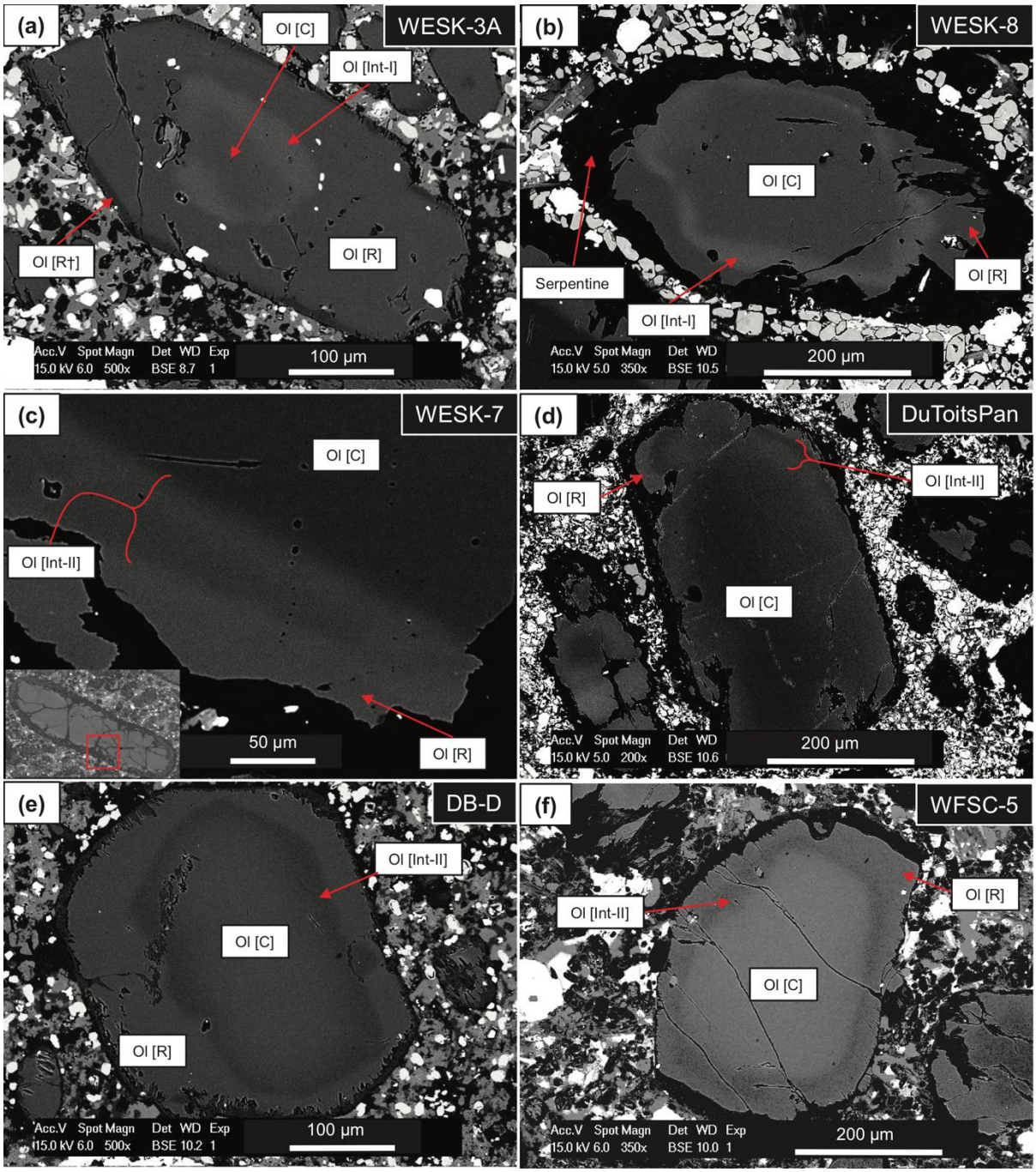

Figure 3-5 Back-scattered electron images of olivine grains from the Kimberley kimberlites. Panels (a) and (b) show grains that contain internal zone (I) (Ol [Int-I]) between the core (Ol [C]) and the rim (Ol [R]). In panel (a) the rim contains oxide mineral inclusions, and is overgrown by a thin rind (Ol [R†]). Panels (c-f) show grains that contain internal zone (II) (Ol [Int-II]). Panels (c) and (d) are normal zoned grains, whereas panels (e) and (f) are reverse zoned grains.

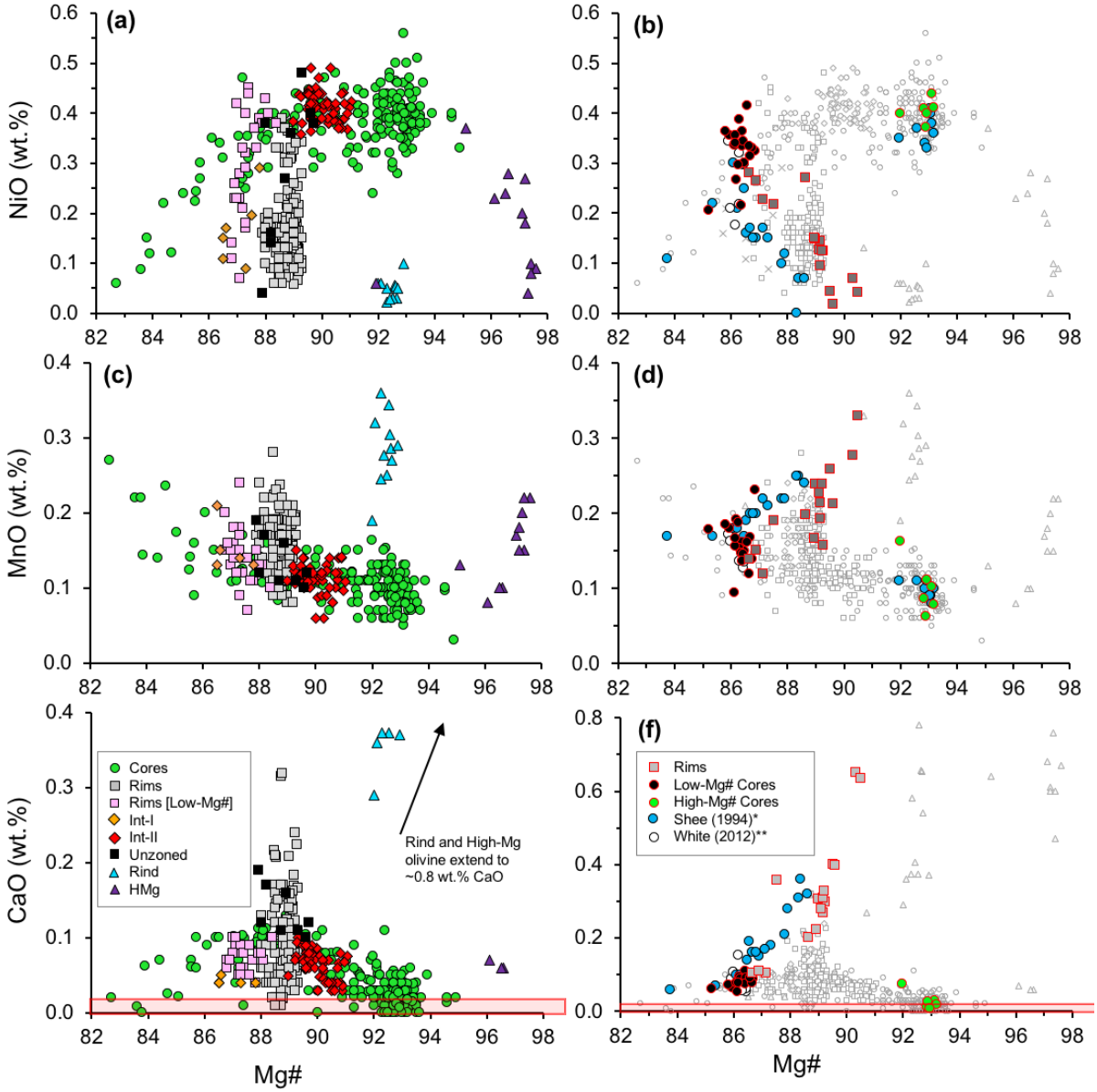

Figure 3-6. The compositions of the different olivine zones observed in this study plotted in bivariate charts of Mg# vs. NiO (wt.%) in panels (a) and (b), Mg# vs. MnO (wt.%) in panels (c) and (d), and Mg# vs. CaO (wt.%) in panels (e) and (f). In panels (b), (d), and (f) the prominent data are from sample P2 of the Wesselton water tunnel sill complex, and these data are overlain on the compositions of olivine grains from other intrusions of the Kimberley cluster (i.e., the smaller light grey symbols). Shown for comparison in panels (b), (d), and (f) are the compositions of olivine from other samples of the Wesselton water tunnel sill complex (White et al., 2012; Shee et al., 1994). The red semi-transparent area in panels (e) and (f) denotes the EPMA detection limit for CaO (see text for details)

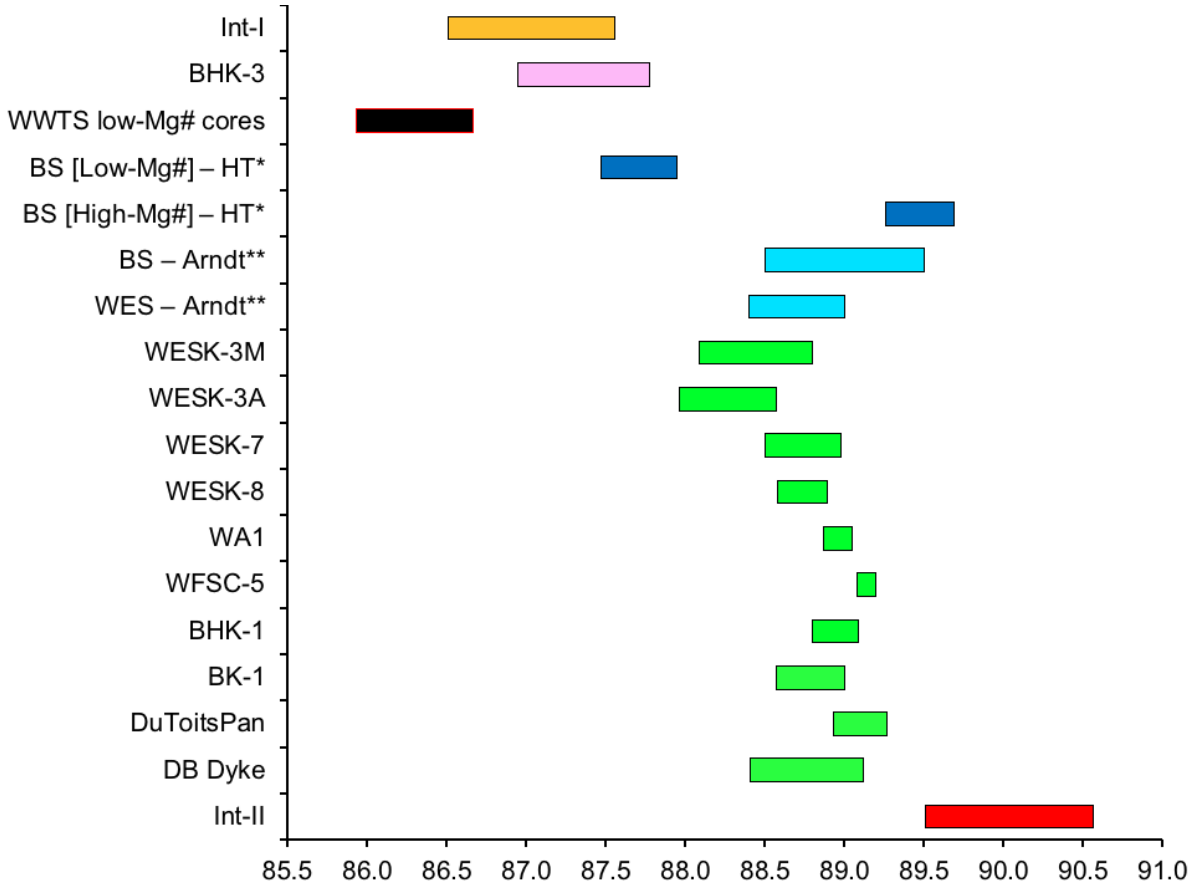

Figure 3-7. A bar chart of the average Mg# (± 1σ) of olivine rims and internal zones from different intrusions of the Kimberley cluster. Shown for comparison are the compositions of olivine rims reported in previous studies of the Benfontein Sills (BS) and Wesselton kimberlite (Howarth & Taylor, 2016; Arndt et al., 2010).

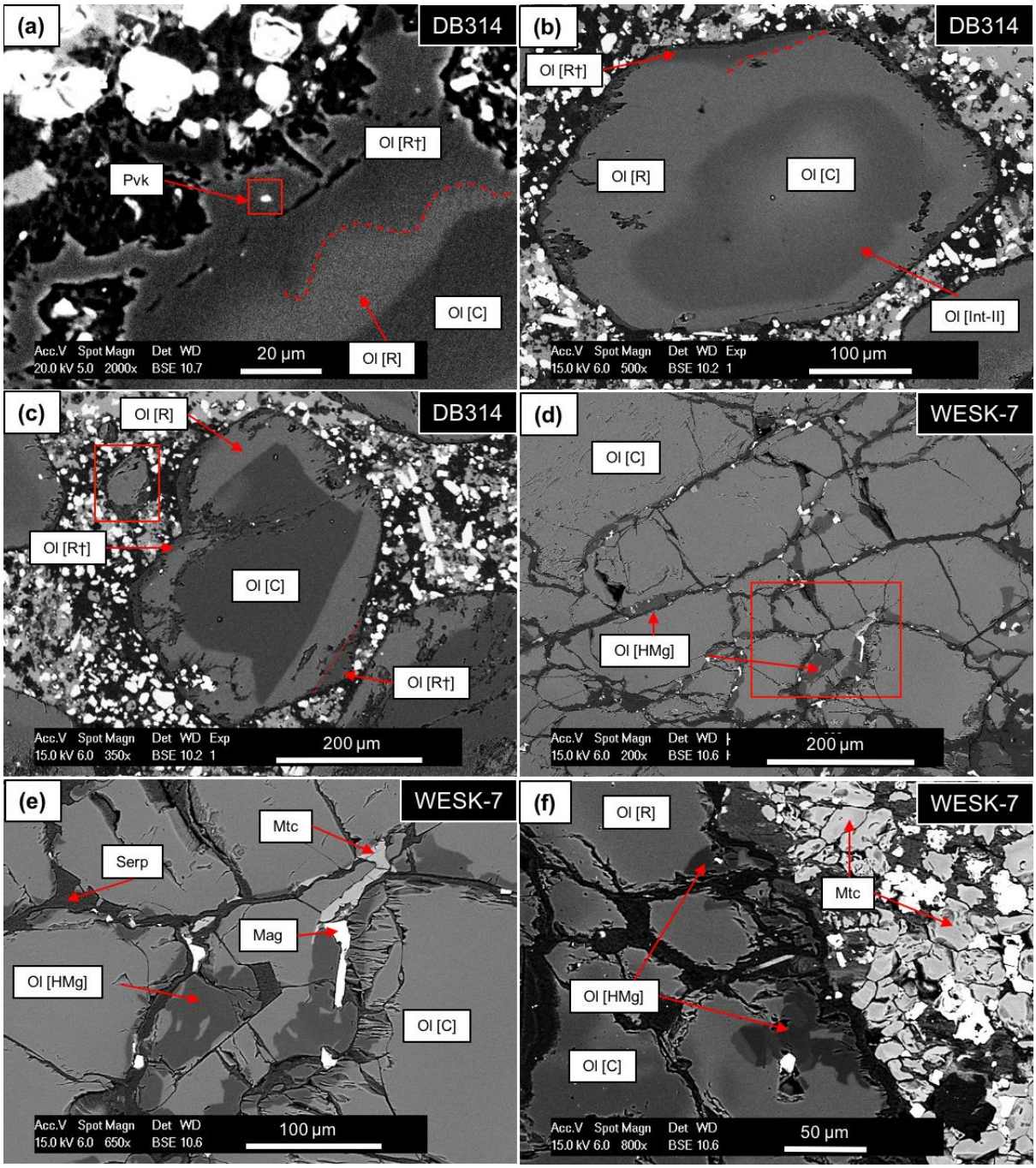

Figure 3-8. Back-scattered electron images of olivine grains from the Kimberley kimberlites. Panels (a-c) show grains which contain rinds (Ol [R†]). In panel (a) the olivine rind contains an inclusion of perovskite (Pvk). Panels (d-f) show olivine grains that contain high-Mg cross-cutting olivine (Ol [High-Mg]). In panels (d) and (e) high-Mg olivine occurs occur along fractures traversing an olivine core (Ol[C]), in association with magnetite (Mag), monticellite (Mtc), and serpentine (Serp).

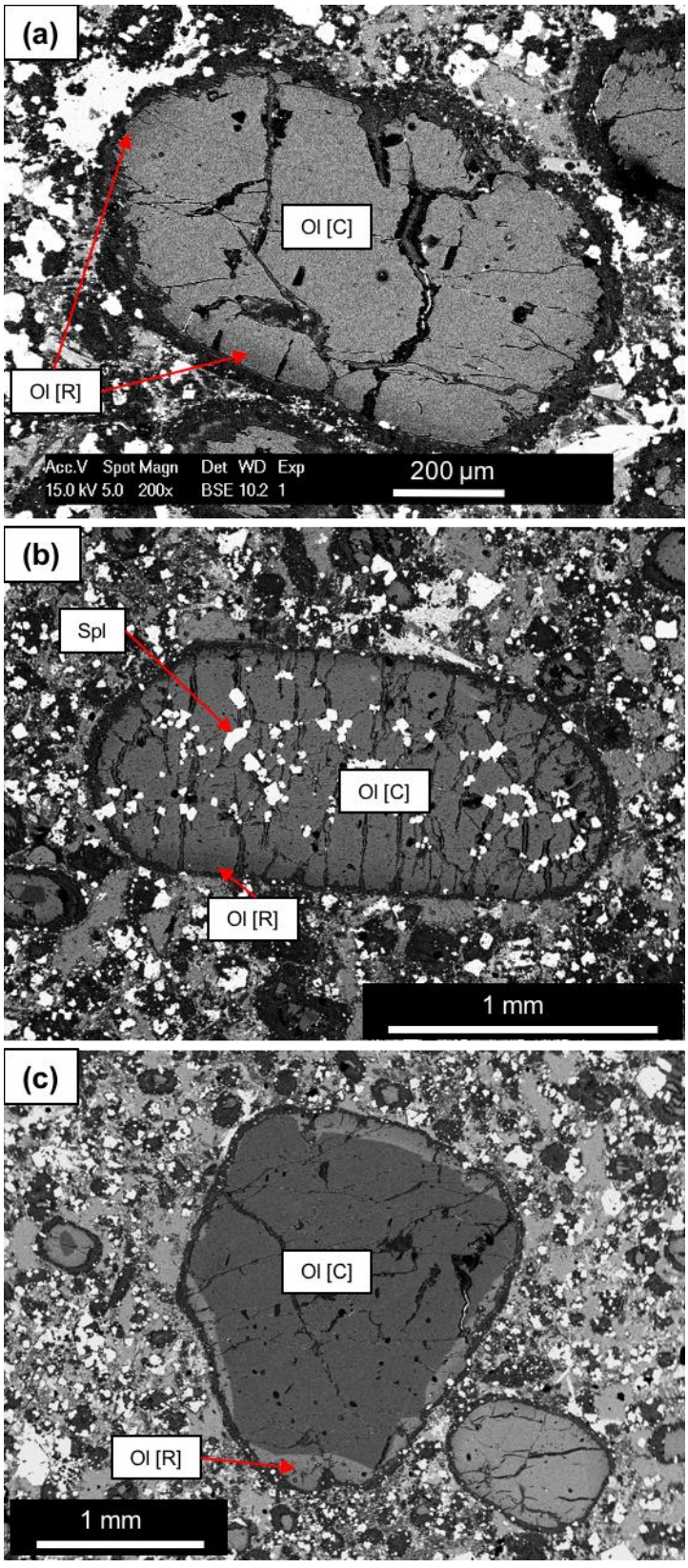

Figure 3-9. Back-scattered electron (BSE) images of olivine grains from sample P2 of the Wesselton water tunnel sills complex. Panel (a) shows a zoned olivine grain, consisting of a low-Mg# core (Ol [C]) that is overgrown by a thin and diffuse rim (Ol [R]). In panel (b) the large low-Mg# olivine core contains abundant euhedral inclusions of spinel (Spl). Panel (c) shows a large olivine grain that contains a high-Mg# (xenocrystic) core which is overgrown by olivine that has a BSE response consistent with zonation from Low-Mg# 'cores' to rims.

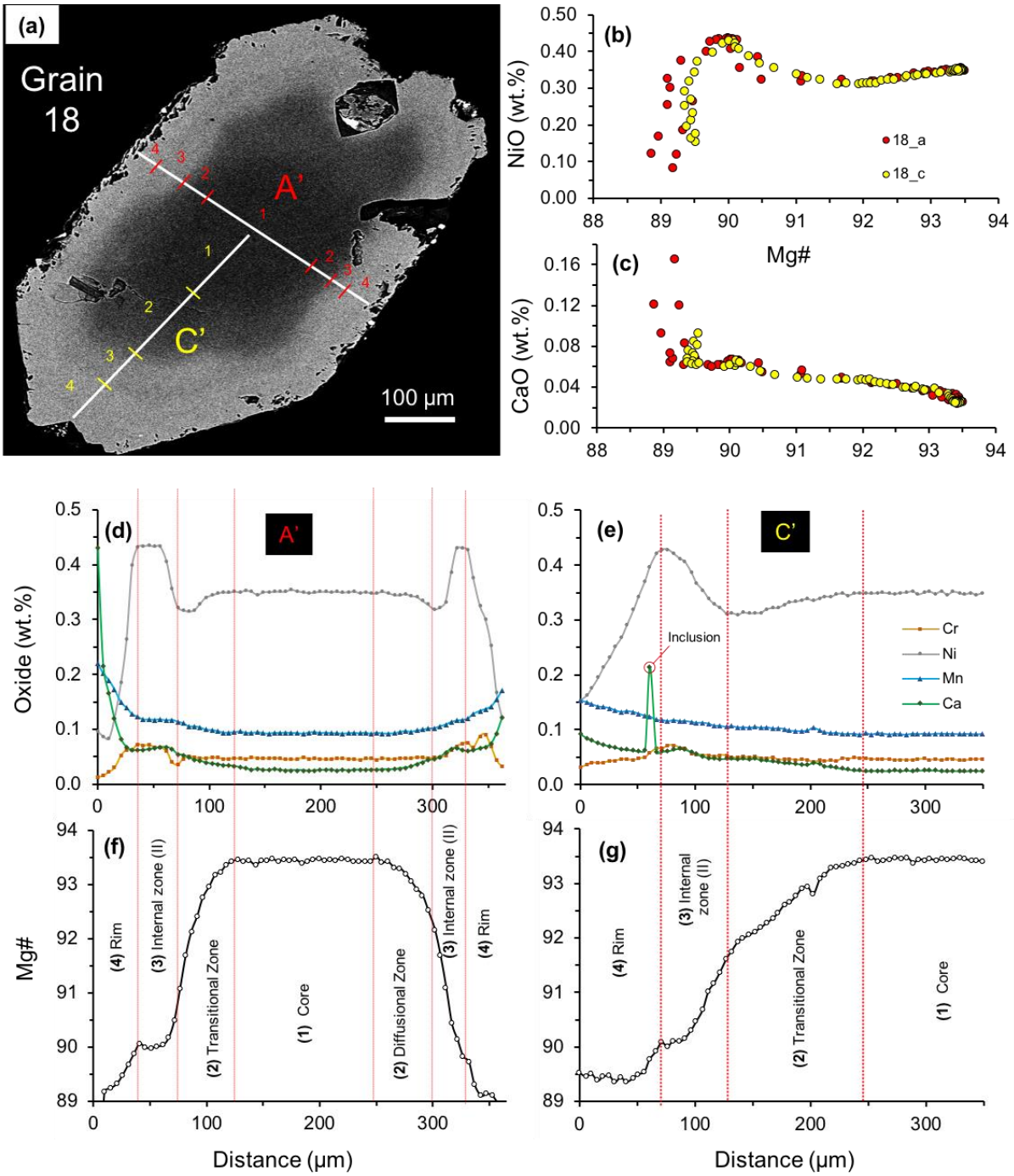

Figure 3-10. Representative electron probe micro-analyser traverses across a normal zoned grain from the Bultfontein kimberlite.

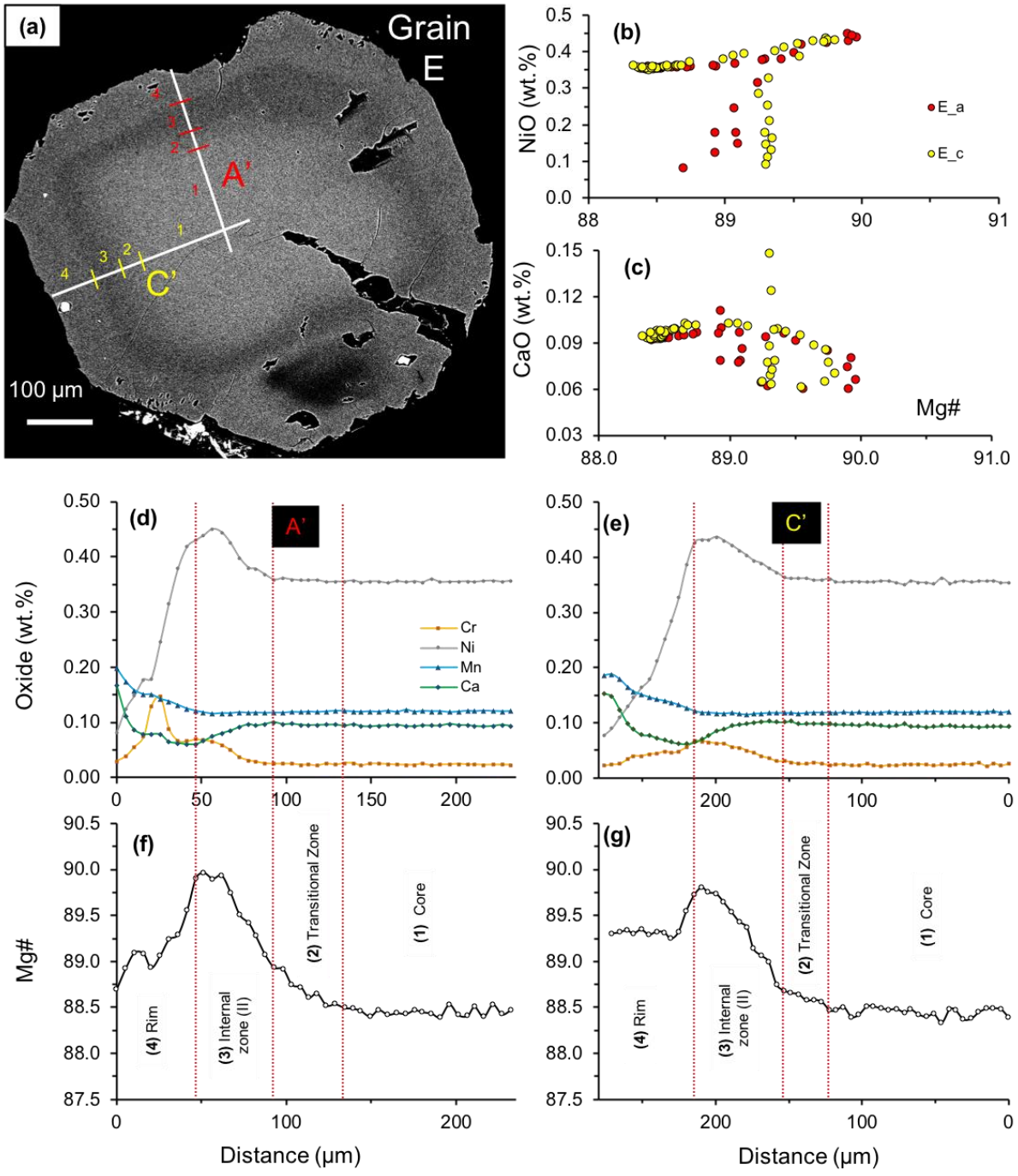

Figure 3-11 Representative electron probe micro-analyser traverses across a reverse zoned grain from the Bultfontein kimberlite.

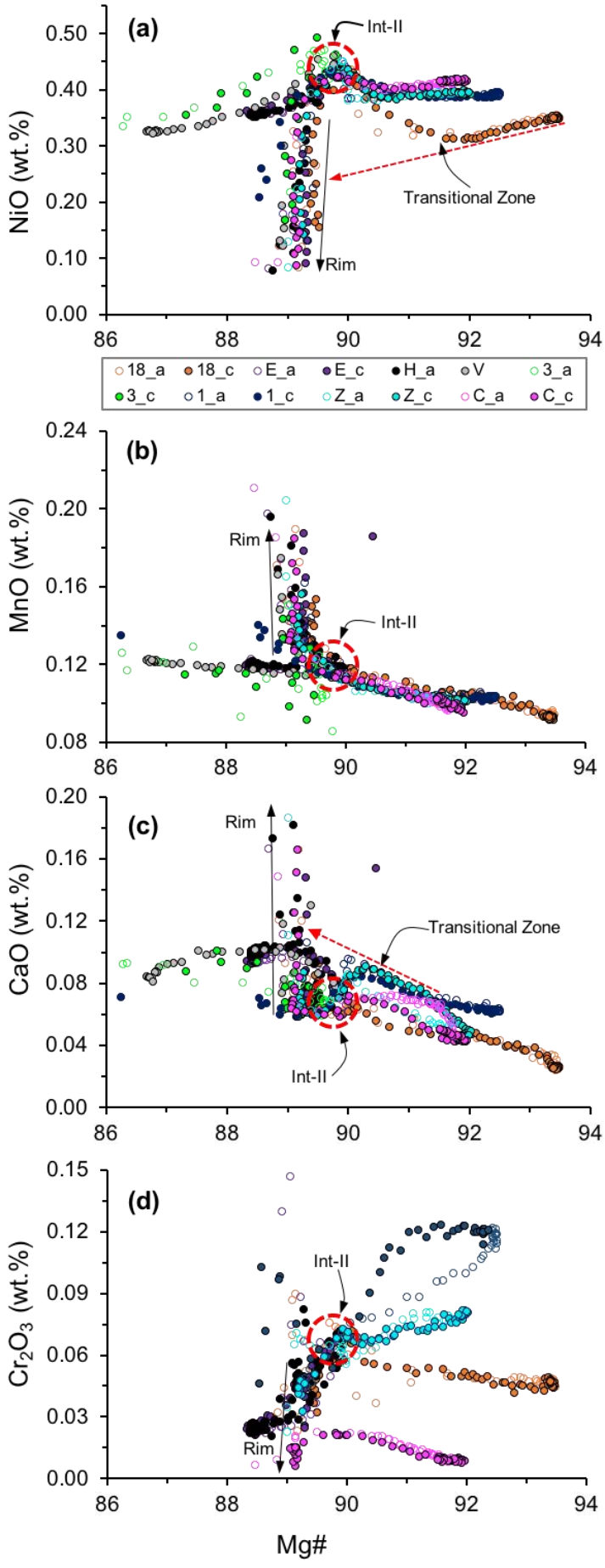

Figure 3-12. All electron probe micro-analyser traverses across olivine grains from the Bultfontein kimberlite sample BK-1 plotted in bivariate charts of Mg# vs. NiO (wt.%) in panel (a), Mg# vs. MnO (wt.%) in panel (b), and Mg# vs. CaO (wt.%) in panel (c). Note that the transitional olivine zones broadly trend toward compositions consistent with rims (shown by a dashed red arrows in panels (a) and (c)).

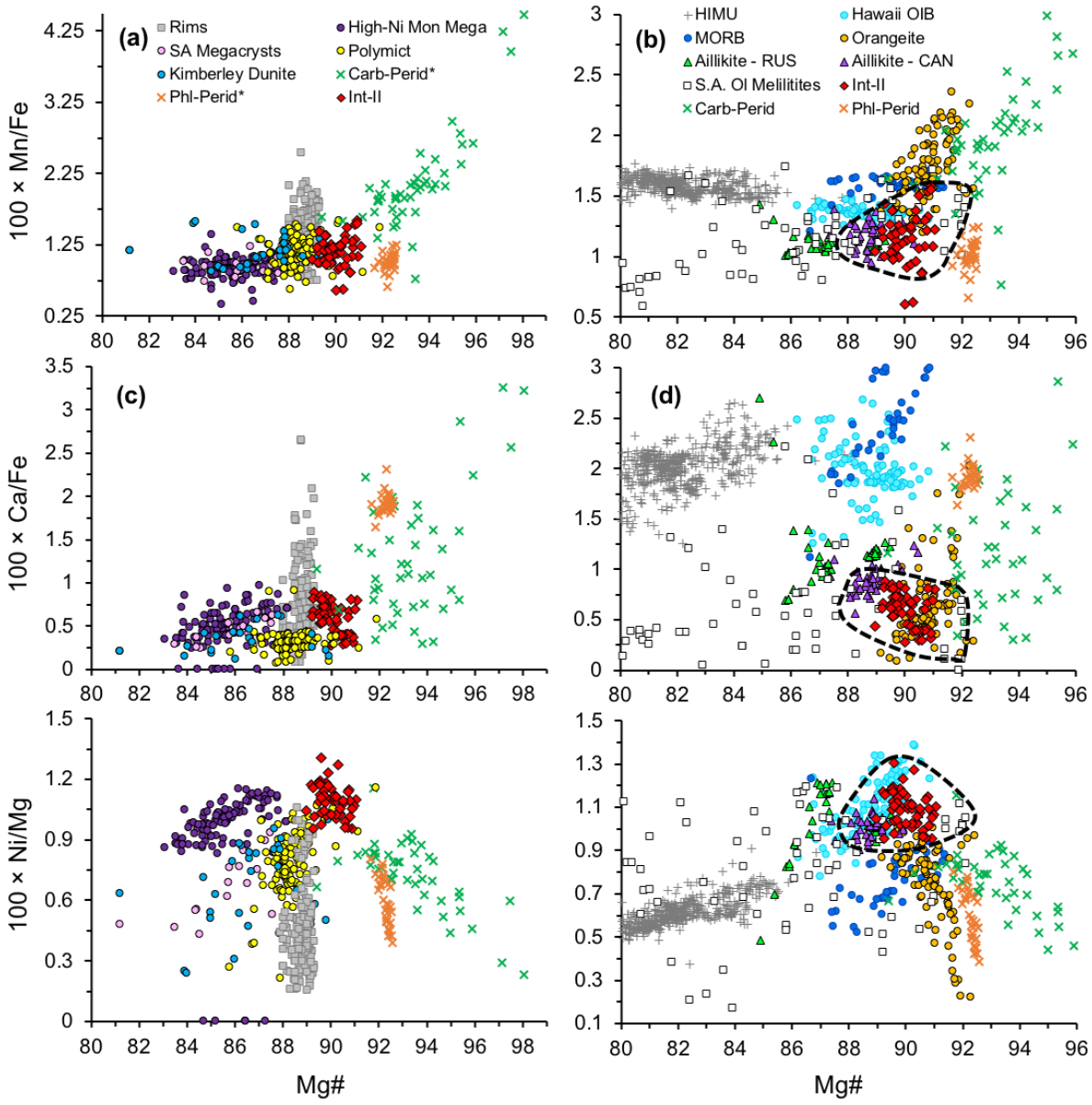

Figure 3-13. The compositions of internal olivine zones (II) plotted in bivariate charts of Mg# vs. (100×) Mn/Fe in panels (a) and (b); Mg# vs. (100×) Ca/Fe in panels (c) and (d); and Mg# vs. (100×) Ni/Mg in panels (e) and (f). Shown for comparison in panels (a), (c), and (e) are the composition of olivine rims (this study) as well as high-Ni-Mg# megacrysts from the Monastery kimberlite, olivine megacrysts from other southern African kimberlites, cumulate Fe-rich dunite xenoliths from the Kimberley kimberlites, and magmatic olivine in polymict breccia xenoliths from the Kimberley kimberlites (literature compilation – Supp. Table S5). In panels (b), (d), and (f) the composition of liquidus olivine from other rock types including HIMU basalt (Weiss et al., 2016), Hawaii OIB, and MORB (Sobolev et al., 2007), ailikites (Veter et al., 2017; Nosova et al., 2018), olivine melilitites (Day et al., 2014), and orangeites (Howarth, 2018) are shown for comparison. In all panels the composition of olivine in melting experiments of carbonated peridotite (carb-perid – Brey et al., 2008; 2009; Dalton & Wood, 1993) and phlogopite-bearing peridotite (phl-perid – Förster et al., 2017).

Tables

Table 3-1. Summarised petrographic features of the studied samples

Locality	Sample Nº	Sample Information and Unit	Petrograhphic type	Macrocrysts	Olivine Alteration (see also Supp. Fig. S1)
Kimberley mine	BHK-1	Donated by Kimberley Museum	Cal-Serp	Ol, Phl, Ilm, Grt	~50-100 µm GBR**, grains <200 µm completely replaced
	BHK-3	Donated by Kimberley Museum	Cal-Serp	Ol	Highly altered, rare grains >500 µm retain fresh crystal faces
De Beers Dyke	(DB-D)	535m level – Dyke centre	Mtc-dol	Ol, Phl, Minor Ilm	Unalatered, except minor (5-10 µm) GBR by Dol ± Serp
Dutoitspan	173/33/K6/37	Unknown	Mtc-oxide	Ol, Cpx, Grt, Ilm	~50-200 µm of GBR, grains <200 µm completely replaced
Bultfontein	BK-1	Likley B3	Phl-rich	Ol, Phl, Ilm	Unaltered grading to minor (20-50 µm) GBR
Wesselton	WESK-8	995m level – W3	Mtc-rich	Ol, Ilm, Phl	<50 µm of GBR, locally grains up to ~500 µm completely replaced
	WESK-7	995m level – W7	Mtc-rich	Ol, Ilm	~50-200 µm of GBR, grains <500 µm completely replaced
	WESK-3A	995m level – Late cross-cutting dyke	Cal-rich	Minor Ol, Phl	Unalatered, except minor (~5 µm) GBR
	WESK-3M	995m level – W2	Cal-Serp	Ol, Phl, Ilm	Unalatered, except minor (~5-10 µm) GBR
	W-A1	660m level – near pipe contact.	Cal-rich		~10-20 µm of Serp
WWTS*	P2	"Macrocrystic sill"	Cal-Ap-Phl-rich	Ol*	generaly <75 µm of Serp, localy all olivine is completely replaced
WFS	173/33/K119/5	Drill Core	Cal-Serp	Ol, Phl	<10-50 µm of Serp locally around some olivine

*These are atypical macrocrysts in that they contain magmatic cores – see main text.
** GBR = Grain Boundry Replacement [by serpetine unless otherwise specified]
WWTS = Wesselton Water Tunnel Sills; WFS = Wesselton Floors Sill.

Table 3-2. The compositions of different olivine zones in the Kimberley Kimberlites (data from this study; Giuliani et al., 2017; Soltys et al., 2018b). Analysis of unzoned grains and grains from sample BHK-3 are reported in Supp. Table S1.

	Cores* (*n* = 182)		Int (I) (*n* = 6)		Int (II) (*n* = 52)		Rim (*n* = 153)		Rind (*n* = 11)		HMg (*n* = 12)		
	Avg.	**S.D.**	**Avg.**	**S.D.**	**Avg.**	**S.D.**	**Avg.**	**S.D.**	**Avg.**	**S.D.**	**Avg.**	**S.D.**	
SiO_2	40.7	0.7	40.1	0.3	40.5	0.5	40.3	0.6	40.9	0.7	41.9	0.4	
FeO	8.7	2.4	12.6	0.5	9.7	0.5	10.9	0.3	7.4	0.3	3.6	1.5	
NiO	0.37	0.07	0.17	0.07	0.41	0.03	0.17	0.07	0.05	0.02	0.18	0.10	
MnO	0.11	0.03	0.16	0.03	0.11	0.02	0.15	0.04	0.28	0.05	0.17	0.06	
MgO	50.2	2.0	47.2	0.3	49.3	0.6	48.4	0.5	51.0	0.5	54.4	1.2	
CaO	0.04	0.03	0.04	0.01	0.06	0.02	0.09	0.05	0.49	0.15	0.49	0.25	
Mg#	91.1	2.5	87.0	0.5	90.0	0.5	88.8	0.3	92.5	0.3	96.5	1.5	

	WWTS Cores** (*n* = 18)		WWTS Rims (n = 16)	
	Avg.	**S.D.**	**Avg.**	**S.D.**
SiO_2	40.0	0.2	40.4	0.3
FeO	13.2	0.3	10.9	1.0
NiO	0.33	0.05	0.15	0.08
MnO	0.16	0.03	0.21	0.05
MgO	46.6	0.3	48.3	0.8
CaO	0.08	0.01	0.31	0.16
Mg#	86.3	0.4	88.8	1.1

*Cores include the high-Mg# cores from the WWTS

** WWTS Cores only includes the low-Mg# Cores

Mg# = (Mg/Mg+Fe) × 100

bdl = below detection limit

CHAPTER 4: CRYSTALLISATION SEQUENCE AND MAGMA EVOLUTION OF THE DE BEERS DYKE (KIMBERLEY, SOUTH AFRICA)

Ashton Soltys[1], Andrea Giuliani[1,2], David Phillips[1]

[1] KiDs (Kimberlites and Diamonds), School of Earth Sciences, The University of Melbourne, Parkville, 3010 Victoria, Australia

[2] ARC Centre of Excellence for Core to Crust Fluid Systems and GEMOC, Department of Earth and Planetary Sciences, Macquarie University, North Ryde, 2019 NSW, Australia

Abstract

We present petrographic and mineral chemical data for a suite of samples derived from the De Beers dyke, a contemporaneous, composite intrusion bordering the De Beers pipe (Kimberley, South Africa). Petrographic features and mineral compositions indicate the following stages in the evolution of this dyke: (1) production of antecrystic material by kimberlite-related metasomatism in the mantle (i.e., high Cr-Ti phlogopite); (2) entrainment of wall-rock material during ascent through the lithospheric mantle, including antecrysts; (3) early magmatic crystallisation of olivine (internal zones and subsequently rims), Cr-rich spinel, rutile, and magnesian ilmenite, probably on ascent to the surface; and (4) crystallisation of groundmass phases (i.e., olivine rinds, Fe-Ti-rich spinels, perovskite, apatite, monticellite, calcite micro-phenocrysts, kinoshitalite-phlogopite, barite, and baddeleyite) and the mesostasis (calcite, dolomite, and serpentine) on emplacement in the upper crust. Groundmass and mesostasis crystallisation likely forms a continuous sequence with deuteric/hydrothermal modification.

The petrographic features, mineralogy, and mineral compositions of different units within the De Beers dyke are indistinguishable from one another, indicating a common petrogenesis. The compositions of antecrysts (i.e., high Cr-Ti phlogopite) and magmatic phases (e.g., olivine rims, magnesian ilmenite, and spinel) overlap those from the root zone intrusions of the main Kimberley pipes (i.e., Wesselton, De Beers, Bultfontein). However, the composition of these magmatic phases is distinct from those in ‘evolved’ dykes/sills of the Kimberley cluster (e.g., Benfontein, Wesselton water tunnel sills). Although the effects of syn-emplacement flow processes are evident (e.g., alignment of phases parallel to contacts), there is no evidence that the De Beers dyke has undergone significant pre-emplacement crystal fractionation (e.g., olivine, spinel, ilmenite). This study demonstrates the requirement for detailed petrographic and mineral chemical studies to assess whether individual intrusions are in fact ‘evolved’; and that dykes are not necessarily produced by differentiated magmas.

Introduction

Hypabyssal kimberlites are holocrystalline, aphanitic to inequigranular igneous rocks that crystallised from kimberlite magmas in a sub-volcanic environment. Hypabyssal kimberlites typically occur in dykes, sills or irregular root zones (e.g., Clement 1982; Field et al. 2008; Mitchell, 2008; Scott Smith et al. 2013). These intrusions typically form by the injection of multiple discrete magma batches (e.g., Clement 1982).

Many kimberlite dykes and sills show textural evidence of in-situ magmatic differentiation (e.g., Dawson and Hawthorne 1973; Shee et al. 1994; White et al. 2012) and some may have undergone significant crystal fractionation before emplacement (e.g., Mitchell 2008). For instance, Shee et al. (1994) argued that the magma parental to the Wesselton water tunnel (WWT) sills stalled at depths of ~85 km, causing loss of macrocrystic components and early crystallised spinel. Similar processes were inferred to have affected the De Beers dyke (Donaldson and Reid 1982). If magmas parental to hypabyssal kimberlites in dykes have undergone fractionation it follows that these rocks may not be representative of primitive kimberlite melts. Understanding whether kimberlite dykes are representative of their parental magmas is important because hypabyssal kimberlite in dykes have previously been utilised to constrain kimberlite melt compositions (e.g., Kopylova et al. 2007; Price et al. 2000; Shee 1985).

To address these questions, we report detailed petrographic and mineral chemical data for a suite of samples from the De Beers dyke. This data allows for discernment of the crystallisation sequence, including deuteric/hydrothermal alteration, and an assessment of mineralogical and magmatic evolution of the dyke. These results are compared with published data on hypabyssal kimberlites in root zones and ‘evolved’ dykes in the Kimberley cluster, to understand the extent of magma fractionation and other processes that may have modified the original magma composition.

Geological setting and previous work

The De Beers dyke (also known as the "Eyebrow" dyke – Clement 1982) is one example of the extensive dyke and sill systems associated with the five main pipes (i.e., Kimberley, De Beers, Wesselton, Dutoitspan, and Bultfontein) and numerous smaller pipes (e.g., Kamfersdam and Olifantsfontein) in the Kimberley area (e.g., Clement 1982; Field et al. 2008 – Fig. 4-1A, B). The age of the Kimberley cluster has been determined by various geochronological techniques, yielding emplacement ages spanning 83-92 Ma (e.g., Allsopp and Barrett 1975; Batumike et al. 2008; Fitch and Miller 1983; Li et al. 2012). $^{40}Ar/^{39}Ar$ dating of phlogopite yielded an emplacement age of 87 ± 2 Ma for the De Beers pipe (Fitch and Miller 1983). The age of the De Beers dyke has not been determined; however, it is inferred to be contemporaneous with the emplacement of the main pipe based on cross-cutting and field relationships (Clement 1982; Fig. 4-1). Previous studies have shown that the Kimberley kimberlites have mineralogical (e.g. Clement 1982; Shee 1985), geochemical (e.g., Becker and le Roex 2006; le Roex et al. 2003), and radiogenic isotope features (Nowell et al. 2004; Smith et al. 1983) consistent with hypabyssal archetypal kimberlites worldwide.

The diatreme facies of the De Beers pipe transitions sharply into a complex and irregular hypabyssal root zone at depths of 400-500 m below the present surface (Fig. 4-1D, E). The De Beers pipe contains at least six discrete units, and the root zone splits into three almost discrete columns (Fig. 4-1D, E), which although largely separated by wall-rock are interconnected by "dyke-like channels" (Clement 1982; Clement et al. 1986). Abundant pre-, syn-, and post-emplacement dykes also occur in the vicinity of the De Beers pipe (Clement 1982).

The De Beers dyke and other ancillary dykes are sub-vertical, and oriented parallel to the curvature of the main De Beers pipe along its north-eastern boundary (Fig. 4-1F). The De Beers dyke is ~25-30 cm wide and is asymmetrically zoned. This zoning was attributed to

multiple injections of discrete magma batches (Donaldson and Reid 1982). Previous studies of the De Beers dyke have focused on macro-scale (handsample) textural features and the prominent carbonate-rich segregations (Donaldson and Reid 1982), as well as the petrography and Sr-isotope systematics of the different carbonate generations (Exley and Jones 1983; Castillo-Oliver et al. 2018). However, detailed petrographic descriptions and mineral composition determinations of the other magmatic phases are sparse (Donaldson and Reid 1982). Pasteris (1980, 1982, 1983) examined samples from various root zone units of the De Beers pipe and the accompanying dykes and sills (including the De Beers dyke), with a focus on the compositions of oxide minerals.

Samples and Methods

The studied samples are from the 500-meter level of the De Beers mine. Two samples were selected adjacent to the north (173/33/K3/310) and south (173/33/K3/315) wall-rock contacts, whereas two other samples (173/33/K3/311, 173/33/K3/314) are from the dyke centre. Sample 173/33/K3/310 contains two distinct kimberlite units with a sharp contact zone (Supp. Fig. S4-1).

The effects of flow processes are evident in all samples and are particularly prominent close to the contact zones. Flow textures are defined by weak to moderate alignment of calcite laths, phlogopite macrocrysts (i.e. rounded-anhedral phases >500 μm), and olivine grains (i.e., macrocrysts and phenocrysts). The modal abundance of calcite laths increases, whereas the abundance of carbonate-rich segregations and large macrocrystic components decreases toward the contacts. These macro-scale textural observations are consistent with those of Donaldson and Reid (1982). Despite textural and modal variations, all samples and contained zones are mineralogically identical, and hence are described collectively.

The samples were studied under transmitted and reflected light using a petrographic microscope. Identification of smaller groundmass phases and textural features was achieved using conventional and field-emission scanning electron microscopy (SEM and FE-SEM). Initial SEM investigation was performed at the University of Melbourne, using a Philips (FEI) XL30 environmental SEM, equipped with an OXFORD INCA energy dispersive X-ray spectrometer (EDS). During the production of back-scattered electron (BSE) images and semi-quantitative chemical analysis, a beam acceleration voltage of 15 kV was used.

Detailed FE-SEM investigation was performed at the Central Science Laboratory, University of Tasmania, using a Hitachi SU-70 field emission scanning electron microscope (FE-SEM) equipped with an OXFORD INCA-XMax80 EDS. During the production of BSE images and semi-quantitative chemical analysis, a beam acceleration voltage of 15 kV was used.

Major element compositions of silicate and oxide phases were determined using a Cameca SX-50 electron probe micro-analyser (EPMA) equipped with four vertical wavelength dispersive spectrometers, located at the University of Melbourne. Analytical conditions were as follows: beam acceleration voltage of 15 kV, beam current of 20 or 35 nA, and beam diameter of 2-8 μm; counting times per analysis of 20 s on peak positions and 10 s on two background positions located on either side of the peak position. The calibration materials analysed consisted of natural and synthetic materials, including: Wollastonite (Si-Kα, Ca-Kα), Titanium oxide (Ti-Kα), Aluminium oxide (Al-Kα), Metallic Chromium (Cr-Kα), Hematite (Fe-Kα), Metallic Vanadium (V-Kα), Metallic Manganese (Mn-Kα), Magnesium oxide (Mg-Kα), Metallic Nickel (Ni-Kα), Potassium tantalite (K-Kα), Metallic Niobium (Nb-Lα), Ti-Zr alloy (Zr-Kα), Metallic Zinc (Zn-Kα), Jadeite (Na-Kα), CaF_2 (F-Kα), NaCl (Cl-Kα). In addition, several natural reference materials were also analysed (e.g., San Carlos olivine, Stillwater chromite, Durango Apatite). Data reduction was performed using the PAP matrix

correction software program (Pouchou and Pichoir 1984). The limit of detection for most major oxides are ~0.02 wt.%.

Petrography and mineral compositions

The current samples are fresh (i.e. minimal alteration), xenolith- and macrocryst-poor (i.e., <5 and <15 vol% respectively), inequigranular hypabyssal kimberlites (Fig. 4-2). Granular phlogopite-spinel harzburgitic micro-xenoliths are present in most samples (Supp. Fig. S4-1). The macrocryst assemblage includes olivine, phlogopite, spinel, and resorbed orthopyroxene (Supp. Fig. S4-1). In addition, rare garnet macrocrysts/megacrysts and MARID suite xenoliths were reported by Donaldson and Reid (1982). Micro-phenocrysts (generally <500 μm) include olivine, calcite laths, and magnesian ilmenite. Groundmass phases are generally smaller (i.e., <75 μm) and subhedral-euhedral, and include olivine, spinel, apatite, perovskite, monticellite, calcite, phlogopite-kinoshitalite, barite, and accessory baddeleyite. This macrocryst, (micro-)phenocryst, and groundmass assemblage is set in a fine-grained mesostasis of calcite, dolomite, and serpentine.

Average major element compositions of olivine, phlogopite, rutile, magnesian ilmenite, and spinel, determined by EPMA analysis are reported in Table 1. The full data set is reported in Supplementary Tables S1-5.

Olivine

Olivine macrocrysts and groundmass grains contain a core(s) and up to three distinct overgrowths (Fig. 4-3A, C). Olivine cores are mostly rounded, contain occasional mineral inclusions of spherical Ni-Fe-Cu sulfides (<5 μm; Fig. 4-3A), and exhibit a range of forsterite (Fo 85.5-93.3 mol%) and NiO contents (0.22-0.41 wt%), coupled with low CaO and moderate MnO (0.01-0.10 and 0.09-0.13 wt%, respectively). This compositional range overlaps olivine

cores, and olivine in mantle xenoliths from the Kimberley kimberlites (e.g., Dawson et al. 1981; Erlank et al. 1987; Giuliani et al. 2017; Howarth and Taylor 2016; Rehfeldt et al. 2007; Fig. 5A, B).

Olivine internal zones have a diffuse contact with the core, and a relatively sharp contact with the subsequent overgrowth (Fig. 4-3A; Supp. Fig. 4-S2). These zones were observed in ~25% of grains, are up to 100 μm thick, contain inclusions of TIMAC spinel (titanian magnesian aluminous chromite; Mitchell 1986), and commonly have a euhedral habit (Fig. 4-3A; Supp. Fig. S4-2). Internal zones have a restricted range of Fo contents (90.6 ± 0.4 mol%), coupled with high NiO (0.43 ± 0.01 wt%), and low CaO and MnO concentrations (0.07 ± 0.01 and 0.11 ± 0.01 wt%, respectively). These compositions overlap similar internal zones (termed "transitional zones") in olivine from the Benfontein sills in terms of Fo content, although at marginally higher NiO contents (Howarth and Taylor 2016; Fig. 4-5A).

Internal zones are overgrown by ubiquitous olivine 'rims', which are generally <200 μm thick, and contain mineral inclusions of TIMAC and lesser MUM spinel (solid solution between magnesian-ulvöspinel, ulvöspinel, and magnetite; Mitchell 1986), rutile, and magnesian ilmenite (1-40 μm; Fig. 4-3B). Occasionally TIMAC spinel and magnesian ilmenite grains coexist within the same inclusion (Supp. Fig. S4-3). Olivine rims have relatively homogeneous Fo contents (89.1 ± 0.2 mol%), although values increase slightly towards grain margins (i.e., 88.8-89.3 mol%), coupled with increasing CaO and MnO (0.07-0.22 and 0.13-0.20 wt%, respectively; Fig. 4-5B), and decreasing NiO (0.20-0.07 wt%; Fig. 4-5A). These compositions overlap olivine rims from other root zone intrusions in the Kimberley cluster (i.e., Bultfontein ($Fo_{88.8}$) – Giuliani et al. 2017; Wesselton ($Fo_{88.9}$) – Shee 1985; De Beers (~Fo_{88-90}) – Boyd and Clement 1977; Moore 1988; Fig. 4-5A), including the high Fo compositional group from the Benfontein sills (~$Fo_{89.5}$; Howarth and Taylor 2016). However, these compositions

are distinct from those of olivine rims in the WWT sills (i.e., ~Fo_{87} – Shee et al. 1994) and the low Fo compositional group from the Benfontein sills (~$Fo_{87.5}$; Howarth and Taylor 2016).

Olivine rims are overgrown by a zone termed 'rinds', which are present in ~10% of grains (Fig. 4-2C; Supp. Fig. S4-4). Olivine rinds have a sharp contact with rims, are commonly <50 μm thick, and contain inclusions (<5 μm) of MUM spinel, perovskite, and apatite (Fig. 4-2C). Olivine rinds have high Fo (92.5 ± 0.1 mol%) and lowest NiO contents (≤0.06 wt%) of the olivine zones. The contents of CaO and MnO increase towards the grain margin (0.37-0.78 and 0.24-0.34 wt%, respectively). These compositions are within the range of olivine rinds from the Benfontein sills (Howarth and Taylor 2016; Fig. 4-5A).

The zonation features of olivine from the De Beers dyke are typical of olivine from other kimberlites worldwide (e.g., Bussweiler et al. 2015; Kamenetsky et al. 2008; Lim et al. 2018; Pilbeam et al. 2013).

Phlogopite and kinoshitalite mica

Mica occurs in two textural generations: large (~100 μm to 3 mm), blocky-rounded phlogopite macrocrysts (Fig. 4-3D), as well as phlogopite-olivine micro-xenoliths (Fig. 4-3E, Supp. Fig. S2, S5); and smaller (~5-10 μm) euhedral groundmass grains of high-Ba phlogopite-kinoshitalite (Supp. Fig. 5). Groundmass phlogopite-kinoshitalite occurs predominantly within serpentine-rich areas of the mesostasis and as thin (<10 μm) overgrowths on phlogopite macrocrysts (Supp. Fig. S4-5). Groundmass mica could not be analysed by EPMA due to the small grain size.

The cores of phlogopite macrocrysts contain occasional mineral inclusions (~10 μm) of subhedral Cr-spinel (Supp. Fig. S5), i.e., the low-Ti spinel typical of mantle peridotites (e.g., Schultze 2001). Phlogopite cores exhibit a range of Mg# values (83.8-91.5), and relatively homogeneous SiO_2 (42.2 ± 0.5 wt%), TiO (1.0 ± 0.4 wt%), Al_2O_3 (10.6 ± 0.1 wt%), and Cr_2O_3

(0.2 ± 0.1 wt%) contents. These compositions overlap phlogopite megacryst, macrocryst, and microcryst cores, as well as phlogopite in mantle xenoliths from the Kimberley kimberlites (Giuliani et al. 2016 and references therein; Fig. 4-5C).

Some macrocryst cores (~10% of grains) are overgrown by irregular and discontinuous rims (up to ~200 μm thick; Fig. 4-3D) showing homogeneous Mg# (90.6 ± 0.3), higher TiO_2 (3.3 ± 0.2 wt%), Al_2O_3 (13.3 ± 0.04 wt%) and Cr_2O_3 (1.4 ± 0.4 wt%), and lower SiO_2 (40.1 ± 0.4 wt%) than the cores (e.g., Fig. 4-5C). These compositions overlap those of 'antecrystic' phlogopite sampled by the Kimberley kimberlites (i.e., Wesselton and Bultfontein – Giuliani et al. 2016 and references therein; Fig. 4-5C).

Rutile

Rutile occurs in two textural populations. Rutile (I) occurs as 50-100 μm (rarely up to 250 μm) grains that contain thin (<5 μm) oriented lamellae of magnesian ilmenite, and are overgrown by magnesian ilmenite (Supp. Fig. S4-6). Rutile (I) has relatively homogeneous TiO_2 contents (94.3 ± 1.1 wt%), consistent with the analysis reported by Donaldson and Reid (1982). Minor elements include Cr_2O_3 (2.7 ± 0.8 wt%), Nb_2O_5 (1.5 ± 0.2 wt%), ZrO_2 (0.9 ± 0.2 wt%), FeO (0.4 ± 0.2 wt%), and V_2O_3 (0.3 ± 0.1 wt%). The composition of rutile (I) overlaps rutile xenocrysts associated with Lindsleyite–Mathiasite (LIMA), Yimengite-Hawthorneite (YIHA), and other metasomatic phases (e.g., Haggerty 1991) reported from the Kimberley (Jones 1982; Schultze 1990), and Jagersfontein kimberlites (~130 km SE of Kimberley; Haggerty 1983; Fig. 4-5D). However, the composition of rutile (I) is distinct from rutile derived from eclogitic xenoliths and included in eclogitic diamonds (e.g., Sobolev and Yefimova 2000), groundmass rutile from kimberlites (e.g., Tappe et al. 2014; Boctor and Boyd 1981), and rutile-ilmenite intergrowths (Tollo and Hagerty 1987; Fig. 4-5D).

Rutile (II) occurs as elongate (i.e., <20 μm long, and <5 μm wide) inclusions in olivine rims (Fig. 4-3B). Semi-quantitative EDS analysis indicates rutile (II) contains significant quantities of Cr_2O_3 and Nb_2O_5 (estimated at a few wt%). These geochemical features are broadly consistent with EPMA analyses of rutile included in olivine rims from the Ekati kimberlites (Canada; Fedortchouk and Canil 2004).

Magnesian ilmenite

Magnesian ilmenite occurs as inclusions in olivine rims (Supp. Fig. S4-2), and as anhedral groundmass grains, typically ~50-400 μm large (rarely up to ~600 μm; Figs. 4-2; 4-3F; 4-4A). Approximately 25% of groundmass magnesian ilmenite grains contain a core of rutile (I). Many magnesian ilmenite grains contain monomineralic inclusions of euhedral-subhedral olivine (<20 μm) as well as rare inclusions of TIMAC spinel (e.g., Fig 4-3F). Where fractures traverse these inclusions, olivine is replaced by dolomite (Fig. 4-3F, G). Olivine included in magnesian ilmenite has a Fo content of 89.5 mol% (n = 2), intermediate between olivine rims and internal zones (Fig. 4-3F, G; 4-5A; Supp. Table S4-1).

The compositions of magnesian ilmenite included in olivine rims overlap groundmass magnesian ilmenite (Fig. 4-6A); hence these two textural varieties are discussed collectively. Magnesian ilmenite has relatively homogeneous MgO (14.88 ± 0.48 wt%), MnO (0.41 ± 0.04 wt%), and V_2O_3 (0.23 ± 0.04 wt%) contents. TiO and FeO increase towards grain margins (i.e., 52.3-56.7 and 19.1-24.3 wt%, respectively), whereas Cr_2O_3 (4.35-0.42 wt%) and Al_2O_3 (0.3-0.1 wt%) values decrease. Fe_2O_3 contents are variable, but appear to decrease towards grain margins. These compositions are consistent with the analysis reported by Donaldson and Reid (1982) in a different sample of the De Beers dyke. They also overlap magnesian ilmenite included in olivine rims from the Wesselton kimberlite (Shee 1985), and groundmass ilmenite from the De Beers pipe (Pasteris 1980), but differ from ilmenite in the WWT sills, which have

lower MgO contents (Shee et al. 1994; Fig. 4-6A). The zonation of magnesian ilmenite is similar to that described for Wesselton and other southern African kimberlites (e.g., Apter et al. 1984). The De Beers dyke does not contain the late-stage Mg-rich ilmenite as observed in other intrusions of the Kimberley kimberlites (e.g., Shee 1985; Pasteris 1980; Fig. 4-6A), and other kimberlites worldwide (e.g., Mitchell 1986).

Magnesian ilmenite is resorbed and overgrown by a mantle (~20 μm thick) of MUM spinel ± perovskite (Fig. 4-4A; Supp. Fig. S4-5). The contact between magnesian ilmenite and the overgrowth phases contains abundant inclusions (<10 μm; Fig. 4-4B; Supp. Fig. S4-6) of ilmenite (II), Cr-spinel, monazite, TiO_2 (perhaps rutile), and Nb-rich ilmenite (up to ~8 wt% Nb_2O_5; EDS analysis). EDS analysis shows that ilmenite (II) is enriched in FeO and MnO, but depleted in MgO and Cr_2O_3 compared with magnesian ilmenite, whereas rutile inclusions are pure TiO_2, distinct from rutile (I) and (II).

Spinel

Spinel occurs as large (~1 mm), anhedral, macrocrysts (and in micro-xenoliths; Supp. Fig S4-1), and as subhedral to euhedral, concentrically zoned groundmass grains (generally <50 μm; Fig. 4-4C; Supp. Fig. S4-7).

Groundmass spinel exhibits poorly developed atoll textures (Fig. 4-4C; Supp. Fig. S4-6). Euhedral TIMAC spinel (~30 μm) occurs in the core, contains <10 μm inclusions of olivine, and is overgrown by MUM spinel. MUM spinel commonly occurs as discrete grains and constitutes much of the groundmass spinel by volume, generally occurring as <30 μm euhedral grains. MUM spinel is encircled by an additional generation of magnetite, which is separated from MUM spinel by a 'lagoon' of dolomite and serpentine.

Compositional zonation of groundmass spinel is defined by decreasing Cr_2O_3 (54-0.8 wt%), coupled with increasing TiO_2 (3.8-20.5 wt%), FeO (19.3-27.1 wt%), Fe_2O_3 (5.0-28.5

wt%), and MgO (10.6-15.3 wt%) contents towards grain margins (Fig. 4-6C). This zonation (i.e., TIMAC-MUM-magnetite) is typical of spinel from other root zone intrusions in the Kimberley cluster (i.e., Wesselton – Shee 1985; Roeder and Schultze 2008, De Beers – Pasteris 1980, Bultfontein; Giuliani et al. 2017; Fig. 4-6C; Supp. Fig. S13), and most kimberlites worldwide (e.g., Mitchell 1986; Roeder and Schultze 2008). However, these spinels are distinct in composition from spinel in the WWT (Shee 1985; White et al., 2012) and Benfontein sills (Boctor and Boyd 1981; Gaspar and Wyllie 1984; McMahon and Haggerty 1984; Roeder and Schultze 2008), with the latter containing lower maximum and average Cr_2O_3 contents (Fig. 4-6C; Supp. Fig. S4-13). In addition, the WWT and Benfontein sills contain abundant magnetite, which is rare in the De Beers dyke.

Perovskite

Perovskite occurs as euhedral to subhedral groundmass grains (<50 μm), and as overgrowths on magnesian ilmenite. Most perovskite grains are concentrically zoned, from REE-rich cores to REE-poor rims (EDS analysis), whereas others appear unzoned in BSE images (Supp. Fig. S4-8). This zonation pattern is typical of perovskite from kimberlites worldwide (e.g., Chakhmouradian and Mitchell 2000), including other intrusions of the Kimberley cluster (i.e., Dutoitspan – Ogilvie-Harris et al. 2009; Bultfontein – Giuliani et al. 2017). Grain margins of perovskite may be partially replaced by TiO_2 (possibly anatase; Supp. Fig. S4-7) as is common in multiple kimberlites worldwide (e.g., Chakhmouradian and Mitchell 2000 and references therein).

Perovskite cores contain inclusions (<10 μm) of anhedral MUM spinel, and euhedral olivine (Supp. Fig. S4-8). Perovskite rims and unzoned grains contain inclusions of MUM spinel with evolved compositions (i.e., Cr-poor, Ti-rich), and baddeleyite (Supp. Fig. S4-8).

Apatite

Apatite occurs as discrete euhedral grains with a typical size distribution of ~5-20 μm (rare grains up to ~100 μm). Apatite displays textures which resemble hopper crystals (Fig. 4-4 E, F; Supp. Fig. S4-9). Similar growth shapes have been reported from other kimberlites (e.g., Malarkey et al. 2011). The 'lagoon' of apatite contains mesostasis phases, such as carbonates, barite, and serpentine. We also note that larger barite grains are intergrown with, and host inclusions of apatite (Supp. Fig. S4-9).

Monticellite

Monticellite has been extensively pseudomorphed and replaced by dolomite, but its original presence is confirmed by rare, ~20 μm, euhedral grains (Fig. 4-4F; Supp. Fig. S4-10). These grains are zoned from FeO-rich cores to FeO-poor rims (EDS analysis), with a sharp boundary between zones (Supp. Fig. S4-10). Similar core to rim zonation patterns in monticellite have been reported from kimberlites worldwide (e.g., Mitchell 1978; Abersteiner et al. 2018). Monticellite rims contain spherical inclusions (<5 μm) of MUM spinel with evolved compositions.

Carbonates

There are at least three distinct generations of carbonate: (I) mesostasis carbonate (Supp. Fig. S11); (II) euhedral laths (Figs. 4-2, 4-4D, F); and (III) segregations (Supp. Fig. S11). The petrographic features of these carbonate generations are generally consistent with other descriptions of carbonates from the De Beers dyke (Castillo-Oliver et al. 2018; Donaldson and Reid 1982; Exley and Jones 1983). Therefore, we only report important or new details here.

Mesostasis carbonates consist of calcite and dolomite intergrowths. Mesostasis calcite contains clusters of <5 μm, spherical inclusions of Sr-Ba-rich carbonates (Supp. Fig. S4-11), which were not observed in mesostasis dolomite.

Euhedral poikilitic laths of calcite (up to ~1.3 mm long and <100 μm wide; Fig. 4-2; 4-4D), terminate at phlogopite macrocryst or olivine grain boundaries. Calcite laths contain chadacrysts of monticellite pseudomorphed by dolomite, apatite, spinel, and perovskite (Fig. 4-4F; Supp. Fig. S4-11). Calcite laths do not contain inclusions of Sr-Ba-rich carbonates, but are enriched in SrO and BaO compared with mesostasis calcite, and have distinct cathode-luminescence response (Castillo-Oliver et al. 2018). Similar elongate growth habits of calcite have been reported in dykes from kimberlites worldwide (e.g., Armstrong et al. 2004; Chakhmouradian and Mitchell 1999; Kopylova et al. 2007; Malarkey et al. 2010; Mitchell and Meyer 1980). However, to our knowledge, none of these other occurrences are poikilitic, as in the De Beers dyke.

Segregations are sparse in the studied samples, but are common in other units of the De Beers dyke (Donaldson and Reid 1982). Those observed are serpentine-free and contain angular intergrowths of calcite, dolomite, and barite. Dolomite occurs interstitial to calcite and at segregation margins. Barite is located at the contact between calcite and dolomite. Segregations may have a thin poly-crystalline rim of magnetite (Supp. Fig. S4-11).

In addition, dolomite replaces monticellite and olivine (Fig. 4-2K, L; Supp. Fig. S4-11) and calcite laths are locally replaced by dolomite. In turn, groundmass dolomite is locally replaced by serpentine (Fig. 4-4E, F; Supp. Fig. S4-11), while it is unclear if serpentine has also replaced calcite. We note that the replacement of carbonates (calcite and dolomite) by serpentine has been reported in other intrusions of the Kimberley cluster (Giuliani et al. 2017; Sparks et al. 2009, White et al. 2012).

Discussion

In this section, we discuss the origin of phases contained in the De Beers dyke and their relative crystallisation sequence, based on mineral inclusions and textural relationships (Fig. 4-7). The crystallisation sequence, combined with zonation patterns of magmatic phases, permits assessment of magma evolution and pre-emplacement differentiation by crystal fractionation.

Incorporation of xenocrystic and antecrystic material

Mineral inclusions (e.g., mantle Cr-spinel in phlogopite macrocryst cores; Supp. Fig. S4-4), textural features (i.e., phlogopite-spinel-harzburgite xenoliths in varying stages of disaggregation), and mineral compositions (Fig. 4-5) suggest the cores of olivine grains and phlogopite macrocrysts, as well as rutile (I), Cr-spinel, and orthopyroxene are xenocrysts derived from the disaggregation of variously metasomatised lithospheric mantle wall-rock. These findings are consistent with previous studies on olivine and phlogopite from the Kimberley kimberlites (e.g., Giuliani et al. 2016, 2017; Howarth and Taylor 2016; Shee 1985). The entrainment of abundant strongly metasomatised peridotite (as well as MARID suite xenoliths) by the De Beers dyke magma is consistent with sampling of strongly metasomatised lithologies by other intrusions of the Kimberley cluster (e.g., Erlank et al. 1987; Giuliani et al. 2014a; Jones et al. 1982).

Assuming equilibration with harzburgitic wall rocks (i.e., log $aSiO_2$ = -0.85), the Zr-in-Rutile thermometer of Ferry and Watson (2007) indicates equilibration of rutile (I) at 732-805˚C (1GPa). Extrapolation of this thermometer to lithospheric mantle pressures (i.e., >3 GPa) indicates that calculated temperatures intersect the Bultfontein palaeogeotherm of Mather et al. (2011) at ~4.2 GPa and ~1000˚C, further supporting a xenocrystic origin.

The compositions of phlogopite macrocryst rims from the De Beers dyke overlap those of high Cr-Ti ‘antecrystic’ phlogopite entrained by other intrusions in the Kimberley cluster

(Giuliani et al. 2016 and references therein; Fig. 4-5C). 'Antecrystic' components are produced by earlier melt batches and subsequently entrained by genetically related magmas (e.g., Ubide et al. 2014).

Magmatic and deuteric/hydrothermal stages

Textural relationships (e.g., olivine zonation) and mineral inclusion populations (e.g., olivine included in magnesian ilmenite; Fig. 4-3F, G, and magnesian ilmenite included in olivine; Supp. Fig. S4-3) indicate early crystallisation of olivine (internal zones and rims) and oxide minerals (i.e., TIMAC-MUM spinel, rutile (II), and magnesian ilmenite; Fig. 4-7). These features are typical of kimberlites worldwide, including other intrusions of the Kimberley cluster (e.g., Shee 1985; Fedortchouk and Canil 2004; Kamenetsky et al. 2008; Pilbeam et al. 2013). TIMAC spinel appears to have crystallised first, cotectic with olivine internal zones and, subsequently, olivine rims (Fig. 4-3B and 4-7; Supp. Fig. S4-2). Both rutile (II) and magnesian ilmenite crystallised together with olivine rims (but not internal zones) and TIMAC spinel (Fig. 4-3B and 4-7). Based on the location of rutile (II) and magnesian ilmenite inclusions within single olivine grains (e.g., Supp. Fig. S4-2), it appears likely that rutile (II) crystallised before magnesian ilmenite (see also Pasteris 1980). However, rutile (II) is not present in the groundmass and may have been completely replaced by magnesian ilmenite (e.g., Mitchell 1986), as observed for xenocrystic rutile (I) (Supp. Fig. S4-5). MUM spinel crystallisation overlapped the later stages of olivine rim crystallisation, but probably only began to crystallise after the cessation of magnesian ilmenite crystallisation (see below).

Early olivine-oxide crystallisation was followed by a change in mineralogy and mineral compositions of the crystallising phases. This is demonstrated by the replacement of magnesian ilmenite with MUM spinel ± perovskite, as well as changes in spinel (i.e., TIMAC to MUM) and olivine (i.e., rim to rind) compositions. The replacement of magnesian ilmenite by spinel

and perovskite is common to the Kimberley kimberlites (e.g., Shee 1985; Pasteris 1980) and other kimberlites worldwide (Mitchell 1986). The concentration of mineral inclusions at the contact between magnesian ilmenite and overgrowth phases (e.g., Fig. 4-4A, B; Supp. Fig. S4-6) indicates reaction between magnesian ilmenite and the melt crystallising MUM spinel and perovskite. This reaction may account for the general paucity of early crystallising magnesian ilmenite in the groundmass of kimberlites, compared to its common inclusion in olivine rims here and in kimberlites elsewhere (e.g., Fedortchouk and Canil 2004; Pilbeam et al. 2013).

Mineral inclusion relationships, i.e. MUM spinel inclusions in perovskite rims (Supp. Fig. S4-7), but not vice versa, indicate that MUM spinel began to crystallise before perovskite (Fig. 4-7). Both MUM spinel and perovskite crystallised together with olivine rinds (e.g., inclusions of olivine in MUM spinel, and MUM spinel in olivine rinds; e.g., Supp. Fig. S4-6). Inclusions of baddeleyite and MUM spinel with evolved compositions (Supp. Fig. S4-7) indicate these phases crystallised before or with perovskite. Olivine rinds host inclusions of apatite, which indicates rind crystallisation overlapped the onset of apatite crystallisation (Fig. 4-3C and 4-7).

The lack of monticellite inclusions in olivine from the De Beers dyke and most kimberlites worldwide (e.g., Kamenetsky et al. 2008; Pilbeam et al. 2013), indicates monticellite crystallised after olivine. Monticellite contains inclusions of MUM spinel with evolved compositions, potentially indicating continued MUM spinel crystallisation after olivine. Although many kimberlites also contain monticellite with inclusions of perovskite (e.g., Abersteiner et al. 2018), this was not observed in the De Beers dyke, possibly due to the extent of monticellite alteration.

Calcite laths contain chadacrysts of pseudomorphed monticellite, apatite, perovskite, and spinel (Fig. 4-4D, F; Supp. Fig. 4-10), and therefore crystallised after (or with) these phases (Fig. 4-7). The euhedral habit, elevated SrO and BaO contents, and Sr-isotope composition of

calcite laths from the De Beers dyke (Castillo-Oliver et al. 2018; Exley and Jones 1983) indicate a magmatic origin. Therefore, these laths are termed micro-phenocrysts.

The crystallisation of calcite phenocrysts was followed by crystallisation of several late-stage groundmass phases, including phlogopite-kinoshitalite, magnetite, barite, as well as mesostasis calcite, dolomite, and serpentine, as indicated by the absence of these phases included in poikilitic calcite micro-phenocrysts (e.g., Fig. 4-4F, Supp. Fig. S4-11). It is not possible to resolve the relative crystallisation sequence of these phases, due to their small size; however, some inferences can be made. Inclusions of Sr-Ba-rich carbonates in mesostasis calcite (Supp. Fig. S4-11) have been reported in kimberlites worldwide (e.g., Armstrong et al. 2004; Abersteiner et al. 2018), and suggest crystallisation after calcite micro-phenocrysts. The absence of dolomite phenocrysts and lack of Sr-Ba-rich carbonate inclusions in groundmass dolomite suggests that at least some calcite crystallised prior to dolomite. This is consistent with observations that calcite is in textural equilibrium with olivine and monticellite, whereas dolomite replaces olivine, monticellite and, locally, calcite phenocrysts. Moreover, the textural relationships within carbonate segregations (i.e., dolomite and barite interstitial to calcite; Supp. Fig. S4-11) indicate calcite crystallisation before dolomite.

There is a strong textural association between apatite and barite (e.g., Supp. Fig. S4-9) indicating that apatite crystallisation extended to the later stages of groundmass and mesostasis crystallisation. Protracted apatite crystallisation is also consistent with Sr-isotope systematics in the Jos kimberlite (Malarkey et al. 2011).

Textural relationships indicate that deuteric/hydrothermal replacement of pre-existing phases occurred during the latest stages of groundmass crystallisation. This involved the crystallisation of mesostasis serpentine and replacement of dolomite (Fig. 4-4E, F), crystallisation of phlogopite-kinoshitalite in serpentine-rich areas of the mesostasis (Supp. Fig.

S4-5), crystallisation of magnetite and the formation of atoll spinels (probably by replacement of pleonaste; Pasteris 1980), and replacement of perovskite by a TiO_2 phase (Supp. Fig. S4-8).

Evolution of De Beers dyke magma

The evolution of olivine (i.e., internal zone to rim), magnesian ilmenite, and TIMAC spinel is defined by decreases in Mg/Fe^{2+} ratios (Figs. 4-5A; 4-6B, D). These trends, combined with decreasing Cr_2O_3 contents in magnesian ilmenite, and NiO in olivine toward grain margins, can be explained by fractional crystallisation of olivine and oxide phases. Conversely, olivine rim and MUM spinel display a progressive increase in Mg/Fe^{2+} ratios, which continues through the crystallisation of olivine rinds (Figs. 4-5A; 4-6D). Groundmass crystallisation follows this trend of increasing Mg/Fe^{2+} as evident from the zonation of monticellite towards FeO poor rims (Supp. Fig. S4-11). This increase in Mg/Fe^{2+} ratios is also recorded in other Kimberley kimberlites by late-stage MgO enrichment of magnesian ilmenite (e.g., Shee 1985; Pasteris 1980) and, potentially, the high Mg/Fe^{2+} ratios of early formed serpentine (Giuliani et al. 2017). Increasing melt Mg/Fe^{2+} with progressive differentiation may be attributed to increasing oxidation of the residual melt and extensive crystallisation of increasingly Fe-rich spinels (i.e., MUM spinel, and subsequently magnetite). This may be accentuated by the earlier crystallisation of magnesian ilmenite (and to a lesser extent TIMAC), which may have depleted the melt in Fe prior to the late stages of olivine rim crystallisation. A progressive decrease in V/Sc ratio in olivine rims and rinds of the Benfontein kimberlite (Howarth and Taylor 2016) supports increasing melt oxidation with differentiation.

Progressive enrichment of the melt in CaO is indicated by increasing contents in olivine rims and rinds, and the subsequent crystallisation of apatite, monticellite and, finally, carbonates. We find it unlikely that CaO enrichment of olivine rims and rinds is significantly controlled by pressure, because we argue that olivine internal zones, rims, and rinds all

crystallised from an ascending kimberlite melt. Moreover, the replacement of magnesian ilmenite by perovskite confirms an increase in the Ca activity of the melt (Shee 1985). This increase in CaO contents of the melt can be attributed to the extensive crystallisation of CaO-free phases (i.e., olivine, spinel, ilmenite). The later stages of groundmass and mesostasis crystallisation show further enrichment in SrO and BaO, as represented in the composition of calcite laths and the crystallisation of Sr-Ba carbonates, barite, and phlogopite-kinoshitalite.

The replacement of olivine and monticellite by dolomite likely occurred in a relatively CO_2-rich and H_2O-poor fluid, possibly at temperatures above the serpentinisation window (i.e., ~400˚C; Mitchell 2008). Estimates of ≥500 ˚C for dolomite crystallisation provided by Armstrong et al. (2004) seem reasonable in this respect. The subsequent replacement of dolomite by serpentine may result from fluid differentiation towards increasingly H_2O rich compositions (e.g., Mitchell 1986 2008), and/or mixing of deuteric fluids with groundwater (e.g., Giuliani et al. 2014b, 2017; Sparks et al. 2009).

The alteration style observed in the De Beers dyke is consistent with that described by Armstrong et al. (2004), who noted that H_2O-poor, dolomite-bearing kimberlites from Lac de Gras contain well-preserved olivine, whereas monticellite is extensively altered. Therefore, the presence of dolomite may be a reasonable indicator of high CO_2/H_2O ratios during the later stages of crystallisation, imparting a strong control on the alteration style. The CO_2/H_2O ratios during deuteric alteration are invariably linked, although not directly, with the ratios in the primitive kimberlite melt (see Soltys et al., 2018).

Conclusions

The following events occurred during evolution of the magma parental to the De Beers dyke: (1) Production of antecrystic material (i.e., high Cr-Ti phlogopite rims). We suggest all the Kimberley kimberlites produced similar, or sampled the same antecrystic material; (2)

Incorporation of xenocrystic material (i.e., olivine and phlogopite (I) cores, spinel macrocrysts, rutile (I), and orthopyroxene), with a significant proportion derived from strongly metasomatised peridotite; (3) Early magmatic crystallisation of internal zone and rim olivine, TIMAC-MUM spinel, rutile (II), and magnesian ilmenite occurred after the sampling of spinel facies lithospheric material, probably on ascent to the surface; and (4) Crystallization of the rest of the groundmass phases (i.e., olivine rinds, Cr-poor MUM spinel, perovskite, apatite, calcite phenocrysts, and barite) and mesostasis phases (carbonates and serpentine), likely on emplacement in the upper crust. Magmatic crystallisation forms a continuous sequence with deuteric/hydrothermal alteration.

The compositions of magmatic phases (i.e., olivine rims, spinel, magnesian ilmenite) from the De Beers dyke overlap those from other root zone intrusions of the Kimberley cluster, but are distinct from those of the WWT and Benfontein sills (Fig. 4-5, 4-6). Therefore, we suggest that the De Beers dyke, in contrast to previous findings has not undergone pre-emplacement crystal fractionation. It follows that most of the melts parental to the Kimberley kimberlites were similar in composition during the early stages of magmatic crystallisation. These findings are consistent with those of le Roex et al. (2003), who based on bulk rock compositions (including samples from dykes and root zones) suggested the majority of the Kimberley kimberlites derive from a single parental magma composition affected by differing degrees of mantle contamination and syn-emplacement magmatic differentiation. This study demonstrates that individual intrusions require detailed petrographic and mineral chemical studies to assess if they are in fact ‘evolved’; and that dykes are not necessarily produced by differentiated magmas.

Early magmatic crystallisation decreases Mg/Fe^{2+}, Ni and Cr in the melt due to fractional crystallisation of olivine, ilmenite and spinel. Conversely, during the later stages of olivine rim crystallisation, and throughout groundmass crystallisation the Mg/Fe^{2+} ratio

increases, which we attribute to increasing oxygen fugacity and extensive crystallisation of Fe-rich spinel. The later stages of groundmass crystallisation show progressive increases in CaO, MnO, BaO and SrO as well as CO_2 and H_2O contents as previously documented by melt inclusion studies (e.g., Abersteiner et al., 2018; Giuliani et al. 2017).

Acknowledgements

We thank Graham Hutchison for assistance with SEM and EPMA analysis at the University of Melbourne, and Karsten Goemann for help with FE-SEM and EPMA analysis at the University of Tasmania. We are grateful to the John J. Gurney Upper Mantle Room Collection (University of Cape Town) and the De Beers Group for providing the studied samples. Reviews by Matt Gaudet and an anonymous reviewer improved the manuscript. We thank Bruce Kjarsgaard for his thorough review, and efficient editorial handling. Andrea Giuliani acknowledges funding from the Australian Research Council through a Discovery Early Career Research Award (DECRA, grant n. DE-150100009). This is publication 33 from the Kimberlites and Diamonds Research Group at the University of Melbourne, also listed as contribution 1165 from the ARC Centre of Excellence for Core to Crust Fluid Systems and 1128 from the GEMOC Key Centre.

Figures

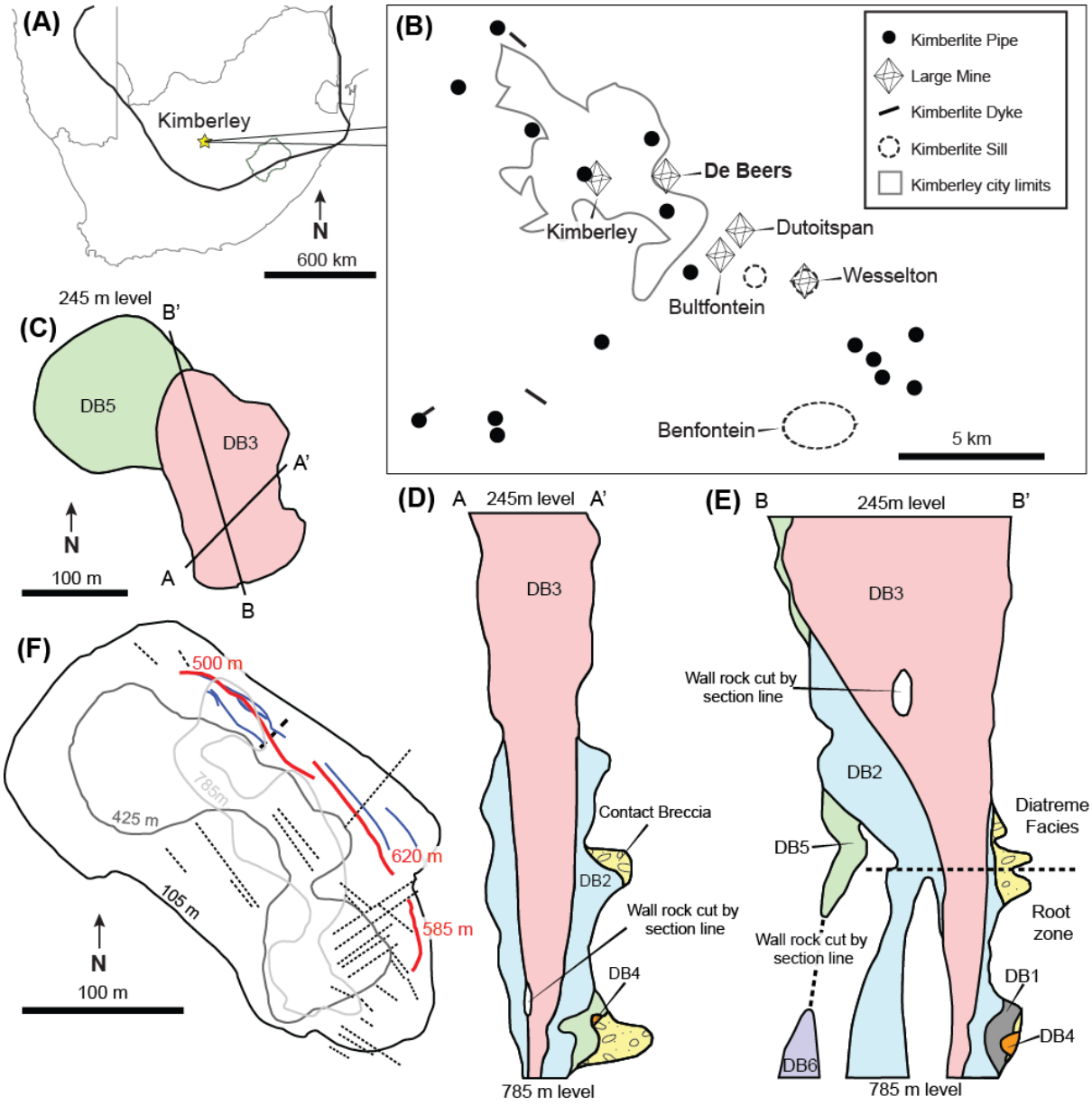

Figure 4-1. Map showing the location of the Kimberley kimberlite cluster. The thick line in panel (A) denotes the inferred location of the craton margin (modified from Field et al. 2008). (C) Plan view of the De Beers pipe on the 245 m level. (D, E) Cross sections across lines A-A' and B-B' (in panel C) between the 245 and 785 m levels of the De Beers pipe. (F) Plan view of the De Beers pipe and associated dykes (dashed lines) between the 245 and 785 m levels. The location of the De Beers dyke at various levels is demarcated by the thick red line (the De Beers dyke parallels the boundary of the main pipe; hence it is also referred to as the "Eyebrow" dyke). Also shown are the ancillary dykes associated with the De Beers pipe (thin blue lines)

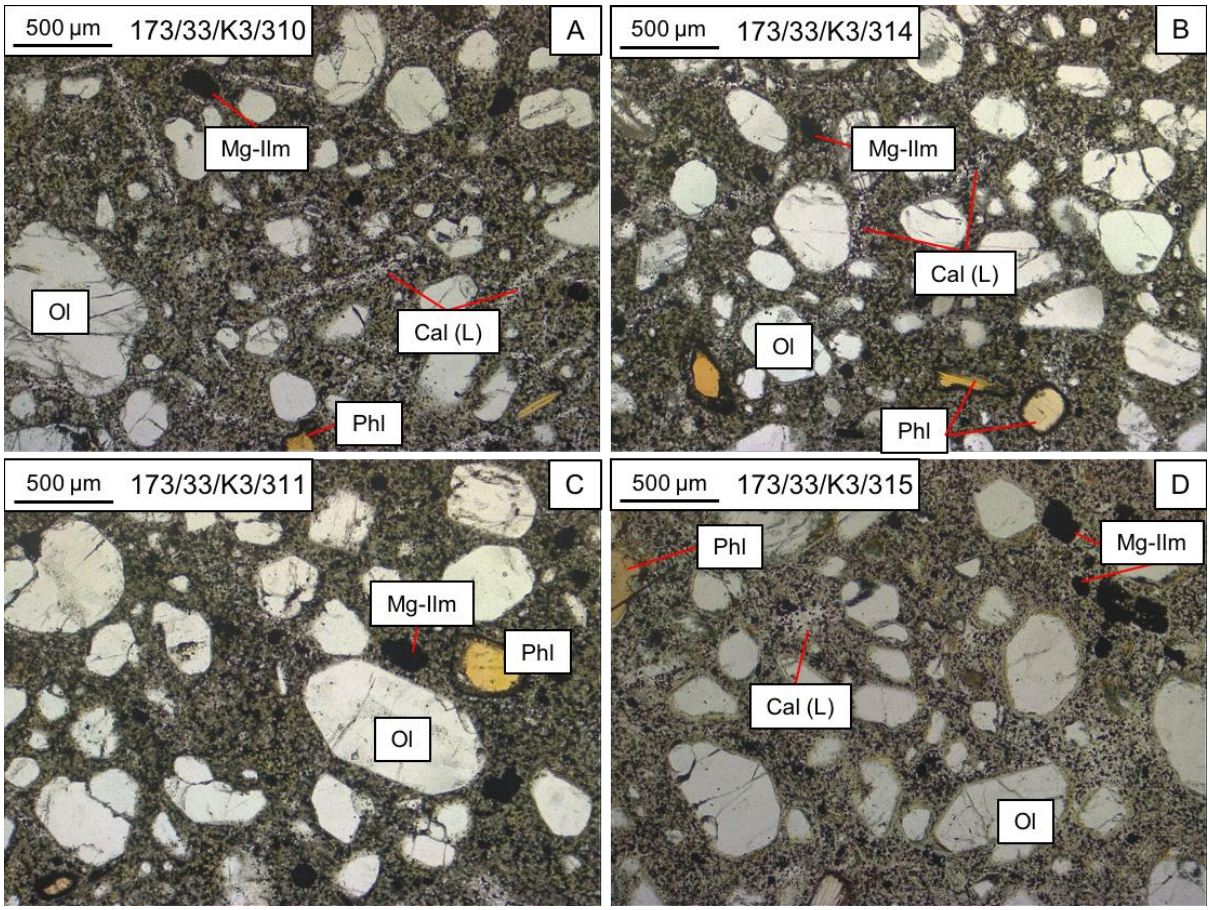

Figure 4-2. Plane-polarised transmitted-light photomicrographs of the samples studied from the De Beers dyke, showing the porphyritic texture of olivine (Ol), magnesian ilmenite (Mg-Ilm), macrocrystic phlogopite (Phl), and calcite laths [Cal (L)] set in a fine-grained mesostasis

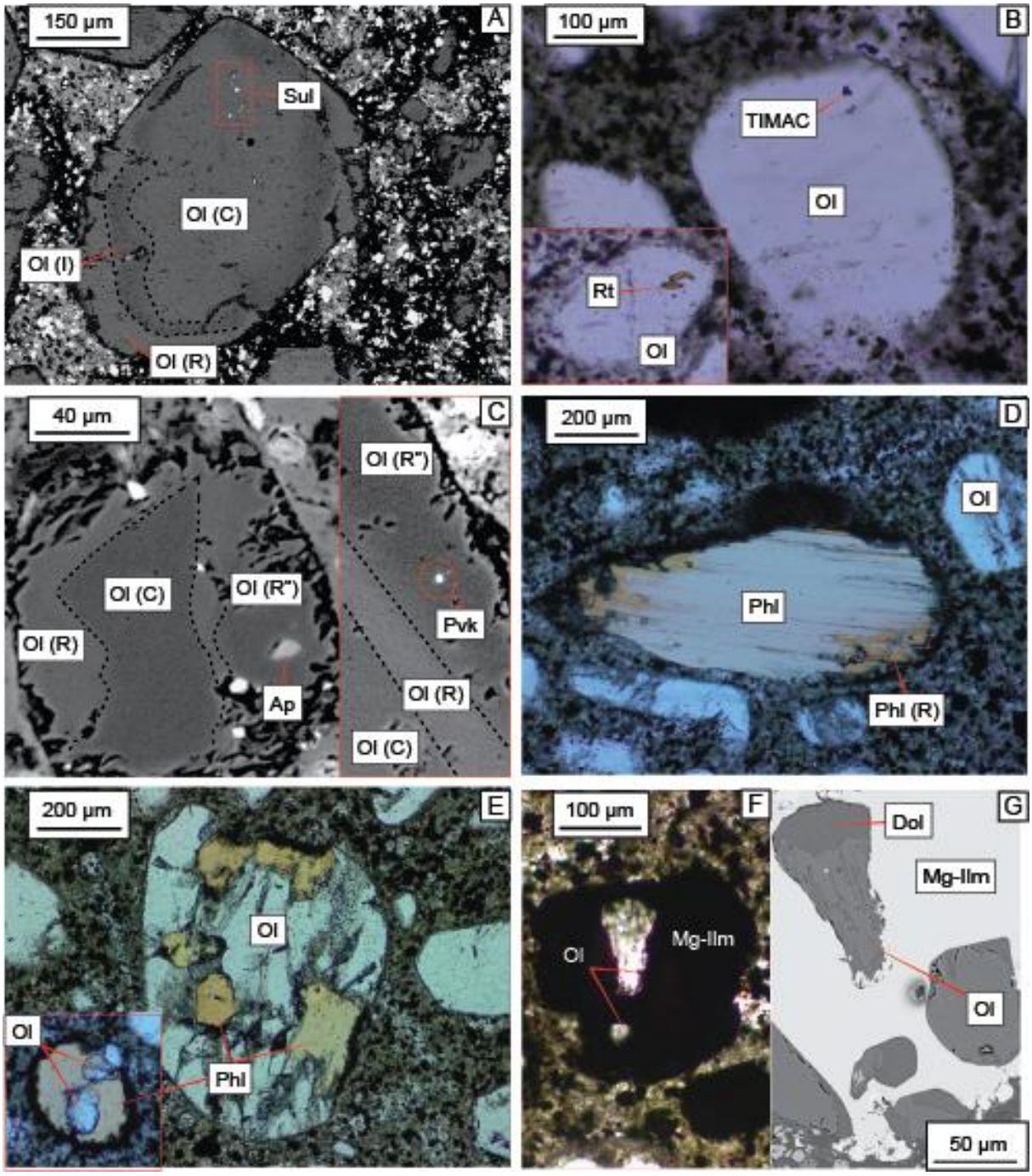

Figure 4-3. Back scattered electron images (A, C), plane-polarised transmitted-light photomicrographs (B, D, E, F), and plane-polarised reflected light photomicrographs (G) of the studied samples. (A) Zonation of an olivine grain containing a core [Ol (C)] with inclusions of sulfides (Sul), a euhedral internal zone [Ol (I)], and rim [Ol (R)]. (B) Inclusions of TIMAC spinel and rutile (Rt) in olivine rims. (C) Inclusions of apatite (Ap) and perovskite (Pvk) in olivine rinds [Ol (R")]. (D) A phlogopite macrocryst (Phl) overgrown by a discontinuous rim [Phl (R)]. (E) Phlogopite-olivine micro-xenoliths. (F, G) Inclusions of olivine, partially replaced by dolomite (Dol), in magnesian ilmenite (Mg-ilm)

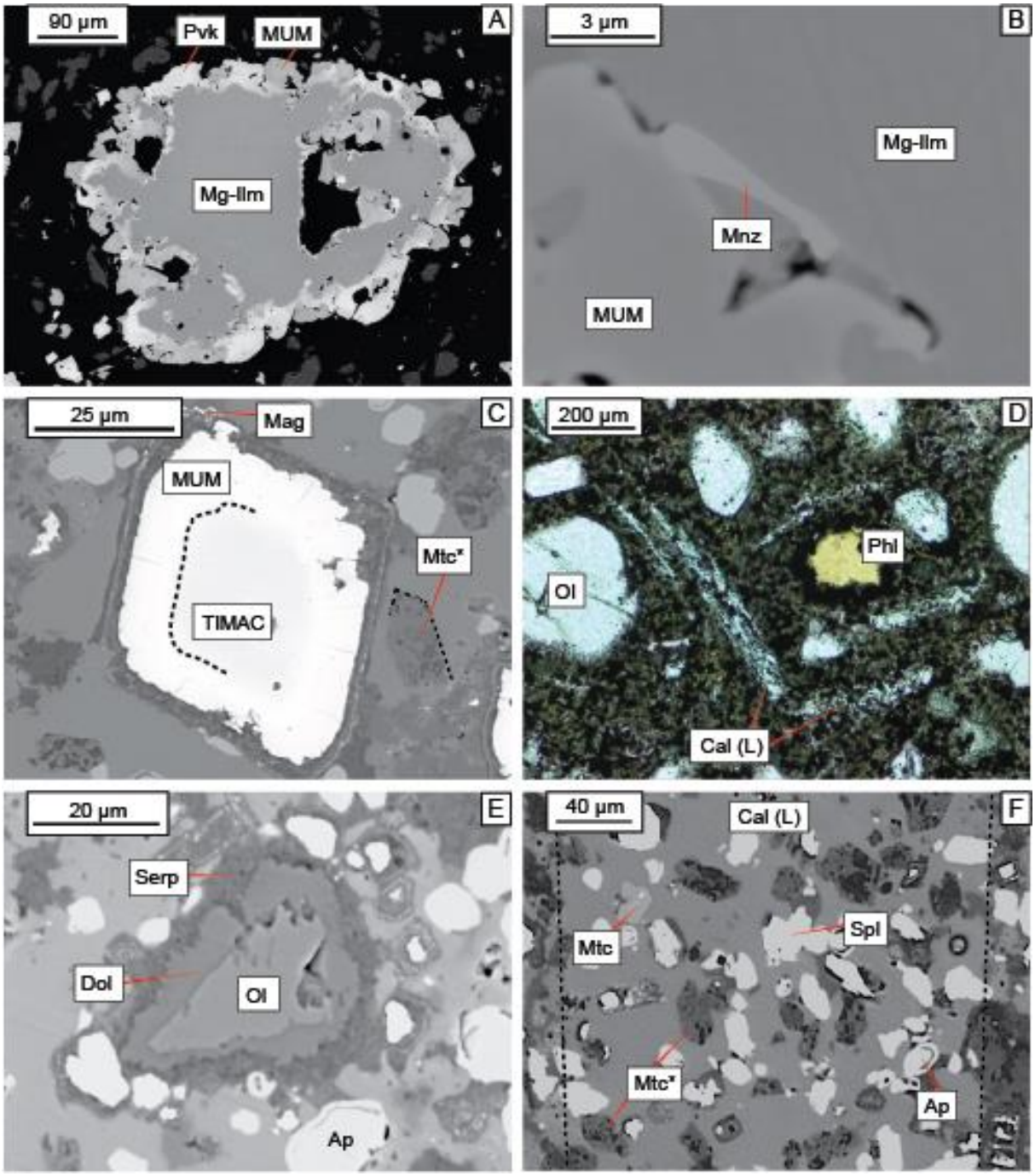

Figure 4-4. Back scattered electron images (A, B, C, E, F) and plane-polarised transmitted light photomicrographs (D) of the studied samples (A) Resorbed magnesian ilmenite overgrown by MUM spinel and perovskite. (B) Inclusion of monazite (Mnz) at the contact between magnesian ilmenite and MUM spinel. (C) Groundmass spinel with a TIMAC core, MUM overgrowth, and a poorly developed atoll texture with a thin rim of magnetite. Note that monticellite (Mtc*) has been replaced by dolomite, which in turn is replaced by serpentine. (D) Calcite laths, olivine, and phlogopite macrocrysts in a fine-grained mesostasis. (E) Olivine replaced by dolomite, which in turn is replaced by serpentine (Serp). (F) A calcite lath which contains chadacrysts of monticellite (Mtc), pseudomorphed monticellite (Mtc*), spinel (Spl), and apatite (Ap)

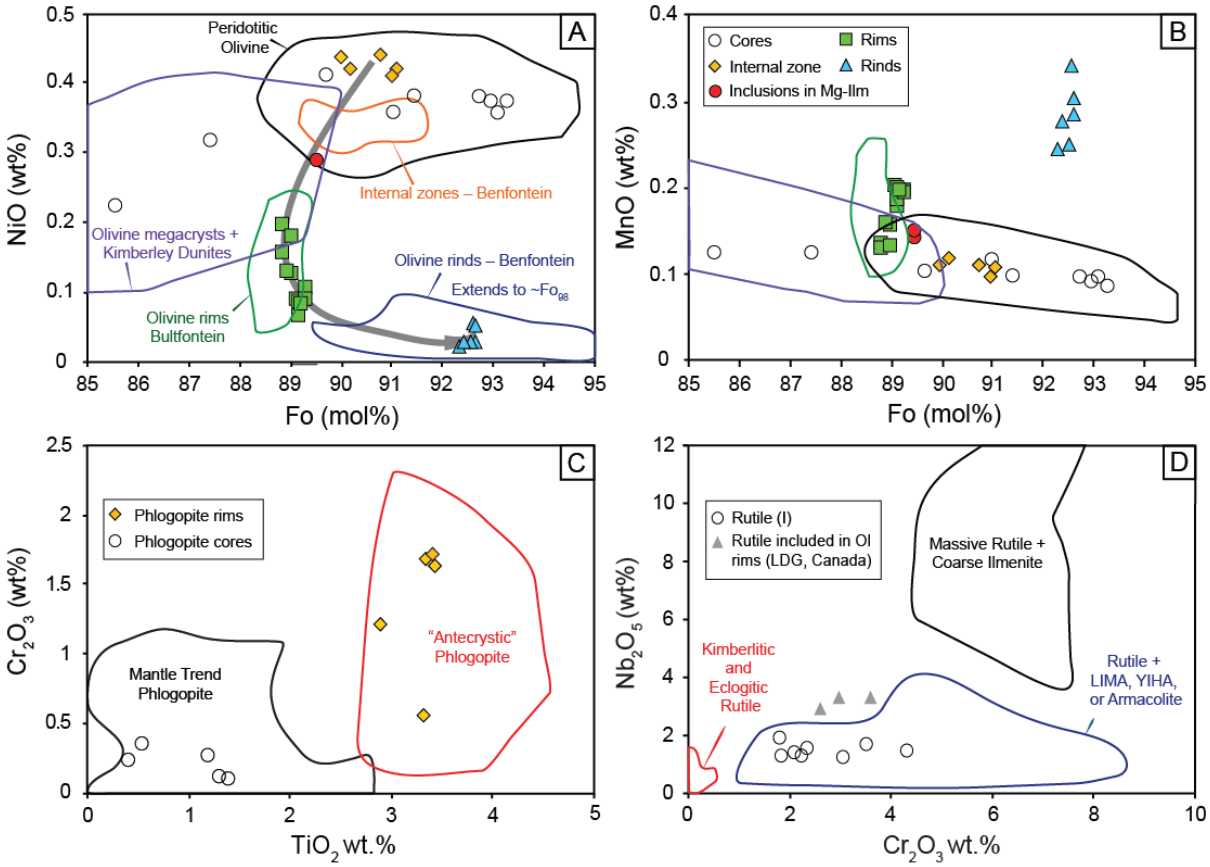

Figure 4-5. Bi-variate major element plots for phases contained in the De Beers dyke. (A, B) Different olivine zones illustrated in plots of Fo mol% vs. (A) NiO, and (B) MnO wt% space (see legend in panel B). Shown for comparison are the compositions of: olivine in mantle peridotite xenoliths from the Kimberley kimberlites (black outline – literature compilation); olivine megacrysts from southern Africa and Kimberley dunites (purple outline – compilation from Lim et al. 2018, as well as data from Dawson et al. 1981; Rehfeldt et al. 2007); olivine internal zones from the Benfontein sills (orange outline – Howarth and Taylor 2016); olivine rims from the Bultfontein kimberlite (green outline – Giuliani et al. 2017); and olivine rinds from the Benfontein sills (blue outline – Howarth and Taylor 2016). The grey arrow represents the compositional evolution of magmatic olivine. (C) Compositions of phlogopite macrocryst cores and rims plotted in Cr2O3 vs. TiO2 wt% space. Shown for comparison are the fields of mantle phlogopite, and antecrystic phlogopite (Giuliani et al. 2016, and references therein). (D) Compositions of rutile (I) plotted in Nb_2O5 vs Cr_2O_3 wt. % space. Shown for comparison are the compositions of: rutile included in kimberlitic olivine rims (grey triangles – Fedortchouk and Canil 2004); massive rutile intergrown with coarse ilmenite (black outline - Haggerty 1983); rutile xenocrysts associated with LIMA, YIHA, and other metasomatic phases (blue outline - Haggerty 1983); groundmass rutile from Benfontein sills (red outline - Boctor and Boyd 1981), as well as rutile from eclogitic paragenesis entrained by kimberlites worldwide (red outline - Sobolev and Yefimova 2000).

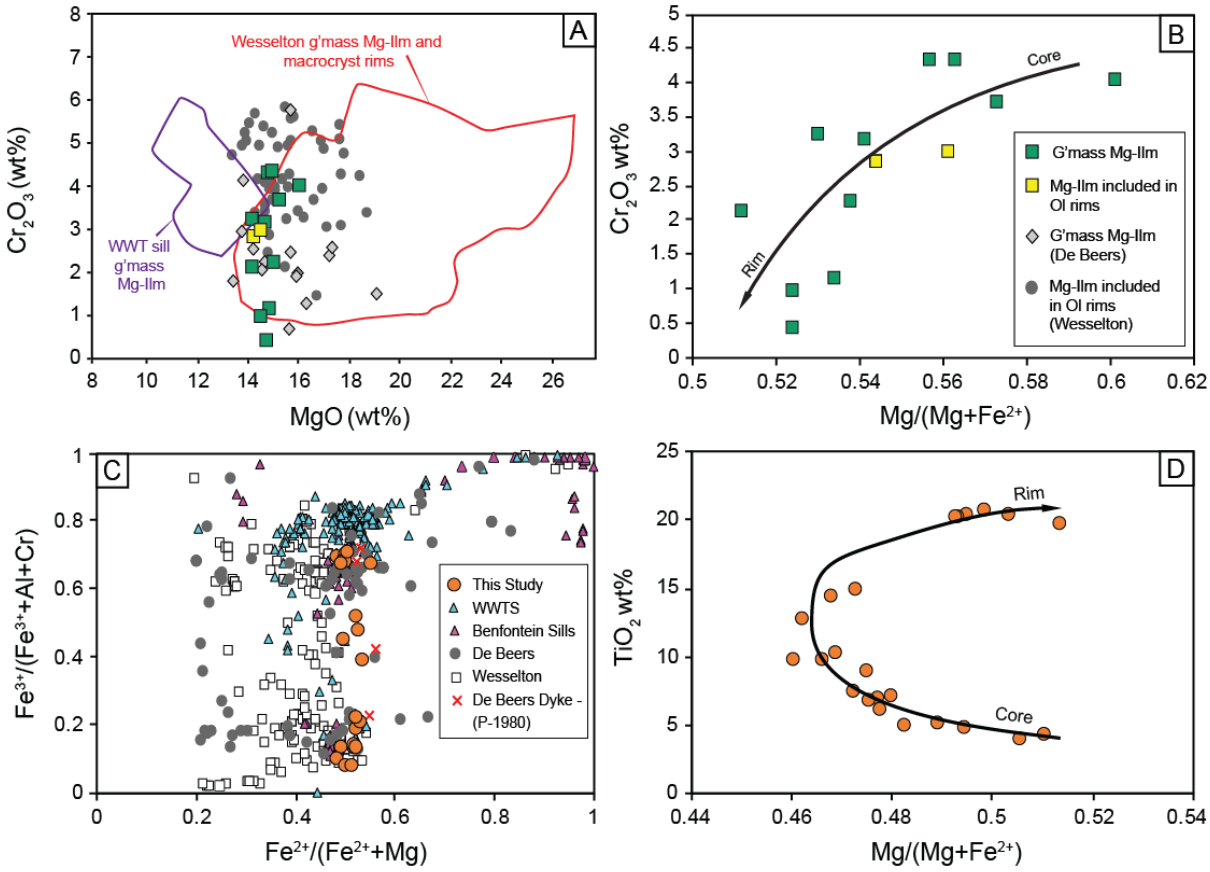

Figure 4-6. (A) Compositions of groundmass magnesian ilmenite and magnesian ilmenite included in olivine rims plotted in Cr_2O_3 vs. MgO wt% space (see legend in panel B). Shown for comparison are the compositions of magnesian ilmenite included in olivine from Wesselton (Shee 1985), and groundmass magnesian ilmenite from De Beers (Pasteris 1980). The purple and red outlines show the compositions of groundmass magnesian ilmenite from the WWT sills (Shee et al. 1994) and Wesselton kimberlite (Shee 1985), respectively. (B) The composition of magnesian ilmenite plotted in Cr_2O_3 wt% vs. $Mg/(Mg+Fe^{2+})$ space. (C) The composition of spinel plotted in $Fe^{3+}/(Fe^{3+}+Al+Cr)$ vs. $Fe^{2+}/(Fe^{2+}+Mg)$ space. Shown for comparison are the compositions of spinel from Wesselton (Shee 1985; Roeder and Schultze 2008), De Beers, including the De Beers dyke (Pasteris 1980), WWT sills (Shee 1985; White et al. 2012), and Benfontein sills (Boctor and Boyd 1981; Gaspar and Wyllie 1984; McMahon and Haggerty 1984; Roeder and Schultze 2008). (D) The composition of spinel plotted in TiO_2 wt% vs. $Mg/(Mg+Fe^{2+})$ space

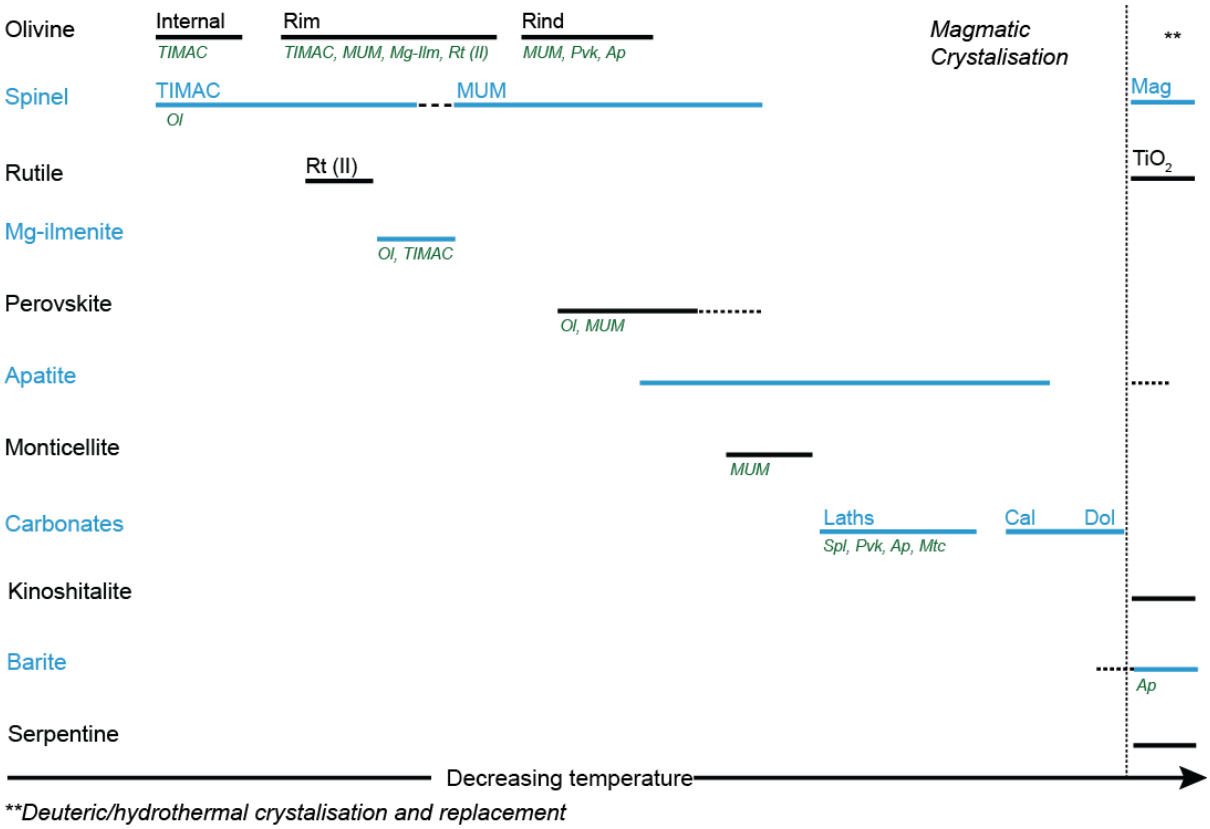

Figure 4-7. Crystallisation sequence of the De Beers dyke. The inclusions in any given phase are demarcated by the accompanying italicised green text (e.g., olivine rims contain inclusions of TIMAC and MUM spinel, magnesian ilmenite, and rutile (II)).

Tables

Table. 4-1 Average major element compositions of phases contained in the De Beers dyke

Phase	Olivine								Phlogopite				
Zone	Cores		Internal zones		Rims		Rinds		Cores			Rims	
	n = 9		*n* = 5		*n* = 12		*n* = 6		*n* = 5			*n* = 5	
	Mean	1sd	Mean	1sd	Mean	1sd	Mean	1sd	Mean	1sd		Mean	1sd
SiO_2	41.16	0.49	41.16	0.17	41.16	0.17	41.41	0.26	42.18	0.48		40.05	0.35
TiO_2									0.96	0.41		3.29	0.20
Al_2O_3									10.56	0.06		13.27	0.04
Cr_2O_3									0.21	0.10		1.35	0.44
Fe_2O_3(c)													
FeO	9.02	2.39	9.23	0.41	9.23	0.41	7.40	0.15	5.60	1.26		4.33	0.12
V_2O_3													
MnO	0.10	0.01	0.11	0.01	0.11	0.01	0.28	0.03					
MgO	50.15	2.15	49.83	0.33	49.83	0.33	51.32	0.25	25.27	1.07		23.32	0.32
NiO	0.35	0.05	0.43	0.01	0.43	0.01	0.04	0.01	0.14	0.06		0.19	0.02
K_2O									10.21	0.29		9.92	0.14
Na_2O									0.23	0.13		0.33	0.02
CaO	0.06	0.03	0.07	0.01	0.07	0.01	0.54	0.16					
Nb_2O_5													
ZrO_2													
F									0.37	0.09		0.39	0.19
Cl									0.04	0.02		0.04	0.02
BaO									0.06	0.09		0.04	0.06
H_2O(c)									4.01	0.06		4.04	0.10
O=F									0.15	0.04		0.17	0.08
O=Cl									0.01	0.00		0.01	0.01
Total	100.84	0.40	100.82	0.36	100.82	0.36	100.99	0.33	99.82	0.50		100.50	0.47

Table 1. Continued

Phase	Mg-Ilmenite		Rutile (I)		Spinel	
Zone						
	n = 13		*n* = 8		*n* = 23	
	Mean	1sd	Mean	1sd	Mean	1sd
SiO_2						
TiO_2	54.54	1.40	94.27	1.12	10.9	6.0
Al_2O_3	0.20	0.05			5.9	1.4
Cr_2O_3	2.74	1.24	2.67	0.83	31.5	20.6
Fe_2O_3(c)	4.80	1.66			15.5	8.9
FeO	22.06	1.57	0.39	0.22	23.1	2.7
V_2O_3	0.23	0.04	0.33	0.06	0.2	0.1
MnO	0.41	0.04			0.4	0.1
MgO	14.88	0.48			12.2	1.7
NiO					0.1	0.0
K_2O						
Na_2O						
CaO					0.3	0.2
Nb_2O_5			1.54	0.21		
ZrO_2			0.88	0.18		
F						
Cl						
BaO						
H_2O(c)						
O=F						
O=Cl						
Total	100.26	0.44	100.26	0.13	100.3	0.7

CHAPTER 5: APATITE COMPOSITIONS AND GROUNDMASS MINERALOGY RECORD DIVERGENT MELT/FLUID EVOLUTION TRAJECTORIES IN COHERENT KIMBERLITES CAUSED BY DIFFERING EMPLACEMENT MECHANISMS

Ashton Soltys[a]*, Andrea Giuliani[a,b], David Phillips[a]

[a] KiDs (Kimberlites and Diamonds), School of Earth Sciences, The University of Melbourne, Parkville, 3010 VIC, Australia

[b] Institute of Geochemistry and Petrology, Department of Earth Sciences, ETH Zurich, Clausiusstrasse 25, Zurich 8092, Switzerland

Abstract

Kimberlites are pipe-like igneous bodies, consisting of a pyroclastic crater and diatreme, commonly underlain by coherent root zone rocks, and with associated dyke/sill complexes. The processes that control the different modes of coherent kimberlite emplacement remain uncertain. In addition, late evolution of kimberlite melts during emplacement into the upper crust remains poorly constrained. Therefore, it is unclear whether there is a link between melt composition/evolution and the emplacement mechanism of coherent kimberlites (i.e., planar dykes/sills *vs*. irregular bodies in the root zone). An absence of comparative studies on late stage magmatic phases across the different emplacement modes of coherent kimberlite from the same locality hamper resolution of these issues. Therefore, we report petrographic and mineral chemical data for groundmass apatite in samples of dyke, sill, and root zone kimberlites from the Kimberley cluster (South Africa).

Early crystallised phases (olivine, spinel, Mg-ilmenite) in dyke/sill and root zone kimberlites have indistinguishable compositions, and hence crystallised from similar primitive melts. Conversely, apatite compositions, are generally distinct in dyke/sill (low Sr, high and variable Si) and root zone kimberlites (high and variable Sr, low Si). The Si-enrichment of apatite in dykes/sills is attributed here to the coupled incorporation of CO_3^{2-} and SiO_4^{4-} for PO_4^{3-}, reflecting higher CO_2 contents in their parental melts, and potentially higher Si contents due to the preferential crystallisation of carbonates over mica/monticellite. The low Sr contents of apatite in dyke/sill kimberlites reflect equilibrium with a (kimberlite) melt (i.e., D_{Sr} is close to unity for carbonate and silicate melts), whereas the higher Sr contents of apatite in root zone kimberlites require crystallisation from, or overprinting by a $H_2O \pm CO_2$ fluid (significantly higher D_{Sr}).

The relative enrichment of CO_2 in kimberlite dykes/sills is evident from the abundance of carbonates, the presence of mesostasis dolomite and calcite phenocrysts in some samples, and concomitant reduced proportions of other groundmass phases (e.g., serpentine, mica, monticellite). During late alteration of kimberlite dykes/sills, monticellite is typically replaced by carbonates, whereas olivine and pleonaste are relatively stable, indicating the melts which form dykes/sills evolve to higher CO_2/H_2O ratios.

It is unlikely that these two distinct evolutionary paths were caused by crustal contamination before or during near surface magma emplacement, because crustal assimilation is not recorded in the O and Sr isotopic composition of late crystallising olivine rinds or carbonates, respectively. We suggest that higher concentrations of CO_2 are retained in kimberlite dykes/sills due to higher confining pressures (i.e., lack of breakthrough to the surface). In contrast, exsolution of CO_2 from root zone kimberlites increased melt H_2O/CO_2 ratios and promoted the crystallisation of mica and monticellite at the expense of dolomite and calcite.

Apatite compositions have the potential to aid in the discrimination of kimberlites from lamproites (higher LREE, Sr, F, and S, lower Si contents) and carbonatites (higher LREE, F, Cl and S, lower Fe contents). However, the compositions of kimberlitic apatite overlap those from aillikites, probably due to similar late-stage melt compositions.

Introduction

Kimberlites occur as small-volume igneous bodies confined to intra-plate cratonic and peri-cratonic settings (Giuliani and Pearson 2019), and have been emplaced during much of Earth's history (i.e., ~2.85 Ga to ~12 Ka – Henning et al. 2003; and Brown et al. 2012, respectively). In southern Africa and many other worldwide occurrences, kimberlites have several morphological modes that include a volcanoclastic crater facies (rarely preserved), an underlying conical steeply-dipping diatreme, which transitions into an irregular root zone at depth (or directly into a feeder dyke), as well as dykes and sills that may, or may not, be associated with a diatreme (e.g., Clement, 1982; Dawson and Hawthorne 1973; Field and Scott Smith 1999). Dyke, sill, and root zone kimberlites are commonly considered coherent hypabyssal rocks formed by direct crystallisation of a kimberlite magma. Whilst there has been significant focus on the mechanisms that control the different emplacement modes of coherent and volcanoclastic kimberlites (e.g., Moussallam et al. 2016; Skinner and Marsh, 2004), the controls on the different emplacement modes of coherent kimberlites also remain poorly understood (e.g., Sparks, 2013). Some studies have suggested a lithological control on kimberlite emplacement mode, whereby competent units (e.g., Karoo dolerite sills in the Kimberley area) prevent explosive magma eruption and promote emplacement as sills rather than diatremes (e.g., Field and Scott Smith 1999). However, Karoo dolerite sills are widespread in the Kimberley area, and many kimberlite magmas breach these units. Therefore, it would appear that the host lithology cannot be the only controlling factor on the emplacement mechanism. For example, interaction with ground water can also influence the style of kimberlite emplacement (e.g., Lorenz and Kurszlaukis, 2007).

In this study, we test the hypothesis that the different emplacement styles of coherent kimberlite might be related to variations in the later stages of melt evolution (i.e., during ascent

and emplacement into the upper crust). To this end, we compared petrographic observations for groundmass phases and the compositions of groundmass apatite in coherent kimberlites from the Kimberley cluster (South Africa), which show different styles of emplacement – i.e., planar dykes/sills *vs*. irregular bodies in the root zone of pipes. We show that groundmass mineralogy and apatite compositions systematically differ between dyke/sill and root zone kimberlites, which we attribute to different compositional evolutionary paths, particularly with respect to the melt H_2O/CO_2 ratios. This study is concerned only with coherent kimberlites associated with diatremes that contain Kimberley-type pyroclastic kimberlites (Scott Smith et al. 2013; Mitchell et al. 2019), and without additional studies it is not clear whether the conclusions reached here are directly applicable to other types of coherent kimberlites such as those associated with Fort-a-la-Corne type pyroclastic infill in some Canadian occurrences.

Kimberlite mineralogy

Kimberlites are inequigranular rocks, containing components ranging in size from ~10 cm to <1 um, and are also hybrid in nature containing components of xenocrystic, magmatic, and secondary origins (e.g., Mitchell 1986), as well as more recently discovered antecrystic compomnents (Giuliani et al. 2016; Mitchell et al. 2019). The predominantly magmatic groundmass contains olivine, Mg-ilmenite, spinel group minerals, perovskite, monticellite, apatite, and mica, cemented by a mesostasis of serpentine, calcite, and sometimes dolomite.

A significant proportion of the mineral chemical and petrographic data reported for kimberlite rocks concerns their xenocrystic components (olivine, phlogopite, and ilmenite cores – e.g., Boettcher and O'Neil, 1980; Dawson and Smith, 1975; Moore, 1987, 1988; Pasteris 1980; Shee, 1985) and ‘early’ crystallised magmatic phases (olivine rims, Mg-ilmenite, and Ti-

Mg-Al-chromite – e.g., Brett et al. 2009; Fedortchouk and Canil 2004; Kamenetsky et al. 2008; Nielsen and Sand, 2008; Pilbeam et al. 2013; Roeder and Schultze, 2008; Soltys et al. 2018a). There is a growing body of evidence to suggest that these 'early' phases crystallise on ascent through the lithosphere, but before emplacement into the upper crust (e.g., Arndt et al. 2010; Brett et al. 2009; Soltys et al. submitted; Lim et al. 2018; Giuliani 2018).

In contrast, beyond mica (e.g., Giuliani et al. 2016; Mitchell 1995; Reguir et al. 2009) there are few data for other late crystallising groundmass phases (i.e., apatite, magnetite, monticellite, carbonates, and serpentine – see Armstrong et al. 2004; Beard et al. 2000; Dalton et al. 2020; Giuliani et al. 2017; Kopylova et al. 2010; Malarkey et al. 2010; White et al. 2012; Willcox et al. 2015), which inhibits our understanding of late-stage kimberlite melt evolution. The study of these later stage groundmass phases is complicated by small grain size and common alteration (e.g., monticellite and pleonaste – O'Brien and Tiny, 1999; Pasteris 1980); and the presence of components of uncertain origins (e.g., serpentine – Giuliani et al. 2017; Sparks, 2013 and references therein).

Apatite is a near ubiquitous mineral in kimberlites worldwide (Mitchell 1986; Mitchell et al. 2019). It is resistant to alteration, and forms numerous solid solutions incorporating a number of minor, trace, and volatile elements (e.g., fluorapatite, chlorapatite, hydroxyapatite, strontium-apatite - Chakhmouradian et al. 2017; Pan and Fleet 2002; Piccoli and Candela 2002). Based on its euhedral habit, inclusions of magmatic spinel and monticellite, and the fact that it does not replace pre-existing magmatic phases, kimberlitic apatite is considered a primary phase that forms in the later stages of kimberlite melt crystallisation (e.g., Malarkey et al. 2010). Consequently, apatite has the potential to trace late-stage kimberlite melt evolution, as it has been employed in a similar way in studies of many other igneous rock types (e.g., Chakhmouradian et al. 2017; Webster and Piccoli, 2015). Unfortunately, little is known about the compositional variability and crystallisation environment of apatite in kimberlites, due to a

limited number of studies where all key elements are measured (i.e., F, Cl, Si, Sr, and LREE – Chakhmouradian et al. 2002; Chalapathi Rao et al. 2010; Dalton et al. 2020; Malarkey et al. 2010; Sarkar et al., 2018; Shaikh et al. 2018).

Geological setting, sample selection, and methods

The Cretaceous (~80-92 Ma) Kimberley kimberlites were emplaced into Archean basement gneisses, andesitic-basaltic lavas of the Ventersdorp supergroup, and a package of sedimentary rocks, dolerite dykes, and lavas of the Karoo sequence (Clement, 1982). The Kimberley cluster consists of five main pipes (i.e., Kimberley mine, De Beers, Bultfontein, Wesselton, and Dutoitspan), which have been mined almost continuously for over a century. Numerous (i.e., ~30) smaller sub-economic pipes occur within a ~10 km radius, and the cluster is associated with extensive dyke and sill complexes (e.g., Clement, 1982; Dawson and Hawthorne 1973; Shee, 1985).

The samples studied here represent the different emplacement modes of coherent kimberlites – i.e., dyke, sills, and root zone kimberlites (Table 1). The studies samples (n = 10) were selected from a larger collection (i.e., >50 samples) for their larger apatite grain size and better preservation, as well as to cover different kimberlite pipes (i.e., Wesselton, De Beers, and Kimberley mine) and dyke/sill complexes (i.e., De Beers dyke, Benfontein sills, Wesselton water tunnel sills [WWTS], Bultfontein dyke), including different units from the same pipe (Wesselton) and different samples from the same unit (i.e., Wesselton W2 and W3). Samples collected from root-zone kimberlites and the centre of some dykes tend to be highly macrocrystic (i.e., ~30 vol.% olivine macrocrysts – e.g., Wesselton and the Kimberley Mine – e.g., Fig. 5-1b; Supp. Fig. S1-11). In contrast, samples from sills and many dykes are

macrocryst-poor to aphanitic (i.e., devoid of olivine and other macrocrysts – e.g., Benfontein, and the WWTS – e.g., Fig. 5-1a; Supp. Fig. S12-17).

Petrographic observations utilised a Philips (FEI) XL30 environmental scanning electron microscope SEM, equipped with an OXFORD INCA energy dispersive X-ray spectrometer (EDS), housed at the University of Melbourne. During semi-quantitative chemical analysis and the production of back-scattered electron (BSE) images a beam acceleration voltage of 15 kV and a spot size of 5 μm was used.

Major element mineral compositions were determined on apatite grains larger than 20 μm using a Cameca SX-50 electron probe micro-analyser (EPMA) equipped with four vertical wavelength dispersive spectrometers, located at the University of Melbourne. Conditions during analysis were as follows: beam acceleration voltage of 15 kV, beam current of 4 nA (apatite), and a beam diameter of 8 μm; counting times per analysis were 20 s on peak positions and 10 s on two background positions located on either side of the peak position. The low beam current and large spot size used in this study to measure apatite compositions are similar to protocols designed to minimise the potential issues when analysing F and Cl by EMPA (e.g., Słaby et al. 2016). The calibration materials analysed consisted of natural and synthetic materials as well as metal oxides (e.g., Durango apatite [P], hematite [Fe], wollastonite [Si, Ca], jadeite [Na], magnesium oxide [Mg], Edinburgh REE glass [La, Ce], and celestine [Sr]). The limit of detection for most oxides is ~0.02-0.03 wt.% (e.g., Si, P, S), although slightly higher Sr (~0.08 wt.%), La (~0.13 wt.%), and Ce (0.08 wt.%) and F (~0.3 wt.%). Data reduction was performed using the PAP matrix correction software program (Pouchou and Pichoir 1984).

Kimberlite petrography

The Kimberley kimberlites contain macrocrysts (0.5-10 mm) and less common megacrysts (1-20 cm) of olivine, Mg-ilmenite, phlogopite, clinopyroxene, orthopyroxene, garnet, and spinel (e.g., Fig. 5-1b; Supp. Fig. S1-17; see also Clement, 1982; Shee, 1985). Groundmass phases and micro-phenocrysts include olivine, Mg-ilmenite, spinel-group minerals, perovskite, apatite, monticellite, phlogopite-kinoshitalite mica, and calcite (e.g., Fig. 5-1; Supp. Fig. S1-17). These phases are set in a fine-grained mesostasis consisting of carbonates (calcite ± dolomite) and serpentine. The modal abundance of these phases has been modified by syn-emplacement processes in some samples (e.g., flow differentiation in the De Beers dyke – Donaldson and Reid, 1982; in-situ magmatic differentiation in the Benfontein sills – Dawson and Hawthorne 1973; Abersteiner et al. 2019).

Some dyke/sill kimberlites from the Kimberley cluster (i.e., De Beers dyke, Benfontein Sills, Bultfontein) contain locally abundant dolomite (i.e., up to ~50% of the mesostasis carbonates; Supp. Fig. S18 – see also Dawson and Hawthorne 1973; Donaldson and Reid, 1982; Exley and Jones, 1982; Giuliani et al. 2017; Soltys et al. 2018a). These samples may also contain calcite phenocrysts (Fig. 5-1a; Supp. Fig. S12, S16, S17; see also Dawson and Hawthorne 1973; Castillo-Oliver et al. 2018; Donaldson and Reid, 1982; Soltys et al. 2018a). In contrast, samples from root zone kimberlites are devoid of calcite phenocrysts and mesostasis dolomite. Samples from dyke/sill kimberlites also have a higher ratio of mesostasis carbonates to serpentine, compared to samples from root zone kimberlites (Fig. 5-1; cf. Supp. Fig. S1-11 with Supp. Fig. S12-17). Although samples from both emplacement modes may be monticellite-rich, samples of the root zone kimberlites commonly contain a significantly higher modal abundance of monticellite than dyke/sill kimberlites (e.g., Fig. 5-1; Supp. Fig. S12-17; Table 1).

Finally, there are differences in the alteration styles. In dykes and sills, monticellite is commonly replaced by carbonates, which in turn may be replaced by serpentine, whereas

olivine is commonly fresh (Fig. 5-1; Supp Fig. S1-11; see also Giuliani et al. 2017; Soltys et al. 2018a). In the root-zone kimberlites, monticellite is commonly fresh, but olivine is extensively replaced by serpentine (e.g., Fig. 5-1; Supp. Fig. S12-17). Pleonaste was not observed in many of the studies samples, either because it did not crystallise, or due to alteration. However, the samples in which pleonaste is preserved all correspond to carbonate-rich dykes/sills (i.e., WESK-3A, Benfontein – Supp. Fig. S18; see also Abersteiner et al. 2019).

Samples from the WWTS have petrographic features which are unique compared to other samples of the Kimberley kimberlites, in that they contain a high modal abundance of large groundmass mica (Supp. Fig. S15; see also Shee, et al. 1994) and a higher ratio of mesostasis carbonate to serpentine (Supp. Fig. S15). These mineralogical characteristics probably reflect the evolved nature of the kimberlite melt parental to these sills.

Apatite petrography

The petrographic features of apatite in the studied samples are broadly consistent with previous reports of apatite in kimberlites (e.g., Malarkey et al. 2010). In the current samples, apatite occurs in two main textural settings:

I. Discrete subhedral-euhedral hexagonal prisms that are evenly dispersed throughout the groundmass and range in size from ~1-100 μm, with a dominant size distribution of ~20-50 μm (e.g., Fig. 5-2 a, b).
II. Aggregates of elongate (from ~20 μm to 400 μm in length), acicular apatite, with radial growth forms (Fig. 5-2c, d). This textural generation is commonly confined to carbonate-serpentine segregations, where it has sometimes nucleated from the segregation wall.

In samples of dykes (e.g., De Beers Dyke, Bultfontein) and sills (WWTS, Benfontein) both textural generations of apatite may display hopper-like crystal forms, where the 'lagoon' may be filled by carbonates, serpentine, and barite (e.g., Supp. Fig. S19). These hopper crystal forms were not observed in samples of root zone kimberlites, with the exception of an aphanitic sample from the Wesselton pipe, which was sampled adjacent to the wall rocks (Supp. Fig. S19e, f).

Groundmass apatite belonging to textural type (I) occurs as discrete grains, as inclusions in groundmass mica and/or the rims of mica macrocrysts and microcrysts (e.g., Fig. 5-3b; Supp. Fig. S5, S17), and very rarely as inclusions in the outer regions of olivine (i.e., rinds; see Soltys et al. 2018a). In most instances, groundmass mica occurs interstitial to apatite, although apatite may show straight equilibrium contacts with mica (e.g., Fig. 5-3a). Apatite rims and apatite in carbonate-serpentine segregations may be intergrown with (or contain inclusions of) groundmass mica (e.g., Fig. 5-3a; Supp. Fig. S4; S17; S20; S21). In addition, apatite rims sometimes contain inclusions of Ti-magnetite (Fig. 5-3c). Some apatite grains are imbedded in the lagoon of atoll-spinel grains, where the outer magnetite 'reef' is disrupted by apatite (Fig. 5-3b). In some samples, particularly those from root-zone kimberlites, apatite of textural type (I) has developed a poikilitic habit and contains chadacrysts of monticellite, MUM spinel, and perovskite (e.g., Fig. 5-3e, f).

Most apatite grains belonging to textural type (I) appear unzoned in back-scattered electron (BSE) images, however, there are some exceptions. Apatite from the Kimberley mine (sample BHK-3) is characterised by a homogeneous core that is overgrown by a thin (<5 μm) rim with a slightly darker BSE response (Supp. Fig. S20). Semi-quantitative SEM-EDS analyses indicate that these rims are enriched in Na_2O (i.e., ~3.5 wt.%) relative to their cores. Some rare apatite grains from the Wesselton kimberlite (sample WESK-6) have fine scale irregular zonation in BSE images (Fig. 5-3c).

In contrast, radial acicular apatite (i.e., textural type (II)) occurring in carbonate-serpentine segregations is generally devoid of primary mineral inclusions (e.g., Fig. 5-2c, d; Supp. Fig. S15; S21c, d; S23a-d). One exception is apatite from the root-zone of the De Beers pipe (samples DB26 and DB76), where apatite is sometimes intergrown with phlogopite (e.g., Fig. 5-3d; Supp. Fig. S4). These acicular apatite grains appear unzoned in BSE images, but display zonation under cathode luminescence (CL – see below).

Apatite from sample P3 of the WWTS exhibits distinct petrographic features. The cores of groundmass grains show some affinity with type (I) apatite grains, in that they generally have equant euhedral shapes, and occur as inclusions in groundmass mica (Fig. 5-4c). These cores may host abundant monomineralic inclusions of olivine (incipiently altered to serpentine), perovskite, spinel, an unidentified Ca-Zr phase, and a K-rich aluminosilicate (kalsilite?) (Fig. 5-4a-d). These inclusion-rich cores are overgrown by a rim that generally does not contain inclusions (e.g., Sup. Fig. S23).

Textural type (II) apatite in sample P3 (WWTS) is much larger (i.e., up to 400 μm in its longest dimension – Fig. 5-2d; Supp. Fig. S15; S23) and occurs in carbonate-rich segregations. This generation of apatite is generally devoid of primary mineral inclusions but may host calcite, barite, and serpentine in the ‘lagoons’ of hopper crystals, which may represent crystalised melt inclusions (Supp. Fig. S12). These apatite grains are analogous to the inclusion-free overgrowths described above for this sample. In rare instances apatite in segregations may be in close textural association with a Ca-Ti-Fe silicate (probably andradite), which in turn contains inclusions of apatite (Supp. Fig. S21c, d).

The above apatite generations in the WWTS can be distinguished by CL imaging. The inclusion-rich cores of apatite (I) have a bright CL response (Supp. Fig. S22), which is similar to that of apatite included in groundmass mica (Supp. Fig. 23e, f). The inclusion-free rims that overgrow the inclusion-rich cores, as well as the cores of textural type (II) apatite (i.e., acicular

grains in segregations) have a dull CL response (Supp. Fig. S22, S23). Apatite (II) grains may show a progressive increase in CL response towards the apices of grains, and in some cases oscillatory zonation (Supp. Fig. S22, S23a-d). This progressive change in CL response in type (II) apatite grains may be due to minor increases in REE contents (see next section).

Apatite composition

The average compositions of apatite in the studied samples is reported in Table 2, and the full data set is available in Supplementary Tables S1.

Regardless of magma emplacement style**,** apatite from the Kimberley kimberlites features a dominant fluorapatite component (2.2 ± 0.5 wt.% F; *n* = 153), with a negligible chlorapatite component (i.e., Cl was below the EPMA limits of detection in most instances – Table 2). These apatite grains contain relatively homogeneous CaO (55.0 ± 1.3 wt.%) and P_2O_5 (39 ± 0.8 wt.%) contents, but low concentrations of Na_2O (0.2 ± 0.2 wt.%) and FeO (0.2 ± 0.1 wt.%), which show no systematic variations (Table 2; Supp. Table S1). We did not observe systematic differences between the two petrographic types of apatite described above (i.e., apatite (I and II)).

The contents of some minor elements vary between samples, and between kimberlites with different emplacement modes (Fig. 5-5; Table 2; Supp. Table S1). Apatite from dykes and sills are enriched in SiO_2 (1.2 ± 0.4 wt.%; *n* = 64) and, to a lesser extent, $LREE_2O_3$ (i.e., La_2O_3 + Ce_2O_3 = 0.27 ± 0.19 wt.%), but are generally poor in SrO (0.8 ± 0.6 wt.%), compared with apatite from root-zone kimberlites (i.e., SiO_2 = 0.5 ± 0.2 wt.%, $LREE_2O_3$ = 0.07 ± 0.07 wt.% (many grains contain LREE's contents below detection limits), and SrO = 2.8 ± 1.3 wt.%, respectively; *n* = 89; Fig. 5-5; Table 2). Due to the high abundance of inclusions in apatite (I)

cores from the WWTS (e.g., Fig. 5-4; Supp. Fig. S22), this generation of apatite could not be analysed by EPMA, and the data reported here all correspond to the inclusion-free rims of apatite (I), or textural type (II) apatite in carbonate-rich segregations. Apatite (II) from the WWTS shows geochemical features consistent with apatite from other dyke/sill kimberlites in the Kimberley area, albeit with slightly higher SrO contents (Fig. 5-5; Table 2; Supp. Table S1).

Apatite from different root zone kimberlites show substantial compositional overlap (Fig. 5-5). Although SrO, SiO_2, NaO, LREE, and F contents can be used to discriminate some samples (e.g., Fig. 5-5; Table 2), different samples of the same unit (samples WESK-5 and WESK-6 from Wesselton W2; and WESK-8 and WESK-9 from Wesselton W3) only show minor compositional overlap (Fig. 5-5). Therefore, it is unlikely that apatite compositions alone can be used to reliably discriminate different kimberlite units in the same pipe or cluster. On the other hand, the SrO contents of apatite may be useful in discriminating some individual sill/dyke complexes (Fig. 5-5).

Discussion

In the following sections, we first evaluate the crystallisation sequence of late-stage groundmass phases. We then use the apatite compositions to assess the late-stage melt evolution of the Kimberley kimberlites. Following this, we discuss the relationship between melt evolution and the emplacement modes of coherent kimberlite. Finally, we compare the composition of apatite in the Kimberley kimberlites with those from other kimberlites worldwide, and with apatite from petrographically ‘similar’ rock types (i.e., orangeites, lamproites, carbonatites, and aillikites).

Apatite crystallisation in the Kimberley kimberlites

In the studied samples the earliest textural generation of apatite to crystallise were the cores of euhedral groundmass grains that also occur as inclusions in magmatic olivine rinds and mica (e.g., Fig. 5-3b; Supp. Fig. S5, S17; and Fig. 3C of Soltys et al. 2018a). Evidence for the co-precipitation of apatite and late-stage olivine in at least some kimberlites elsewhere comes from the presence of apatite inclusions in the outermost olivine zones (e.g., Jos, Somerset Island – Malarkey et al. 2010; Limpeza-18, Brazil – Lim et al. 2018). It has been argued, based on Mg-enrichment (i.e., Mg# >94) and O-isotope compositions (i.e., deviation from mantle values at Koala, Canada), that these late olivine rinds crystallised after magma emplacement into the upper crust (Bussweiler et al. 2015; Fedortchouk and Canil 2004; Giuliani 2018; Giuliani et al. 2019; Lim et al. 2018; Pilbeam et al, 2013; Shaikh et al. 2018; Soltys et al. 2018a). Assuming that olivine rinds and apatite co-precipitate, this implies that the onset of apatite crystallisation also occurred during or after magma emplacement into the upper crust. On the other hand, poikilitic apatite with chadacrysts of spinel, perovskite, and monticellite indicates that apatite continued to crystallise after the cessation of olivine rind crystallisation, because monticellite only began to crystallise after the formation of olivine rinds (Bussweiler et al. 2015; Soltys et al. 2018a, submitted). The occurrence of intergrowths of groundmass mica and apatite rims and straight equilibrium contacts between these phases (Fig. 5-3a), indicate that apatite and mica co-precipitated during the later stages of kimberlite crystallisation.

The occurrence of apatite (II) grains in carbonate-serpentine segregations (e.g., Fig. 5-3a; Supp. Fig. S4; S17; S20; S21) suggests that apatite crystallisation persisted until the final stages of kimberlite consolidation. It is unclear whether crystallisation of this apatite was

continuous, or if there was a hiatus in the crystallisation sequence. The protracted crystallisation of apatite, i.e., beginning from pristine mantle-derived melts during olivine rind crystallisation and extending to precipitation from deuteric or hydrothermal fluids, which form carbonate-serpentine segregations, is consistent with the large variations in Sr-isotope compositions from magmatic to crustal values recorded in apatite from the Jos kimberlite (Somerset Island; Malarkey et al. 2010). Finally, apatite cores in some Canadian kimberlites (Koala and Grizzly), but notably not others (Leslie, Panda, Misery, Beartooth, and Snap Lake), were interpreted as crustal xenocrysts based on resorption features as well as fractionated and flat REE patterns, respectively (Milligan et al., 2017). In the studied Kimberley samples, apatite cores commonly host inclusions of monticellite, a typical magmatic phase. Therefore, we do not believe xenocrystic cores are present (or at least common) in the Kimberley kimberlites.

Melt evolution of the Kimberley kimberlites – the apatite perspective

Apatite saturation in silicate magmas is largely dependent on temperature and melt composition, specifically P and Si concentrations (e.g., Piccoli and Candela, 2002; Tollari et al. 2008; Watson, 1980). In kimberlites, apatite is likely to crystallise after extensive fractional crystallisation of phases that do not readily accommodate phosphorus (i.e., olivine, spinel, ilmenite, perovskite), combined with a decrease in temperature probably resulting from emplacement into the upper crust.

The late stage SiO_2 enrichment of apatite in dyke/sill kimberlites (Table 2; Fig. 5-5) may be partially explained by the lack of extensive mica and monticellite crystallisation (see Table 1). Late-stage Si-enrichment of residual kimberlite melts, particularly in evolved dykes and sills, is indicated by the occurrence of primary quartz in late-stage segregations of the Benfontein sills (Dawson and Hawthorne 1973).

In the apatite structure SiO_4^{4-} replaces PO_4^{3-} (e.g., Fig. 5-6a) but requires charge balance, usually by one of the following coupled substitutions:(1) $REE^{3+} + SiO_4^{4-} \Leftrightarrow Ca^{2+} + PO_4^{3-}$; (2) $SO_4^{2-} + SiO_4^{4-} \Leftrightarrow 2\,PO_4^{3-}$; and/or (3) $SiO_4^{4-} + CO_3^{2-} \Leftrightarrow 2\,PO_4^{3-}$ (Pan and Fleet, 2002; Piccoli and Candela, 2002; and references therein). We note here that other substitutions mechanisms involving SiO_4^{4-} exsisit (e.g., $Th^{3+} + SiO_4^{4-} \Leftrightarrow Ca^{2+} + PO_4^{3-}$), however only those listed above are considered likely to account for the elevated Si concentrations of the measured apatite grains. Substitutions mechanisms (1) and (2) alone are unable to explain the elevated SiO_2 concentrations of the measured apatite grains, because the Si/(S + REE) ratio varies between 5:1 and 10:1 in the studied samples (expressed as a.p.f.u; Fig. 5-6). This suggests that Si may also be incorporated by substitution mechanism (3), which has been demonstrated to occur in carbonatitic apatite (e.g., Sommerauer and Katz-Lehnert, 1985). The operation of substitution mechanism (3) in kimberlitic apatite is consistent with the CO_2 rich nature of kimberlite magmas (e.g., le Roex et al. 2003; Kjarsgaard et al. 2009; Kopylova et al. 2007; Price et al. 2000; Soltys et al. 2018b).

The Sr content of apatite in igneous rocks usually mirrors the bulk rock Sr content, and therefore has been used as a proxy for the degree of magma fractionation (Belousova et al. 2002; Piccoli and Candela, 2002). If fractionation controls the Sr content of the studied grains, then Sr-poor apatite in dyke/sill kimberlites could be explained by fractional crystallisation of earlier apatite and perovskite. However, the modal abundance of apatite and perovskite in the current samples show no systematic variation with the emplacement mode. In addition, there are no variations in the composition of groundmass carbonate (which crystallise after apatite) between root-zone and dyke/sill kimberlites in the Kimberley area (Castillo-Oliver et al. 2018). Therefore, below we employ Sr partition coefficients (D_{Sr}) between apatite and various melt and fluid compositions, which combined with constraints from bulk-rock measurements help elucidate the nature of the medium from which apatite crystallised.

The D_{Sr} values between apatite and carbonate or silicate melt compositions are similar, being reasonably close to or slightly above unity (i.e., carbonate melt = 0.7-2.4 – Klemme and Dalpé, 2003; mafic silicate melt = 1.1-1.6 – Watson and Green, 1981; Prowatke and Klemme, 2006). These apatite-melt D_{Sr} values show no systematic variations with temperature or pressure (Prowatke and Klemme, 2006; Watson and Green, 1981). In contrast the D_{Sr} values between apatite and H_2O-rich fluid are substantially higher (i.e., 17.5-27.8 – Ayers and Watson, 1993). Constraints on kimberlite melt Sr contents are derived from bulk analysis of the Kimberley kimberlites, which contain 0.04-0.27 wt.% SrO ($\bar{x}$ = 0.15 ± 0.05 wt.% – le Roex et al. 2003). The removal of 25% olivine xenocrysts would increase the average SrO content of the melt to ~0.2 wt.%. Similar SrO contents of kimberlite melts from the Kimberley area are calculated using perovskite compositions (~0.3 wt.% SrO – Ogilvie-Harris et al. 2009) and perovskite-kimberlite partition coefficients (i.e., D_{Sr} = 1.1-1.3 – Beyer et al., 2013; Chakhmouradian et al. 2013), with no variation between root zone and volcanoclastic kimberlites. Assuming that Sr is concentrated further in late-stage melts, which crystallise the groundmass corresponding to ~50% of the kimberlite, increases these values up to ~0.4 wt.%. This later value is supposed to approximate Sr contents in the melt at the time of apatite crystallisation.

The SrO contents of apatite in dyke/sill kimberlites show limited variability with an average of 0.43 wt.% (excluding the WWTS, which crystallised from evolved kimberlite melts; White et al., 2012; Soltys et al., submitted). A carbonate melt in equilibrium with this apatite would contain 0.18-0.61 wt.% SrO, whereas a mafic silicate melt would contain 0.27-0.39 wt.% SrO. This range in melt SrO contents (i.e., 0.2-0.6 wt.%) calculated using apatite compositions and the above partition coefficient is consistent with the SrO contents of late-stage kimberlite melts estimated above (i.e., ~0.4 wt.%).

Apatite in root-zone kimberlites has more variable SrO contents averaging 2.8 wt.%, and a maximum value of ~6 wt.% regardless of the petrographic type of apatite (Supp. Table S1). A carbonate melt in equilibrium with the average apatite composition from root zone kimberlites would contain 1.2-4.0 wt.% SrO (or 2.5-8.6 wt.% for the most Sr-rich apatite), and a mafic silicate melt would contain 1.8-2.5 wt.% SrO (or 3.8-5.5 wt.% for the most Sr-rich apatite). This range in melt SrO contents (i.e., 1.2-8.6 wt.%) is substantially higher than the estimated contents in late-stage kimberlite melts (i.e., ~0.4 wt.%), with such high SrO contents appearing unreasonable. The high Sr contents of apatite in root zone kimberlites can be reconciled with kimberlitic compositions if the significantly higher distribution coefficients between apatite and hydrous fluids are employed (Ayers and Watson, 1993). A fluid in equilibrium with the average root zone apatite would contain 0.10-0.16 wt.% SrO, or in the case of the most Sr-rich apatite, 0.22-0.34 wt.% SrO. While there are no constraints on Sr partitioning between kimberlite or similar melts and exsolved H_2O (+ CO_2) fluids, we note that these values are much closer to the estimated late-stage kimberlite composition (i.e., ~0.4 wt.% SrO). In summary, consideration of D_{Sr} values indicates that the low Sr contents of apatite from dyke/sill kimberlites can be explained by apatite crystallisation directly from a kimberlite melt. However, the Sr contents of apatite from root zone kimberlites are more consistent with apatite crystallisation from, or overprinting by, hydrous fluids of likely deuteric or hydrothermal origin.

Light rare earth element contents in the measured apatite grains are generally below detection limits or low (i.e., La + Ce <0.8 wt.%), and probably reflect REE depletion of the melt following perovskite crystallisation (e.g., Mitchell 1986). The slightly higher ∑LREE contents in apatite from some dykes/sills (e.g., Fig. 5-5b) could also be explained by late Si enrichment of these residual kimberlite melts (e.g., see above – Dawson and Hawthorne 1973),

because REE distribution coefficients between apatite and carbonate-rich melt are positively correlated with melt SiO_2 contents (Hammouda et al. 2010; Klemme and Dalpé 2003).

Late Na-rich apatite rims in sample BHK-3 of the Kimberley mine (Supp. Fig. S20) are consistent with Na enrichment of residual kimberlite melts/fluids following the crystallisation of most groundmass phases. Similar Na-enrichment is also recorded in late perovskite rims (Lac de Gras – Chakhmouradian and Mitchell 2001), as well as melt inclusions in perovskite, apatite, and monticellite (e.g., Kamenetsky et al. 2013; Giuliani et al. 2017), and secondary fluid inclusions in olivine from kimberlites worldwide (e.g., Giuliani et al. 2017; Kamenetsky et al. 2004, 2014 and references therein).

Links between groundmass mineralogy and emplacement mechanisms

Carbonates

Calcite is the most abundant carbonate mineral in the majority of kimberlites worldwide, although minor (and in some instances abundant) dolomite occurs in the groundmass of a number of kimberlites, such as the De Beers Dyke, Benfontein Sills, Bultfontein dyke (BK-1) – Kimberley (Dawson and Hawthorne 1973; Donaldson and Reid, 1982; Exley and Jones, 1983; Giuliani et al. 2017; Soltys et al. 2018a; This study); Wemindji Sills, Canada (Zurevinski and Mitchell 2004); Majuagaa Dyke, Greenland (Nielsen and Sand, 2008); various dykes in the Lac de Gas (LDG) field (i.e., Rattler, Rat, Anaconda), Canada (Armstrong et al. 2004); Igwisi Hills lava, Tanzania (Willcox et al. 2015); and Snap Lake Dyke, Canada (Kopylova et al. 2010). Most of these examples represent dykes or sills and to the best of our knowledge, the only root zone kimberlite that contains dolomite is the hypabyssal phase (P7) of the Koala pipe, LDG (Lim et al. 2018). However, this kimberlite is somewhat unusual, as the oxygen isotope compositions of olivine rinds from this kimberlite unit extend above the mantle range (unlike

other kimberlites globally), likely reflecting crustal contamination (Giuliani et al. 2019). Based on textural evidence (i.e., intergrowths with calcite) and Sr-isotope compositions (e.g., Exley and Jones, 1983), dolomite appears to have a magmatic origin, crystallising with or after calcite (e.g., Armstrong et al. 2004; Castillo-Oliver et al. 2018; Soltys et al. 2018a; Wilson et al. 2007).

Armstrong et al. (2004) found that dolomite-bearing kimberlites from the LDG field define the low H_2O/CO_2 end of the whole-rock compositional spectrum for these kimberlites (i.e., $H_2O/(H_2O+CO_2) < 0.35$). This is similar to the low $H_2O/(H_2O+CO_2)$ ratio of a dolomite-bearing sample from a Bultfontein dyke (i.e., 0.25 – Soltys et al. 2018b). Dykes and sills from the Kimberley kimberlites have a higher carbonate/serpentine ratio than root-zone kimberlites (e.g., Supp. Figs. S1-S17; Table 1), consistent with their bulk CO_2 enrichment (le Roex et al. 2003). Similar observations regarding carbonate/serpentine ratios were made by Kopylova et al. (2016) when comparing dyke and root-zone samples from the Udachnaya-East kimberlite. Finally, Nowicki et al., (2008) noted that pipe-infill coherent kimberlites from the Ekati mine (Lac de Gras; Canada) are relatively depleted in CO_2 and enriched in SiO_2 compared to kimberlite dykes, which favoured an interpretation of the pipe-filling coherent kimberlites as the products of mild pyroclastic activity.

Mica, monticellite and pleonaste

Dyke and sill kimberlites from Kimberley generally contain a lower modal abundance of mica and monticellite compared to root-zone kimberlites (Table 1). In addition, pleonaste only occurs in carbonate-rich dykes/sills in the Kimberley area (e.g., Benfontein, WESK-3A – Supp. Fig. S19; Abersteiner et al. 2019). These features can also be explained by variations in melt/fluid volatile ratios and contents. The higher melt CO_2/H_2O ratio in dykes and sills favour the crystallisation of calcite and dolomite, which incorporate Mg and Ca, and may limit both mica and monticellite crystallisation. In addition, lower H_2O contents suppress mica crystallisation,

and favour pleonaste preservation (Fedortchouk, 2015; Pasteris 1980). This interpretation is further supported by substantially higher concentrations of late crystallised barite in dyke/sill kimberlites as a function of suppressed kinoshitalite mica crystallisation (e.g., De Beers dyke, Benfontein – see also Soltys et al. 2018a).

Monticellite in dyke/sill kimberlites appears to be less stable than olivine during deuteric alteration by CO_2-rich fluids, and is commonly pseudomorphed by carbonates, which in turn may be replaced by serpentine during later hydrothermal alteration (see also Kopylova et al. 2010; Giuliani et al. 2017; Soltys et al. 2018a). The relative instability of monticellite compared to olivine is consistent with experimental data in the CaO-MgO-SiO_2[CMS]-CO_2-H_2O system at 2 Kbar, where forsterite is stable below ~1000 °C, but monticellite unstable (e.g., Otto and Wyllie, 1993). Similar correlations between emplacement style and the primary and alteration mineralogy have been observed in other kimberlite occurrences. For example, in samples studied by Armstrong et al. (2004) (LDG, Canada) serpentine and mica is generally more abundant in dykes/sills, and monticellite is generally only fresh in pipe fill CK (see their Table 1). These lines of evidence indicate that the magmas parental to kimberlite dykes and sills are enriched in CO_2 and/or have higher CO_2/H_2O ratios than those parental to root zone kimberlites.

Magma CO_2-H_2O contents and emplacement mechanism

The correlation between volatile ratios and contents and the emplacement mode of coherent kimberlites implies that either the magma composition controls the emplacement style, or *vice versa*.

Variations in magma volatile compositions have been used to explain the petrogenetic difference between coherent and pyroclastic kimberlites (Moussallam et al. 2016; Skinner and Marsh, 2004). Theoretical and experimental data suggest that kimberlite magmas with higher

H_2O (and SiO_2) contents reach the point of catastrophic volatile release and magma fragmentation at relatively greater depths (Moussallam et al. 2016; Skinner and Marsh, 2004), resulting in pyroclastic kimberlites. However, it is unclear if this interpretation can be extended to root-zone coherent kimberlites, which are commonly assumed to be shallow intrusive bodies (e.g., Clement, 1982; Field and Scott Smith, 1999; Scott Smith et al. 2013; Skinner and Marsh, 2004). An alternative model for the origin of root-zone coherent kimberlites entails formation by intense welding of pyroclastic material based on gradational contacts with pyroclastic rocks and space-filling geometries rather than discordant intrusive relationships (Brown et al. 2008; Buse et al. 2010; Sparks, 2013; Sparks et al. 2006). The higher H_2O contents and lower CO_2/H_2O ratios of the magmas parental to root zone kimberlites inferred in this study lends support to such model, i.e. a pyroclastic origin of root-zone coherent kimberlites. In addition, the overprinting of root zone CK by H_2O-CO_2 rich fluids, which is not observed in dyke/sill CK, may reflect a relatively higher porosity of root zone CK deposits, seemingly consistent with welding of pyroclastic material (e.g., Buse et al., 2010).

In turn, if volatile (CO_2, H_2O) contents and ratios control the mechanism of magma emplacement, then one would expect the melts parental to dyke/sill and root-zone kimberlites to have different compositions. However, the compositions and evolutionary trends of liquidus olivine rims as well as early TiMAC-MUM spinel from dyke/sill and root zone kimberlites are indistinguishable (Fig. 5-7). This implies that dyke/sill and root zone kimberlites in the Kimberley area share a common primitive melt composition. This includes volatile contents, because CO_2 concentrations influence olivine-melt Fe-Mg distribution coefficients (K_D). Similarly Tovey et al. (2020) reported indistinguishable olivine and spinel compositions in hypabyssal and pyroclastic rocks from the Diavik mine (Lac de Gras, Canada) and concluded that primitive melt composition had no influence on emplacement style.

Olivine, spinel, and Mg-ilmenite are considered to have crystallised before emplacement into the upper crust (e.g., Arndt et al. 2010; Giuliani 2018; Lim et al. 2018; Soltys et al. submitted), whereas apatite likely formed during or after emplacement. Therefore, the process(es) that caused the observed compositional divergence must have occurred during the later stages of ascent and/or coincident with emplacement into the upper crust. Crustal assimilation has the potential to increase the Si content of the melt, in turn lowering the CO_2 solubility (e.g., Brooker et al. 2011; Russell et al. 2012; Moussallam et al. 2016), which might lead to (potentially explosive) exsolution of a CO_2-rich phase. However, indistinguishable Sr-isotope compositions of carbonates (i.e., groundmass and phenocrysts) in dyke/sill and root zone kimberlites from the Kimberley cluster, including samples studied here (Castillo-Oliver et al. 2018), suggests limited, if any, contribution from assimilated crustal material to the late petrogenesis of the Kimberley kimberlites. Likewise, the oxygen isotope composition of olivine rinds (crystallised on or after emplacement – Lim et al. 2018; Soltys et al. submitted) in dyke and root zone kimberlites from Kimberley preserve mantle values, with no indication of crustal assimilation (Giuliani et al. 2019).

Alternatively, volatile ratios and contents might have been controlled by the emplacement style and not *vice versa*. An obvious way to change the volatile composition of the melt is by exsolution of volatile components. For instance, surface breakthrough controlled by external factors (e.g., the local stress regime and local geology) reduces the confining pressure and results in a decrease in the volatile solubility, potentially leading to exsolution of a CO_2-rich fluid phase (e.g., Moussallam et al. 2016 and references therein). This may explain the formation of root-zone kimberlites (regardless of an intrusive or extrusive origin) and may be extended to pyroclastic kimberlites (Tovey et al., 2020). When surface breakthrough does not occur, e.g., due to the physical barrier represented by Karoo dolerite sills at Benfontein and the Wesselton water tunnels (Abersteiner et al. 2019; Dawson and Hawthorne 1973; Field and

Scott Smith 1999; Shee et al. 1994), more CO_2 is retained and kimberlite magmas may emplace as dyke/sill complexes.

Apatite in other kimberlites and petrographically 'similar' rock types

Here we compare the compositions of Kimberley apatite from this study with apatite from other kimberlites. We then compare the pooled data for kimberlitic apatite with apatite in petrographically 'similar' rock types (i.e., lamproites, carbonatites, and aillikites) to determine whether apatite major element compositions can aid in the discrimination of these rock types.

Apatite in other kimberlites

Apatite from most kimberlites plot within the compositional fields defined by the Kimberley kimberlites (Fig. 5-8a, c, e). Apatite in samples from kimberlite dykes/sills, e.g., Jos dyke (Somerset Island, Canada – Malarkey et al., 2010), Siddanpalli dykes (India – Chalapathi Rao et al., 2010), and some of the Kuusamo kimberlites, Finland (i.e., Kalettomanpuro and Kasma 47 – Dalton et al., 2020) plot within the field of the Kimberley kimberlite dykes/sills (Fig. 5-8a). In contrast, other kimberlites from the Kuusamo field (i.e., Kattaisenvaara and Kasma 45 – Dalton et al., 2020) have compositions which overlap the low-Sr end of the root zone field defined in this study (Fig. 5-8a). Apatite in hypabyssal samples (of uncertain emplacement mode) from the Renard kimberlites (Canada – Birkett et al. 2004) span both the root zone and dyke/sill fields (Fig. 5-8a). Apatite in samples of the Wajilitage kimberlites (NW China – Cheng et al. 2014) show little compositional variation and plot at the intersection of the dyke/sill and root zone fields (Fig. 5-8a).

Although the above examples all show apatite compositions consistent with those reported here, there are some exceptions. Chakhmourdian et al. (2002) reported exceptionally SrO-rich apatite (i.e., up to ~40 wt.%) in hypabyssal samples of the Lac de Gras kimberlites. This apatite has an unusual morphology (i.e., spherulites) and occurs in association with atypical kimberlite minerals (i.e., tetraferriphlogopite and suolunite [$Ca_2Si_2O_5(OH)_2•(H_2O)$]), which suggest interaction with groundwaters, and/or contamination by crustal material.

Apatite from the Wajrakarur (Shaikh et al. 2018) and Arkhangelsk 'kimberlites' (Beard et al. 2004) are enriched in SrO compared to most other kimberlites (Fig. 5-8a), and are similar to apatite from orangeites or olivine lamproites (see below). This is consistent with the hybrid nature of the Wajrakarur and Arkhangelsk fields which also contains olivine lamproites, ultramafic lamprophyres, and/or transitional rock types that are broadly coeval to apparently archetypal kimberlites.

To conclude, although it was previously assumed that kimberlitic apatite is poor in SrO (i.e., <1 wt.% – Mitchell 1986), recent studies (including the current data) indicate that Sr-poor apatite is generally limited to dyke/sill kimberlites. The compositional fields identified here for the different emplacement modes of coherent kimberlite appear to be applicable to the kimberlites for which data are available. However, Sr-enrichment may occur in response to crystallisation from, or overprinting by kimberlitic/deuteric fluids (root-zone kimberlites), or hydrothermal fluids (Chakhmourdian et al. 2002). On the other hand, Sr-rich apatite from the Wajrakarur and Arkhangelsk kimberlites may reflect the more transitional nature of these rocks.

Apatite in carbonatites, orangeites/lamproites, and ultramafic lamprophyres

The composition of apatite in carbonate-rich olivine lamproites (previously known as orangeites) varies with locality, and many grains are zoned to Sr-LREE rich rims (Mitchell 1995). Some primitive orangeites contain apatite with similar Sr and Si contents to those in

kimberlites (Fig. 5-8a), although kimberlitic apatite generally contains less LREE, Sr, F, and to some extent S, but more Si (Fig. 5-8; Supp. Fig. S24). In addition, apatite in some carbonate-poor lamproites (e.g., those from Western Australia – Edgar, 1989) contain elevated TiO_2 contents (up to 0.8 wt.%), whereas TiO_2 contents of kimberlitic apatite are usually <0.02 wt.%. These differences in apatite composition reflect differences in bulk compositions, whereby lamproites are generally enriched in SrO, SiO_2, and F compared to kimberlites (e.g., Mitchell 1995 and references therein).

The compositional data available for apatite in aillikites is limited, with the only data available for Dyke 15 (Kuusamo, Finland; Dalton et al. 2020). These apatite compositions plot within the kimberlite field with respect to all major elements (Fig. 5-8; Supp. Fig. S24). The compositional similarities between apatite in kimberlites and aillikites may indicate similar melt compositions during late crystallisation of these magmas. Indeed, kimberlites and aillikites both evolve towards residual carbonate-rich compositions by fractional crystallisation (e.g., Dawson and Hawthorne 1973; Tappe et al. 2009, 2017).

The composition of kimberlitic apatite is broadly similar to that in carbonatites with respect to their SiO_2 and SrO, contents (Fig. 5-8a). However, carbonatitic apatites generally contains higher LREE, S, Cl, and F, but lower Fe contents compared to those from kimberlites (Fig. 5-8; Supp. Fig. S19). In summary, apatite may prove to be an addition discriminatory tool for some kimberlites, lamproites/orangeites, and carbonatites when used in combination with existing criteria based on petrography, and mica/spinel compositions.

Conclusions

We observe a correlation between emplacement mode, mineralogy, petrography, and apatite compositions in samples of coherent kimberlites from the Kimberley cluster. Dykes and sills (may) contain dolomite and calcite phenocrysts, are generally enriched in mesostasis carbonates over serpentine and show a lower modal abundance of monticellite and mica. In addition, the alteration style differs, in dykes and sills monticellite is commonly replaced by carbonates, whereas olivine and pleonaste tend to be more stable. The opposite features are typical of root-zone kimberlites.

Apatite is a late-crystallising (i.e., after emplacement into the upper crust) phase in the kimberlites and other kimberlites worldwide. Apatite major-element compositions can effectively discriminate the two emplacement modes of coherent kimberlite, i.e., dykes/sills (low Sr, high and variable Si) from root-zone kimberlites (high and variable Sr, low Si). Low SrO contents in apatite from samples of dykes and sills is attributed to crystallisation from a melt, whereas the higher SrO contents of apatite from root-zone kimberlites suggests crystallisation from, or overprinting by a (H_2O-CO_2-rich) fluid. Silica enrichment of apatite from dykes/sills is interpreted to stem from the coupled substitution of CO_3^{2-} and SiO_4^{4} for PO_4^{3}, which may reflect higher CO_2 contents in melts that form dykes and sills, and/or higher Si contents due to the suppression of mica/monticellite crystallisation. Further studies are required to quantitative determine the structural incorporation of carbonate anions into kimberlitic apatite. These features are best explained by different melt/fluid compositions, specifically higher CO_2/H_2O ratios in the magmas that emplace as dykes and sills. These differences are unlikely to stem from variable primitive melt compositions, because the compositions of early crystallised olivine, spinel, and Mg-ilmenite are indistinguishable in dykes/sills and root-zone kimberlites in the Kimberley area. It seems more plausible that external factors control the emplacement mechanism of kimberlite magmas, leading to variable

extents of fluid (largely CO_2) exsolution and, therefore, distinct residual melt/fluid compositions and mineralogical assemblages.

Apatite compositions have the potential to aid in the discrimination of kimberlites from lamproites (higher LREE, Sr, F, and S, lower Si contents) and potentially carbonatites (higher LREE, F, Cl and S, but lower Fe contents). However, kimberlitic apatites overlap those from aillikites, probably due to similar late-stage melt compositions.

ACKNOWLEDGMENTS

We thank Graham Hutchinson for his tireless assistance during SEM and EPMA analysis at the University of Melbourne. We are grateful to Phillip Janney for facilitating access to the John J. Gurney Upper Mantle Room Collection (University of Cape Town), from which samples of the De Beers dyke were loaned. In addition, we thank the De Beers Group and Petra Diamonds for provision of additional samples and for allowing access to the Wesselton mine and Benfontein Farm for sample collection. Jock Robey organised access to various sites in the Kimberley area and supervised sample collection, for which we are exceptional appreciative. We also thank Stephen Sparks for supplying samples of the Wesselton water tunnel sills. AS thanks Angus Fitzpayne, Hayden Dalton, Madeline Tovey, Lynton Jaques, Simon Shee, and Bruce Wyatt for fruitful discussions on kimberlite emplacement. AG acknowledges funding from the Swiss National Science Foundation (Ambizione grant n. PZ00P2_180126/1).

Figures

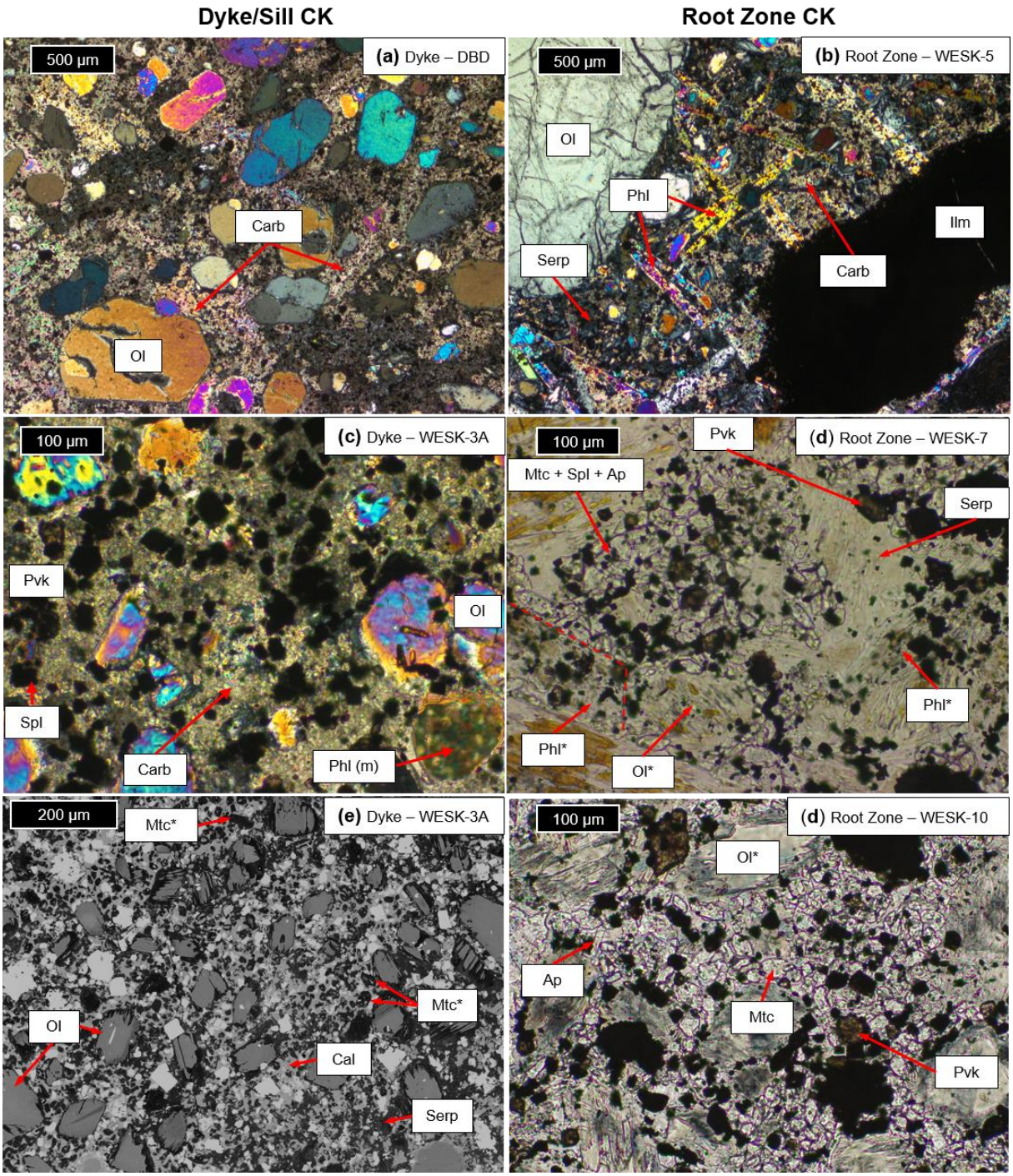

Figure 5-1. Representative images showing the different petrographic features of dyke/sill kimberlites (a, c, e) and root zone kimberlites (b, d, e). Panels (a-c) are cross polarised transmitted light photomicrographs, panel (e) is a plane-polarised transmitted light photomicrograph, and panels (e, f) are back-scattered electron images. Carb = carbonate; Serp = serpentine; Ol = olivine; Phl = phlogopite-kinoshitalite mica; Ilm = ilmenite; Phl (m) = phlogopite macrocryst; Mtc = monticellite; Spl = spinel; Pvk = perovskite; * = partially replaced – mica by serpentine/chlorite, olivine by serpentine, and monticellite by carbonates/serpentine.

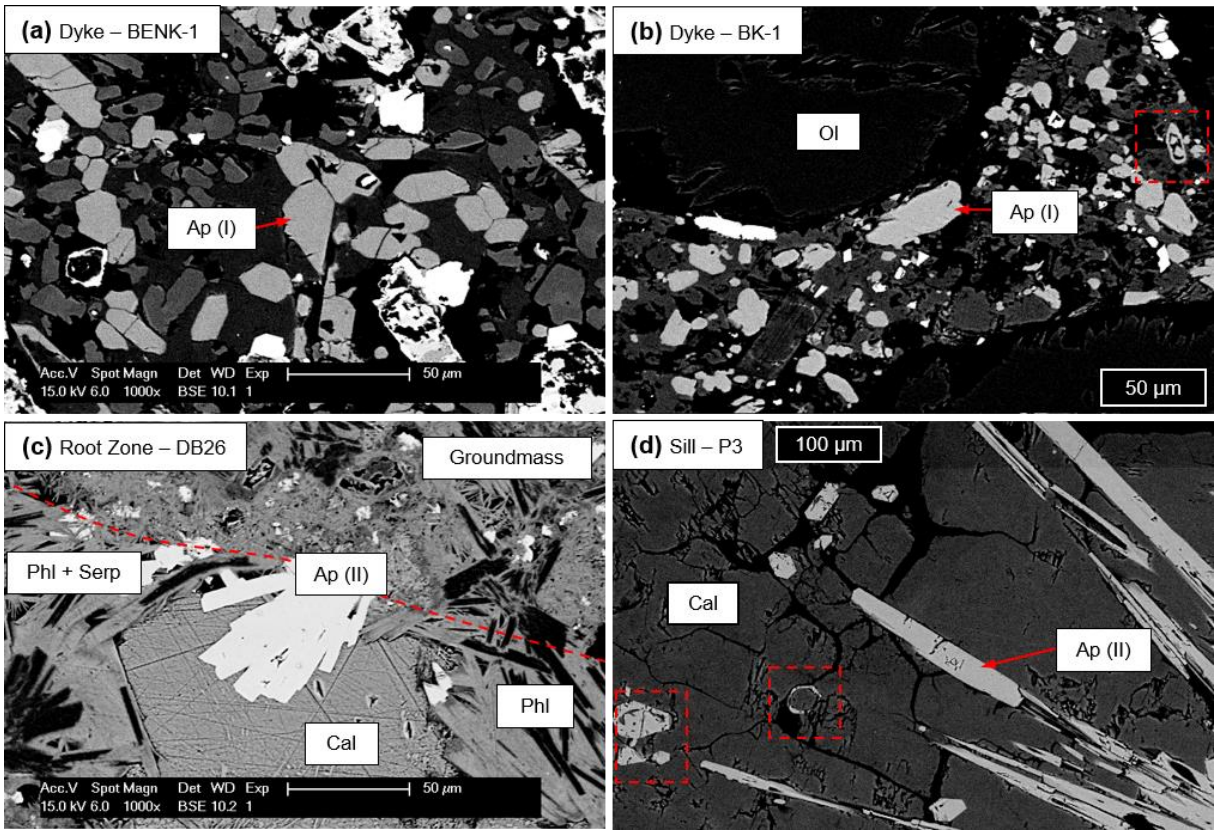

Figure 5-2. Back-scattered electron images showing the two textural types of apatite (Ap) in the Kimberley kimberlites. (a, b) textural generation (I): euhedral groundmass grains; (c, d) textural generation (II): radiating acicular aggregates in late-stage segregations. Note the occurrence of apatite hopper crystals in panel (b, d) [highlighted by red dashed boxes]. In panel (c) the dashed red line indicates the boundary between a carbonate-serpentine segregation (with apatite and phlogopite (Phl)) and the kimberlite groundmass. Cal = calcite, Phl = phlogopite, Serp = serpentine.

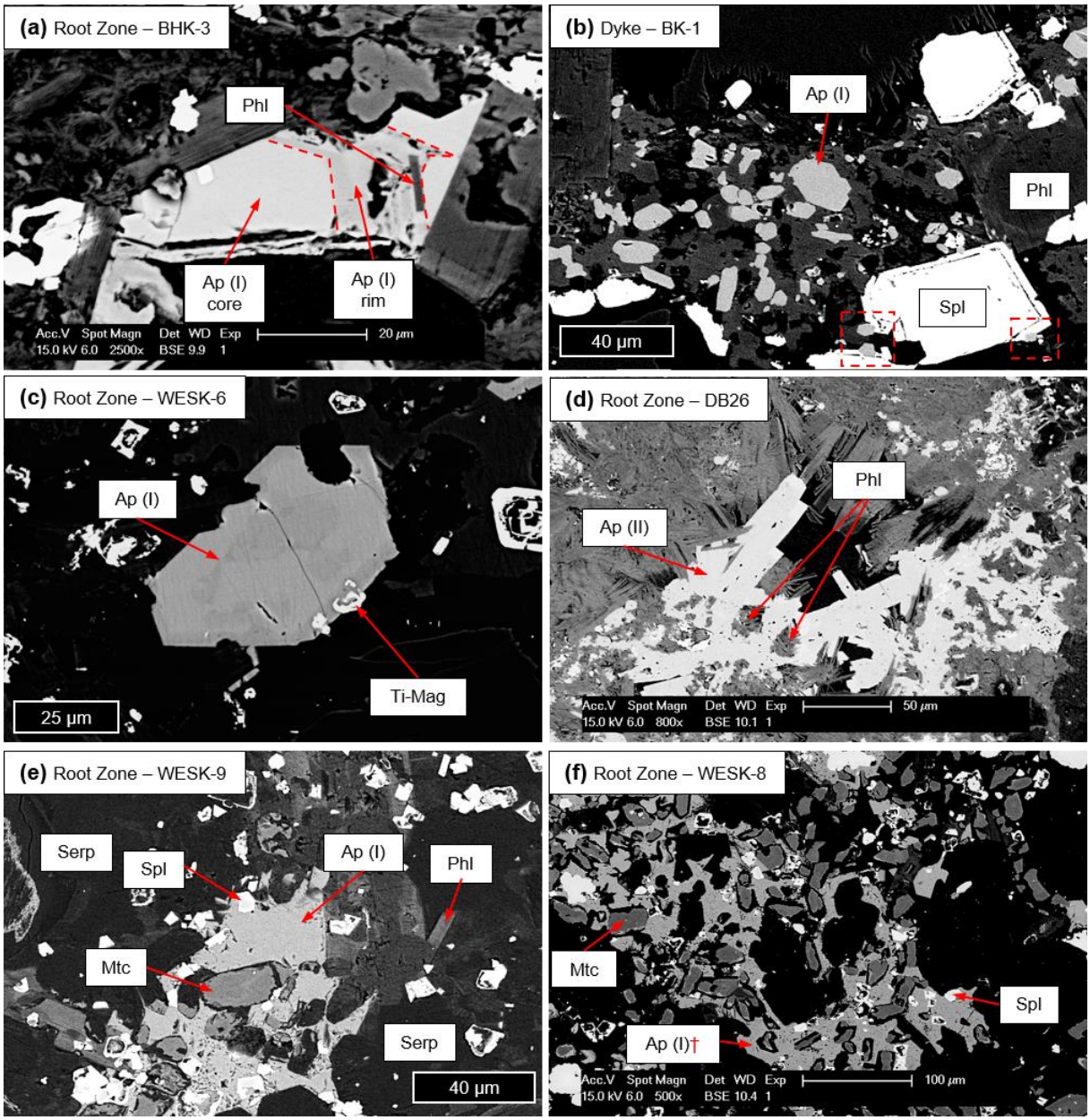

Figure 5-3. Back-scattered electron images showing the textural relationships between apatite (Ap) and other groundmass phases in the Kimberley kimberlites. All apatite grains correspond to textural type (I), except those in panel (d). (a) An apatite grain that exhibits straight equilibrium contacts with groundmass mica, with the apatite rim (highlighted by a dashed line) including groundmass mica. (b) Apatite embedded in the magnetite 'reef' of an atoll-textured spinel (Spl) [bottom right, highlighted by dashed red boxes]. (c) An irregularly zoned apatite grain that contains inclusions of Ti-bearing magnetite (Ti-mag). (d) Apatite in a mica-rich carbonate-serpentine segregation, which contains inclusions of, and is intergrown with phlogopite. (e, f) Poikilitic apatite which contains chadacrysts of monticellite (Mtc) and spinel.

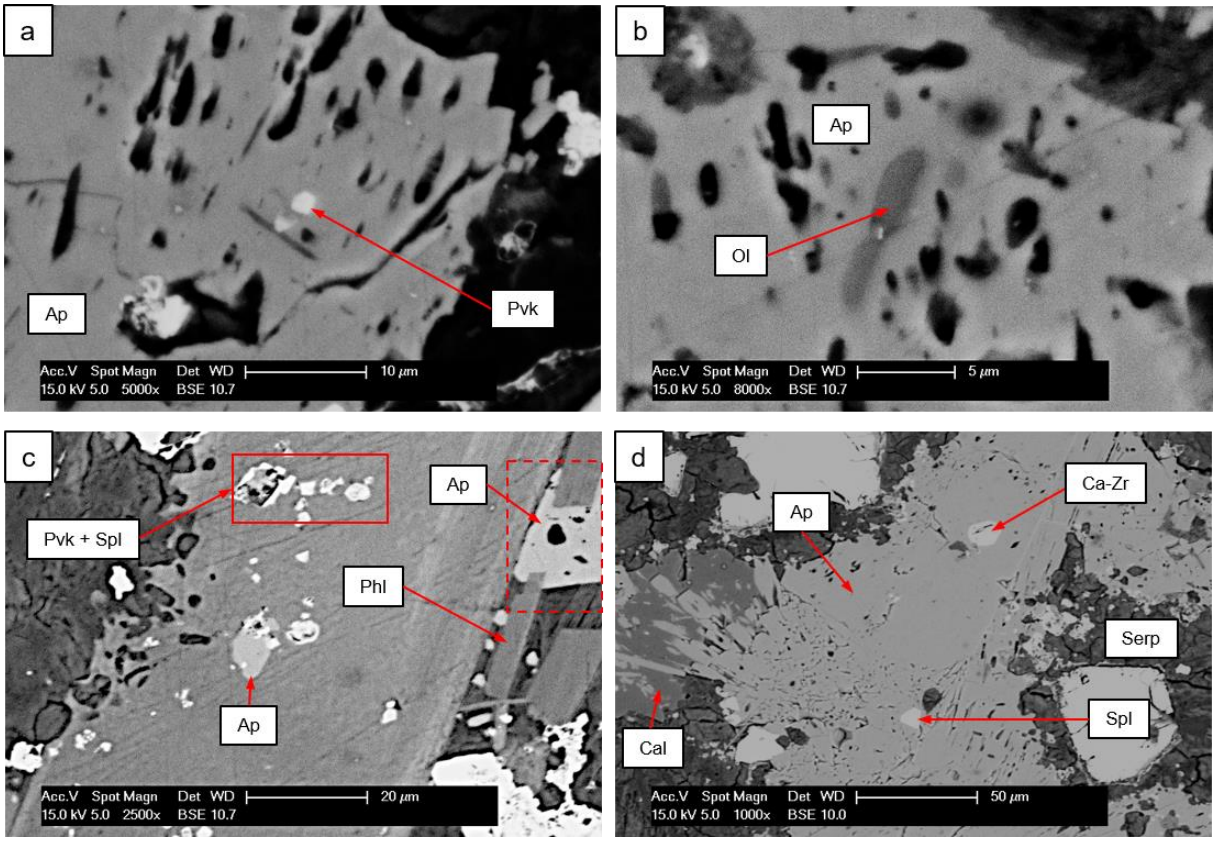

Figure 5-4. Back-scattered electron images showing the textural relationships between apatite (Ap) and other groundmass phases in the Wesselton Water Tunnel sills. (a, b) apatite (I) which contains inclusions of perovskite (Pvk) and olivine (Ol). (c) Groundmass mica with inclusions of spinel (Spl), perovskite (Pvk), and apatite. Note that in this sample groundmass mica is partially overgrown by apatite [highlighted by a dashed red box]. (d) Large apatite grain with inclusions of spinel and an unidentified Ca-Zr phase.

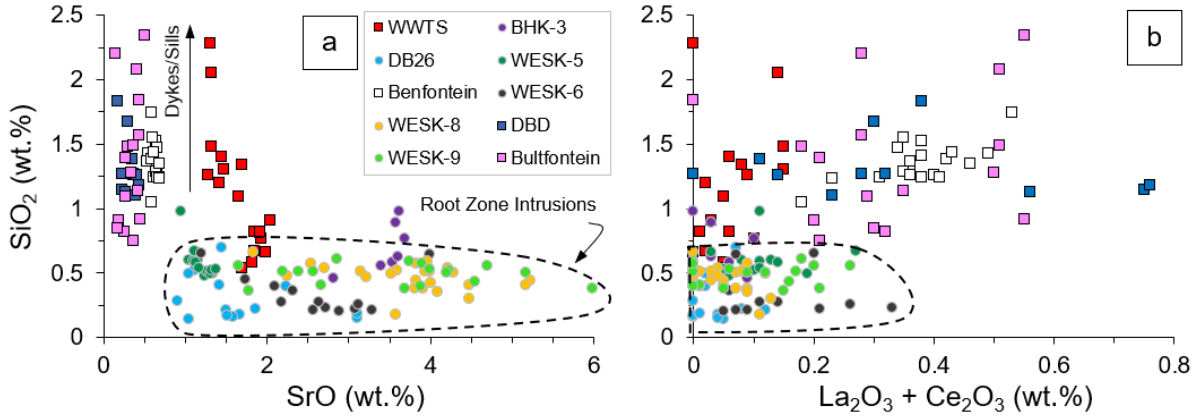

Figure 5-5. SiO2 wt.% vs. (a) SrO wt.%, and (b) La2O3 + Ce2O3 wt.% charts showing the compositions of apatite from the Kimberley kimberlites. Circle symbols represent samples of root zone kimberlites, and square symbols represent samples of dykes and sills.

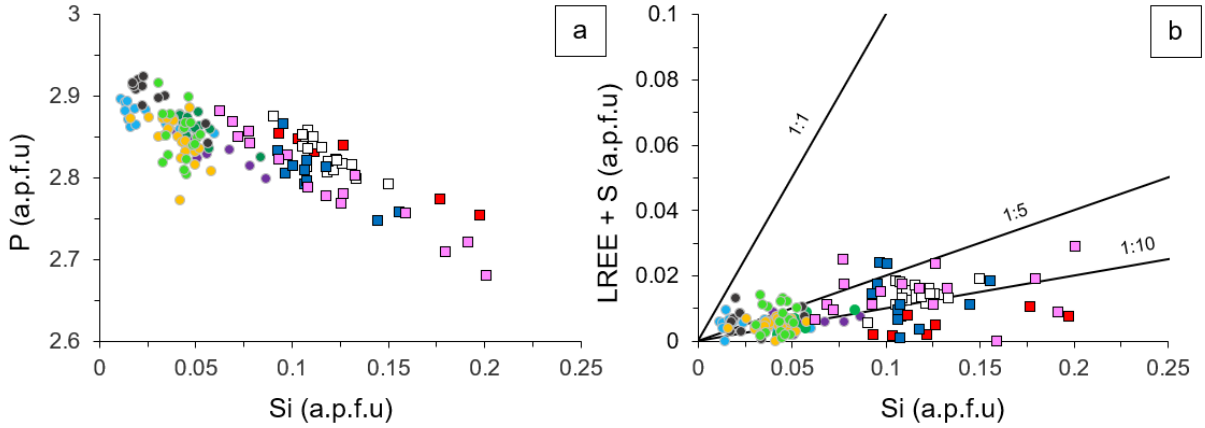

Figure 5-6. (a) P vs. Si (a.p.f.u.), and (b) S + LREE vs. Si (a.p.f.u) charts showing the compositions of apatite from the Kimberley kimberlites examined in this study. Circle symbols represent samples of root zone kimberlites, and square symbols represent samples of dyke/sill kimberlites. The 1:1 line in panel b shows where apatite compositions would plot if they followed substitutions mechanisms (1) and (2) (see text for details).

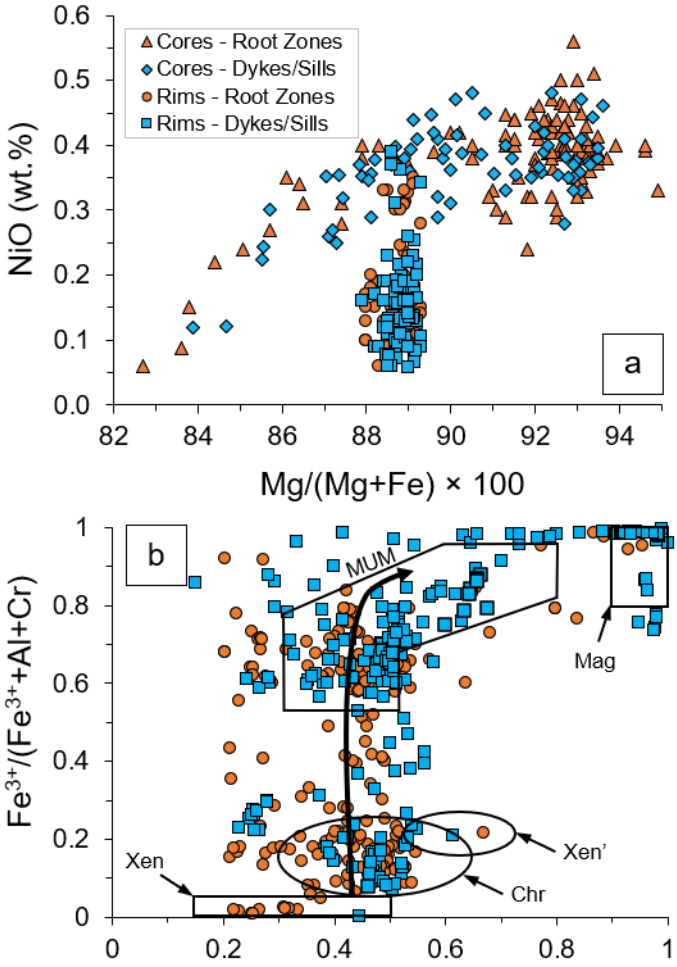

Figure 5-7. (a) NiO (wt.%) vs. Mg# [Mg/(Mg+Fe) × 100] chart showing the composition of olivine in dyke/sill kimberlites (blue diamonds [cores] and squares [rims]) and root zone kimberlites (orange triangles [cores] and circles [rims]) kimberlites from the Kimberley area (Soltys et al. submitted). (b) Fe3+/(Fe3++Al+Cr) vs. Fe2+/(Fe2++Mg) chart showing the compositions of spinel from dyke/sill and root zone kimberlites from the Kimberley area (Boctor and Boyd, 1981; Gaspar, and Wyllie, 1984; Giuliani et al. 2017; McMahon and Haggerty, 1984; Pasteris 1980; Roeder and Schultze, 2008; Shee 1985; Soltys et al. 2018a)

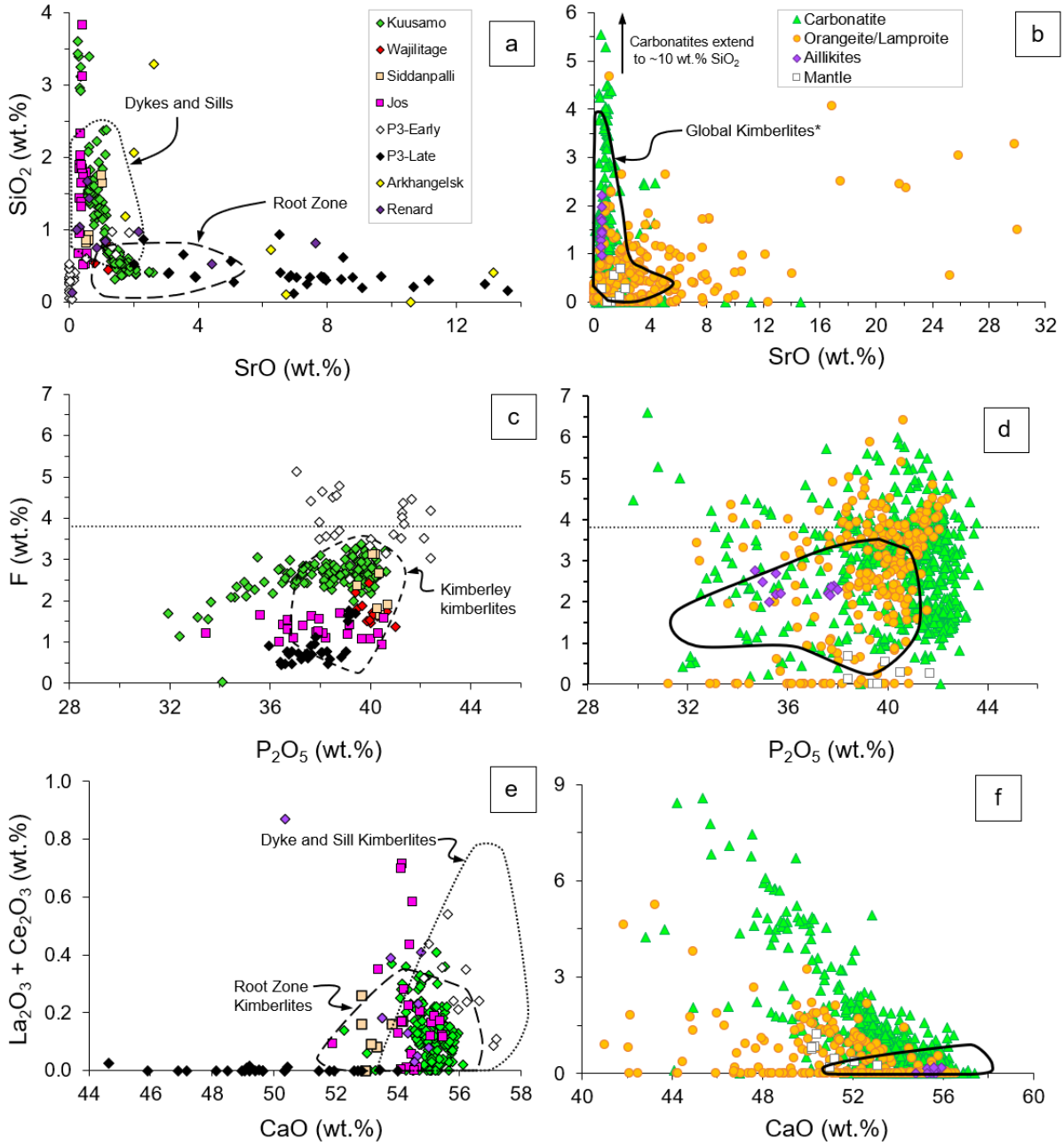

Figure 5-8. (a, b) SiO2 vs. SrO, (c, d) F vs. P2O5, and (e, f) La2O3 + Ce2O3 vs. CaO (wt.%) charts showing the composition of apatite. Panels (a, c, e) show the composition of apatite from the Kimberley kimberlites (this study) compared with apatite from kimberlites worldwide. Panels (b, d, e) show the composition of kimberlitic apatite comparted with apatite in aillikites, carbonatites, orangeites/lamproites, and mantle rocks. In panels (a, c, e) square symbols represent samples from dykes/sills, whereas diamond symbols represent samples of uncertain emplacement morphology. In panels (b, d, e) the field of global kimberlites excludes the samples from Arkhangelsk and Wajrakarur (see main text for details). The compiled literature data is reported in Supp. Table S2.

Tables

Table 5-1. Summarised petrographic features of the studied samples

Locality	Label (unit)	Intrusion	Matrix[1]	Apatite[2]	Monticelite[3]	Groundmass Mica[4]	Dol/Ple	
Kimberley mine	BHK-1	Root Zone**	Serp-rich (Alterted)	Type 1 (N)	**m** - Rep-Serp	m, <100 µm, Rep-Serp	N/N	
	BHK-3	Root Zone**	Serp-Phl-Cal	Type 1 (Y)	M - Rep-Serp (**L**)	M/**M**, ~100 µm, Rep-Chl, (N)	N/N	
De Beers Dyke	DBD	External Dyke	Carb-Serp	Type 1 (Y)	m – Rep-Dol	tr, <10 µm, Fresh	Y/N	
De Beers	DB-26	Root Zone	Serp-Mtc-Phl (Alterted)	Type 2 (Y)	M/**M** - Fresh	M, <250µm, Rep-serp/chl(**L**)	N/N	
	DB-76	Root-Zone	Serp-Cal-Phl	Type 1 (N)	M - Rep-Serp (**L**)	M/**M**, <500µm, Rep-serp (**L**)	N/N	
Wesselton	WESK-1	Internal Dyke	Cal-Serp-Mtc	Type 1 & 2 (N)	M - Rep-Serp	m, <20 µm, Fresh	N/N	
	WESK-3A	Internal Dyke	Cal-Serp-Mtc	Type 1 (N)	m/M - Rep-serp	tr, <20 µm, Fresh	N/Y	
	WESK-5 (W2)	Root Zone	Serp-Phl-Cal	Type 1 (Y)	M – Fresh/Rep-Serp (**L**)	**M,** <2 mm, Fresh	N/N	
	WESK-6 (W2)	Root Zone	Serp-Cal	Type 1 (Y)	M – Rep-Serp	M, <150 µm, Fresh	N/N	
	WESK-7 (W7)	Root Zone	Mtc-Serp	Type 1 (N)	**M** – Fresh	m/M, <500 µm, Rep-Serp/Chl(**L**)	N/N	
	WESK-8 (W3)	Root Zone	Mtc-Serp	Type 1† (Y)	**M** – Fresh	M, 300 µm, Rep-Chl	N/N	
	WESK-9 (W3)	Root Zone	Mtc-Serp	Type 1† (Y)	M - Fresh	M, <1 mm, Rep-Serp/Chl	N/N	
	WESK-10 (W3)	Root Zone	Mtc-Serp	Type 1 (N)	**M** – Fresh	M, <300 µm, Fresh	N/N	
WWTS	P3 (Macro)	Sill	Cal-Ap-Phl-Serp	Type 1 & 2 (Y)	No	**M,** <500 µm, Fresh	N/N	
Benfontein	BENK-1	Sill	Cal-Ox	Type 1 (Y)	M*	tr, <<10µm, Fresh	Y/Y	
Bultontein	BK-1	Dyke	Cal-Serp	Type 1 (Y)	m – Rep-Carb/Serp	M/**M** ~300µm, Fresh	Y/N	
DuToitsPan	DT37	Root Zone	Mtc-Serp	Type 1 (N)	M - Fresh	m, <100 µm, Rep-Serp	N/N	

Mineral abreviations are as follows: Cal = calcite; Dol = Dolomite; Serp = Serpetine; Carb = Carbonate; Phl = Phlogopite-Kinoshitalite; Ox = Oxide minerals; Ap = Apatite; Ple = Pleonaste; and Chl = chlorite.

[1] The major groundmass/mesostasis phases in their relative order of abundance

[2]The textural variety of apatite (see main text for details); (Y/N) denotes whether or not apatite was analysed in the current study

[3]The abundance of monticellite: tr = trace; m = minor; M = moderate; **M** = Major; and alteration style, where Rep = replaced by, and (L) denotes the replacement is localised

[4]The abundance of groundmass mica; its size in the longest dimension; and its alteration style

M* = concentrated by in-situ diffirentiation

**Samples from the Kimberley mine are of uncertain orgin [the mine closed in 1914], but based on textural/mineralogical features and apatite compositions are infered to represent pipe CK

† Development of poikilitic crystal forms

Table 5-2. Average major element composition (wt.%) of groundmass apatite in the studied samples

Sample (*n*)	**BHK-3 *(7)***		**DB26 *(14)***		**WESK-5 *(13)***		**WESK-8 *(24)***		**P3 *(17)***		**BENK *(19)***	
Intrusion Mode	**Root Zone**		**Root Zone**		**Root Zone**		**Root Zone**		**Sill**		**Sill**	
	Avg	**1σ**	**Avg**	**1σ**	**Avg**	**1σ**	**Avg**	**1σ**	**Avg**	**1σ**	**Avg**	**1σ**
SiO_2	0.70	0.18	0.30	0.17	0.60	0.12	0.47	0.10	1.13	0.48	1.36	0.15
Fe_2O_3	0.26	0.07	0.13	0.05	0.21	0.06	0.28	0.07	0.05	0.04	0.16	0.08
MgO	0.12	0.13	0.02	0.02	0.04	0.03	0.03	0.04	0.04	0.05	0.07	0.02
CaO	53.58	0.56	55.75	0.62	56.05	0.38	53.98	0.75	54.62	0.65	55.47	0.41
Na_2O	0.24	0.07	0.13	0.11	0.05	0.02	0.19	0.10	0.06	0.06	0.08	0.02
P_2O_5	38.03	0.45	39.50	0.45	39.50	0.37	38.52	0.56	39.05	0.66	38.91	0.43
SrO	3.46	0.27	1.68	0.67	1.18	0.12	3.73	0.80	1.65	0.26	0.61	0.07
La_2O_3	0.04	0.04	0.02	0.03	0.08	0.05	0.04	0.04	0.04	0.04	0.16	0.05
Ce_2O_3	0.00	0.00	0.02	0.03	0.03	0.03	0.00	0.01	0.02	0.03	0.22	0.06
SO_3	0.06	0.03	0.07	0.03	0.03	0.02	0.05	0.03	0.03	0.03	0.04	0.03
F	2.65	0.34	1.56	0.23	2.55	0.22	2.33	0.22	2.37	0.31	2.01	0.18
Cl	0.00	0.00	0.02	0.04	0.01	0.01	0.01	0.01	0.01	0.01	0.03	0.01
H_2O(c)	0.45	0.16	1.00	0.11	0.54	0.10	0.61	0.10	0.72	0.11	0.78	0.08
O=F	1.11	0.14	0.66	0.09	1.08	0.09	0.98	0.09	0.91	0.10	0.85	0.08
O=Cl	0.00	0.00	0.00	0.01	0.00	0.00	0.00	0.00	0.00	0.00	0.01	0.00
Total	98.58	0.48	99.61	0.71	99.86	0.53	99.32	0.63	99.17	0.48	99.10	0.57
formula (12 oxygens)												
Si	0.06	0.02	0.02	0.01	0.05	0.01	0.04	0.01	0.09	0.04	0.11	0.01
Fe	0.02	0.01	0.01	0.00	0.01	0.00	0.02	0.00	0.00	0.00	0.01	0.01
Mg	0.01	0.02	0.00	0.00	0.01	0.00	0.00	0.00	0.00	0.01	0.01	0.00
Ca	4.85	0.03	4.93	0.02	4.94	0.03	4.85	0.08	4.86	0.03	4.90	0.03
Na	0.04	0.01	0.02	0.02	0.01	0.00	0.03	0.02	0.01	0.01	0.01	0.00
P	2.72	0.02	2.76	0.01	2.75	0.02	2.74	0.02	2.74	0.04	2.72	0.02
Sr	0.17	0.02	0.08	0.03	0.06	0.01	0.18	0.04	0.08	0.01	0.03	0.00

La	0.00	0.00	0.00	0.00	0.00	0.00	0.00	0.00	0.00	0.00	0.00	0.00
Ce	0.00	0.00	0.00	0.00	0.00	0.00	0.00	0.00	0.00	0.00	0.01	0.00
S	0.00	0.00	0.00	0.00	0.00	0.00	0.00	0.00	0.00	0.00	0.00	0.00
F	0.71	0.10	0.41	0.06	0.66	0.06	0.62	0.06	0.62	0.09	0.53	0.05
Cl	0.00	0.00	0.00	0.01	0.00	0.00	0.00	0.00	0.00	0.00	0.00	0.00

Table 2. Continued.

Sample (*n*)	**WESK-6 *(13)***		**DBD *(12)***		**WESK-9 *(18)***		**BK-1 *(16)***	
Intrusion Mode	**Root Zone**		**Dyke**		**Root Zone**		**Feeder Dyke**	
	Avg	**1σ**	**Avg**	**1σ**	**Avg**	**1σ**	**Avg**	**1σ**
SiO_2	0.34	0.15	1.22	0.41	0.49	0.08	1.38	0.51
Fe_2O_3	0.22	0.07	0.21	0.09	0.30	0.11	0.22	0.11
MgO	0.03	0.06	0.22	0.10	0.02	0.02	0.18	0.06
CaO	54.44	0.63	56.70	0.53	53.73	1.04	56.48	0.65
Na_2O	0.03	0.04	0.19	0.09	0.65	0.36	0.21	0.10
P_2O_5	39.76	0.63	39.21	0.79	38.84	0.77	38.76	1.15
SrO	2.60	0.69	0.28	0.12	3.56	1.20	0.33	0.11
La_2O_3	0.08	0.09	0.12	0.16	0.07	0.09	0.19	0.15
Ce_2O_3	0.04	0.06	0.20	0.18	0.03	0.05	0.14	0.10
SO_3	0.04	0.03	0.03	0.04	0.06	0.05	0.07	0.08
F	2.42	0.20	1.87	0.80	2.35	0.58	1.97	0.74
Cl	0.01	0.01	0.10	0.03	0.02	0.03	0.05	0.03
H_2O(c)	0.59	0.10	0.86	0.39	0.61	0.27	0.82	0.35
O=F	1.02	0.08	0.79	0.34	0.99	0.24	0.83	0.31
O=Cl	0.00	0.00	0.02	0.01	0.00	0.01	0.01	0.01
Total	99.63	0.65	100.52	0.81	99.82	0.71	100.10	0.88
formula (12 oxygens)								

Si	0.03	0.01	0.10	0.03	0.04	0.01	0.11	0.04
Fe	0.02	0.00	0.01	0.01	0.02	0.01	0.02	0.01
Mg	0.00	0.01	0.03	0.01	0.00	0.00	0.02	0.01
Ca	4.82	0.04	4.95	0.04	4.80	0.07	4.96	0.07
Na	0.00	0.01	0.03	0.01	0.11	0.06	0.03	0.02
P	2.78	0.02	2.70	0.04	2.74	0.03	2.69	0.06
Sr	0.12	0.04	0.01	0.01	0.17	0.06	0.02	0.01
La	0.00	0.00	0.00	0.00	0.00	0.00	0.01	0.00
Ce	0.00	0.00	0.01	0.01	0.00	0.00	0.00	0.00
S	0.00	0.00	0.00	0.00	0.00	0.00	0.00	0.01
F	0.63	0.06	0.48	0.21	0.62	0.15	0.51	0.19
Cl	0.00	0.00	0.01	0.00	0.00	0.00	0.01	0.00

CHAPTER 6: A NEW APPROACH TO RECONSTRUCTING THE COMPOSITION AND EVOLUTION OF KIMBERLITE MELTS: A CASE STUDY OF THE ARCHETYPAL BULTFONTEIN KIMBERLITE (KIMBERLEY, SOUTH AFRICA)

Ashton Soltys[a*], Andrea Giuliani[a,b], David Phillips[a]

[a] KiDs (Kimberlites and Diamonds), School of Earth Sciences, The University of Melbourne, Parkville, 3010 Victoria, Australia

[b] ARC Centre of Excellence for Core to Crust Fluid Systems and GEMOC, Department of Earth and Planetary Sciences, Macquarie University, North Ryde, 2019 NSW, Australia

Abstract

The compositions of kimberlite melts at depth and upon emplacement in the upper crust remain elusive. This can be attributed to the unquantified effects of multiple processes, such as alteration, assimilation, xenocryst contamination, and fractional crystallisation. The inability to accurately constrain the composition and physical properties of kimberlite melts prevents a comprehensive understanding of their petrogenesis.

To improve constraints on the compositions of kimberlite melts, we have combined modal analysis including the discrimination of xenocrystic from magmatic phases, with mineral chemistry determinations to reconstruct a whole-rock composition. We apply this approach to a sample of 'fresh' macrocrystic hypabyssal kimberlite (sample BK-1) from the Bultfontein mine (Kimberley, South Africa). The accuracy of this whole-rock reconstruction method is validated by the similarity between reconstructed and measured whole-rock compositions. A series of corrections are then applied to account for the effects of post-emplacement serpentinisation, pre-emplacement olivine crystallisation, and the inclusion and assimilation of mantle material. This approach permits discernment of melt compositions at different stages of kimberlite evolution.

The primitive melt parental to the Bultfontein kimberlite is estimated to contain 17.4-19.0 wt.% SiO_2, 20.2-22.8 wt.% MgO, 20.9-21.9 wt.% CaO, 2.1-2.3 wt.% P_2O_5, 1.2-1.4 wt.% TiO_2, 0.9-1.1 wt.% Al_2O_3, and 0.6-0.7 wt.% K_2O, and has a Mg# of 83.4-84.4. Primary volatile contents (i.e., after an attempt to account for volatile loss) are tentatively estimated at ~2.1-2.2 wt.% H_2O and ~22.9-25.4 wt.% CO_2. This composition is deficient in SiO_2, MgO and H_2O, but enriched in CaO and CO_2 compared with most previous estimates of primitive kimberlite melts. We suggest that the primitive melt parental to the Bultfontein kimberlite was a transitional silicate-carbonate melt, which was progressively enriched in SiO_2, MgO, Al_2O_3, Cr_2O_3, and Na_2O through the assimilation of lithospheric mantle material. Comparisons with

experimentally produced low-degree melts of carbonated lherzolite indicate that the Bultfontein kimberlite could have formed by ~0.5% melting of asthenospheric mantle at ~6.0-8.6 GPa (i.e., ~190-285 km) and ~1400-1500 °C. The low calculated Na_2O contents (<0.2 wt.%), which are inconsistent with derivation from low-degree melting of lherzolite, suggest that an alkali-bearing, volatile-rich fluid was exsolved during ascent or released after emplacement, and subsequently removed.

Introduction

Kimberlites are volumetrically minor igneous rocks, but occur on all continents (e.g., Jelsma et al., 2009; Yaxley et al., 2013). Their deep derivation provides invaluable insights into the processes operating in the sub-continental mantle. However, despite extensive studies the composition of kimberlite melts remains poorly constrained. Kimberlite melts have been described as volatile-rich ultramafic silicate melts (e.g., Kopylova et al., 2007; le Roex et al., 2003; Price et al., 2000); "carbonatitic" melts (e.g., Russell et al., 2012); or transitional silicate-carbonate melts (e.g., Nielsen and Sand, 2008; Brooker et al., 2011). Uncertainty surrounding kimberlite melt compositions prevents a comprehensive understanding of many aspects of their petrogenesis, including the depth of melt generation (i.e., lithosphere – Becker and le Roex, 2006; le Roex et al., 2003; shallow asthenosphere – Bailey, 1980, 1993; Moore et al., 2008; Tappe et al., 2013, 2016; or transition zone – lower mantle – Haggerty, 1994; Ringwood et al., 1992); and the causes of magmatism, which have been attributed to mantle plumes (e.g., Haggerty, 1994; le Roex, 1986), subduction of oceanic lithosphere (e.g., McCandless, 1999), or rapidly changing stress regimes during tectonic plate reconfiguration (e.g., Bailey, 1993; Jelsma et al., 2009; Moore et al., 2008; Tappe et al., 2016).

Deciphering the composition of kimberlites is currently hampered by pre-, syn- and post-emplacement processes that modify the composition of kimberlites. These include: (1)

hydrothermal alteration (e.g., Afanasyev et al., 2014; Giuliani et al., 2014, 2017; Stripp et al., 2006); (2) volatile loss through reactions with wall-rocks, fluid exsolution during ascent, and degassing upon emplacement (e.g., Brooker et al., 2011, Moussallam et al., 2016, Russell et al., 2012); (3) magmatic differentiation (e.g., Mitchell, 2008; Kjarsgaard, 2007); (4) inclusion and assimilation of xenogenic material (e.g., Brett et al., 2009; Giuliani et al., 2016; Kamenetsky et al., 2008; Schultze, 2001; Soltys et al., 2016).

Accordingly, parental kimberlite melt compositions cannot be determined directly from whole-rock geochemical analyses without taking the above processes into account. Previous studies have reconstructed kimberlite melt compositions using several approaches: (1) Whole-rock measurement of aphanitic kimberlites (e.g., Kopylova et al., 2007; Price et al., 2000; Shee, 1985); (2) subtraction of xenocrystic components from whole-rock compositions (e.g., Kjarsgaard et al., 2009; Nielson and Sand, 2008); and (3) projections in geochemical plots using large whole-rock datasets from a single locality (e.g., le Roex et al., 2003). Most of these reconstructions imply that primitive kimberlites are Al- and Na-poor, volatile-rich, ultramafic melts containing ~25-35 wt.% SiO_2 and MgO, and ~12-20 wt.% CaO with variable H_2O and CO_2 concentrations (e.g., Becker and le Roex., 2006; Kjarsgaard et al., 2009; Kopylova et al., 2007; le Roex et al., 2003; Price et al., 2000). However, these reconstructed melt compositions cannot be considered primary because they are too Mg-rich to have been in equilibrium with potential mantle source rocks (e.g., Kopylova et al., 2007). Moreover, experimental studies have shown that these reconstructed compositions do not form pure melts at the pressure-temperature conditions of kimberlite emplacement (i.e., 100-200 MPa and 1100-1275 °C), and are unable to dissolve the measured whole-rock volatile contents (Brooker et al., 2011; Moussallam et al., 2016; Sparks et al., 2009).

Since the last attempts to reconstruct kimberlite melt compositions, there have been significant advances in our understanding of the origin of minerals contained in kimberlites

(i.e., magmatic vs. xenocrystic vs. secondary/hydrothermal – e.g., Kamenetsky et al., 2008; Roeder and Schultze, 2008; Giuliani et al., 2017). These advances permit a new approach to estimating kimberlite melt compositions. This contribution focuses on a sample of 'fresh' hypabyssal macrocrystic kimberlite (sample BK-1) from the diamondiferous (ca. 84 Ma; Kramers et al., 1983) Bultfontein kimberlite, Kimberley (South Africa). This sample was selected for melt reconstruction as the petrography, mineral chemistry and isotope systematics are well constrained and representative of the Kimberley kimberlites (Giuliani et al., 2016; 2017). In this study, we employed detailed image analysis to provide modal mineral abundances and to discriminate magmatic from xenocrystic components. These data were then combined with mineral densities and compositions to reconstruct the whole-rock composition. Finally, a series of corrections were applied to account for the syn- and post-emplacement alteration, the inclusion and assimilation of mantle material, and pre-emplacement crystallisation. The resulting reconstructed primitive melt composition is used to provide an assessment of the conditions of generation of the Bultfontein kimberlite.

Background

Primary kimberlite mineralogy

Kimberlites are holocrystalline and inequigranular igneous rocks that exhibit textures ranging from aphanitic to macrocrystic. They are notoriously susceptible to post-emplacement alteration; however, the origin of the fluids responsible for alteration are highly contentious (see next section). Kimberlites are hybrid rocks, containing a mixture of xenolithic and xenocrystic components of various origins (i.e., mantle and crustal) as well as magmatic and secondary (i.e. post-magmatic) phases. Discerning the origin of phases contained in kimberlites is challenging because many minerals can have multiple origins (e.g., Giuliani et al., 2016; Kamenetsky et al., 2008; Mitchell, 1986; Schultze, 2001). Nevertheless, the mineralogy of

hypabyssal kimberlites is broadly similar worldwide, typically including liquidus olivine, spinel group minerals, micas, perovskite, apatite, monticellite, and ilmenite, set in a cryptocrystalline matrix of carbonates (calcite and lesser dolomite) and serpentine (e.g., Mitchell, 1986, 2008).

Post-, syn- and pre-emplacement modification of kimberlites

Serpentinisation

In this section, we refer only to pervasive syn- and post-emplacement alteration of 'relatively fresh' hypabyssal kimberlites and not to subaerial weathering (e.g., Mitchell, 2008). Serpentinisation is the predominant style of alteration, where serpentine may constitute up to 50 vol.% of kimberlites and is the major host of H_2O (e.g., Mitchell, 1986). Serpentine commonly replaces silicate phases (i.e., olivine, monticellite and phlogopite), but can also replace carbonates and apatite (e.g., Giuliani et al., 2017; Mitchell, 1986; Sparks et al., 2009). Serpentinisation reactions have the potential to increase whole-rock H_2O/CO_2, MgO/CaO, and SiO_2/CaO ratios (e.g., Sparks et al., 2009), although quantifying these effects is challenging. In addition, serpentine occurs in the kimberlite matrix where it apparently does not replace a previous magmatic phase. Understanding the origin of this matrix serpentine is significant to modelling kimberlite melt compositions, because in otherwise 'fresh' kimberlite samples (i.e., those with little pseudomorphic serpentine) it is volumetrically the most abundant form of serpentine.

There are two main opposing views on the origin of serpentine-forming fluids in hypabyssal kimberlite rocks:

(1) Deuteric (i.e., late-stage magmatic) fluids, derived entirely from the kimberlite melt (Mitchell, 2008, 2013). In this model, serpentine is viewed as an inherent part of the kimberlite crystallisation sequence and should be included in melt reconstructions.

(2) Fluids largely (or completely) derived from external sources (i.e. groundwater; Afanasyev et al., 2014; Brooker et al., 2011; Sparks et al., 2009; Stripp et al., 2006), which may mix with residual deuteric components (Giuliani et al., 2014; 2017). Here, the dissolved components (i.e., MgO and SiO_2) are largely derived from the alteration of kimberlitic phases; whereas serpentine is a secondary, pore filling or replacement phase. In this case, most of the serpentine should not (or only partly) be included in melt reconstructions.

The experimental studies of Brooker et al. (2011), Moussallam et al. (2016) and Sparks et al. (2009) have shown that the amount of H_2O required for an entirely deuteric origin of serpentine in some hypabyssal kimberlite rocks (i.e., ~5-10 wt.% H_2O) exceeds the solubility of H_2O in a large spectrum of analogue kimberlite melts (i.e., 18-28 wt.% SiO_2; Moussallam et al., 2016) at the pressure-temperature conditions of emplacement. Kimberlites evidently retain some magmatic H_2O, as they crystallise primary mica, and there may be a deuteric component in early generations of serpentine (Giuliani et al., 2017). However, following emplacement, there is likely extensive mixing of residual deuteric fluids with groundwater, which hampers accurate estimation of the H_2O content of parental kimberlite melts. Therefore, it appears no simple end-member model (i.e., entirely deuteric or external) can accurately explain the origin of serpentine in kimberlite rocks.

Incorporation and assimilation of xenocrystic material

Kimberlites host an assortment of xenocrystic and xenolithic components of diverse origins and it is evident from reaction textures between the host kimberlite and these entrained phases that kimberlite melts are highly reactive (e.g., Shee, 1985; Smith et al., 2004; Russell et al., 2012; Soltys et al., 2016). There is abundant petrographic and experimental evidence that orthopyroxene and, to a lesser extent, clinopyroxene and garnet are assimilated by kimberlite melts (Chepurov et al., 2013; Hunter and Taylor, 1982; Kamenetsky and Yaxley, 2015;

Kamenetsky et al., 2009; Luth, 2009). However, the extent of assimilation of mantle material, particularly of clinopyroxene and garnet, is poorly constrained. Previous melt reconstructions have accounted for the complete assimilation of mantle orthopyroxene (e.g., Kopylova et al., 2007), or complete assimilation of average bulk peridotite (minus olivine; e.g., Kjarsgaard et al., 2009). In these studies, the volume of orthopyroxene, clinopyroxene and garnet available for assimilation was estimated based on the abundance of xenocrystic olivine in the studied samples, or what is considered the average amount of olivine macrocrysts (inferred to represent xenocrystic olivine) in kimberlites (i.e., 25 wt.%; Kopylova et al., 2007) combined with the ratio of olivine to orthopyroxene in mantle xenoliths.

Other phases have both magmatic and xenocrystic origins (e.g., olivine, phlogopite, spinel and ilmenite – e.g., Kamenetsky et al., 2008; Schultze, 2001; Giuliani et al., 2016), which have not always been accurately accounted for during previous melt reconstructions. For example, in previous studies, kimberlitic olivine was classified based on size and shape, where anhedral olivine macrocrysts (>1 mm) were deemed to be xenocrysts, and olivine phenocrysts were considered magmatic (e.g., Mitchell, 1986, 2008). However, recent studies have shown that most olivine grains are zoned, regardless of their textural affinity, and include core(s) overgrown by one or more rims (e.g., Fedortchouk and Canil, 2004; Brett et al., 2009; Bussweiler et al., 2015; Giuliani et al., 2017; Howarth and Taylor, 2016; Kamenetsky et al., 2008; Sobolev et al., 2015). Based on the compositions and mineral inclusion assemblages, the cores of olivine grains are usually interpreted as xenocrysts, derived from the disaggregation of mantle wall-rocks, whereas the rims are interpreted to be a liquidus kimberlite phase.

Geological Setting and Sample Description

The Kimberley cluster is located towards the centre of the Western terrane of the Kaapvaal craton and comprises five main kimberlite pipes (Kimberley, De Beers, Dutoitspan, Wesselton

and Bultfontein), numerous smaller pipes as well as dyke and sill complexes (Fig. 6-1; Clement, 1982; Field et al., 2008). Previous studies have demonstrated that the Kimberley kimberlites have mineralogical (e.g. Clement, 1982; Giuliani et al., 2017; Shee, 1985), geochemical (e.g., Becker and le Roex., 2006; le Roex et al., 2003) and isotopic features (i.e., Sr-Nd-Hf-Pb; Nowell et al., 2004; Smith et al., 1983; Woodhead et al., 2009) typical of archetypal kimberlites worldwide.

Sample BK-1 is an offcut (8×6×1.5 cm) of a larger sample of hypabyssal kimberlite from the De Beers collection. The sample was collected from the Boshof road dumps, which contains waste material from the mining of the Bultfontein kimberlite (J.V.A. Robey, pers. comm.). The Bultfontein pipe contains a single unit of hypabyssal kimberlite, which is proposed to represent an enlargement of the feeder dyke (inferred from drilling, but not intersected by mining activity – Clement 1982; Field et al., 2008). It is highly probable that sample BK-1 originates from this unit.

The petrography and mineral chemistry of sample BK-1 were described by Giuliani et al. (2016, 2017) and are only summarised briefly here. Sample BK-1 is classified as a massive, moderately macrocrystic, hypabyssal kimberlite, with no textural evidence of significant in-situ magmatic differentiation (Fig. 6-2; Supplementary Fig. S6-4, 6-5; see also Giuliani et al., 2017). Sample BK-1 contains olivine as well as subordinate phlogopite and ilmenite macrocrysts. Olivine and phlogopite also occur as euhedral phenocrysts (>0.5 mm) and micro-phenocrysts. Groundmass phases include apatite, oxide minerals (spinel, perovskite and ilmenite), phlogopite and monticellite (pseudomorphed by serpentine and minor carbonate), set in a matrix of carbonates (calcite and lesser dolomite) and serpentine.

Other samples of the Bultfontein kimberlite, and of other intrusions of the Kimberley cluster were also examined. However, sample BK-1 was deemed the most appropriate for melt reconstruction, because it is substantially fresher than other samples, has undergone

comparatively less olivine accumulation, and contains a lower abundance of xenolithic material.

Whole-rock and Melt Reconstruction Methodology

A fresh, representative area (~7 mm^2) of sample BK-1, free of macrocrystic ilmenite was selected for whole-rock reconstruction (Fig. 6-2). The representativeness of this area is attested to by the size of groundmass phases (i.e., < to << 50 um – Giuliani et al., 2017), and the similarity between the reconstructed and measured whole-rock compositions (see section 5.2).

The reconstruction was conducted in the following steps:

Step 1: Modal mineral abundances and the proportions of magmatic and xenocrystic components in olivine macrocrysts and phenocrysts were measured on back-scattered electron (BSE) images by manually tracing the relevant phases and internal zones using the image analysis software ImageJ (Schneider et al., 2012 – Electronic Appendix A1; Supplementary Fig. S6-1). In most cases xenocrystic olivine cores can be discerned from magmatic rims in BSE images due to differences in their forsterite content (e.g., Giuliani et al., 2017; Supplementary Fig. S6-1). Minor pseudomorphic serpentine replacing olivine along fractures and grain margins was included in the whole-rock reconstruction as olivine rather than serpentine. This assumes that serpentine replacing olivine is entirely secondary in origin (see Giuliani et al., 2017). The reconstructed whole-rock composition is given by the equation:

$$\text{Whole} - \text{rock composition} = \sum_{\text{n=m}} (\text{vol.}\,\%_i \times \rho_i \times \text{c}_i)_{\text{m}}$$

where m is a given phase in sample BK-1, vol.% is the volumetric percentage of that phase approximated by its modal abundance, ρ is the phase density, and *c* is the major element oxide composition from electron microprobe data reported in Giuliani et al. (2016, 2017) (model compositions are reported in Supplementary Table S6-2). To evaluate the accuracy of

this approach, we compare the reconstructed whole-rock composition (**Step 1**) with XRF measurements of sample BK-1 (methods reported in Electronic Appendix A1). As kimberlites are inherently variable in terms of their modal mineral abundances, for each phase we have included an uncertainty in the volume estimate equal to ±10% of its relative modal abundance. The applied relative variation of modal abundances is based on the measured variation of olivine macrocrysts in a larger section of sample BK-1 (i.e., +8%; see Electronic Appendix A1). This uncertainty is propagated through the subsequent steps of melt reconstruction, and therefore compositions are reported in tables and figures as a range. All major elements in the reconstructed whole-rock composition show a good correlation with the measured whole-rock composition, except for P_2O_5 and CaO (see below). This deviation in P_2O_5 and CaO contents is attributed to the heterogeneous distribution of apatite in the groundmass. Therefore, we have constrained the modal abundance of apatite so that the reconstructed whole-rock P_2O_5 content matches the measured value. This correction reduces the CaO misfit significantly, but does not significantly affect any other major element concentrations.

To calculate melt compositions at various stages of kimberlite evolution, the reconstructed whole-rock composition is then corrected to progressively remove the effects of processes which modify the composition of kimberlites pre- and post-emplacement (**Steps 2-4**).

Step 2: Correction for pseudomorphic serpentinisation of monticellite. We assume that serpentinisation is a constant volume replacement process occurring in an open system (e.g., Sparks et al., 2009). We model this generation of pseudomorphic serpentine as having a deuteric origin, because it is compositionally distinct from later generations of pseudomorphic serpentine replacing olivine (Giuliani et al., 2017), and is typically enclosed in carbonates with magmatic textures and compositions. It should be noted that the abundance of monticellite may

be slightly underestimated because pseudomorphed monticellite contained entirely in serpentine-rich portions of the matrix could not always be identified conclusively.

Step 3: Correction for matrix serpentine assuming derivation from deuteric, external or mixed fluids. Given the uncertainty in serpentine source(s) and the phases replaced (if any), we consider the following scenarios:

(1) *Model I*: matrix serpentine is an entirely deuteric (i.e., magmatic) phase (e.g., Mitchell, 2008), that did not replace pre-existing kimberlitic minerals.

(2) *Model II*: matrix serpentine is a secondary phase (i.e., formed entirely from external components), that did not replace pre-existing kimberlitic minerals (e.g., Afanasyev et al., 2014).

(3) *Model III*: matrix serpentine is a secondary phase which replaced original matrix calcite and dolomite, in their existing proportions. This model is based on petrographic observations and carbonate C-O isotope compositions, which show that the carbonates appear to have re-crystallised and been partly replaced during serpentinisation of sample BK-1 (Giuliani et al., 2017).

(4) *Model IV*: matrix serpentine is 30% deuteric, and 70% secondary replacing calcite and dolomite in their existing proportions. This is our favoured model, because it appears unlikely that the origin of matrix serpentine can be described by any simple end-member model (see section 2.2.1).

Step 4: Removal of xenocrystic components (i.e., olivine and phlogopite). The abundance of xenocrystic olivine (i.e. cores of olivine grains) was determined by image analysis. For phlogopite we assumed that all macrocrysts are xenocrystic, and all micro-phenocrysts and groundmass grains are magmatic. This is justified by the rarity of phlogopite macrocrysts (<3 vol.%), which only have thin overgrowths (<50-100 μm) on large cores (>0.5-1 mm; Giuliani et al., 2016); and the paucity of xenocrystic cores included in groundmass and micro-

phenocrystic phlogopite (≤10% of examined grains). Chromite xenocrysts are volumetrically insignificant and are not considered in this model.

Compositions derived from **Step 4** should approximate the kimberlite melt on emplacement in the upper crust, if no olivine had crystallised before emplacement. However, the presence of well-developed magmatic olivine overgrowths on xenocrystic cores in volcaniclastic kimberlites (e.g., Brett et al., 2009; Kopylova et al., 2016) indicates possible extensive pre-emplacement crystallisation of olivine. We therefore also consider an alternative scenario where 80% of magmatic olivine crystallised before emplacement as this may significantly modify the composition of the melt on emplacement.

We now introduce the steps necessary to reconstruct the primitive kimberlite melt prior to assimilation of lithospheric mantle material.

Step 5: Correction for orthopyroxene assimilation. The amount of orthopyroxene assimilated is estimated from the volume of xenocrystic olivine in sample BK-1 and the average ratio of olivine to orthopyroxene in mantle xenoliths from the Kaapvaal craton (see Electronic Appendix A2). This approach is identical to that employed by previous studies (e.g., Kopylova et al., 2007).

Step 6: Correction for clinopyroxene and garnet assimilation. The amount of clinopyroxene and garnet assimilated is estimated in the same way as orthopyroxene (see Electronic Appendix A2). However, because the extent of assimilation is uncertain, we consider two scenarios: complete [C]; and partial ([P]; 40% garnet and 60% clinopyroxene) assimilation of these phases. Whilst these values are arbitrary, this approach is supported by experimental studies, which suggest clinopyroxene is assimilated to a greater extent than garnet in silica-undersaturated melts (e.g., Chepurov et al., 2013).

Electronic Appendix A4 is a Microsoft Excel spreadsheet used to reconstruct the composition of kimberlite whole-rocks, and parental magmas/melts at various stages of their

evolution. This template allows all the input values and assumptions made during melt reconstruction to be varied. Therefore, the models outlined above are simply presented to demonstrate the potential effects of the processes which modify kimberlites melts.

Results

The modal abundances of phases contained in sample BK-1 are reported in Table 1. Measured (XRF) and reconstructed (**Step 1**) whole-rock compositions are reported in Table 2. Reconstructed melt compositions from *Model I* and *IV* (**Steps 2-6**) are also reported in Table 2 (normalised to 100 wt.%), whereas the other reconstructed melt compositions (*Models II* and *III*) are reported in Supplementary Table S3. Kimberlite melt compositions on emplacement in the upper crust estimated from *Models I* and *IV* are reported in Table 3.

Measured whole-rock composition

A whole-rock analysis of sample BK-1 contains 30.7 wt.% SiO_2, 31.4 wt.% MgO, 10.9 wt.% CaO, 1.8 wt.% P_2O_5, 1.5 wt.% TiO_2, 1.8 wt.% Al_2O_3 and 1.1 wt.% K_2O, and has a Mg# of 85.7. The composition of sample BK-1 is within the range of compositions of previously studied samples from the Kimberley kimberlites in terms of all reported major elements (le Roex et al., 2003). The composition of sample BK-1 plots along the 'olivine accumulation' trend typical of macrocrystic kimberlites from the Kimberley cluster (Fig. 6-3). Various contamination indexes (e.g., Clement's contamination index (C.I.), ln(Si/Al) and SiO_2/MgO) indicate that sample BK-1 has not undergone significant contamination by crustal material (Table 6-2; Fig. 6-3). Although, we note that these indices do not provide conclusive evidence of contamination (or lack thereof) because incorporation of peridotitic material can mask low degrees of crustal contamination (see Kjarsgaard et al., 2009).

Reconstruction of the whole-rock composition (Step 1)

The modal abundance of minerals and composition of sample BK-1

The olivine content of sample BK-1 (i.e., ~44 vol.%; Table 1) overlaps the tightly clustered 40-50 vol.% of olivine which typifies hypabyssal kimberlites worldwide (e.g., Clement, 1982; Mitchell, 1986, 2008). Moreover, concentrations of components dominated by olivine (i.e., MgO, SiO_2, and FeO) in the reconstructed and measured whole-rock are consistent with other macrocrystic hypabyssal kimberlite samples from the Kimberley cluster (Fig. 6-3; Table 6-4)

The modal abundance of phlogopite in sample BK-1 (Table 1) is consistent with other estimates for the Kimberley kimberlites (i.e., >2 vol.% macrocrysts and 2-16 vol.% (micro-) phenocrysts; Shee, 1985; le Roex et al., 2003). In addition, the measured and reconstructed whole-rock K_2O concentrations (0.9 and 0.8-1.0 wt.%, respectively) of sample BK-1 are within the range of previously studied samples of the Kimberley kimberlites (le Roex et al., 2003), as well as kimberlites worldwide, which typically contain ~1 wt.% K_2O (Table 4).

Apatite constitutes 6.5 vol.% of sample BK-1 (Table 1). Marginal overestimation in the reconstructed whole-rock (i.e., 2.7 wt.% P_2O_5; not shown) compared with the measured whole-rock (i.e., 1.8 wt.%; Table 2), is attributed to the small size of apatite (i.e., <30 μm) and its heterogeneous distribution in the groundmass. This variance in P_2O_5 contents is the motivation for forcing the modal abundance of apatite (i.e., to ~4.3 vol.%) so that the reconstructed whole-rock P_2O_5 composition matches that of the measured whole-rock (i.e., 1.8 wt.%; Table 2). Nevertheless, sample BK contains significantly more P_2O_5 than most kimberlites worldwide (commonly <0.8 wt.% P_2O_5; see Table 4). Such high P_2O_5 contents are common to the Kimberley kimberlites (~2 wt.%; le Roex et al., 2003; Becker and le Roex, 2006), and are also a feature of several other southern African kimberlites (e.g., Becker and le Roex, 2006; Smith et al., 1985).

Accurate estimates of the modal abundance of other kimberlitic phases (i.e., oxides minerals and monticellite) are scarce. Sample BK-1 contain abundances of these phases consistent with other samples from the Kimberley kimberlites (A. Soltys, unpublished data). Moreover, concentrations of Al_2O_3, TiO_2 and Cr_2O_3 are within the range of whole-rock compositions reported for the Kimberley kimberlites (le Roex et al., 2003).

In summary, after forcing the modal abundance of apatite, the reconstructed whole-rock composition closely resembles the measured composition of sample BK-1in terms of all measured elements (Table 2). This validates the reconstruction method and confirms that the area analysed is representative of sample BK-1.

Xenocrystic and magmatic olivine components

Image analysis indicates that olivine phenocrysts (n = 61) in sample BK-1 consist, on average, of 30 vol.% xenocrystic core and 70 vol.% magmatic rim (e.g., Supplementary Figure S6-1). In contrast, olivine macrocrysts (n = 5) average 78 vol.% xenocrystic and 22 vol.% magmatic components (Table 1; Supplementary Table S1). Given that sample BK-1 contains 30.7 vol.% olivine phenocrysts and 13.3 vol.% olivine macrocrysts (Table. 1), magmatic and xenocrystic olivine contents are estimated at 24.4 vol.% and 19.6 vol.% of the whole rock, respectively. The contribution to the magmatic olivine budget is dominated by phenocryst rims (~88%), whereas the phenocrysts and macrocrysts contribute equally to the xenocrystic olivine budget.

These results indicate olivine in sample BK-1 consists of approximately 55 vol.% magmatic and 45 vol.% xenocrystic components. These results are broadly similar to previous estimates for kimberlite rocks worldwide where image analysis was employed – e.g., 44% magmatic and 56% xenocrystic olivine in the Udachanaya-East kimberlite, Russia (Kamenetsky et al., 2008); and 45% magmatic and 55% xenocrystic olivine in the Leslie kimberlite, Canada (Bussweiler et al., 2015). These estimates are significantly different from

those based on crystal size modelling or mass balance calculations (i.e., ~5-15% liquidus olivine; Brett et al., 2009; Nielsen and Sand, 2008). Chemical mass balance calculations that employ average Ni concentrations in olivine and the whole-rock probably provide accurate measures of total olivine abundance (e.g., Nielsen and Sand, 2008), but cannot accurately constrain the relative proportions of xenocrystic and magmatic olivine, because Ni contents in these phases overlap (e.g., Sobolev et al., 2015). Modelling based on olivine crystal size distributions and maximum thicknesses of magmatic rims (i.e., Brett et al., 2009), may not account for the complexity of olivine in kimberlite rocks. For example, the width of magmatic rims often varies due to irregular core shapes, and many olivine grains do not have a spherical shape.

Reconstruction of the Kimberlite Melt Composition Upon Emplacement in the Upper-crust

To reconstruct the composition of the kimberlite melts on emplacement, we must consider the effects of post-emplacement alteration (**Steps 2** and **3**), the inclusion of xenocrystic material (**Step 4**), and when olivine appears on the liquidus.

*Post-emplacement modification (**Steps 2** and **3**)*

Sample BK-1 contains ~5.6 vol.% of serpentinised monticellite pseudomorphs (Table 1). Assuming deuteric alteration, re-addition of this monticellite component during **Step 2** increases the CaO (1.1-1.3 wt.%) and SiO_2 (0.3-0.4 wt.%) concentrations, whereas FeO (0.1-0.2 wt.%), MgO (0.5-0.7 wt.%), and CO_2 (0.4-0.5 wt.%) concentrations decrease (Table 2).

For the correction applied to matrix serpentine (i.e., **Step 3**) we focus on the results of *Models I* and *IV*. In *Model I* we assume all matrix serpentine is deuteric, which is analogous to the assumption made by previous melt reconstructions (Becker and le Roex, 2006; Kopylova

et al., 2007; Kjarsgaard et al., 2009; le Roex et al., 2003; Price et al., 2000). Therefore, in **Step 3** of *Model I* no correction is necessary. In the case of *Model IV* (our preferred model), we consider that matrix serpentine is partly deuteric, and partly secondary replacing carbonates (see section 4). In this model, the concentrations of SiO_2 (3.4-4.5 wt.%), MgO (2.0-2.6 wt.%), FeO (0.7-0.9 wt.%) and H_2O (0.9-1.2 wt.%) decrease, whereas CaO (3.7-4.9 wt.%) and CO_2 (3.4-4.5 wt.%) concentrations increase (Table 2).

As expected, serpentinisation of monticellite by deuteric fluids in an open system, and matrix serpentine having a deuteric origin (**Steps 2** and **3**, *Model I*) produces only marginal variation in MgO/CaO and SiO_2/MgO ratios (Fig. 6-4). In contrast, if matrix serpentine is derived from mixed fluids (i.e. 70% external and 30% deuteric; *Model IV*), where some matrix serpentine replaced carbonates, there is a significant decrease in MgO/CaO and to a lesser extent SiO_2/MgO ratios (Fig. 6-4). In addition, in *Model IV*, the $H_2O/(H_2O+CO_2)$ ratio decreases by ~50% (Table 2). These results are consistent with the suggestions of Brooker et al. (2011) and Sparks et al. (2009), that kimberlite rocks contained significantly more CaO and CO_2, and less MgO, SiO_2 and H_2O prior to alteration. The effects of serpentinisation by fluids dominated by external components (i.e., **Step 3** of *Model IV*) are significant considering that sample BK-1 is considered to be 'fresh' (e.g., Fig. 6-1 and Giuliani et al., 2016a; Giuliani et al., 2017).

*The removal of included xenocrystic components (**Step 4**)*

The removal of xenocrystic olivine and phlogopite results in lower SiO_2 (2.4-2.7 and 3.9-4.0 wt.%) and MgO (4.9-5.2 wt.%) concentrations, with negligible changes in K_2O concentrations (≤0.1 wt.%), whereas CaO (3.7-4.0 and 4.8-5.0 wt.%), CO_2 (2.0-2.4 and 3.2-3.4 wt.%) and H_2O (0.6-0.7 and ~0.3 wt.%) concentrations increase for *Models I* and *IV*, respectively (Table 2). The results are consistent with those reported by Bussweiler et al. (2015), who removed a

similar amount of xenocrystic olivine with a similar model composition (i.e., $Fo_{91.7}$), resulting in a decrease in SiO_2, and increase in CaO concentrations of ~3 wt.%.

In summary, the difference between the reconstructed whole-rock compositions from **Step 1** and the melt compositions from **Step 4** of *Model IV*, demonstrate that the composition of the Bultfontein kimberlite on emplacement was likely significantly lower in SiO_2 (7.0-8.0 wt.%), MgO (7.6-8.1 wt.%), and, to a lesser extent, H_2O (0.8-1.1 wt.%), whilst enriched in CaO (10.0-11.1 wt.%) and CO_2 (6.3-7.4 wt.%) (Table 2). In addition, there is a 1.4-2.0 unit decrease in the Mg# when compared with the whole-rock composition (Table 2).

Estimating the effects of pre-emplacement olivine crystallisation

If no pre-emplacement crystallisation occurred, then the compositions reconstructed in **Step 4** should approximate the kimberlite melt on emplacement in the upper crust (Table 2). Assuming 80% of the magmatic olivine crystallised before emplacement, the SiO_2 (3.1-5.5 and 4.9-8.7 wt.%) and MgO (6.0-10.0 and 6.8-11.6 wt.%) concentrations decrease further, whereas CaO (4.7-7.4 and 4.8-8.7 wt.%) and CO_2 (2.4-4.6 and 2.8-6.2 wt.%) concentrations increase for *Models I* and *IV*, respectively (Table 3). In addition, the Mg# decreases further by 3.0-5.2 (*Model I*) and 9.8-14.6 units (*Model IV*).

Reconstruction of the primitive melt composition

To reconstruct the composition of the primitive melt parental to the Bultfontein kimberlite we must consider the effects of assimilation of lithospheric mantle material (**Steps 5** and **6**). In these steps the amount of assimilant removed varies due to the ±10% uncertainty applied to the volumetric abundance of all phases, and the differences in abundance of groundmass phases following the assumptions made during **Steps 2-4**, which in turn change the relative abundance of olivine.

*Assimilation of orthopyroxene (**Step 5**)*

The removal of a component equal to 4.8-5.8 wt.% of orthopyroxene (see Electronic Appendix A2) produces a decrease in SiO_2 (2.0-2.3 and 2.3-2.7 wt.%) and, to a lesser extent, MgO (~0.6 and 0.7-0.8 wt.%) and FeO (0.2-0.3 and 0.1-0.2 wt.%) concentrations for Models I and IV, respectively (Table 2). These compositional changes are broadly similar to those calculated by Kopylova et al. (2007), i.e. decreases of ~2 wt.% SiO_2 and ~0.5 wt.% MgO due to the removal of 6 vol.% orthopyroxene.

*Assimilation of clinopyroxene and garnet (**Step 6**)*

Accounting for the complete assimilation of clinopyroxene (1.0-1.2 wt.%) and garnet (1.6-1.9 wt.%) reduces SiO_2 (0.7-0.9 and 1.0-1.1 wt.%), Al_2O_3 (0.4-0.5 wt.%) and Cr_2O_3 (0.1-0.2 and ~0.1 wt.%) concentrations, whereas CaO (~0.3 and ~0.5 wt.%), MgO (0.2-0.4 and 0.1-0.3) and CO_2 (~0.4 and ~0.6) concentrations increase for *Models I* and *IV*, respectively. The effects of partial assimilation are subtler (Table 2).

In summary, the reconstructed primitive melt composition following our preferred model (i.e., **Step 6** of *Model IV*[**P**]) contains less SiO_2 (10-10.9 wt.%) and MgO (8.2-8.8 wt.%), and more CaO (11.8-12.9 wt.%) and CO_2 (7.6-8.8 wt.%) than the reconstructed whole-rock composition (i.e., **Step 1**). In addition, concentrations of FeO (0.9-1.3 wt.%) and H_2O (0.6-1.0 wt.%) decrease marginally, whereas P_2O_5 (0.5-0.7 wt.%) and TiO_2 (0.3-0.4 wt.%) increases slightly (Table 2). The Mg# decreases by 2.0-2.7 units to 83.4-84.4 (Table 2). For *Model I*, the changes are less pronounced (e.g., -4.4-5.0 wt.% SiO_2, +6.2-6.7 wt.% CaO; Table 2).

Discussion

How Representative is Sample BK-1 of the Kimberley Kimberlites, and of Archetypal Kimberlites Worldwide?

The modal mineral abundances, whole-rock geochemistry, mineral compositions, and isotope systematics of sample BK-1 overlap those of other samples of macrocrystic hypabyssal kimberlite from the Kimberley cluster, including those from dykes and root zone intrusions (see sections 5.1 and 5.2; Fig. 6-3 and Table 6-4; also Giuliani et al., 2017). Therefore, it is evident that sample BK-1 has not undergone pre-emplacement fractionation.

The H_2O contents (i.e., 2.3-2.7 wt.%; Table 2) and $H_2O/(H_2O+CO_2)$ ratios (i.e., 0.2-0.3 Table 2) of the reconstructed whole-rock are at the lower end of the range of previously analysed samples from the Kimberley kimberlites (i.e., 1.4-9.9 wt.%, and 0.1-0.9, respectively; Clement, 1982; le Roex et al., 2003). The lower H_2O content may be due to crystallisation from a melt with a comparatively higher CO_2/H_2O ratio than some other samples from the Kimberley cluster. This is consistent with the presence of dolomite in the matrix of sample BK-1. For example, in the Lac de Gras kimberlites (Canada) dolomite only occurs in samples with whole-rock $H_2O/(H_2O+CO_2)$ ratios <0.4 (see Fig. 6 of Kjarsgaard et al., 2009), consistent with a ratio of ~0.25 for sample BK-1 (Table 2).

This low H_2O/CO_2 ratio is consistent with the fact that sample BK-1 derives from a feeder dyke or its enlargement, because dolomite kimberlites are typically restricted to dykes in the Lac de Gras area (Armstrong et al., 2004). Therefore, it appears that sample BK-1 represents a composition which lies at the H_2O-poor end of the spectrum of volatile contents for the Kimberley kimberlites.

It is noteworthy that kimberlites worldwide show variations at the local and regional scale (e.g., high and low TiO_2 groups in the Lac de Gras field (Canada) – Kjarsgaard et al., 2009; anomalous P_2O_5 enrichment in many southern African kimberlites –Becker and le Roex 2006). We therefore recognise that the primitive melt calculated in this study (or any study based on a

single locality) should not be considered representative of kimberlites worldwide. The primary aim of this contribution is to provide a new methodology to calculate primitive kimberlite melt compositions, and to demonstrate the potential effects of processes which modify kimberlites.

The Composition of Kimberlite Melts on Emplacement in the Upper Crust

Previously reconstructed kimberlite melt compositions have failed to reproduce pure melts at the pressure-temperature conditions of kimberlite emplacement in experimental studies (e.g., Sparks et al., 2009). This was attributed to the unaccounted for effects of serpentinisation on whole-rock kimberlite compositions (e.g., Brooker et al., 2011, Moussallam et al., 2016; Sparks et al., 2009). Based on the failure of these experimental studies, Sparks et al. (2009) and Brooker et al. (2011) suggested that natural kimberlite melts must contain significantly less SiO_2 and MgO than previous reconstructions, probably less than 25 wt.% SiO_2. We also note that the timing, and therefore depth of olivine crystallisation (i.e., pre- vs. post-emplacement) may exert a strong control on the composition of kimberlite melts on emplacement.

The reconstructed melt compositions on emplacement (i.e. **Step 4**) using our preferred model (i.e., *Model IV)* meets this criterion (i.e., 22.3-24.5 and 15.8-17.4 and wt.% SiO_2; Table 3) when 0 and 80% pre-emplacement olivine crystallisation is considered. In contrast, the range of reconstructed melt compositions on emplacement from *Model I* (i.e. matrix serpentine of deuteric origin) predominantly fall above this target value (i.e., 28.0-29.5 and 24.0-25.0 wt.% SiO_2, considering 0 and 80% olivine crystallisation; Table 3). Moreover, our preferred reconstructed melt composition contains MgO concentrations (i.e., 23.3-26.0 and 14.4-16.6 wt.%,) which are generally lower than most previous melt reconstructions (Table. 3).

The lower SiO_2+Al_2O_3, and higher CaO content of the melts estimated from *Model IV* compared with previously reconstructed melt compositions (Table 3) should increase CO_2 solubility at the low pressures of emplacement (i.e., >15 wt.% CO_2; Fig. 6-5). This is significant

as the compositions previously tested experimentally failed to accommodate the upper limits of CO_2 contents found in natural kimberlite rocks (i.e., up to ~15 wt.% CO_2; Kjarsgaard et al., 2009). The upper limits of CO_2 contents measured on natural rocks probably represent minimum constraints, because CO_2 is inevitably lost due to degassing. Moreover, Brooker et al. (2011) suggested that slight decreases in the SiO_2 concentrations of the tested compositions may cause drastic changes in the phase relations, potentially allowing evolution toward carbonate-rich residual melts typical of natural kimberlites, but thus far unable to be replicated in experimental studies.

It is noteworthy that the lower H_2O contents on emplacement calculated in this study (i.e., <5 wt.%; Table 3, see also section 6.7), compared with previous reconstructions (i.e., up to 14 wt.%; e.g., Price et al., 2000; Kjarsgaard et al., 2009) are more consistent with experimental results, which indicate analogue kimberlite melts (i.e., 18-28 wt.% SiO_2) can only accommodate up to ~4 wt.% H_2O at the conditions of kimberlite emplacement (Moussallam et al., 2016). In summary, the lower SiO_2, MgO and H_2O, and higher CaO and CO_2 content of the reconstructed melt on emplacement (i.e., **Step 4** of *Model IV*; Table 3) would appear to make for a more promising candidate to replicate natural kimberlite melts in the upper crust. However, further experimental studies are required to test this hypothesis.

The Evolution and Variability of Kimberlite Melts Through the Assimilation of Lithospheric Mantle Material

Orthopyroxene assimilation in kimberlite melts that ascend through silica-rich lithospheric mantle (e.g., Kaapvaal and Slave cratons; Griffin et al., 2009 and references therein) probably produces an increase of ~2-3 wt.% SiO_2 and ~0.5-1 wt.% MgO in the melt (Kopylova et al., 2007; this study). This is assuming orthopyroxene assimilation is complete, and given the paucity of orthopyroxene xenocrysts in kimberlites (e.g., Shee 1985) this assumption appears

justified. However, the effects of orthopyroxene assimilation on kimberlites which intrude lithospheric columns poorer in orthopyroxene (e.g., western Greenland; Bernstein et al., 2007) is probably less pronounced. This may contribute to the lower whole-rock SiO_2 contents, absence of monticellite, and lower proportion of magmatic olivine in the Majuagaa kimberlite (Greenland – Neilson and Sand, 2008), compared with southern African kimberlites (Becker and le Roex, 2006; this study).

The heterogeneous distribution of clinopyroxene and garnet in the lithospheric mantle, combined with uncertainties surrounding the extent of assimilation, renders it difficult to accurately quantify the effects of assimilation of these phases on kimberlite melts. The effects of even complete clinopyroxene and garnet assimilation on kimberlite SiO_2 and MgO compositions are subordinate to those of orthopyroxene assimilation (e.g., SiO_2 increase ≤1.2 wt.%; **Step 6** of *Model IV*[C]; Table 2). Specific minor elements, including Al_2O_3, Cr_2O_3, and Na_2O, may be more susceptible, with increases of ~30%, 80% and 20%, respectively (*Model IV*[C]; Table 2). However, the effects of clinopyroxene and garnet assimilation reported here may be more pronounced compared with kimberlites from other cratons, because the Kaapvaal lithosphere is anomalously enriched in clinopyroxene and garnet (e.g., Griffin et al., 2009 and references therein).

It has been suggested that kimberlite melts evolve from essentially SiO_2-free 'carbonatitic' melts to kimberlitic compositions through the assimilation of mantle material (e.g., Kamenetsky et al., 2014; Russell et al., 2012). If this is the case, it would require further assimilation (i.e., beyond what we consider 'complete') of bulk peridotite, inclusive of olivine. Modelling of further assimilation of bulk peridotite shows that the Cr_2O_3 concentrations of this reconstructed kimberlite melt limits the amount of assimilation possible. For instance, if the primary kimberlite melt contained no Cr_2O_3, the reconstructed primitive melt composition at **Step 6** of *Model IV*[C] could have assimilated, at most, a further ~13 wt.% of bulk peridotite.

The assimilation of 13 wt.% of bulk peridotite would decrease the SiO_2 content of the primitive melt to ~14 wt.%. We note that in a more refractory lithospheric column, richer in Cr_2O_3, assimilation by the kimberlite melt would likely be less than estimated in this study. This calculation supports thermodynamic (Kavanagh and Sparks, 2009), isotopic and trace element modelling (Tappe et al., 2013; 2017), as well as experimental evidence (e.g., Chepurov et al., 2013; Luth, 2009; Stamm and Schmidt, 2017) which suggest extensive assimilation of bulk peridotite is unlikely. Despite the continuum (i.e., carbonatitic-kimberlitic) of melt compositions produced in experimental studies, it appears likely that any primary low-degree melt in equilibrium with peridotite will contain significant quantities of SiO_2 (e.g., Girnis et al., 2011; Tappe et al., 2017; Stamm and Schmidt, 2017).

Nature of the Primitive Melt Parental to the Bultfontein Kimberlite

Our preferred primitive melt composition (i.e., **Step 6** of *Model IV* [P]) contains 19.5-21.3 wt.% SiO_2, 22.7-25.5 wt.% MgO, 22.4-24.6 wt.% CaO, 2.4-2.5 wt.% P_2O_5, 1.4-1.6 wt.% TiO_2, 1.0-1.2 wt.% Al_2O_3, 0.7-0.8 wt.% K_2O, 1.7-1.8 wt.% H_2O, 14.6-16.8 wt.% CO_2, and has a Mg# of 83.4-84.4 (Table 2). These results suggest generation of the Bultfontein kimberlite as a transitional silicate-carbonate melt (i.e., 20.7-22.3 wt.% SiO_2+Al_2O_3 – see Brooker et al., 2011), which was progressively enriched in SiO_2, MgO, and to a lesser extent Al_2O_3, Cr_2O_3 and Na_2O through the assimilation of orthopyroxene, and lesser clinopyroxene and garnet. However, this composition does not account for volatile loss and therefore all other oxide concentrations may be slightly overestimated (see section 6.6 for further discussion). This reconstructed primitive melt composition is most similar to the reconstructed melt parental to the Majuagaa kimberlite dyke (Greenland; Nielsen and Sand, (2008); Table 5). We postulate this is because the lithosphere beneath western Greenland is anomalously poor in orthopyroxene, clinopyroxene and garnet, and this kimberlite occurrence is exceptionally fresh (i.e., containing little

pseudomorphic serpentine). Therefore, the Majuagaa samples may only require minor corrections to approximate their primitive melt composition. Our melt reconstruction generally contains less SiO_2, MgO and H_2O, but more CaO and CO_2 than most previous melt reconstructions of southern African and Canadian kimberlites (Table 5). This may be because previous reconstructions (e.g., Kjarsguard et al., 2009; le Roex et al., 2003) do not completely account for the inclusion of xenocrystic material or post-emplacement alteration.

Potential Source Regions of the Bultfontein Kimberlite

A problem with previously reconstructed primitive kimberlite melt compositions is their MgO enrichment, which prevents equilibrium with potential mantle source rocks (e.g., Kopylova et al., 2007). Here we apply olivine/melt $K_{D\ Fe\text{-}Mg}$ values calculated for carbonate-rich melts at high pressure-temperature conditions (i.e., K_D = 0.52-0.66 at >2.5 GPa and 1150-1300°C; Dalton and Wood, 1993; and K_D = 0.8 at 4-5 GPa and 1400-1700°C; Girnis et al., 2005), as well as those suggested for "kimberlitic" melts (i.e., K_D = 0.45 at 4-5 GPa and 1400-1700°C; Girnis et al., 2005). These distribution coefficients are employed to test if our reconstructed melt compositions can be in equilibrium with potential mantle source rocks. We employ these K_D values rather than values for olivine in equilibrium with ultramafic melts used in previous kimberlite melt reconstructions (i.e., K_D = 0.36; Herzberg and O'Hara, 2002). This is because this and previous studies (e.g., Brooker et al., 2011) suggest that primitive kimberlite melts are transitional silicate-carbonate melts, and potentially close to the composition of silica-rich carbonate melts. Therefore, the highest K_D values employed here (i.e., 0.8) should place minimum constraints on the Fo composition of olivine in the source region. On the contrary, melts considered "kimberlitic" by Girnis et al. (2005) contains higher SiO_2 concentrations than those from this study, and therefore probably represent an overestimate of the Fo composition of olivine in the source region.

The application of these olivine/carbonate-kimberlite melt K_D values indicates that olivine in equilibrium with our preferred primitive melt (i.e., **Step 6** of *Model IV*[P]) would have compositions as follows: ~Fo_{92} (K_D = 0.45); ~$Fo_{91\text{-}88}$ (K_D = 0.52-0.66); and ~$Fo_{86\text{-}87}$ (K_D = 0.8). These values are lower than estimates of ~Fo_{95} from previous studies (e.g., Kopylova et al., 2007; le Roex et al., 2003). This is partly due to the higher K_D values used here, and partly because our reconstructed melt has a Mg# (i.e., 83.4-84.4) lower than most previous estimates (Table 5).

It is noteworthy that based on garnet xenocryst data and garnet-olivine equilibrium, olivine at the Lithosphere Asthenosphere Boundray (LAB) beneath the Kaapvaal craton is estimated to have a composition of ~Fo_{91}, which decreases further in the upper asthenosphere (see Fig. 5 of Griffin et al., 2009). In contrast, previous estimates of high-Fo olivine in the source region (i.e., ~Fo_{95}; le Roex et al., 2003; Kopylova et al., 2007) required a refractory (and recently metasomatised) peridotite source, which can only exist within the lithospheric mantle (e.g., Griffin et al., 2003). A lithospheric source is inconsistent with sampling of LAB material (i.e., garnet xenocrysts; e.g., Griffin et al., 2003, 2009), sub-lithospheric xenoliths (Haggerty, 2017), and ultra-deep diamonds with unequilibrated majorite inclusions (Stachel, 2001) in kimberlites worldwide.

Estimating the Extent of Partial Melting and Primitive Volatile Contents

The extent of melting required to produce our preferred reconstructed primitive melt composition (i.e., **Step 6** of *Model V*[P]) is estimated using equation (2) from Price et al. (2000) (see Electronic Appendix A3). This calculation is limited by the experimental conditions employed by Dalton and Presnall (1998) on which this calculation is based, i.e., melting of carbonated (0.15 wt.% CO_2) lherzolite at 6 GPa and 1380-1505°C in the $CaO\text{-}Al_2O_3\text{-}MgO\text{-}SiO_2\text{-}CO_2$ (CAMS-CO_2) system. Whilst these conditions are broadly consistent with what we

consider reasonable for production of the Bultfontein kimberlite (see section 6.7), they do not entirely replicate natural conditions and, therefore, the results of this calculation should be considered a semi-quantitative guide. This calculation indicates our preferred primitive melt composition can be produced by ~0.5% melting of carbonated lherzolite. This melt fraction is similar to that calculated (using the same method) by Nielson and Sand (2008) (i.e., 0.5-0.6%) for the Majuagaa Kimberlite (Greenland), but slightly lower than previous melt reconstructions based on southern African and Canadian kimberlites (i.e., ≥0.8%; Price et al., 2000; Shee, 1985).

The volatile composition of kimberlite melts remains poorly constrained. Whilst we have attempted to account for volatile modification by alteration (i.e., **Steps 2** and **3**), volatile contents will also be modified by interaction with wall rocks, fluid exsolution during ascent, and degassing on emplacement (e.g., Brooker et al., 2011; Moussallam et al., 2016; Russell et al., 2012; Fedortchouk et al., 2017). Therefore, the reported volatile contents of our reconstructed primitive melts (i.e., Table 2) should only be considered minimum values. The relative concentrations of non-volatile elements in our reconstructed primitive melt can be used to estimate the initial amount of CO_2 (i.e., at source) by using equation (3) of Price et al. (2000), and the melt fraction calculated above (see Electronic Appendix A3). This model suggests 11.0-11.7 wt.% CO_2 was lost from the primary melt, which is broadly consistent with other estimates (e.g., 10.5 and ≥8 wt.% CO_2 loss for the Wesselton aphanitic kimberlite, South Africa, and the Jericho macrocrystic kimberlite, Canada; Price et al., 2000). We provide a renormalised primitive melt composition which accounts for this amount of CO_2 loss (labelled "+CO_2" in Table 2). However, because the calculated amount of CO_2 loss is model dependant, we are reluctant to label this the 'primary' kimberlite melt.

Estimating H_2O loss is more difficult. In the absence of appropriate experimental constraints, we consider that CO_2 and H_2O are effected equally by the processes which cause

volatile loss (during ascent and on emplacement). Maximum and minimum estimates of the primitive H_2O contents are provided by *Models I* and *II* of **Step 6** (i.e., completely deuteric, and secondary origins for matrix serpentine), which equate to 3.9-4.5 and 1.7-1.8 wt.% H_2O, respectively, in the primitive melt. In our preferred primitive melt reconstruction (i.e., *Model IV*) this would equate to 2.1-2.2 wt.% H_2O ("+CO_2+H_2O" in Table 2).

The suggested volatile contents for the Bultfontein kimberlite primitive melt (i.e., 22.9-25.4 wt.% CO_2 and 2.1-2.2 wt.% H_2O) are within the range estimated based on kimberlite saturation experiments at asthenospheric conditions (i.e., 15-27 wt.% CO_2 and 0.5-7.1 wt.% H_2O; Stamm and Schmidt, 2017). However, as sample BK-1 lies at the lower-end of the H_2O/CO_2 spectrum of whole-rock compositions for the Kimberley kimberlites (see section 6.2), we stress that the calculated H_2O contents probably represent close to a minimum estimate for parental melts of the Kimberley kimberlites.

Comparison with Experimental Studies

Comparison of our preferred primitive melt composition (i.e., **Step 6** of *Model V*[P]) with experimental studies on the melting behavior in the systems lherzolite+(C-O-H) and CAMS+CO_2 at upper mantle conditions (i.e., 3-10 Gpa; Dalton and Presnall, 1998; Foley et al., 2009; Gudfinnsson and Presnall, 2005; Brey et al., 2008; Dasgupta et al., 2009) show our reconstructed primitive melt composition plots close to several melt compositions produced experimentally between 5.9 and 8.6 Gpa at 1400-1500°C (Fig. 6-6). Moreover, our preferred primitive melt composition overlaps those obtained from forced saturation experiments conducted at 1525-1650°C (with 0.23 wt.% H_2O), or at 1400°C (with 2.5–3.5 wt.% H_2O; similar to the inferred H_2O contents of this study) (Stamm and Schmidt, 2017).

The major discrepancy between kimberlite melts proposed in this and previous studies, and experimental melts of carbonate lherzolite or kimberlite saturation experiments, is the low

Na_2O contents of natural kimberlites (~0.1-0.2 wt.%; e.g., Kjarsgaard et al., 2009 vs. 0.3-4.5 wt.%; e.g., Brey et al., 2008; Dasgupta et al., 2009; Stamm and Schmidt, 2017). The low Na_2O contents in kimberlite whole-rocks and reconstructed melts is at odds with the high Na_2O concentrations in late crystallising perovskite from the Lac de Gras kimberlites (i.e., up to 3.3 wt.% Na_2O; Chakhmouradian and Mitchell, 2001), late crystallising apatite in the Kimberley kimberlites (i.e., ~3 wt.% Na_2O; Soltys. A. unpublished data), and with the occurrence of alkali carbonate inclusions in olivine rims at Bultfontein (Giuliani et al., 2017). Therefore, we suggest the calculated Na_2O concentrations in our primitive melt represent minimum values.

Sodium loss may have occurred due to exsolution of a volatile- and alkali-bearing fluid during ascent, and/or Na_2O partitioning into late stage fluids following fractional crystallisation. These residual fluids may be lost during degassing and/or alteration potentially after mixing with groundwater (Giuliani et al., 2017; Veksler and Keppler, 2000). Residual saline fluids are preserved as trails of secondary inclusions in olivine in kimberlites worldwide (e.g., Kamenetsky et al., 2014).

Conclusions

We have employed a new approach to reconstruct the composition of kimberlite melts using modal analysis, including discrimination of xenocrystic, magmatic and secondary components, and mineral chemical compositions. This methodology provides a new template which should be applied to a large range of representative kimberlite samples to generate the likely spectrum of primitive kimberlite melt compositions.

For the Bultfontein kimberlite, the calculated melt compositions on emplacement are transitional between silicate and carbonate melts, and contain less SiO_2 and MgO, whilst more CaO when compared with most previous reconstructions. Based on the results of previous

experimental studies at the pressure-temperature conditions of kimberlite emplacement, we suggest this melt composition is a promising candidate to replicate natural kimberlite melts.

Our preferred reconstruction of the primitive melt parental to the Bultfontein kimberlite contains 17.4-19.0 wt.% SiO_2, 20.2-22.8 wt.% MgO, 20.9-21.9 wt.% CaO, 2.1-2.3 wt.% P_2O_5, 1.2-1.4 wt.% TiO_2, 0.9-1.1 wt.% Al_2O_3, and 0.6-0.7 wt.% K_2O, and has a Mg# of 83.4-84.4. Primary volatile contents (i.e., after an attempt to account for volatile loss) are tentatively estimated at ~2.1-2.2 wt.% H_2O and ~22.9-25.4 wt.% CO_2.

This composition contains less SiO_2, MgO and H_2O, whilst more CaO and CO_2 than previous reconstructions of primitive melts based on southern African or Canadian occurrences. These differences are attributed to the fact that our preferred reconstruction accounts for the effects of post-emplacement alteration, as well as the inclusion and assimilation of mantle material. Our modelling shows that the Bultfontein kimberlite was progressively enriched in SiO_2, MgO, Al_2O_3, Cr_2O_3 and Na_2O through the assimilation of orthopyroxene, but also subordinate clinopyroxene and garnet. However, this process appears insufficient to convert carbonatitic to 'kimberlitic' melts through extensive assimilation.

Evidence from experimental studies on melting of carbonated peridotites at upper mantle conditions suggests the Bultfontein kimberlite could be produced by ~0.5% melting of carbonated lherzolite at the pressures conditions of the LAB or upper asthenosphere (i.e., 6.0-8.6 GPa and ~1400-1500 °C). However, Na_2O contents are inconsistent with derivation from a clinopyroxene bearing source, which suggests loss of Na_2O and volatiles on ascent and/or during or after emplacement.

Acknowledgments

The authors thank Kelly Russell, Barbara Scott Smith, Tom Nowicki and Kimberley Webb as well as members and advisors of the KiDs research group for insightful discussions and

feedback. In addition, we are grateful to Kelly Russell for providing a spreadsheet for the calculation of melt fraction values and CO_2 loss. AS also thanks Angus Fitzpayne for advice on the application of partition coefficients. The authors thank Yves Moussallam, Maya Kopylova, and an anonymous reviewer for their comprehensive and constructive reviews which improved the manuscript; and Nelson Eby for efficient editorial handling. This research was supported by an Australia Research Council DECRA award (grant n. DE-150100009) to AG.

Figures

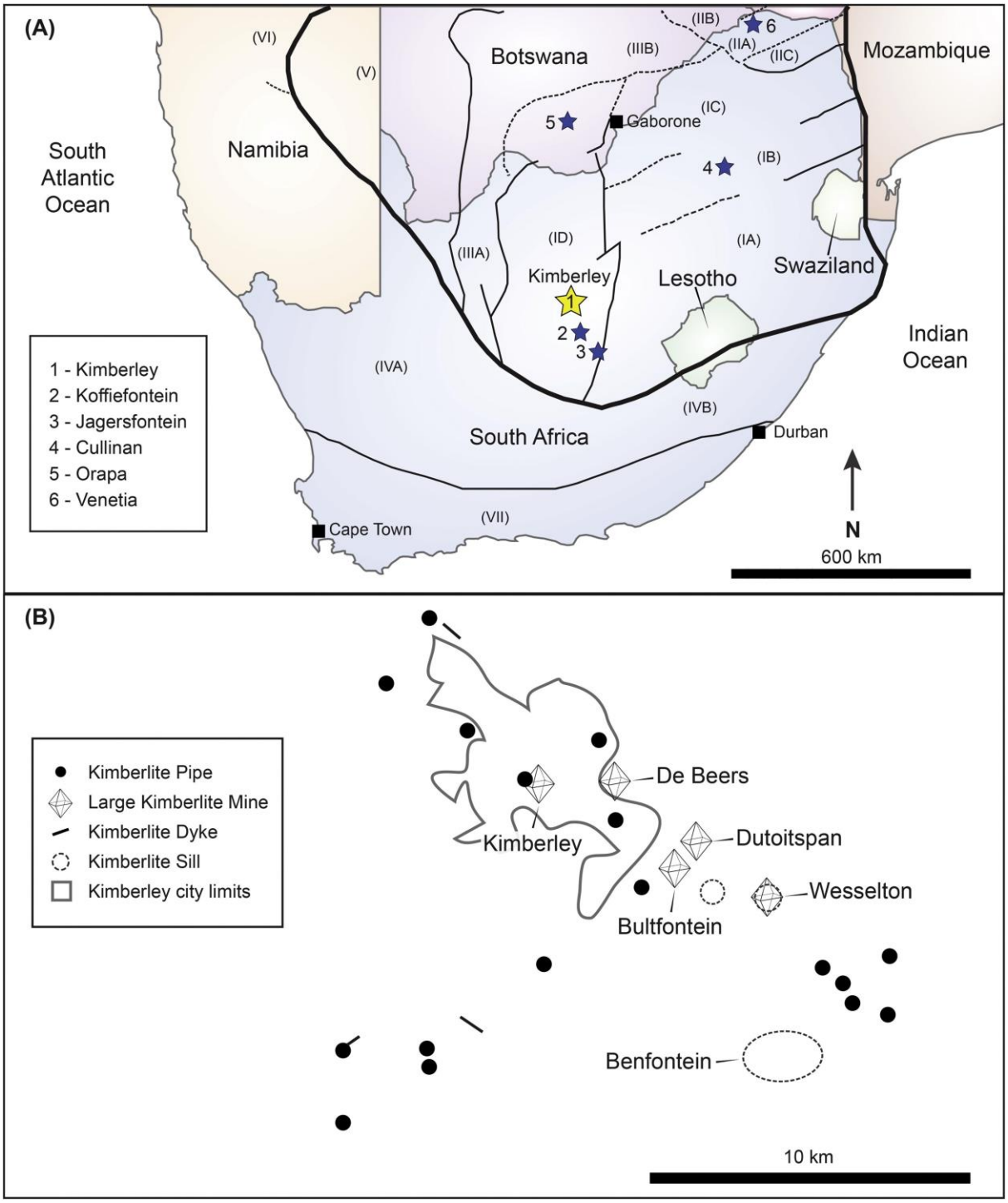

Figure 6-1. (A) A map of the main structural units and locations of major kimberlite mines in southern Africa (modified from Field et al., 2008). (B) Schematic map of the Kimberley area showing the location of the main kimberlite mines, and kimberlite pipes, dykes and sills (modified from Clement 1982).

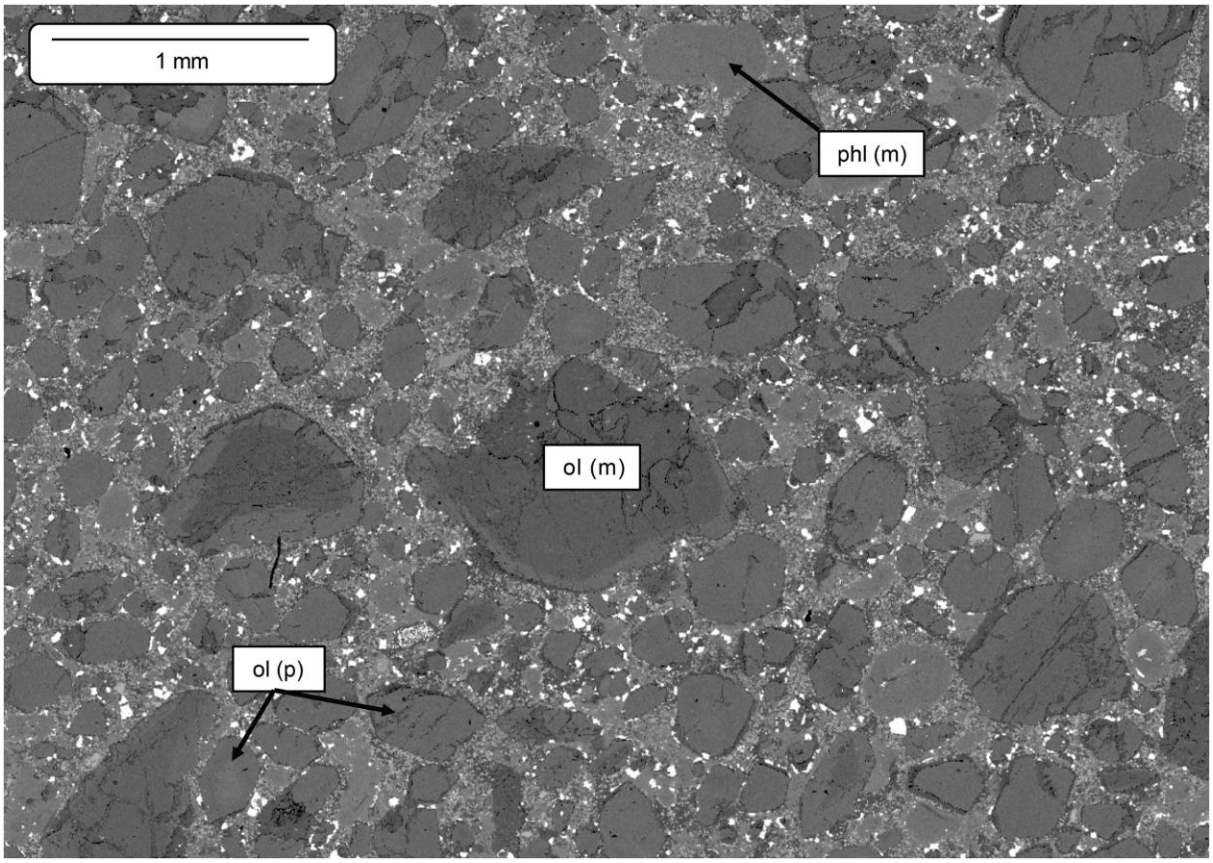

Figure 6-2. Back-scattered electron (BSE) SEM image of the area of sample BK-1 used for reconstruction of the whole-rock composition. Note the inequigranular texture of olivine macrocrysts (ol (m)), phenocrysts (ol (p)) and phlogopite macrocrysts (phl (m)) in a fine-grained groundmass.

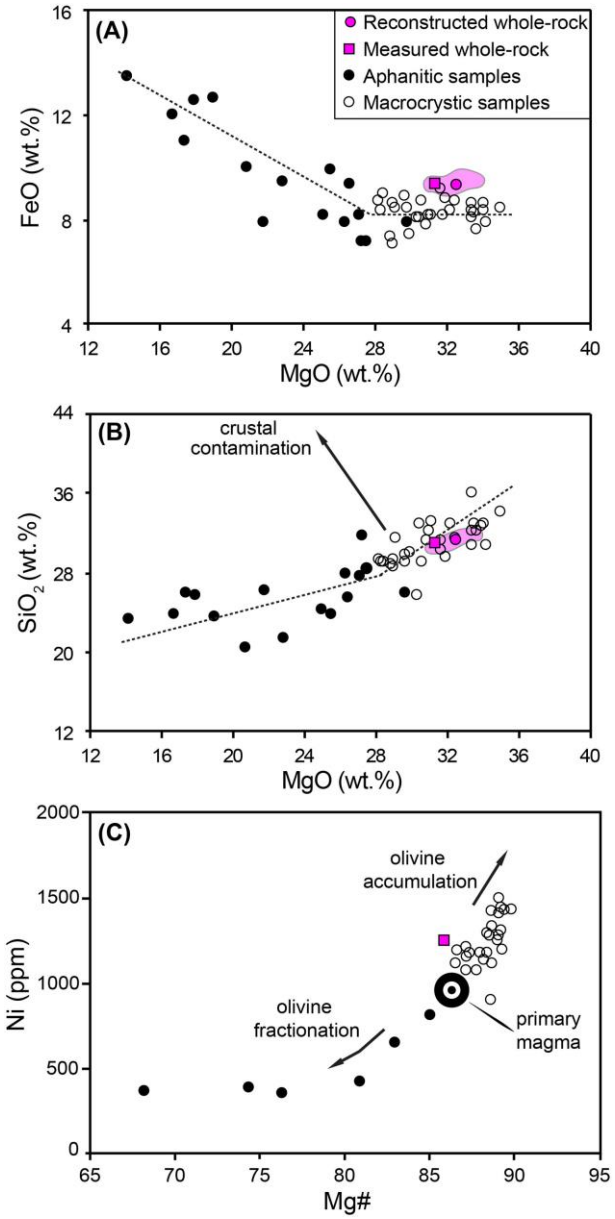

Figure 6-3. The range of reconstructed and measured whole-rock compositions of sample BK-1 (Table 2), plotted in (A) FeO vs MgO, (B) SiO_2 vs MgO, and (C) Ni vs Mg# space. Aphanitic and macrocrystic kimberlite compositions are from le Roex et al., (2003), and Giuliani and Soltys, unpublished data. The dashed lines in panels (A) and (B) are the trends which define macrocrystic and aphanitic sample suits, where the change in slope approximates the parental magma composition according to le Roex et al. (2003). In panel (C) the parental kimberlite magma composition is also from le Roex et al. (2003).

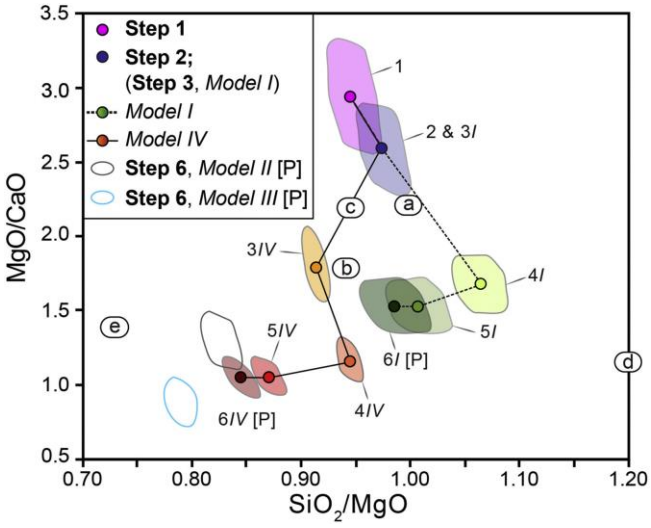

Figure 6-4. The range of reconstructed melt compositions from this study plotted in MgO/CaO vs SiO_2/MgO space (symbols from Fig. 3). Previously reconstructed melt/magma compositions for comparison are shown as follows: (a) le Roex et al. (2003); (b) Shee (1985); (c) Kopylova et al. (2007); (d) Price et al. (2000) – (JD69); and (e) Nielson and Sand (2008) (see Table 5).

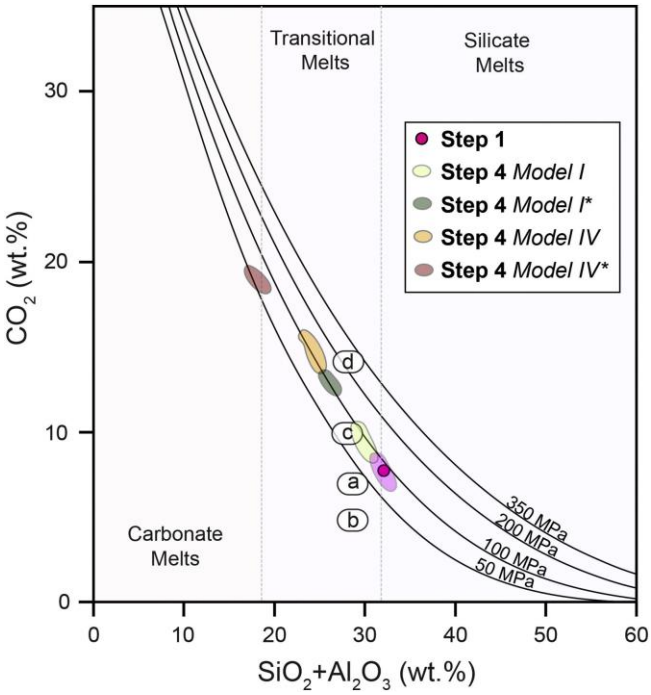

Figure 6-5. CO_2 solubility in carbonate, transitional silicate-carbonate, and silicate melts as a function of SiO_2+Al_2O_3 content (modified from Moussallam et al., 2015). The range of reconstructed melt compositions on emplacement in the upper crust from **Step 4** of *Models I* and *IV* (Table. 4). The asterisk denotes compositions with 80% of the magmatic olivine subtracted (see Table. 4). Previous melt reconstructions are shown for comparison, with symbols carried over from Fig. 4.

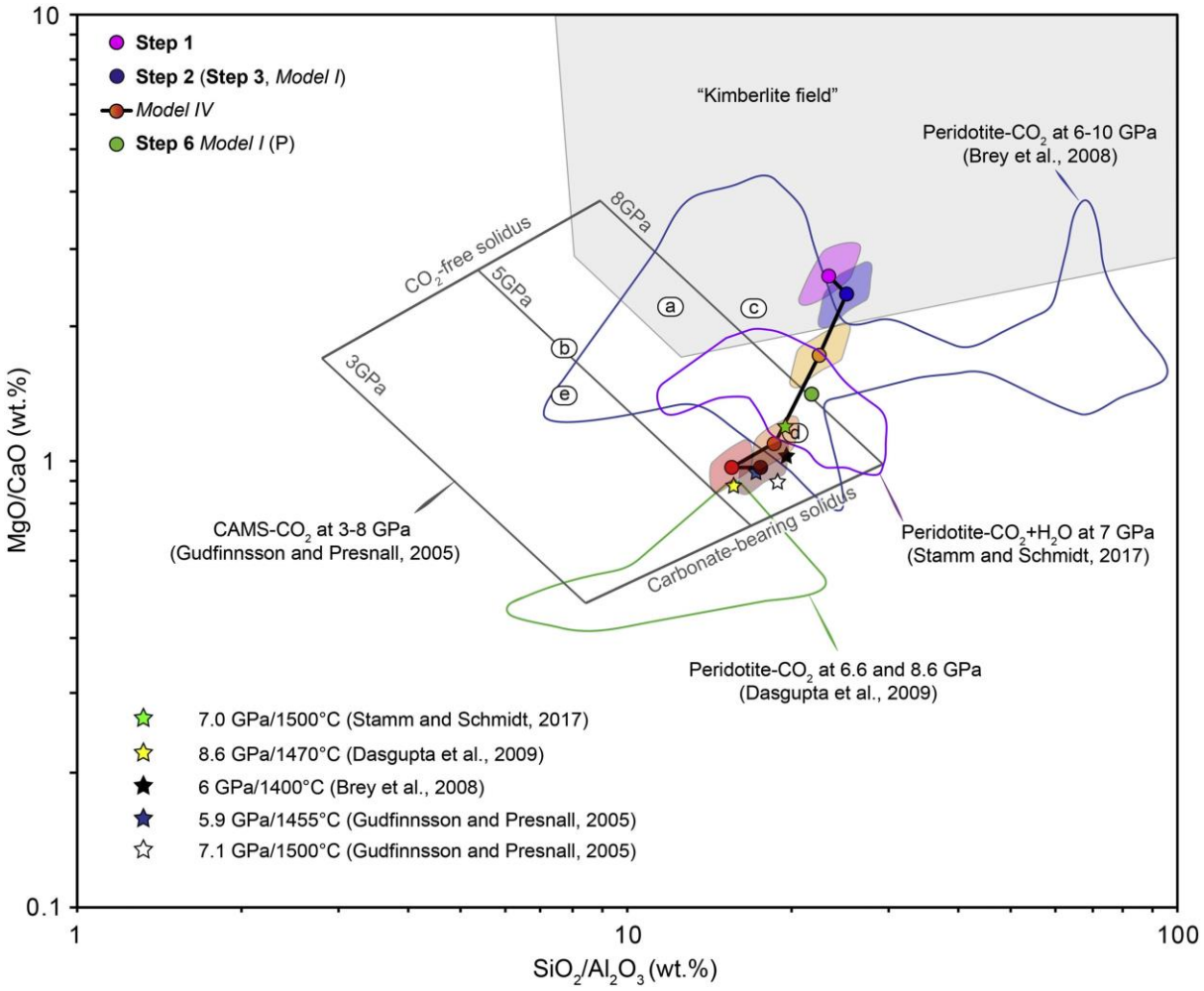

Figure 6-6 MgO/CaO vs SiO_2/Al_2O_3 plot comparing the range of reconstructed whole-rock and melt compositions from this study (Table 2; symbols from Fig. 3, 4), and the compositions of experimentally produced melts in the peridotite+CO_2 and CAMS-CO_2 systems (Brey et al., 2008; Dasgupta et al., 2009; Gudfinnsson and Presnall, 2005; Stamm and Schmidt, 2017). Previous reconstructions of kimberlite melts are shown for comparison, with symbols carried over from Fig. 4. The grey shaded area represents 'uncontaminated' whole-rock kimberlite compositions from worldwide localities (Rock, 1991).

Tables

Table 6-1. Measured modal mineral abundances and the proportions of xenocrystic and magmatic componenets in olivine of sample BK-1

Phase	**Vol.%**		**Mean %**
Olivine macrocrysts	13.3	**Olivine phenocrysts (*n* = 61)**	
Olivine phenocrysts	30.7	Xenocrystic component	30.1
Phlogopite macrocrysts	2.5	Magmatic component	69.9
Phlogopite microphenocrysts	4.2		
Groundmass phlogopite	1.6	**Olivine macrocrysts (*n* = 5)**	
Apatite*	4.4	Xenocrystic component	77.7
Calcite	13.6	Magmatic component	22.3
Dolomite	4.5		
Serpentine†	20.4		
Matrix	14.8		
Pseudomorphic after Monticellite	5.6		
Perovskite	0.3		
TIMAC	0.1		
Ulvöspinel	1.7		
Magnetite	0.3		
Groundmass ilmenite	0.3		
Sum	97.9		

* The volumetric abundance of apatite has been forced to a value where the P_2O_5 content of the reconstructed whole-rock matches that of the measured whole-rock. For this reason, the sum of volumetric percentages is <100.

† Serpetine includes matrix serpetine and serpetine replacing moticellite

The standard deviation of the magmatic and xenocrystic components in olivine is 12.1% for phenocrysts and 4.4% for macrocrysts.

Table 6-2. Measured whole-rock, and reconstructed whole-rock and melt compositions for *Models I* and *IV*.

	XRF	Step 1	Step 2 & 3		Step 4		Step 5	
			I	***IV***	***I***	***IV***	***I***	***IV***
SiO_2	30.66	30.1-31.6	30.6-31.9	26.1-28.4	28.0-29.5	22.3-24.5	25.9-27.3	20.0-21.8
TiO_2	1.54	1.1-1.3	1.0-1.2	1.0-1.2	1.3-1.6	1.3-1.5	1.4-1.7	1.4-1.6
Al_2O_3	1.83	1.2-1.4	1.1-1.4	1.1-1.3	1.2-1.4	1.2-1.4	1.3-1.5	1.2-1.4
Cr_2O_3	0.18	0.1-0.2	0.1-0.2	0.1-0.2	0.2	<0.2	0.1-0.2	0.1-0.2
FeO_t	9.35	9.1-9.5	8.9-9.3	8.1-8.5	8.9-9.4	7.8-8.3	9.1-9.6	7.9-8.4
MnO	0.18	0.1	0.1	0.1	0.1	0.1	0.1	0.1
MgO	31.42	31.2-33.8	30.8-33.2	28.3-31.2	25.9-28.0	23.3-26.0	23.5-27.4	22.6-25.3
NiO		0.1	0.1	0.1	<0.1	<0.1	<0.1	<0.1
CaO	10.93	10.4-12.0	11.7-13.3	15.6-18.1	15.4-17.3	25.0	16.6-18.5	22.2-24.4
Na_2O	0.19	0.2	0.2	0.1	0.2-0.3	0.1	0.2-0.3	0.1
K_2O	1.07	0.8-1.0	0.7-0.9	0.7-0.9	0.7-0.8	0.6-0.8	0.7-0.9	0.7-0.8
P_2O_5	1.82	1.8	1.7	1.7	2.2-2.3	2.2-2.3	2.4-2.5	2.3-2.5
BaO	0.17	0.1	0.1	0.1	0.1	<0.1	0.1	0.1
F		0.1	0.1	0.1	0.1	0.1	0.1	0.1
LOI*	9.20							
H_2O		2.3-2.7	2.1-2.6	1.2-1.4	2.7-3.2	1.5-1.6	2.9-3.4	1.6-1.7
CO_2		6.8-8.3	6.4-7.8	10.0-12.3	8.5-10.2	13.2-15.5	9.1-11.0	14.3-16.6
Sum	98.5	100.0	100	100.0	100.0	100.0	100	100.0
Mg#	85.7	85.7-86.5	85.8-86.6	86.0-86.8	83.5-84.4	84.1-85.0	82.9-83.8	83.4-84.4
ln(Si/Al)	2.69	2.9-3.1	3.0-3.2	2.8-3.1	2.8-3.0	2.7-2.9	2.7-2.9	2.5-2.7
Si/Mg	0.98	0.9-1.0	1	0.90	1.10	0.9-1.0	1.0	0.90
Cl†	0.97	0.9-1.0	0.1	0.90	1.10	0.9-1.0	1.0	0.90
H_2O#		0.2-0.3	0.2-0.3	0.10	0.2-0.3	0.10	0.2-0.3	0.10

* Lost on ignition

† Contamination Index after Clement, (1982) = (SiO_2 + Al_2O_3+ Na_2O)/(2K_2O + MgO)

H2O/(H2O+CO2)

‡ Total change represents the absolute difference between reconstructed melts at **Step 6** and the reconstructed whole-rock at **Step 1.**

Table 6-2. Continued

	Step 6						Total change‡	
	I[**P**]	*IV*[**P**]	*IV*[**P**] +CO_2	*IV*[**P**] + Volatiles	*I*[**C**]	*IV*[**C**]	*I*[**P**]	*IV*[**P**]
SiO_2	25.5-26.9	19.5-21.3	17.5-19.1	17.4-19.0	25.0-26.5	19.0-20.7	5.0-4.3	10.9-10.0
TiO_2	1.4-1.7	1.4-1.6	1.2-1.5	1.2-1.4	1.5-1.7	1.4-1.6	0.4-0.5	0.3-0.4
Al_2O_3	1.1-1.3	1.0-1.2	0.9-1.1	0.9-1.1	0.7-1.1	0.7-1.0	<0.2	0.2-0.1
Cr_2O_3	0.1	0.1	~0.1	~0.1	<0.1	<0.1	<0.1	<0.1
FeO_t	9.2-9.7	7.9-8.5	7.1-7.6	7.1-7.6	9.2-9.8	8.0-8.5	<0.3	1.3-0.9
MnO	0.1	0.1	~0.1	~0.1	0.1	≤0.1	<0.1	<0.1
MgO	25.4-27.6	22.7-25.5	20.3-22.9	20.2-22.8	25.5-27.8	22.7-25.6	6.2-5.8	8.8-8.2
NiO	<0.1	<0.1	<0.1	<0.1	<0.1	<0.1	≤0.1	<0.1
CaO	16.7-18.6	22.4-24.6	20.2-22.0	20.1-21.9	16.8-18.8	22.7-24.9	6.2-6.7	11.8-12.9
Na_2O	0.2-0.3	0.1	~0.1	~0.1	0.2-0.3	0.1	<0.1	<0.1
K_2O	0.7-0.9	0.7-0.8	0.6-0.8	0.6-0.7	0.8-0.9	0.7-0.9	<0.1	≤0.1
P_2O_5	2.4-2.6	2.3-2.5	2.1-2.3	2.1-2.3	2.4-2.6	2.4-2.6	0.6-0.7	0.5-0.7
BaO	0.1	0.1	<0.1	~0.1	≤0.1	0.1	<0.1	<0.1
F	0.1	0.1	~0.1	~0.1	0.1	0.1	<0.1	<0.1
LOI*								
H_2O	3.0-3.5	1.6-1.8	1.5-1.6	2.1-2.2	3.0-3.6	1.7-1.8	0.7-0.8	0.6-1.0
CO_2	9.3-11.2	14.6-16.8	23.1-25.5	22.9-25.4	9.5-11.4	15.0-17.1	2.5-2.8	7.6-8.8
Sum	100.0	100.0	100.0	100	100	100.0	0.00	0.00
Mg#	82.9-83.8	83.4-84.4	83.4-84.4	83.4-84.4	82.9-83.8	83.4-84.4	3.2-2.6	2.0-2.7
ln(Si/Al)	2.8-3.1	2.6-2.9	2.6-2.9	2.6-2.9	3.0-3.4	2.8-3.2	<0.2	0.2-0.4
Si/Mg	1.0	0.8-0.9	15.8-21.1	15.8-21.1	0.9-1.0	0.80	<0.1	0.10
Cl†	1.0	0.8-0.9	0.8-0.9	0.8-0.9	0.9-1.0	0.80	<0.1	0.10
H_2O#	0.2-0.3	0.10	<0.1	<0.1	0.2-0.3	0.10	<0.1	0.2-0.1

Table 6-3. Reconstructed melt compositions parental to sample BK-1 on emplacement in the upper crust, compared with previously reconstructed compositions tested in experimental studies

1 **Step 4**, *Model I*

2 **Step 4**, *Model I* – minus 80% magmatic olivine

3 **Step 4**, *Model IV*

4 **Step 4**, *Model IV* – minus 80% magmatic olivine

5 J - (Sparks et al., 2009)

6 LR - (Sparks et al., 2009)

7 WR - (Sparks et al., 2009)

8 WSRox - (Brooker et al., 2011)

Ref.	**1**	**1***	**2**	**2***	**3**	**3***	**4**	**4***	**5***	**6***	**7***	**8***
SiO_2	28.0-29.5	32.2-33.3	23.9-24.9	29.0-29.8	22.3-24.5	26.9-28.7	15.8-17.4	20.1-21.8	34.37	36.28	26	17.34
TiO_2	1.3-1.6	1.5-1.8	1.9-2.1	2.3-2.5	1.3-1.5	1.5-1.8	1.8-1.9	2.2-2.4	0.65	0.9	8.27	8.46
Al_2O_3	1.2-1.4	1.4-1.6	1.7-1.9	2.1-2.3	1.2-1.4	1.4-1.6	1.6-1.7	2.0-2.2	0.26	0.92	4.19	3.71
Cr_2O_3	0.2	0.2	0.2	0.3	<0.2	0.2	0.2	0.30	1.65			0.15
FeO_t	8.9-9.4	10.1-10.7	8.4-8.6	10.2	7.8-8.3	9.3-9.8	10.2-10.8	12.8-13.7	7.16	10.25	15.67	17.84
MnO	0.1	0.1	0.1	0.1	0.1	0.1	0.1	0.10	0.18	0.21	0.37	0.23
MgO	25.9-28.0	29.8-31.6	18.0-19.9	21.8-23.8	23.3-26.0	28.2-30.5	14.4-16.6	18.4-20.8	28.19	34.52	23.63	20.32
NiO	<0.1	0.1	<0.1	<0.1	<0.1	0.1	<0.1	<0.1				
CaO	15.4-17.3	17.4-19.9	21.7-23.1	25.9-28.0	25.0	24.1-27.7	27.7-29.2	34.7-37.2	24.99	14.65	14.68	25.44
Na_2O	0.2-0.3	0.3	0.3-0.4	0.4	0.1	0.1-0.2	0.2	0.20	0.18	0.4	0.07	0.12
K_2O	0.7-0.8	0.8-0.9	1.0-1.1	1.2-1.3	0.6-0.8	0.8-0.9	0.9	1.1-1.2	0.52	0.34	1.32	1.27
P_2O_5	2.2-2.3	2.5-2.6	3.0-3.2	3.6-3.9	2.2-2.3	2.6-2.7	2.8-3.0	3.5-3.8	0.79	1.4	4.43	4.57
BaO	0.1	0.1	0.1	0.1-0.2	<0.1	0.1	0.1	0.10	0.67			0.1
F	0.1	0.1	0.2	0.2	0.1	0.1	0.1-0.2	0.20				
H_2O	2.7-3.2		3.9-4.2		1.5-1.6		2.0-2.1					
CO_2	8.5-10.2		12.4-13.2		13.2-15.5		18.3-19.4					
Mg#	83.5-84.4		79.3-80.6		84.1-85.0		70.5-74.3		87.5	85.7	72.9	67.0

* Compositions reported on a volatile free basis.

Table 6-4. Reconstructed whole-rock composition of sample BK-1 compared with worldwide whole-rock hypabyssal kimberlite data.

1 This study (measured - XRF)
2 This study (reconstructed) – **Step 1**
3 Kimberley (le Roux et al., 2003)
4 Kimberley (le Roux et al., 2003)
5 Southern Africa - On Craton only (Becker and le Roux, 2006)
6 Lekkerfontein (Becker and le Roux, 2006)
7 Southern Africa "Group IB" (Smith et al., 1985)
8 Lac de Gras (Kjarsgaard et al., 2009)
9 Jericho (Price et al., 2000)
10 Gahcho Kué (Kamenetsky et al., 2009)
11 Udachnaya-East - Low H_2O (Kamenetsky et al., 2009)
12 Udachnaya-East - High H_2O (Kamenetsky et al., 2009)
13 Majuagaa (Nielson and Sand, 2008)

Reference	**1**	**2**	**3**	**4**	**5**	**6**	**7**	**8**	**9**	**10**	**11**	**12**	**13**
Country	SA	SA	SA	SA	SA	SA	SA	Canada	Canada	Canada	Russia	Russia	Greenland
n	1	1	21	12	12	1	7	76	10	5	9	14	19
Texture	M	M	M	A	M	A	-	-	A	**-**	**-**	**-**	M
SiO_2	30.66	30.1-31.6	30.34	26.00	28.59	22.47	32.1	32.46	28.71	35.8	26.71	29.29	25.84
TiO_2	1.54	1.1-1.3	1.87	2.58	2.49	4.53	2	0.60	0.74	0.68	1.25	1.27	3.62
Al_2O_3	1.83	1.2-1.4	1.98	2.64	2.56	4.43	2.6	2.01	1.68	2.58	1.75	1.79	1.42
FeO_t	9.35	9.1-9.5	8.25	9.40	7.26	12.00	9.2	7.59	6.57	7.8	8.09	8.34	10.32
MgO	31.42	31.2-33.8	30.84	23.63	27.54	18.63	28.5	34.28	25.76	33.88	31.33	33.14	33.36
CaO	10.93	10.4-12.0	9.80	14.21	10.69	15.37	8.2	8.34	15.39	6.29	12.19	11.84	10.72
Na_2O	0.19	0.2	0.14	0.26	0.27	0.25	0.2	0.07	0.16	0.14	3.23	0.31	0.09
K_2O	1.07	0.8-1.0	1.08	1.10	0.85	1.63	1.1	0.72	0.36	1.46	1.33	1.01	0.2
P_2O_5	1.82	1.8	1.39	2.05	2.07	1.49	1.1	0.52	0.74	0.27	0.49	0.44	0.5
LOI	9.20												
H_2O		2.3-2.7	7.31	6.94	7.41	5.92	8.6	6.54	6.15	4.42	0.38	2.84	n.d.
CO_2		6.8-8.3	5.46	7.69	5.22	9.63	4.3	6.07	11.25	4.95	9.42	7.96	n.d.
Mg#	85.7	85.7-86.5	88.3	82.7	84.3	74.6	84.7	88.9	87.1	88.6	87.3	87.6	85.2

The texures denoted "M" and "A" represent Macrocrystic and Apahnitic samples, respectivly.

Table 6-5. Reconstructed primitive melt compositions parental to sample BK compared with previously estimates of primitive kimberlite melt/magma compositions.

1	**Step 5**, *Model I*	**8**	Lac de Gras - Low Ti Parental magma (Kjarsgaard et al., 2009)
2	**Step 6**, *Model I* [**P**]	**9**	Lac de Gras - High Ti Parental magma (Kjarsgaard et al., 2009)
3	**Step 5**, *Model IV*	**10**	Jerico - Primitive melt before orthpyroxene assimilation (Kopylova et al., 2009)
4	**Step 6**, *Model IV* [**P**]	**11**	Jerico - Primitive melt, sample JD69, Median of 3 analyses (Price et al., 2000)
5	Kimberley - Primary magma (le Roux et al., 2003)	**12**	Jerico - Primitive melt, Sample JD82, Median of 3 analyses (Price et al., 2000)
6	Southern African - Primary magma (Becker and le Roux, 2006)	**13**	Majuagaa - Parental melt (Nielson and Sand, 2008)
7	Wesselton - Primitive melt (Shee, 1985)	**14**	Majuagaa - Parental melt (Nielson and Jensen, 2005)

Ref.	**1**	**2**	**3**	**4**	**5**	**6**	**7**	**8**	**9**	**10**	**11**	**12**	**13**	**14**
Country	South Africa	South Africa	South Africa	South Africa	South Africa	Southern Africa	South Africa	Canada	Canada	Canada	Canada	Canada	Greenland	Greenland
SiO_2	25.9-27.3	25.5-26.9	20.0-21.8	19.5-21.3	26.50	26.15	25.60	31.79	27.46	26.70	27.00	28.13	17.47	20.48
TiO_2	1.4-1.7	1.4-1.7	1.4-1.6	1.4-1.6	2.20	2.58	3.35	0.72	1.12	1.73	0.51	0.71	4.99	0.19
Al_2O_3	1.3-1.5	1.1-1.3	1.2-1.4	1.0-1.2	2.20	2.76	3.31	3.08	2.54	1.57	1.33	1.61	2.27	2.33
Cr_2O_3	0.1-0.2	0.1	0.1-0.2	0.1	n.d.	0.18	0.24	n.d.	n.d.	0.36	0.01	0.02	0.28	n.d.
FeO_t	9.1-9.6	9.2-9.7	7.9-8.4	7.9-8.5	8.00	9.65	10.30	8.28	7.29	7.58	5.43	6.59	10.61	9.62
MnO	0.1	0.1	0.1	0.1	n.d.	0.19	0.21	0.19	0.17	0.18	0.14	0.16	0.24	0.2
MgO	23.5-27.4	25.4-27.6	22.6-25.3	22.7-25.5	26.50	25.20	27.20	30.77	27.46	28.25	22.39	23.09	23.98	25.67
NiO	<0.1	<0.1	<0.1	<0.1	0.01	0.10	0.01	n.d.	n.d.	n.d.	0.01	0.01	0.02	n.d.
CaO	16.6-18.5	16.7-18.6	22.2-24.4	22.4-24.6	12.00	13.26	15.30	9.23	14.24	12.90	19.37	16.66	17.27	17.96
Na_2O	0.2-0.3	0.2-0.3	0.1	0.1	n.d.	0.16	0.28	0.10	0.09	0.10	0.15	0.19	0.13	0.16
K_2O	0.7-0.9	0.7-0.9	0.7-0.8	0.7-0.8	1.50	0.83	0.70	1.03	0.61	1.26	0.43	0.46	0.32	0.33
P_2O_5	2.4-2.5	2.4-2.6	2.3-2.5	2.3-2.5	n.d.	2.04	1.83	0.97	0.71	0.40	0.61	0.78	0.81	0.83
BaO	0.1	0.1	0.1	0.1	n.d.	n.d.	0.01	n.d.	n.d.	n.d.	0.04	0.03	0.16	n.d.
F	0.1	0.1	0.1	0.1	n.d.	n.d.	n.d.	n.d.	n.d.	n.d.	n.d.	n.d.	n.d.	n.d.
H_2O	2.9-3.4	3.0-3.5	1.6-1.7	1.6-1.8	12.30	7.33	6.20	8.72	6.10	9.07	7.10	6.70	n.d.	n.d.
CO_2	9.1-11.0	9.3-11.2	14.3-16.6	14.6-16.8	7.00	8.19	4.77	5.13	12.20	9.88	14.01	12.06	n.d.	n.d.
Mg#	82.9-83.8	82.9-83.8	83.4-84.4	83.4-84.4	86	84.5	82.5	86.9	87.0	86.9	88.0	86.2	80.1	82.6

CHAPTER 7: CONCLUSIONS

This dissertation documents the petrography, mineralogy, and geochemistry of a suite of coherent kimberlite samples from the Kimberley cluster (South Africa). This final chapter provides a summary of kimberlite crystallisation and melt evolution processes, following a "bottom-up" approach, i.e., starting with pre-ascent kimberlite metasomatism of the lithospheric mantle, and finishing with kimberlite modification and alteration in the upper crust. This is followed by a summary of the results of geochemical modelling of kimberlite melt compositions.

The earliest event that can be confidently ascribed a kimberlitic origin is the pre-ascent metasomatism of the lithospheric mantle. This is recorded by (in no specific order) the production of:

(1) transitional olivine zones (i.e., heterogeneous metasomatised xenocrystic cores);

(2) antecrystic olivine (i.e., internal olivine zone (I));

(3) antecrystic phlogopite (i.e., high Cr-Ti phlogopite rims);

(4) megacrystic suite minerals; and

(5) sheared peridotites.

A significant proportion (~45%) of the xenocrystic olivine (and probably other entrained material) in the Kimberley kimberlites represents kimberlite metasomatised material, rather than typical granular peridotitic material. This suggests that the xenocrystic cargo entrained by kimberlites may not be representative of the wider lithospheric mantle; i.e., it has been extensively metasomatised by previous kimberlite activity. This supports the argument that extensive kimberlite metasomatism may assist, or even be a prerequisite for, the kimberlite melt to ascend through the lithospheric mantle and reach the upper crust without being consumed by wall-rock interaction.

In the Kimberley kimberlites, and probably most other kimberlites, the first phases to crystallise directly from the kimberlite melt are olivine internal zone (II) and Cr-rich spinel. This olivine is characterized by elevated Mg# and Ni contents relative to the rims, and has a euhedral shape when overgrowing smaller cores. This zone is argued to have crystallised from a primitive kimberlite melt during ascent through, and partial assimilation of, lithospheric mantle material. The Ni/Mg, Ca/Fe, and Mn/Fe ratios of this liquidus olivine are remarkably similar to primitive olivine from other mantle-derived carbonate-rich magmas (i.e., orangeites, lamproites, ultramafic lamprophyres), and lie at the extremity of a linear trend defined by olivine produced in melting experiments of carbonated peridotite at mantle conditions. Therefore, it is proposed that olivine with these compositions is the hallmark of olivine in equilibrium with melts derived from carbonate-rich peridotite sources.

Crystallisation of olivine internal (II) zones ± Cr-spinel is followed by the crystallisation of olivine rims, TIMAC-MUM spinel, rutile, and magnesian ilmenite. Many of the rimward geochemical variations displayed by these phases are consistent with fractional crystallisation (e.g., Cr decreases in spinel and ilmenite, Ni decreases coupled with Ca and Mn increases in olivine). These geochemical features, combined with petrographic evidence (e.g., mechanical abrasion of the rims due to attrition, olivine rim compositions lining decompression fractures) indicate crystallisation before emplacement into the upper crust (i.e., during ascent through the lithosphere). The compositions of these early crystallising phases (i.e., olivine internal zones (II) and rims, Cr-spinel, Mg-ilmenite) are indistinguishable across different pipes of the Kimberley cluster, and across different intrusion styles of CK (i.e., dykes, sills, and root zones). There are however rare exceptions, with some sills (or individual magma batches within these sills) appearing to have undergone pre-emplacement fractionation of these early crystallising phases (i.e., Wesselton Water Tunnel Sills and some units of the Benfontein sills). Not all dykes/sills represent crystallisation of fractionated magmas, but it appears that fractionated

magmas may be more likely to emplace as dykes/sills. The indistinguishable compositions of early crystallised phases across most of the Kimberley kimberlites, regardless of emplacement style, imply indistinguishable primitive melt compositions.

Following early olivine and oxide mineral crystallisation, the mineralogy and mineral compositions of the crystallising phases record a change in melt composition. This marks the onset of groundmass crystallisation of an assemblage that typically includes olivine rinds, MUM spinel, magnetite, perovskite, monticellite, apatite, and kinoshitalite mica. These phases record the following geochemical features: (I) increasing Ca activity of the melt (e.g., perovskite replacing ilmenite, olivine compositions from rim to rind, late crystallisation of monticellite, apatite, and calcite); (II) increasing Mg/Fe^{2+} ratios as indicated by zonation of monticellite, olivine zonation from rim to rind, and late-stage Mg-rich ilmenite; (III) late-stage enrichment in Mn, Ba, Sr, Na, Zr, S (e.g., secondary Na-, Sr-, and Ba-carbonate inclusions in olivine and groundmass carbonates, crystallisation of sulfides, barite and (Ca-)Zr phases, Mn-rich olivine rinds, late Na-rich apatite/perovskite rims). These geochemical features are attributed to a combination of fractional crystallisation (i.e., higher Ca, Mn, Ba, Sr) and increasing oxygen fugacity (higher Mg/Fe). The increase in Mg/Fe ratios may be further accentuated by extensive late crystallisation of Fe-rich spinel.

The composition and petrography of groundmass apatite and mica from multiple samples showing different style of magma emplacement were studied to trace late kimberlite evolution in more detail. In contrast to the relatively homogeneous composition of early crystallising olivine and oxide minerals, later stage apatite shows systematic differences between the different intrusion modes of coherent kimberlite. Apatite from dyke/sill kimberlites have low and constant Sr, with high and variable Si. In contrast, apatite from root-zone kimberlites have high and variable Sr, with low and constant Si. The Si-enrichment of apatite from dykes/sills is attributed to the coupled substitution of CO_3^{2-} and SiO_4^{4-} for P_2O_5, reflecting

higher CO_2 contents in the melts parental to dyke/sill kimberlites. The low Sr contents of apatite in dyke/sill kimberlites indicate melt-apatite equilibrium, because calculated D_{Sr} are close to unity, which is consistent with experimental partitioning of Sr between apatite and carbonate-rich melts. In contrast, the significantly higher Sr contents of apatite from root-zone kimberlites likely requires crystallisation from, or overprinting by, a (H_2O-rich) fluid (D_{Sr} >>1). If correct, near ubiquotus overprinting of root zone samples by hydrous fluids indicates these rocks originally had relativly low porosity, lending support to their formation by the intense welding of classic material.

The higher CO_2/H_2O ratio of the magma parental to kimberlite dykes/sills, relative to those parental to root-zone kimberlites, is corroborated by the higher modal abundance of carbonates, the occasional presence of dolomite and calcite phenocrysts, and concomitant reduced proportions of other groundmass phases (e.g., serpentine, mica, monticellite) in dykes and sills. Additionally, during late alteration of dyke/sill kimberlites by deuteric (i.e. late-stage magmatic) fluids, monticellite is typically replaced by carbonates, whereas olivine and pleonaste are stable. This again indicates that the residual fluids of dyke/sill kimberlites evolve to higher CO_2/H_2O ratios. We suggest that higher concentrations of CO_2 are retained in kimberlite dykes/sills due to a higher confining pressures (i.e., lack of breakthrough to the surface) and therefore volatile retention in the magmatic system. In contrast, exsolution of CO_2-rich fluids from the magmas parental to root zone kimberlites would increase the H_2O/CO_2 ratios in the residual melt and promote the crystallisation of mica, monticellite, and serpentine at the expense of dolomite and calcite.

The results of the above described geochemical and petrographic investigation guided the development of a new quantitative melt reconstruction method. Using the opposite approach to the above summary, a top-down approach, the modelling involves a starting bulk composition of a rock sample with the effects of alteration and assimilation successively

'removed', to reconstruct the composition of the primitive kimberlite melt. The reconstructed bulk-rock composition was obtained using modal mineral abundances and mineral compositions. The accuracy of this whole-rock reconstruction method is validated by the similarity between reconstructed and measured whole-rock compositions. The effects of post-emplacement modification include serpentinisation and replacement of carbonates. During ascent the kimberlite melt is assumed to lose some CO_2, crystallise olivine (internal zones and rims), and entrain assimilated mantle material in the proportions of those in mantle xenoliths. This approach permits discernment of melt compositions at different stages of kimberlite evolution.

The calculated kimberlite melt composition on emplacement into the upper crust is transitional between silicate and carbonate melts, and contains less SiO_2 and MgO, but more CaO, compared to most previous reconstructions. Based on the results of previous experimental studies at the pressure-temperature conditions of kimberlite emplacement, we suggest this melt composition is a promising candidate to replicate natural kimberlite melts in the upper crust.

The preferred primitive melt reconstruction model indicates that the melt parental to the Bultfontein kimberlite, and by extension the Kimberley kimberlites, contains 17.4-19.0 wt% SiO_2, 20.2-22.8 wt% MgO, 20.9-21.9 wt% CaO, 2.1-2.3 wt% P_2O_5, 1.2-1.4 wt% TiO_2, 0.9-1.1 wt% Al_2O_3, and 0.6-0.7 wt% K_2O, and has a Mg# of 83.4-84.4. Primary volatile contents are estimated at ~2.1-2.2 wt% H_2O and ~22.9-25.4 wt% CO_2. These compositions do not resemble estimates based on whole-rock kimberlite analyses (e.g., le Roex et al., 2003), but are closer in composition to those proposed based on the evaluation of experimental studies (Brooker et al., 2011; Sparks et al., 2009). These results imply that extensive assimilation cannot convert carbonatites into kimberlites as proposed in some previous models. This reconstructed melt composition is in equilibrium with asthenospheric source rocks. Comparison with experimental

studies indicates that the Kimberley kimberlites could be produced by ~0.5% melting of carbonated lherzolite in the upper asthenosphere (i.e., 6.0-8.6 GPa and ~1400-1500 °C).

This thesis represents progress toward constraining the composition and evolution of kimberlite melts, with implications for their source composition/location and near-surface emplacement mechanisms. However, despite this study and over a century of dedicated research, many aspects of kimberlite genesis remain enigmatic. The mineral and bulk compositions of kimberlites are generally well understood; however, their variation as a function of time and space is not well constrained. This thesis documents the variation of olivine and apatite compositions from different types of coherent kimberlites (root zones as well as dykes and sills) from a single cluster. Kimberlite research would benefit greatly from similar systematic comparative studies of all kimberlite emplacement modes across a larger geographic distribution (e.g., fields, provinces) as well as through geological time.

REFERENCES

Abersteiner, A., Kamenetsky, V.S., Goemann, K., Giuliani, A., Howarth, G.H., Castillo-Oliver, M., Thompson, J., Kamenetsky, M., Cherry, A. (2019). Composition and emplacement of the Benfontein kimberlite sill complex (Kimberley, South Africa): Textural, petrographic and melt inclusion constraints. Lithos 324-325:297-314

Abersteiner, A., Kamenetsky, V.S., Golovin, A. V., Kamenetsky, M., Goemann, K. (2018b). Was crustal contamination involved in the formation of the serpentine-free Udachnaya-East kimberlite? New insights into parental melts, liquidus assemblage and effects of alteration. Journal of Petrology 59, 1467-1492.

Abersteiner, A., Kamenetsky, V.S., Pearson., D.G., Kamenetsky, M., Goemann, K., Ehrig, K., Rodemann, T. (2018). Monticellite in group-I kimberlites: Implications for evolution of parental melts and post-emplacement CO2 degassing. Chemical Geology 478:76-88.

Afanasyev, A., Melnik, O., Porritt, L., Schumacher, J.C., Sparks, R.S.J. (2014). Hydrothermal alteration of kimberlite by convective flows of external water. Contributions to Mineralogy and Petrology. 168 (1), 1-17.

Allsopp, H.L., Barrett, D.R. (1975). Rb-Sr age determinations on South African kimberlite pipes. Physics and Chemistry of the Earth 9, 605-617.

Ammannati, E., Jacob, D.E., Avanzinelli, R., Foley, S.F. Conticelli, S. (2016). Low Ni olivine in silica-undersaturated ultrapotassic igneous rocks as evidence for carbonate metasomatism in the mantle. Earth and Planetary Science Letters 444, 64-74.

Aoki, K. I. (1975). Origin of phlogopite and potassic richterite bearing peridotite xenoliths from South Africa. Contributions to Mineralogy and Petrology, 53(3), 145-156.

Apter, D.B., Harper, F.J., Wyatt, B.A., Scott Smith, B. (1984). The geology of the Mayeng kimberlite sill complex, South Africa. In Kimberlites II-the mantle and crust–mantle relationships. Proceedings, 3rd International Kimberlite Conference 1:43-58

Araújo, D.P., Griffin W.L., O'Reilly S.Y. (2009). Mantle melts, metasomatism and diamond formation: Insights from melt inclusions in xenoliths from Diavik, Slave Craton, Lithos, 112 (2), 675-682.

Armstrong, J.P., Wilson, M., Barnett, R.L., Nowicki, T., Kjarsgaard, B.A. (2004). Mineralogy of primary carbonate-bearing hypabyssal kimberlite, Lac de Gras, Slave province, Northwest Territories, Canada. Lithos 76, 415-433.

Armstrong, J.T. (1988). Quantitative analysis of silicate and oxide materials: comparison of monte carlo, ZAF, and ψ (ρz) procedures. Microbeam analysis, 239-246.

Arndt, N.T., Guitreau, M., Boullier, A.M., le Roex, A., Tommasi, A., Cordier, P., Sobolev, A. (2010). Olivine, and the origin of kimberlite. Journal of Petrology 51, 573-602.

Aulbach, S., Griffin, W.L., Pearson, N.J., O'Reilly, S.Y. (2013). Nature and timing of metasomatism in the stratified mantle lithosphere beneath the central Slave craton (Canada). Chemical Geology 352, 153-169.

Ayers, J.C., Watson, E.B. (1993). Apatite/fluid partitioning of rare-earth elements and strontium: Experimental results at 1.0 GPa and 1000 C and application to models of fluid-rock interaction. Chemical Geology, 110, 299-314.

Bailey, D.K. (1980). Volatile flux, geotherms, and the generation of the kimberlite-carbonatite-alkaline magma spectrum. Mineralogical Magazine. 43 (330), 695-699.

Bailey, D.K. (1993). Petrogenetic implications of the timing of alkaline, carbonatite, and kimberlite igneous activity in Africa. South African Journal of Geology. 96 (3), 67-74.

Ballhaus, C., Berry, R.F., Green, D.H. (1991). High pressure experimental calibration of the olivine-orthopyroxene-spinel oxygen geobarometer: implications for the oxidation state of the upper mantle. Contributions to Mineralogy and Petrology 107, 27-40.

Banas, A., Stachel, T., Phillips, D., Shimizu, N., Viljoen, K.S., Harris, J.W. (2009). Ancient metasomatism recorded by ultra-depleted garnet inclusions in diamonds from DeBeers Pool, South Africa. Lithos, 112, 736-746.

Batumike, J.M., Griffin, W.L., Belousova, E.A., Pearson, N.J., O'Reilly, S.Y., Shee, S.R. (2008). LAM-ICPMS U-Pb dating of kimberlitic perovskite: Eocene-Oligocene kimberlites from the Kundelungu Plateau, D.R. Congo. Earth and Planetary Science Letters 267, 609-619.

Beard, A.D., Downes, H., Hegner, E., Sablukov, S.M. (2000). Geochemistry and mineralogy of kimberlites from the Arkhangelsk Region, NW Russia: evidence for transitional kimberlite magma types. Lithos 51:47-73

Becker, M., le Roex, A.P., (2006). Geochemistry of South African on-and off-craton, Group I and Group II kimberlites: petrogenesis and source region evolution. Journal of Petrology. 47 (4), 673-703.

Bell, D.R., Gregoire, M., Grove, T.L., Chatterjee, N., Carlson, R.W., Buseck, P.R., (2005). Silica and volatile-element metasomatism of Archean mantle: a xenolith-scale example from the Kaapvaal Craton. Contributions to Mineralogy and Petrology, 150(3), 251.

Belousova, E.A., Griffin, W.L., O'Reilly, S.Y., Fisher, N.I. (2002). Apatite as an indicator mineral for mineral exploration: trace-element compositions and their relationship to host rock type. Journal of Geochemical Exploration, 76, 45-69.

Bernstein, S., Kelemen, P.B., Hanghøj, K., (2007). Consistent olivine Mg# in cratonic mantle reflects Archean mantle melting to the exhaustion of orthopyroxene. Geology. 35 (5), 459-462.

Beyer, C., Berndt, J., Tappe, S., Klemme, S. (2013). Trace element partitioning between perovskite and kimberlite to carbonatite melt: New experimental constraints. Chemical Geology 353:132-139

Birkett, T.C., McCandless, T.E., Hood, C.T. (2004). Petrology of the Renard igneous bodies: host rocks for diamond in the northern Otish Mountains region, Quebec. Lithos, 76:475-490.

Bishop, F.C., Smith, J.V., Dawson, J.B., (1978). Na, K, P and Ti in garnet, pyroxene and olivine from peridotite and eclogite xenoliths from African kimberlites. Lithos, 11(2), 155-173.

Boctor, N.Z. Boyd, F.R. (1981). Oxide minerals in a layered kimberlite-carbonate sill from Benfontein, South Africa. Contributions to Mineralogy and Petrology 76, 253-259.

Boettcher, A.L., O'Neil, J.R. (1980). Stable isotope, chemical, and petrographic studies of high-pressure amphiboles and micas: evidence for metasomatism in the mantle source regions of alkali basalts and kimberlites. American Journal of Science, 280, 594-621.

Boyd, F.R., Clement, C.R., (1977). Compositional zoning of olivines in kimberlite from the De Beers Mine, Kimberley, South Africa. Carnegie Institute Washington Yearbook 76, 485-493.

Brett, R.C., Russell, J.K., Andrews, G.D.M. Jones, T.J., (2015). The ascent of kimberlite: insights from olivine. Earth and Planetary Science Letters 424, 119-131.

Brett, R.C., Russell, J.K., Moss, S., (2009). Origin of olivine in kimberlite: Phenocryst or impostor? Lithos. 112, 201-212.

Brey, G. (1978). Origin of olivine melilitites–chemical and experimental constraints. Journal of Volcanology and Geothermal Research 3, 61-88.

Brey, G.P., Bulatov, V.K., Girnis, A.V. (2009). Influence of water and fluorine on melting of carbonated peridotite at 6 and 10 GPa. Lithos 112, 249-259.

Brey, G.P., Bulatov, V.K., Girnis, A.V., Lahaye, Y. (2008). Experimental melting of carbonated peridotite at 6–10 GPa. Journal of Petrology 49, 797-821.

Brooker, R.A., Sparks, R.S.J., Kavanagh, J.L., Field, M., (2011). The volatile content of hypabyssal kimberlite magmas: some constraints from experiments on natural rock compositions. Bulletin of volcanology. 73 (8), 959-981.

Brown, R.J., Buse, B., Sparks, R.S.J., Field, M. (2008). On the welding of pyroclasts from very low-viscosity magmas: examples from kimberlite volcanoes. The Journal of Geology, 116(4), 354-374.

Brown, R.J., Manya, S., Buisman, I., Fontana, G., Field, M., Mac Niocaill, C., Stuart, F.M. (2012). Eruption of kimberlite magmas: physical volcanology, geomorphology and age of the youngest kimberlitic volcanoes known on earth (the Upper Pleistocene/Holocene Igwisi Hills volcanoes, Tanzania). Bulletin of volcanology, 74(7), 1621-1643.

Bussweiler, Y., Foley, S.F., Prelević, D., Jacob, D.E. (2015). The olivine macrocryst problem: New insights from minor and trace element compositions of olivine from Lac de Gras kimberlites, Canada. Lithos 220, 238-252.

Bussweiler, Y., Pearson, D.G., Stachel, T., Kjarsgaard, B.A., (2018). Cr-rich megacrysts of clinopyroxene and garnet from Lac de Gras kimberlites, Slave Craton, Canada–implications for the origin of clinopyroxene and garnet in cratonic lherzolites. Mineralogy and Petrology, 112(2), 583-596.

Carlson, R.W., Czamanske, G., Fedorenko, V., Ilupin, I., (2006). A comparison of Siberian meimechites and kimberlites: Implications for the source of high-Mg alkalic magmas and flood basalts. Geochemistry, Geophysics, Geosystems, 7(11).

Castillo-Oliver, M., Giuliani, A., Griffin, W.L., O'Reilly, S.Y. (2018). Characterisation of primary and secondary carbonates in hypabyssal kimberlites: an integrated compositional and Sr-isotopic approach. Miner Petrol 12:555-567.

Chakhmouradian, A.R., Mitchell, R.H., (1999). Niobian ilmenite, hydroxylapatite and sulfatian monazite; alternative hosts for incompatible elements in calcite kimberlite from Internatsional'naya, Yakutia. Canadian Mineralogist 37(5):1177-1189

Chakhmouradian, A.R., Mitchell, R.H., (2000) Occurrence, alteration patterns and compositional variation of perovskite in kimberlites. Canadian Mineralogist 38(4):975-994

Chakhmouradian, A.R., Reguir, E.P., Kamenetsky, V.S., Sharygin, V.V., Golovin, A.V. (2013). Trace-element partitioning in perovskite: implications for the geochemistry of kimberlites and other mantle-derived undersaturated rocks. Chemical Geology 353:112-131.

Chakhmouradian, A.R., Reguir, E.P., Mitchell, R.H. (2002). Strontium-apatite: New occurrences, and the extent of Sr-for-Ca substitution in apatite-group minerals. Canadian Mineralogist 40:121-136.

Chakhmouradian, A.R., Reguir, E.P., Zaitsev, A.N., Couëslan, C., Xu, C., Kynický, J.A., Mumin, H., Yang, P. (2017). Apatite in carbonatitic rocks: Compositional variation, zoning, element partitioning and petrogenetic significance. Lithos 274: 188-213.

Chakhmouradian, A.R., Mitchell, R.H. (2001). Three compositional varieties of perovskite from kimberlites of the Lac de Gras field (Northwest Territories, Canada). Mineral Mag 65:133-148.

Chalapathi Rao, N.V., Dongre, A., Kamde, G., Srivastava, R.K., Sridhar, M., Kaminsky, F.V. (2010). Petrology, geochemistry and genesis of newly discovered Mesoproterozoic highly magnesian, calcite-rich kimberlites from Siddanpalli, Eastern Dharwar Craton, Southern India: products of subduction-related magmatic sources? Miner Petrol 98:313-328.

Cheng, Z., Zhang, Z., Santosh, M., Hou, T., Zhang, D. (2014). Carbonate-and silicate-rich globules in the kimberlitic rocks of northwestern Tarim large igneous province, NW China: Evidence for carbonated mantle source. Journal of Asian Earth Sciences, 95, 114-135.

Chepurov, A.I., Zhimulev, E.I., Agafonov, L.V., Sonin, V.M., Chepurov, A.A., Tomilenko, A.A. (2013). The stability of ortho-and clinopyroxenes, olivine, and garnet in kimberlitic magma. Russian Geology and Geophysics. 54 (4), 406-415.

Clement C.R. (1982). A comparative geological study of some major kimberlite pipes in the northern cape and Orange Free State. Ph.D Thesis. University of Cape Town, South Africa

Clement, C.R. (1982). A comparative geological study of some major kimberlite pipes in the Northern Cape and Orange Free State. PhD Thesis, University of Cape Town, 407 pp.

Clement, C.R., Harris, J.W., Robinson, D.N., Hawthorne, J.B. (1986) The De Beers kimberlite pipe – a historic South African diamond mine. In Anhaeusser CR, Maske S (eds) Mineral Deposits of Southern Africa. Geological Society of South Africa, Johannesburg, pp 2193-2214

Clement, C.R., Skinner, E. (1979). A textural genetic classification of kimberlite rocks. Kimberlite Symposium II, Cambridge. In Proceedings Extended Abstracts (Vol. 1985).

Coe, N. (2004). Petrogenesis of the Swartruggens and Star Group II kimberlite dyke swarms, South Africa (Doctoral dissertation, University of Cape Town).

Coetzee, M. (2004). Geochemistry of selected South African group I, group II and transitional kimberlites located on and off the Kaapvaal craton (Doctoral dissertation, University of Cape Town).

Cordier, C., Sauzeat, L., Arndt, N.T., Boullier, A.M., Batanova, V., Barou, F. (2015). Metasomatism of the lithospheric mantle immediately precedes kimberlite eruption: new evidence from olivine composition and microstructures. Journal of Petrology 56, 1775-1796.

Cordier, C., Sauzeat, L., Arndt, N.T., Boullier, A.M., Batanova, V., Barou, F. (2016). The geochemical complexity of kimberlite rocks and their olivine populations: a reply to the comment on Cordier et al. (2015) by Andrea Giuliani & Stephen F. Foley. Journal of Petrology 57, 927-932.

Dalton, H., Giuliani, A., O'Brien, H., Phillips, D., Hergt, J. (2020). Petrogenesis of a hybrid kimberlite-ultramafic lamprophyre cluster in the Kuusamo area, Finland. Journal of Petrology.

Dalton, J.A., Presnall, D.C. (1998). The continuum of primary carbonatitic–kimberlitic melt compositions in equilibrium with lherzolite: data from the system CaO-MgO-Al_2O_3-SiO_2-CO_2 at 6 GPa. Journal of Petrology. 39 (11-12), 1953-1964.

Dalton, J.A., Wood, B.J. (1993). The compositions of primary carbonate melts and their evolution through wallrock reaction in the mantle. Earth and Planetary Science Letters. 119 (4), 511-525.

Dasgupta, R., Hirschmann, M.M., McDonough, W.F., Spiegelman, M., Withers, A.C., (2009). Trace element partitioning between garnet lherzolite and carbonatite at 6.6 and 8.6 GPa with applications to the geochemistry of the mantle and of mantle-derived melts. Chemical Geology. 262 (1), 57-77.

Davis, G.L. (1977). The ages and uranium contents of zircons from kimberlites and associated rocks. Carnegie Institution of Washington Yearbook, 76, 631-654.

Dawson J.B., Hawthorne J.B. (1973). Magmatic sedimentation and carbonatitic differentiation in kimberlite sills at Benfontein, South Africa. Journal of the Geological Society 129, 61-85.

Dawson, J.B., Hervig, R.L., Smith, J.V. (1981). Fertile iron-rich dunite xenoliths from the Bultfontein kimberlite, South Africa. Fortschritte der Mineralogie 59, 303-324

Dawson, J.B., Smith, J.V. (1975). Chemistry and origin of phlogopite megacrysts in kimberlite. Nature, 253:336-338.

Dawson, J., Hill, P., Kinny, P. (2001). Mineral chemistry of a zircon-bearing, composite, veined and metasomatised upper-mantle peridotite xenolith from kimberlite. Contributions to Mineralogy and Petrology, 140(6), 720-733.

Dawson, J.B. (1971). Advances in kimberlite geology. Earth-Science Reviews, 7(4), 187-214.

Dawson, J.B. (1980). Kimberlites and their xenoliths (Vol. 15). Springer Science & Business Media.

Dawson, J.B., Smith, J.V. (1977). The MARID (mica-amphibole-rutile-ilmenite-diopside) suite of xenoliths in kimberlite. Geochimica et Cosmochimica Acta, 41(2), 309-323.

Day, J.M., Peters, B.J., Janney, P.E. (2014). Oxygen isotope systematics of South African olivine melilitites and implications for HIMU mantle reservoirs. Lithos 202, 76-84.

De Hoog, J.C., Gall, L., Cornell, D.H. (2010). Trace-element geochemistry of mantle olivine and application to mantle petrogenesis and geothermobarometry. Chemical Geology 270, 196-215.

De Wit, M.C.J., Bhebe, Z., Davidson, J., Haggerty, S.E., Hundt, P., Jacob, J., Lynn, M., Marshall, T.R., Skinner, C., Smithson, K. and Stiefenhofer, J., Robert, M., Revitt, A., Spaggiari (Spaggs), R., Ward, J. (2016). Overview of diamond resources in Africa. Journal of International Geoscience.

Dohmen, R., Chakraborty, S. (2007). Fe–Mg diffusion in olivine II: point defect chemistry, change of diffusion mechanisms and a model for calculation of diffusion coefficients in natural olivine. Physics and Chemistry of Minerals 34, 409-430.

Donaldson, C.H., Reid, A.M. (1982) Multiple intrusion of a kimberlite dyke. S Afr J Geol 85(1):1-12

Donnelly, C.L., Griffin, W.L., O'Reilly, S.Y., Pearson, N.J., Shee, S.R. (2011). The kimberlites and related rocks of the Kuruman kimberlite province, Kaapvaal craton, South Africa. Contributions to Mineralogy and Petrology, 161(3), 351-371.

Donnelly, C.L., Griffin, W.L., Yang, J.H., O'Reilly, S.Y., Li, Q.L., Pearson, N.J., Li, X.H. (2012). In situ U–Pb dating and Sr–Nd isotopic analysis of perovskite: constraints on the age and petrogenesis of the Kuruman Kimberlite Province, Kaapvaal Craton, South Africa. Journal of Petrology, 53(12), 2497-2522.

Edgar, A.D., Arima, M., Baldwin, D.K., Bell, D.R., Shee, S.R., Skinner, E.M.W., Walker, E.C. (1988). High-pressure-high-temperature melting experiments on a SiO 2-poor aphanitic

kimberlite from the Wesselton Mine, Kimberley, South Africa. AmeriCanadian Mineralogistogist, 73(5-6), 524-533.

Edgar, A.D., Charbonneau, H.E. (1993). Melting experiments on a SiO2-poor, CaO-rich aphanitic kimberlite from 5–10 GPa and their bearing on sources of kimberlite magmas. AmeriCanadian Mineralogistogist, 78(1-2), 132-142.

Eggler, D.H., McCallum, M.E.H., Smith, C.B. (1979). Megacryst Assemblages in Kimberlite from Northern Colorado and Southern Wyoming: Petrology, Geothermometry-Barometry, and Areal Distribution. The Mantle Sample: Inclusion in Kimberlites and Other Volcanics, 16, 213-226.

Erlank, A.J., Waters, F.G., Hawkesworth, C.J., Haggerty, S.E., Allsopp, H.L., Rickard, R.S., Menzies, M.A. (1987) Evidence for mantle metasomatism in peridotite nodules from the Kimberley pipes, South Africa. In: Menzies M, Hawkesworth CJ (eds) Mantle Metasomatism. Academic Press, London, pp 221-311

Exley, R.A., Jones, A.P. (1983) 87Sr/86Sr in kimberlitic carbonates by ion microprobe: hydrothermal alteration, crustal contamination and relation to carbonatite. Contributions to Mineralogy and Petrology 83(3–4):288–292

Fedortchouk, Y. (2015). Diamond resorption features as a new method for examining conditions of kimberlite emplacement. Contributions to Mineralogy and Petrology, 170:36-X.

Fedortchouk, Y., Canil, D. (2004) Intensive variables in kimberlite magmas, Lac de Gras, Canada and implications for diamond survival. Journal of Petrology 45(9):1725-1745

Fedortchouk, Y., Canil, D. (2004). Intensive variables in kimberlite magmas, Lac de Gras, Canada and implications for diamond survival. Journal of Petrology 45, 1725-1745.

Fedortchouk, Y., Chinn, I.L., Kopylova, M.G., (2017). Three styles of diamond resorption in a single kimberlite: Effects of volcanic degassing and assimilation. Geology, 45(10), 871-874.

Feig, S.T., Koepke, J. Snow, J.E. (2006). Effect of water on tholeiitic basalt phase equilibria: an experimental study under oxidizing conditions. Contributions to Mineralogy and Petrology 152, 611-638.

Ferry, J.M., Watson, E.B. (2007) New thermodynamic models and revised calibrations for the Ti-in-zircon and Zr-in-rutile thermometers. Contributions to Mineralogy and Petrology 154(4):429-437

Field, M., Gibson, J.G., Wilkes, T.A., Gabaotse, J., Hhujwe, P. (1997) The geology of the Orapa A/K1 kimberlite, Botswana: Further insight into the emplacement of kimberlite pipes. In International Kimberlite Conference: Extended Abstracts (Vol. 6, pp. 155-157).

Field, M., Scott Scott, B. (1999). Contrasting geology and near-surface emplacement of kimberlite pipes in southern Africa and Canada. In Proceedings of the 7th international kimberlite conference (Vol. 1, pp. 214-237). Red Roof Design Cape Town.

Field, M., Stiefenhofer, J., Robey, J., Kurszlaukis, S. (2008). Kimberlite-hosted diamond deposits of southern Africa: a review. Ore Geology Reviews, 34(1-2), 33-75.

Fitch F.J. Miller J.A. (1983). K-Ar age of the east peripheral kimberlite at De Beers Mine, Kimberley, R.S.A. Geological Magazine 120, 505-512.

Fitzpayne, A., Giuliani, A., Hergt, J., Phillips, D., Janney, P. (2018b). New geochemical constraints on the origins of MARID and PIC rocks: Implications for mantle metasomatism and mantle-derived potassic magmatism. Lithos 318, 478-493.

Fitzpayne, A., Giuliani, A., Phillips, D., Hergt, J., Woodhead, J.D., Farquhar, J., Fiorentini, M.L., Drysdale, R.N., Wu, N. (2018a). Kimberlite-related metasomatism recorded in MARID and PIC mantle xenoliths. Mineralogy and Petrology 112, 71-84.

Foley, S.F., Prelevic, D., Rehfeldt, T., Jacob, D.E. (2013). Minor and trace elements in olivines as probes into early igneous and mantle melting processes. Earth and Planetary Science Letters 363, 181-191

Foley, S.F., Yaxley, G.M., Rosenthal, A., Buhre, S., Kiseeva, E.S., Rapp, R.P., Jacob, D.E. (2009). The composition of near-solidus melts of peridotite in the presence of CO2 and H2O between 40 and 60 kbar. Lithos. 112, 274-283.

Förster, M.W., Prelević, D., Schmück, H.R., Buhre, S., Veter, M., Mertz-Kraus, R., Foley, S.F., Jacob, D.E. (2017). Melting and dynamic metasomatism of mixed harzburgite+ glimmerite mantle source: Implications for the genesis of orogenic potassic magmas. Chemical Geology 455, 182-191.

Fraser, K.J. (1987) Petrogenesis of Kimberlites from South Africa and Lamproites from Western Australia and North America. PhD Thesis, The Open University

Gaffney, A.M., Blichert-Toft, J., Nelson, B.K., Bizzarro, M., Rosing, M., Albarède, F. (2007). Constraints on source-forming processes of West Greenland kimberlites inferred from Hf–Nd isotope systematics. Geochimica et Cosmochimica Acta, 71(11), 2820-2836.

Gaspar, J.C., Wyllie, P.J. (1984) The alleged kimberlite-carbonatite relationship: evidence from ilmenite and spinel from Premier and Wesselton Mines and the Benfontein Sill, South Africa. Contributions to Mineralogy and Petrology 85(2):133-140

Gaudet, M., Kopylova, M., Muntener, C., Zhuk, V., Nathwani, C. (2018). Geology of the Renard 65 kimberlite pipe, Québec, Canada. Mineralogy and Petrology, 112(2), 433-445.

Gaul, O.F., Griffin, W.L., O'Reilly, S.Y., Pearson, N.J. (2000). Mapping olivine composition in the lithospheric mantle. Earth and Planetary Science Letters 182, 223-235.

Gibson, S.A., Malarkey, J., Day, J.A. (2008). Melt depletion and enrichment beneath the western Kaapvaal Craton: evidence from Finsch peridotite xenoliths. Journal of Petrology, 49(10), 1817-1852.

Girnis, A.V., Brey, G.P., Ryabchikov, I.D. (1995). Origin of group 1A kimberlites: fluid-saturated melting experiments at 45–55 kbar. Earth and Planetary Science Letters, 134(3-4), 283-296.

Girnis, A.V., Bulatov, V.K., Brey, G.P. (2005). Transition from kimberlite to carbonatite melt under mantle parameters: an experimental study. Petrology 13, 1-15.

Girnis, A.V., Bulatov, V.K., Brey, G.P. (2011). Formation of primary kimberlite melts – Constraints from experiments at 6-12 GPa and variable CO2/H2O. Lithos. 127, 401-413.

Giuliani, A., Pearson, D.G. (2019). Kimberlites: From Deep Earth to Diamond Mines. Elements 15(6):377-380

Giuliani, A. (2018). Insights into kimberlite petrogenesis and mantle metasomatism from a review of the compositional zoning of olivine in kimberlites worldwide. Lithos 312-313, 322-342.

Giuliani, A., Foley, S.F. (2016). The geochemical complexity of kimberlite rocks and their olivine populations: a comment on Cordier et al. (Journal of Petrology 56, 1775–1796, 2015). Journal of Petrology 57, 921-926.

Giuliani, A., Kamenetsky, V.S., Kendrick, M.A., Phillips, D., Goemann, K. (2013a). Nickel-rich metasomatism of the lithospheric mantle by pre-kimberlitic alkali-S–Cl-rich C–O–H fluids. Contributions to Mineralogy and Petrology 165, 155-171.

Giuliani, A., Martin, L.A.J., Soltys, A., Griffin, W.L. (2019). Mantle-like oxygen isotopes in kimberlites determined by in situ SIMS analyses of zoned olivine. Geochimica et Cosmochimica Acta 266, 274-291

Giuliani, A., Phillips, D., Fiorentini, M.L., Kendrick, M.A., Maas, R., Wing, B.A., Woodhead, J.D., Bui, T.H., Kamenetsky, V.S. (2013b). Mantle oddities: a sulphate fluid preserved in a MARID xenolith from the Bultfontein kimberlite (Kimberley, South Africa). Earth and Planetary Science Letters 376, 74-86.

Giuliani, A., Phillips, D., Kamenetsky, V.S., Fiorentini, M.L., Farquhar, J., Kendrick, M.A., 2014. Stable isotope (C, O, S) compositions of volatile-rich minerals in kimberlites: a review. Chemical Geology. 374, 61-83.

Giuliani, A., Phillips, D., Kamenetsky, V.S., Goemann, K. (2016). Constraints on kimberlite ascent mechanisms revealed by phlogopite compositions in kimberlites and mantle xenoliths. Lithos 240, 189-201.

Giuliani, A., Phillips, D., Kamenetsky, V.S., Kendrick, M.A., Wyatt, B.A., Goemann, K., Hutchinson, G. (2014). Petrogenesis of mantle polymict breccias: insights into mantle processes coeval with kimberlite magmatism. Journal of Petrology 55, 831-858.

Giuliani, A., Phillips, D., Maas, R., Woodhead, J.D., Kendrick, M.A., Greig, A., Armstrong, R.A., Chew, D., Kamenetsky, V.S., Fiorentini, M.L. (2014a) LIMA U-Pb ages link lithospheric mantle metasomatism to Karoo magmatism beneath the Kimberley region, South Africa. Earth and Planetary Science Letters 401:132–147

Giuliani, A., Soltys, A., Phillips, D., Kamenetsky, V.S., Maas, R., Goemann, K., Woodhead, J.D., Drysdale, R.N., Griffin, W.L. (2017). The final stages of kimberlite petrogenesis: Petrography, mineral chemistry, melt inclusions and Sr-C-O isotope geochemistry of the Bultfontein kimberlite (Kimberley, South Africa). Chemical Geology 455, 342-356.

Globig, J., Fernàndez, M., Torne, M., Vergés, J., Robert, A., Faccenna, C. (2016). New insights into the crust and lithospheric mantle structure of Africa from elevation, geoid, and thermal analysis. Journal of Geophysical Research: Solid Earth 121, 5389-5424.

Green, P.F. (1985). Comparison of zeta calibration baselines for fission-track dating of apatite, zircon and sphene. Chemical Geology: Isotope Geoscience section, 58(1-2), 1-22.

Grégoire, M., Bell, D., le Roex, A. (2002). Trace element geochemistry of phlogopite-rich mafic mantle xenoliths: their classification and their relationship to phlogopite-bearing peridotites and kimberlites revisited. Contributions to Mineralogy and Petrology, 142(5), 603-625.

Grégoire, M., Bell, D.R., Le Roex, A.P. (2003). Garnet lherzolites from the Kaapvaal Craton (South Africa): trace element evidence for a metasomatic history. Journal of Petrology 44, 629-657.

Griffin, W.L., Batumike, J.M., Greau, Y., Pearson, N.J., Shee, S.R., O'Reilly, S.Y. (2014). Emplacement ages and sources of kimberlites and related rocks in southern Africa: U–Pb ages and Sr–Nd isotopes of groundmass perovskite. Contributions to Mineralogy and Petrology, 168(1), 1032.

Griffin, W.L., O'Reilly, S.Y., Afonso, J.C., Begg, G.C. (2008). The composition and evolution of lithospheric mantle: a re-evaluation and its tectonic implications. Journal of Petrology, 50(7), 1185-1204.

Griffin, W.L., O'Reilly, S.Y., Afonso, J.C., Begg, G.C. (2009). The composition and evolution of lithospheric mantle: a re-evaluation and its tectonic implications. Journal of Petrology 50 (7), 1185-1204.

Griffin, W.L., O'Reilly, S.Y., Natapov, L.M., Ryan, C.G., (2003). The evolution of lithospheric mantle beneath the Kalahari Craton and its margins. Lithos 71 (2), 215–241

Griffin, W.L., Shee, S.R., Ryan, C.G., Win, T.T., & Wyatt, B.A. (1999). Harzburgite to lherzolite and back again: metasomatic processes in ultramafic xenoliths from the Wesselton kimberlite, Kimberley, South Africa. Contributions to Mineralogy and Petrology, 134(2-3), 232-250.

Gudfinnsson, G.H., Presnall, D.C., (2005). Continuous gradations among primary carbonatitic, kimberlitic, melilititic, basaltic, picritic, and komatiitic melts in equilibrium with garnet lherzolite at 3–8 GPa. Journal of Petrology. 46 (8), 1645-1659.

Haggerty, S.E. (1983) The mineral chemistry of new titanates from the Jagersfontein kimberlite, South Africa: implications for metasomatism in the upper mantle. Geochim Cosmochim Ac 47(11):1833-1854

Haggerty, S.E. (1991) Oxide mineralogy of the upper mantle. In: Lindsey DH (eds) Oxide minerals: Petrologic and magnetic significance. Rev Mineral, vol 25. Miner Soc Am, Washington DC, pp 355-416

Haggerty, S.E. (1994). Superkimberlites: a geodynamic diamond window to the Earth's core. Earth and Planetary Science Letters 122 (1), 57–69.

Haggerty, S.E. (2017). Majorite-indicative ultradeep (> 300 km) xenoliths with spinel associations from the Jagersfontein kimberlite, South Africa. South African Journal of Geology 120, 1-20.

Hanson, E.K., Moore, J.M., Bordy, E.M., Marsh, J.S., Howarth, G., Robey, J.V.A. (2009). Cretaceous erosion in central South Africa: Evidence from upper-crustal xenoliths in kimberlite diatremes. South African Journal of Geology, 112(2), 125-140.

Harte, B. (1983). Mantle peridotites and processes the kimberlites sample. Continental basalts and mantle xenoliths, 46-91.

Harte, B. (2010). Diamond formation in the deep mantle: the record of mineral inclusions and their distribution in relation to mantle dehydration zones. Mineralogical Magazine 74, 189-215.

Hawkesworth, C.J., Erlank, A.J., Kempton, P.D., Waters, F.G. (1990). Mantle metasomatism: isotope and trace-element trends in xenoliths from Kimberley, South Africa. Chemical Geology, 85(1-2), 19-34.

Hawthorne, J.B. (1975). Model of a kimberlite pipe. Physics and Chemistry of the Earth, 9, 1-15.

Henning, A., Kiviets, G., Kurszlaukis, S., Barton, E., Mayaga-Mikolo, F., (2003). Early Proterozoic metamorphosed kimberlites from Gabon. In: Extended Abstracts of the 8th International Kimberlite Conference.

Hervig, R.L., Smith, J.V., Dawson, J.B. (1986). Lherzolite xenoliths in kimberlites and basalts: petrogenetic and crystallochemical significance of some minor and trace elements in olivine, pyroxenes, garnet and spinel. Earth and Environmental Science Transactions of the Royal Society of Edinburgh 77, 181-201.

Herzberg, C. (2004). Geodynamic information in peridotite petrology. Journal of Petrology, 45(12), 2507-2530.

Herzberg, C., O'Hara, M.J., (2002). Plume-associated ultramafic magmas of Phanerozoic age. Journal of Petrology. 43 (10), 1857-1883.

Hetman, C.M., Scott Smith, B., Paul, J.L., Winter, F. (2004). Geology of the Gahcho Kue kimberlite pipes, NWT, Canada: root to diatreme magmatic transition zones. Lithos, 76(1-4), 51-74.

Howarth, G. H. (2018). Olivine megacryst chemistry, Monastery kimberlite: Constraints on the mineralogy of the HIMU mantle reservoir in southern Africa. Lithos 314, 658-668.

Howarth, G. H., Taylor, L.A. (2016). Multi-Step kimberlite evolution tracked in zoned olivine from the Benfontein sill, South Africa. Lithos 262, 384–397.

Howarth, G.H., Michael, E., Skinner, W., Prevec, S.A. (2011). Petrology of the hypabyssal kimberlite of the Kroonstad group II kimberlite (orangeite) cluster, South Africa: Evolution of the magma within the cluster. Lithos, 125(1-2), 795-808.

Howarth, G.H., Taylor, L.A. (2016) Multi-Step kimberlite evolution tracked in zoned olivine from the Benfontein sill, South Africa. Lithos 262:384-397

Hunter, R.H., Taylor, L.A. (1982). Instability of garnet from the mantle: glass as evidence of metasomatic melting. Geology. 10 (12), 617-620.

Ionov, D.A., Doucet, L.S., Ashchepkov, I.V. (2010). Composition of the lithospheric mantle in the Siberian craton: new constraints from fresh peridotites in the Udachnaya-East kimberlite. Journal of Petrology, 51(11), 2177-2210.

Ionov, D.A., Doucet, L.S., von Strandmann, P.A.P., Golovin, A.V., Korsakov, A.V. (2017). Links between deformation, chemical enrichments and Li-isotope compositions in the lithospheric mantle of the central Siberian craton. Chemical Geology 475, 105-121.

Jackson, C.G., Gibson, S.A. (2018). Preservation of systematic Ni and Cr heterogeneity in otherwise homogeneous mantle olivine: Implications for timescales of post-metasomatism re-equilibration. Lithos 318, 448-463.

Jacob, D.E., Viljoen, K.S., Grassineau, N.V. (2009). Eclogite xenoliths from Kimberley, South Africa—a case study of mantle metasomatism in eclogites. Lithos, 112, 1002-1013.

Janney, P.E., le Roex, A.P., Carlson, R.W., Viljoen, K.S. (2002). A chemical and multi-isotope study of the Western Cape olivine melilitite province, South Africa: implications for the sources of kimberlites and the origin of the HIMU signature in Africa. Journal of Petrology, 43, 2339-2370.

Jarosewich, E., Nelen, J.A., Norberg, J.A. (1980). Reference samples for electron microprobe analysis. Geostandards Newsletter 4, 43-47.

Jelsma, H., Barnett, W., Richards, S., Lister, G., (2009). Tectonic setting of kimberlites. Lithos. 112, 155-165.

Jelsma, H., Krishnan, U., Perritt, S., Preston, R., Winter, F., Lemotlo, L., van der Linde, G., Armstrong, R., Phillips, D., Joy, S., Costa, J. (2013). Kimberlites from Central Angola: a case study of exploration findings. In Proceedings of 10th International Kimberlite Conference (pp. 173-190). Springer, New Delhi.

Jelsma, H.A., De Wit, M.J., Thiart, C., Dirks, P.H., Viola, G., Basson, I.J., Anckar, E. (2004). Preferential distribution along transcontinental corridors of kimberlites and related rocks of Southern Africa. South African Journal of Geology, 107(1-2), 301-324.

Jollands, M.C., Hanger, B.J., Yaxley, G.M., Hermann, J., Kilburn, M.R. (2018). Timescales between mantle metasomatism and kimberlite ascent indicated by diffusion profiles in garnet crystals from peridotite xenoliths. Earth and Planetary Science Letters 481, 143-153.

Jones, A.P., Smith, J.V., Dawson, J.B. (1982). Mantle metasomatism in 14 veined peridotites from Bultfontein Mine, South Africa. The Journal of Geology 90, 435-453.

Jourdan, F., Féraud, G., Bertrand, H., Watkeys, M.K., Renne, P.R., (2007). Distinct brief major events in the Karoo large igneous province clarified by new 40Ar/39Ar ages on the Lesotho basalts. Lithos, 98(1-4), 195-209.

Kamenetsky, V.S., Grütter, H., Kamenetsky, M.B., Gömann, K. (2013). Parental carbonatitic melt of the Koala kimberlite (Canada): constraints from melt inclusions in olivine and Cr-spinel, and groundmass carbonate. Chemical Geology 353:96-111.

Kamenetsky, M.B., Sobolev, A.V., Kamenetsky, V.S., Maas, R., Danyushevsky, L.V., Thomas, R., Pokhilenko, N.P., Sobolev, N.V. (2004). Kimberlite melts rich in alkali chlorides and carbonates: a potent metasomatic agent in the mantle. Geology, 32(10), pp.845-848.

Kamenetsky, V.S., Golovin, A.V., Maas, R., Giuliani, A., Kamenetsky, M. B., Weiss, Y., (2014). Towards a new model for kimberlite petrogenesis: Evidence from unaltered kimberlites and mantle minerals. Earth-Science Reviews. 139, 145-167.

Kamenetsky, V.S., Kamenetsky, M.B., Sobolev, A.V., Golovin, A.V., Demouchy, S., Faure, K., Sharygin, V.V., Kuzmin, D.V. (2008). Olivine in the Udachnaya-East kimberlite (Yakutia, Russia): types, compositions and origins. Journal of Petrology 49, 823-839.

Kamenetsky, V.S., Kamenetsky, M.B., Sobolev, A.V., Golovin, A.V., Sharygin, V.V., Pokhilenko, N.P. Sobolev, N.V. (2009). Can pyroxenes be liquidus minerals in the kimberlite magma? Lithos 112, 213-222.

Kamenetsky, V.S., Yaxley, G.M., (2015). Carbonate–silicate liquid immiscibility in the mantle propels kimberlite magma ascent. Geochimica et Cosmochimica Acta 158, 48–56.

Kaminsky, F. (2012). Mineralogy of the lower mantle: A review of 'super-deep' mineral inclusions in diamond. Earth-Science Reviews 110, 127-147.

Kargin, A.V., Nosova, A.A., Postnikov, A.V., Chugaev, A.V., Postnikova, O.V., Popova, L.P., Poshibaev, V.V., Sazonova, L.V., Dokuchaev, A.Y. and Smirnova, M.D. (2016). Devonian ultramafic lamprophyre in the Irkineeva–Chadobets trough in the southwest of the Siberian Platform: Age, composition, and implications for diamond potential prediction. Geology of Ore Deposits, 58(5), 383-403.

Kargin, A.V., Sazonova, L.V., Nosova, A.A. Tretyachenko, V.V. (2016). Composition of garnet and clinopyroxene in peridotite xenoliths from the Grib kimberlite pipe, Arkhangelsk diamond province, Russia: Evidence for mantle metasomatism associated with kimberlite melts. Lithos 262, 442-455.

Kargin, A.V., Sazonova, L.V., Nosova, A.A., Pervov, V.A., Minevrina, E.V., Khvostikov, V.A., Burmii, Z.P. (2017). Sheared peridotite xenolith from the V. Grib kimberlite pipe, Arkhangelsk Diamond Province, Russia: Texture, composition, and origin. Geoscience Frontiers 8, 653-669

Katayama, I., Suyama, Y., Ando, J.I., Komiya, T. (2009). Mineral chemistry and P–T condition of granular and sheared peridotite xenoliths from Kimberley, South Africa: Origin of the textural variation in the cratonic mantle. Lithos, 109(3-4), 333-340.

Kavanagh, J.L., Sparks, R.S.J., (2009). Temperature changes in ascending kimberlite magma. Earth and Planetary Science Letters. 286 (3), 404-413.

Kjarsgaard, B.A. (2007). Kimberlite diamond deposits. Geological Association of Canada, Mineral Deposits Division. 5, 245-272.

Kjarsgaard, B.A., Pearson, D.G., Tappe, S., Nowell, G.M., Dowall, D.P. (2009). Geochemistry of hypabyssal kimberlites from Lac de Gras, Canada: comparisons to a global database and applications to the parent magma problem. Lithos 112, 236–248.

Klemme, S., Dalpé, C. (2003). Trace-element partitioning between apatite and carbonatite melt. AmeriCanadian Mineralogistogist 88:639-646.

Köhler, T.P., Brey, G. (1990). Calcium exchange between olivine and clinopyroxene calibrated as a geothermobarometer for natural peridotites from 2 to 60 kb with applications. Geochimica et Cosmochimica Acta 54, 2375-2388.

Konzett, J., Armstrong, R.A., Sweeney, R. J., Compston, W. (1998). The timing of MARID metasomatism in the Kaapvaal mantle: an ion probe study of zircons from MARID xenoliths. Earth and Planetary Science Letters, 160(1-2), 133-145.

Kopylova, M.G., Mogg, T., Scott Smith, B. (2010). Mineralogy of the Snap Lake kimberlite, Northwest Territories, Canada, and compositions of phlogopite as records of its crystallization. Canadian Mineralogist 48:549-570.

Kopylova, M.G., Gaudet, M., Kostrovitsky, S.I., Polozov, A.G., Yakovlev, D.A. (2016). Origin of salts and alkali carbonates in the Udachnaya East kimberlite: Insights from petrography of kimberlite phases and their carbonate and evaporite xenoliths. Journal of Volcanology and Geothermal Research 327, 116-134.

Kopylova, M.G., Matveev, S., Raudsepp, M. (2007). Searching for parental kimberlite melt. Geochimica et Cosmochimica Acta 71 (14), 3616–3629.

Kopylova, M.G., Nowell, G.M., Pearson, D.G., Markovic, G. (2009). Crystallization of megacrysts from protokimberlitic fluids: geochemical evidence from high-Cr megacrysts in the Jericho kimberlite. Lithos 112, 284-295.

Kramers, J.D., Roddick, J.C.M., Dawson, J. B., (1983). Trace element and isotope studies on veined, metasomatic and "MARID" xenoliths from Bultfontein, South Africa. Earth and Planetary Science Letters. 65 (1), 90-106.

Kramers, J.D., Smith, C.B. (1983). A feasibility study of U− Pb and Pb− Pb dating of kimberlites using groundmass mineral fractions and whole-rock samples. Chemical Geology, 41, 23-38.

Lambart, S., Laporte, D., Schiano, P. (2013). Markers of the pyroxenite contribution in the major-element compositions of oceanic basalts: Review of the experimental constraints. Lithos 160, 14-36.

Lawless, P.J., Gurney, J.J., Dawson, J.B. (1979). Polymict peridotites from the Bultfontein and De Beers mines, Kimberley, South Africa. In: Boyd, F. R. & Meyer, H. O. A. (eds) The Mantle Sample. 2nd International Kimberlite Conference. American Geophysical Union, pp. 145-155.

le Roex, A.P., (1986). Geochemical correlation between southern African kimberlites and South Atlantic hotspots. Nature. 324, 243-245.

le Roex, A.P., Bell, D.R., Davis, P. (2003). Petrogenesis of Group I Kimberlites from Kimberley, South Africa: Evidence from Bulk-rock Geochemistry. Journal of Petrology 44, 2261-2286.

Lee, C.T.A., Luffi, P., Plank, T., Dalton, H., Leeman, W. P. (2009). Constraints on the depths and temperatures of basaltic magma generation on Earth and other terrestrial planets using new thermobarometers for mafic magmas. Earth and Planetary Science Letters, 279(1-2), 20-33.

Leckie, D.A., Kjarsgaard, B.A., Bloch, J., McIntyre, D., McNeil, D., Stasiuk, L., Heaman, L. (1997). Emplacement and reworking of Cretaceous, diamond-bearing, crater facies kimberlite of central Saskatchewan, Canada. Geological Society of America Bulletin, 109(8), 1000-1020.

Li, Q.L., Li, X.H., Liu, Y., Wu, F.Y., Yang, J.H., Mitchell, R.H. (2010) Precise U–Pb and Th–Pb age determination of kimberlitic perovskites by secondary ion mass spectrometry. Chemical Geology 269(3):396-405

Li, Q.L., Li, X.H., Liu, Y., Wu, F.Y., Yang, J.H., Mitchell, R.H. (2010) Precise U–Pb and Th–Pb age determination of kimberlitic perovskites by secondary ion mass spectrometry. Chemical Geology 269, 396-405

Lim, E., Giuliani, A., Phillips, D., Goemann, K. (2018). Origin of complex zoning in olivine from diverse, diamondiferous kimberlites and tectonic settings: Ekati (Canada), Alto Paranaiba (Brazil) and Kaalvallei (South Africa). Mineralogy and Petrology 112, 539-554.

Lorenz, V., Kurszlaukis, S. (2007). Root zone processes in the phreatomagmatic pipe emplacement model and consequences for the evolution of maar–diatreme volcanoes. J Volcanol Geoth Res, 159: 4-32.

Luth, R.W. (2009). The activity of silica in kimberlites, revisited. Contributions to Mineralogy and Petrology. 158 (2), 283-294.

Mainkar, D., Lehmann, B., Haggerty, S.E. (2004). The crater-facies kimberlite system of Tokapal, Bastar district, Chhattisgarh, India. Lithos, 76(1-4), 201-217.

Majumdar, A.S., Hövelmann, J., Vollmer, C., Berndt, J., Mondal, S.K., Putnis, A. (2016). Formation of Mg-rich olivine pseudomorphs in serpentinized dunite from the Mesoarchean Nuasahi Massif, Eastern India: Insights into the evolution of fluid composition at the mineral–fluid interface. Journal of Petrology 57, 3-26.

Malarkey, J., Pearson, D.G., Kjarsgaard, B.A., Davidson, J.P., Nowell, G.M., Ottley, C.J., Stammer, J. (2010) From source to crust: tracing magmatic evolution in a kimberlite and a melilitite using microsample geochemistry. Earth and Planetary Science Letters 299(1):80-90

Masun, K.M., Scott Smith, B. (2008). The Pimenta Bueno kimberlite field, Rondônia, Brazil: Tuffisitic kimberlite and transitional textures. Journal of Volcanology and Geothermal Research, 174(1-3), 81-89.

Mather, K.A., Pearson, D.G., McKenzie, D., Kjarsgaard, B.A., Priestley, K. (2011). Constraints on the depth and thermal history of cratonic lithosphere from peridotite xenoliths, xenocrysts and seismology. Lithos 125, 729-742.

Matzen, A.K., Wood, B.J., Baker, M.B., Stolper, E.M. (2017). The roles of pyroxenite and peridotite in the mantle sources of oceanic basalts. Nature Geoscience 10, 530-535.

McCandless, T.E. (1999). Kimberlites: mantle expressions of deep-seated subduction. In Proceedings of the 7th international kimberlite conference (Vol. 2, pp. 545-549).

McMahon, B.M. Haggerty, S.E. (1984). The Benfontein kimberlite sills; magmatic reactions and high intrusion temperatures. American Journal of Science, 284(8), 893-941.

Mercier, J.C.C. (1979). Peridotite xenoliths and the dynamics of kimberlite intrusion. The Mantle Sample: Inclusion in Kimberlites and Other Volcanics, 16, 197-212.

Milligan, R., Fedortchouk, Y., Normandeau, P.X., Fulop, A., Robertson, A.M. (2017). Features of apatite in kimberlites from Ekati Diamond Mine and Snap Lake, Northwest Territories, Canada: modelling of kimberlite composition. 11th International Kimberlite Conference Extended Abstract

Misra, K.C., Anand, M., Taylor, L.A., Sobolev, N.V., (2004). Multi-stage metasomatism of diamondiferous eclogite xenoliths from the Udachnaya kimberlite pipe, Yakutia, Siberia. Contributions to Mineralogy and Petrology 146, 696-714.

Mitchell, R.H., Giuliani, A., O'Brien, H. (2019). What is a Kimberlite? Petrology and Mineralogy of Hypabyssal Kimberlites. Elements 15(6):381-386

Mitchell, R.H. (1973). Composition of olivine, silica activity and oxygen fugacity in kimberlite. Lithos 6, 65-81.

Mitchell, R.H. (1978) Mineralogy of the Elwin Bay kimberlite, Somerset Island, NWT, Canada. AmeriCanadian Mineralogistogist 63(1-2):47-57

Mitchell, R.H. (1986). Kimberlites: mineralogy, geochemistry, and petrology. Springer Science & Business Media.

Mitchell, R.H. (1994). Accessory rare earth, strontium, barium and zirconium minerals in the Benfontein and Wesselton calcite kimberlites, South Africa. Kimberlites, related rocks and mantle xenoliths. 5th International Kimberlite Conference. CPRM Special Publication, Araxa, Brazil, pp. 115–128.

Mitchell, R.H. (1995). Kimberlites, Orangeites, and Related Rocks. Plenum Press, New York.

Mitchell, R.H. (2004). Experimental studies at 5–12 GPa of the Ondermatjie hypabyssal kimberlite. Lithos, 76(1-4), 551-564.

Mitchell, R.H. (2008). Petrology of hypabyssal kimberlites: relevance to primary magma compositions. Journal of Volcanology and Geothermal Research 174, 1-8.

Mitchell, R.H. (2013). Oxygen isotope studies of serpentine in kimberlite. Proceedings of the 10th International Kimberlite Conference. Geological Society of India, Bangalore, pp. 1–12.

Mitchell, R.H., Meyer, H.O.A. (1980) Mineralogy of micaceous kimberlite from the Jos Dyke, Somerset Island, NWT. Canadian Mineralogist 18(2):241-250

Mitchell, R.H., Skinner, E.M.W., Scott Smith, B. (2009). Tuffisitic kimberlites from the Wesselton Mine, South Africa: Mineralogical characteristics relevant to their formation. Lithos, 112, 452-464.

Moore, A.E. (1987). A model for the origin of ilmenite in kimberlite and diamond: implications for the genesis of the discrete nodule (megacryst) suite. Contributions to Mineralogy and Petrology 95:245-253.

Moore, A.E, Belousova, E. (2005). Crystallization of Cr-poor and Cr-rich megacryst suites from the host kimberlite magma: implications for mantle structure and the generation of kimberlite magmas. Contributions to Mineralogy and Petrology 149, 462-481.

Moore, A.E, Costin, G. (2016). Kimberlitic olivines derived from the Cr-poor and Cr-rich megacryst suites. Lithos 258, 215-227.

Moore, A.E. (1988). Olivine: a monitor of magma evolutionary paths in kimberlites and olivine melilitites. Contributions to Mineralogy and Petrology 99, 238-248.

Moore, A.E. (2017). Quantitative modelling of the apparent decoupling of Mg# and Ni in kimberlitic olivine margins: comment on Cordier et al. (Journal of Petrology, 56, 1775–1796, 2015). Journal of Petrology 58, 385-390.

Moore, A.E., Blenkinsop, T., Cotterill, F. (2008). Controls on post-Gondwana alkaline volcanism in Southern Africa. Earth and Planetary Science Letters 268 (1), 151–164.

Moore, A.E., Lock, N.P. (2001). The origin of mantle-derived megacrysts and sheared peridotites-evidence from kimberlites in the northern Lesotho-Orange Free State (South Africa) and Botswana pipe clusters. South African Journal of Geology, 104(1), 23-38.

Moore, R. O. (1986). A Study of the Kimberlites, Diamonds and Associated Rocks and Minerals from the Monastery Mine, South Africa. PhD Thesis, University of Cape Town, South Africa.

Moss, S., Russell, J.K., Scott Smith, B. Brett, R.C. (2010). Olivine crystal size distributions in kimberlite. AmeriCanadian Mineralogistogist 95, 527-536.

Moussallam, Y., Morizet, Y., Gaillard, F., (2016). H2O–CO2 solubility in low SiO2-melts and the unique mode of kimberlite degassing and emplacement. Earth and Planetary Science Letters. 447, 151-160.

Moussallam, Y., Morizet, Y., Massuyeau, M., Laumonier, M., Gaillard, F., (2015). CO2 solubility in kimberlite melts. Chemical Geology. 418, 198-205.

Muntener, C., Scott Smith, B. (2013). Economic Geology of Renard 3, Quebec, Canada: a diamondiferous, multi-phase pipe infilled with Hypabyssal and Tuffisitic Kimberlite. In

Proceedings of 10th International Kimberlite Conference (pp. 241-256). Springer, New Delhi.

Naidoo, P., Stiefenhofer, J., Field, M., Dobbe, R. (2004). Recent advances in the geology of Koffiefontein Mine, Free State Province, South Africa. Lithos, 76(1-4), 161-182.

Nestola, F., Korolev, N., Kopylova, M., Rotiroti, N., Pearson, D.G., Pamato, M.G., Alvaro, M., Peruzzo, L., Gurney, J.J., Moore, A.E., Davidson, J. (2018). CaSiO3 perovskite in diamond indicates the recycling of oceanic crust into the lower mantle. Nature 555, 237-241.

Nielsen, T.F., Jensen, S.M., Secher, K., Sand, K.K. (2009). Distribution of kimberlite and aillikite in the Diamond Province of southern West Greenland: a regional perspective based on groundmass mineral chemistry and bulk compositions. Lithos, 112, 358-371.

Nielsen, T.F., Sand, K.K. (2008). The Majuagaa kimberlite dike, Maniitsoq region, West Greenland: constraints on an Mg-rich silicocarbonatitic melt composition from groundmass mineralogy and bulk compositions. The Canadian Mineralogist, 46(4), 1043-1061.

Nimis, P., Taylor, W.R. (2000). Single clinopyroxene thermobarometry for garnet peridotites. Part I. Calibration and testing of a Cr-in-Cpx barometer and an enstatite-in-Cpx thermometer. Contributions to Mineralogy and Petrology 139, 541-554.

Nixon, P.H., Boyd, F.R. (1973). The discrete nodule association in kimberlites from northern Lesotho. Lesotho kimberlites, pp. 67-75.

Nosova, A.A., Sazonova, L.V., Kargin, A.V., Smirnova, M.D., Lapin, A.V., Shcherbakov, V.D. (2018). Olivine in ultramafic lamprophyres: chemistry, crystallisation, and melt sources of Siberian Pre-and post-trap aillikites. Contributions to Mineralogy and Petrology 173, 55.

Nowell, G.M., Pearson, D.G., Bell, D.R., Carlson, R.W., Smith, C.B., Kempton, P.D., Noble, S.R. (2004). Hf isotope systematics of kimberlites and their megacrysts: new constraints on their source regions. Journal of Petrology 45, 1583-1612.

Nowicki, T., Porritt, L., Crawford, B., Kjarsgaard, B. (2008). Geochemical trends in kimberlites of the Ekati property, Northwest Territories, Canada: insights on volcanic and resedimentation processes. Journal of Volcanology and Geothermal Research, 174(1-3), 117-127.

O'Reilly, S.Y., Griffin, W.L. (2013). Mantle metasomatism. In Metasomatism and the chemical transformation of rock (pp. 471-533). Springer, Berlin, Heidelberg.

Ogilvie-Harris, R.C., Field, M., Sparks, R.S.J. Walter, M.J. (2009). Perovskite from the Dutoitspan kimberlite, Kimberley, South Africa: implications for magmatic processes. Mineralogical Magazine 73, 915-928.

O'Reilly, S.Y., Griffin, W.L. (2000). Apatite in the mantle: implications for metasomatic processes and high heat production in Phanerozoic mantle. Lithos 53:217-232.

O'Reilly, S.Y., Griffin, W.L. (2006). Imaging global chemical and thermal heterogeneity in the subcontinental lithospheric mantle with garnets and xenoliths: Geophysical implications. Tectonophysics, 416(1-4), 289-309.

Otto, J.W., Wyllie, P.J. (1993). Relationships between silicate melts and carbonate-precipitating melts in CaO-MgO-SiO2-CO2-H2O at 2 kbar. Miner Petrol 48:343-365.

Pan, Y., Fleet, M.E. (2002). Compositions of the apatite-group minerals: substitution mechanisms and controlling factors. Reviews in Mineralogy and Geochemistry,48, 13-49.

Pasteris, J.D. (1980). Opaque Oxide Phases of the De Beers Pipe Kimberlite (Kimberley, South Africa) and Their Petrologic Significance. PhD Thesis, Yale University.

Pasteris, J.D. (1982) Representation of compositions in complex titanian spinels and application to the De Beers kimberlite. AmeriCanadian Mineralogistogist 67(3-4):244-250

Pasteris, J.D. (1983). Spinel zonation in the De Beers kimberlite, South Africa: possible role of phlogopite. Canadian Mineralogist 21, 41-58.

Pasteris, J.D., (1980) The significance of groundmass ilmenite and megacryst ilmenite in kimberlites. Contributions to Mineralogy and Petrology 75(4): 315–325

Paton, C., Hergt, J.M., Woodhead, J.D., Phillips, D., Shee, S.R. (2009). Identifying the asthenospheric component of kimberlite magmas from the Dharwar Craton, India. Lithos, 112, 296-310.

Pearson, D.G., Brenker, F.E., Nestola, F., McNeill, J., Nasdala, L., Hutchison, M.T., Matveev, S., Mather, K., Silversmit, G., Schmitz, S., Vekemans, B. (2014). Hydrous mantle transition zone indicated by ringwoodite included within diamond. Nature, 507, 221-224.

Pearson, D.G., Irvine, G.J., Carlson, R.W., Kopylova, M.G., Ionov, D.A. (2002). The development of lithospheric keels beneath the earliest continents: time constraints using PGE and Re-Os isotope systematics. Geological Society, London, Special Publications, 199(1), 65-90.

Pearson, D.G., Wittig, N. (2008). Formation of Archaean continental lithosphere and its diamonds: the root of the problem. Journal of the Geological Society, 165(5), 895-914.

Piccoli, P.M., Candela, P.A., (2002). Apatite in igneous systems. Rev Mineral Geochem 48:255-292.

Pilbeam, L.H., Nielsen, T.F.D., Waight, T.E. (2013). Digestion fractional crystallization (DFC): an important process in the genesis of kimberlites. Evidence from olivine in the Majuagaa kimberlite, southern West Greenland. Journal of Petrology 54, 1399-1425.

Pivin, M., Femenias, O., Demaiffe, D. (2009). Metasomatic mantle origin for Mbuji-Mayi and Kundelungu garnet and clinopyroxene megacrysts (Democratic Republic of Congo). Lithos, 112, 951-960.

Plechov, P.Y., Shcherbakov, V.D., Nekrylov, N.A. (2018). Extremely magnesian olivine in igneous rocks. Russian Geology and Geophysics 59, 1702-1717.

Pouchou, J.L., Pichoir, F. (1984). A new model for quantitative x-ray microanalysis. I.--application to the analysis of homogeneous samples. Recherche Aérospatiale 3, 167-192.

Poujol, M., Robb, L.J., Anhaeusser, C.R., Gericke, B. (2003). A review of the geochronological constraints on the evolution of the Kaapvaal Craton, South Africa. Precambrian Research, 127(1-3), 181-213.

Price, S.E., Russell, J.K., Kopylova, M.G. (2000). Primitive magma from the Jericho pipe, N.W.T., Canada: constraints on primary kimberlite melt chemistry. Journal of Petrology 41 (6), 789–808.

Prowatke, S., Klemme, S. (2006) Trace element partitioning between apatite and silicate melts. Geochimica et Cosmochimica Acta, 70, 4513-4527.

Putnis, A., Austrheim, H. (2013). Mechanisms of metasomatism and metamorphism on the local mineral scale: The role of dissolution-reprecipitation during mineral re-equilibration. In: ZYZ (eds) Metasomatism and the Chemical Transformation of Rock Springer, Berlin, Heidelberg, pp. 141-170.

Ranger, I.M., Heaman, L.M., Pearson, D.G., Muntener, C., Zhuk, V. (2018). Punctuated, long-lived emplacement history of the Renard 2 kimberlite, Canada, revealed by new high precision U-Pb groundmass perovskite dating. Mineralogy and Petrology, 112(2), 639-651.

Reguir, E.P., Chakhmouradian, A.R., Halden, N.M., Malkovets, V.G., Yang, P. (2009). Major- and trace-element compositional variation of phlogopite from kimberlites and carbonatites as a petrogenetic indicator. Lithos 112:372-384.

Rehfeldt, T., Foley, S.F., Jacob, D.E., Carlson, R.W., Lowry, D. (2008). Contrasting types of metasomatism in dunite, wehrlite and websterite xenoliths from Kimberley, South Africa. Geochimica et Cosmochimica Acta, 72(23), 5722-5756.

Rehfeldt, T., Jacob, D.E., Carlson, R.W. Foley, S.F. (2007). Fe-rich dunite xenoliths from South African kimberlites: cumulates from Karoo flood basalts. Journal of Petrology 48, 1387-1409.

Ringwood, A.E., Kesson, S.E., Hibberson, W., Ware, N. (1992). Origin of kimberlites and related magmas. Earth and Planetary Science Letters, 113(4), 521-538.

Roberts, B. (1976). Kimberley: turbulent city. David Philip Publisher, Cape Town. 413 pp.

Robertson, M. (1974). Diamond Fever: South African Diamond History, 1866-9, from Primary Sources. Oxford University Press.

Rock, N.M. (1991). Lamprophyres. Springer Science & Business Media

Roeder, P.L., Schulze, D.J. (2008). Crystallization of groundmass spinel in kimberlite. Journal of Petrology, 49(8), 1473-1495.

Rowlands, T. (2008) Proposed Emplacement Model for the Finsch Precursor Kimberlites. Masters Thesis, University of the Witwatersrand

Russell, J.K., Porritt, L.A., Lavallée, Y., Dingwell, D.B. (2012). Kimberlite ascent by assimilation-fuelled buoyancy. Nature. 481 (7381), 352-356.

Sautter, V., Haggerty, S.E., Field, S. (1991). Ultradeep (> 300 kilometers) ultramafic xenoliths: Petrological evidence from the transition zone. Science 252, 827-830.

Sarkar, C., Kjarsgaard, B.A., Pearson, D.G., Heaman, L.M., Locock, A.J., Armstrong, J.P. (2018). Geochronology, classification and mantle source characteristics of kimberlites and related rocks from the Rae Craton, Melville Peninsula, Nunavut, Canada. Mineralogy and Petrology, 112(2), 653-672.

Sazonova, L.V., Nosova, A.A., Kargin, A.V., Borisovskiy, S.E., Tretyachenko, V.V., Abazova, Z.M., Griban, Y.G. (2015). Olivine from the Pionerskaya and V. Grib kimberlite pipes, Arkhangelsk diamond province, Russia: types, composition, and origin. Petrology 23, 227-258.

Schmitz, M.D., Bowring, S.A., de Wit, M.J., Gartz, V. (2004). Subduction and terrane collision stabilize the western Kaapvaal craton tectosphere 2.9 billion years ago. Earth and Planetary Science Letters, 222(2), 363-376.

Schneider, C.A., Rasband, W.S., Eliceiri, K.W. (2012). NIH Image to ImageJ: 25 years of image analysis. Nature methods, 9(7), 671-675.

Schulze, D.J. (1990) Silicate-bearing rutile-dominated nodules from South African kimberlites; metasomatized cumulates. AmeriCanadian Mineralogistogist 75(1-2):97-104

Schulze, D.J. (2001). Origins of chromian and aluminous spinel macrocrysts from kimberlites in southern Africa. The Canadian Mineralogist, 39(2), 361-376.

Scicchitano, M.R., Rubatto, D., Hermann, J., Majumdar, A.S., Putnis, A. (2018). Oxygen isotope analysis of olivine by ion microprobe: Matrix effects and applications to a serpentinised dunite. Chemical Geology 499, 126-137.

Scott Smith, B.H., Nowicki, T.E., Russell, J.K., Webb, K.J., Mitchell, R.H., Hetman, C.M., Harder, M., Skinner, E.M.W., Robey, J.V.A. (2013). Kimberlite Terminology and Classification. Proceedings of the 10th International Kimberlite Conference. Special Volume of the Journal of the Geological Society of India 2:1-17

Shaikh, A.M., Kumar, S.P., Patel, S.C., Thakur, S.S., Ravi, S., Behera, D. (2018). The P3 kimberlite and P4 lamproite, Wajrakarur kimberlite field, India: mineralogy, and major and minor element compositions of olivines as records of their phenocrystic vs xenocrystic origin. Mineralogy and Petrology 112, 609-624.

Shaikh, A.M., Patel, S.C., Bussweiler, Y., Kumar, S.P., Tappe, S., Ravi, S., Mainkar, D. (2019). Olivine trace element compositions in diamondiferous lamproites from India: Proxies for magma origins and the nature of the lithospheric mantle beneath the Bastar and Dharwar cratons. Lithos 324-325, 501-518.

Shee, S.R., (1985). The Petrogenesis of the Wesselton Mine Kimberlites, Kimberley, Cape Province, R.S.A. (Ph.D) Department of Geochemistry. University of Cape Town, South Africa.

Shee, S.R., Clement, C.R., Skinner, E.M.W. (1994). The petrology of the Wesselton kimberlite sills, Kimberley, Cape Province, South Africa. In: Meyer, H. O. A. & Leonardos, O. H. (eds) Proceedings of the 5th International Kimberlite Conference. Companhia de Pesquisa de Recursos Minerais, pp. 98-114.

Simon, N.S., Carlson, R.W., Pearson, D.G., Davies, G.R. (2007). The origin and evolution of the Kaapvaal cratonic lithospheric mantle. Journal of Petrology, 48(3), 589-625.

Simon, N.S., Irvine, G.J., Davies, G.R., Pearson, D.G., Carlson, R.W. (2003). The origin of garnet and clinopyroxene in “depleted” Kaapvaal peridotites. Lithos, 71(2-4), 289-322.

Skinner, E.M.W., Marsh, J.S. (2004). Distinct kimberlite pipe classes with contrasting eruption processes. Lithos, 76(1-4), 183-200.

Słaby, E., Koch-Müller, M., Förster, H.J., Wirth, R., Rhede, D., Schreiber, A., Schade, U. (2016). Determination of volatile concentrations in fluorapatite of Martian shergottite NWA 2975 by combining synchrotron FTIR, Raman spectroscopy, EMPA, and TEM, and inferences on the volatile budget of the apatite host-magma. Meteorit Planet Sci 51:390-406.

Smith, C.B. (1983). Pb, Sr and Nd isotopic evidence for sources of southern African Cretaceous kimberlites. Nature, 304(5921), 51.

Smith, C.B., (1983) Pb, Sr and Nd isotopic evidence for sources of southern African Cretaceous kimberlites. Nature 304:51-54

Smith, C.B., Gurney, J.J., Ebrahim, N., Skinner, E.M.W., Clement, C.R. (1985). Geochemical character of southern African kimberlites: a new approach based on isotopic constraints. Transactions of the Geological Society of South Africa. 88 (2), 267-280.

Smith, C.B., Sims, K., Chimuka, L., Duffin, A., Beard, A.D., Townend, R. (2004). Kimberlite metasomatism at Murowa and Sese pipes, Zimbabwe. Lithos. 76 (1), 219-232.

Sobolev, A.V., Hofmann, A.W., Kuzmin, D.V., Yaxley, G.M., Arndt, N.T., Chung, S.L., Danyushevsky, L.V., Elliott, T., Frey, F.A., Garcia, M.O., Gurenko, A.A., Kamenetsky, V.S., Kerr, A.C., Krivolutskaya, N.A., Matvinekov, V.V., Nikogosian, I.K., Rocholl, A., Sigurdsson, I.A., Sushchevskaya N.M., Teklay, M. (2007). The amount of recycled crust in sources of mantle-derived melts. Science 316, 412-417.

Sobolev, N.V., Sobolev, A.V., Tomilenko, A.A., Kovyazin, S.V., Batanova, V.G., Kuz'min, D.V. (2015). Paragenesis and complex zoning of olivine macrocrysts from unaltered kimberlite of the Udachnaya-East pipe, Yakutia: relationship with the kimberlite formation conditions and evolution. Russian Geology and Geophysics 56, 260-279.

Sobolev, N.V., Yefimova, E.S. (2000) Composition and petrogenesis of Ti-oxides associated with diamonds. Int Geol Rev 42(8):758-767

Sokol, A.G., Kupriyanov, I.N., Palyanov, Y.N., Kruk, A.N., Sobolev, N.V. (2013). Melting experiments on the Udachnaya kimberlite at 6.3–7.5 GPa: implications for the role of H2O in magma generation and formation of hydrous olivine. Geochimica et Cosmochimica Acta, 101, 133-155.

Soltys. A., Giuliani, A., Phillips, D., Kamenetsky, V.S. (submitted). Kimberlite metasomatism of the lithosphere and the evolution of olivine in carbonate-rich melts – evidence from the Kimberley kimberlites (South Africa). Journal of Petrology.

Soltys, A., Giuliani, A., Phillips, D. (2018a). A new approach to reconstructing the composition and evolution of kimberlite melts: A case study of the archetypal Bultfontein kimberlite (Kimberley, South Africa). Lithos 304, 1-15.

Soltys, A., Giuliani, A., Phillips, D. (2018b). Crystallisation sequence and magma evolution of the De Beers dyke (Kimberley, South Africa). Mineralogy and Petrology 112, 503-518.

Soltys, A., Giuliani, A., Phillips, D., Kamenetsky, V.S., Maas, R., Woodhead, J., Rodemann, T. (2016). In-situ assimilation of mantle minerals by kimberlitic magmas—direct evidence from a garnet wehrlite xenolith entrained in the Bultfontein kimberlite (Kimberley, South Africa). Lithos, 256, 182-196.

Sommerauer, J., Katz-Lehnert, K. (1985). A new partial substitution mechanism of CO32−/CO3OH3− and SiO44− for the PO43− group in hydroxyapatite from the Kaiserstuhl alkaline complex (SW-Germany). Contributions to Mineralogy and Petrology 91:360-368.

Sparks, R.S.J. (2013). Kimberlite volcanism. Annu Rev Earth Pl Sc 41:497-528.

Sparks, R.S.J., Baker, L., Brown, R.J., Field, M., Schumacher, J., Stripp, G., Walters, A. (2006). Dynamical constraints on kimberlite volcanism. Journal of Volcanology and Geothermal Research, 155(1-2), 18-48.

Sparks, R.S.J., Brooker, R.A., Field, M., Kavanagh, J., Schumacher, J.C., Walter, M.J., White, J. (2009). The nature of erupting kimberlite melts. Lithos, 112, 429-438.

Stachel, T. (2001). Diamonds from the asthenosphere and the transition zone. European Journal of Mineralogy 13, 883-892.

Stamm, N., Schmidt, M.W. (2017). Asthenospheric kimberlites: volatile contents and bulk compositions at 7 GPa. Earth and Planetary Science Letters, 474, 309-321.

Stone, R.S., Luth, R.W. (2016). Orthopyroxene survival in deep carbonatite melts: implications for kimberlites. Contributions to Mineralogy and Petrology, 171(7), 63.

Stripp, G.R., Field, M., Schumacher, J.C., Sparks, R.S.J., Cressey, G. (2006). Post-emplacement serpentinization and related hydrothermal metamorphism in a kimberlite from Venetia, South Africa. Journal of Metamorphic Geology, 24(6), 515-534

Tainton, K.M., (1992). The Petrogenesis of group II kimberlites and lamproites from the northern Cape Province, South Africa. PhD. thesis, University of Cambridge, UK.

Tainton, K.M., McKenzie, D.A.N. (1994). The generation of kimberlites, lamproites, and their source rocks. Journal of Petrology, 35(3), 787-817.

Tappe, S., Romer, R.L., Stracke, A., Steenfelt, A., Smart, K.A., Muehlenbachs, K., Torsvik, T.H. (2017). Sources and mobility of carbonate melts beneath cratons, with implications for deep carbon cycling, metasomatism and rift initiation. Earth and Planetary Science Letters, 466:152-167.

Tappe, S., Steenfelt, A., Heaman, L.M., Simonetti, A. (2009). The newly discovered Jurassic Tikiusaaq carbonatite-aillikite occurrence, West Greenland, and some remarks on carbonatite–kimberlite relationships. Lithos 112:385-399.

Tappe, S., Brand, N.B., Stracke, A., van Acken, D., Liu, C.Z., Strauss, H., Wu, F., Luguet, A., Mitchell, R.H., (2017). Plates or plumes in the origin of kimberlites: U/Pb perovskite and Sr-Nd-Hf-Os-C-O isotope constraints from the Superior craton (Canada). Chemical Geology 455, 57–83.

Tappe, S., Foley, S.F., Jenner, G.A., Heaman, L.M., Kjarsgaard, B.A., Romer, R.L., Stracke, A., Joyce, N., Hoefs, J. (2006). Genesis of ultramafic lamprophyres and carbonatites at Aillik Bay, Labrador: a consequence of incipient lithospheric thinning beneath the North Atlantic craton. Journal of Petrology, 47(7), 1261-1315.

Tappe, S., Foley, S.F., Jenner, G.A., Kjarsgaard, B.A. (2005). Integrating ultramafic lamprophyres into the IUGS classification of igneous rocks: rationale and implications. Journal of Petrology, 46(9), 1893-1900.

Tappe, S., Foley, S.F., Kjarsgaard, B.A., Romer, R.L., Heaman, L.M., Stracke, A., Jenner, G.A. (2008). Between carbonatite and lamproite—diamondiferous Torngat ultramafic lamprophyres formed by carbonate-fluxed melting of cratonic MARID-type metasomes. Geochimica et Cosmochimica Acta, 72(13), 3258-3286.

Tappe, S., Foley, S.F., Stracke, A., Romer, R.L., Kjarsgaard, B.A., Heaman, L.M., Joyce, N. (2007). Craton reactivation on the Labrador Sea margins: 40Ar/39Ar age and Sr–Nd–Hf–Pb isotope constraints from alkaline and carbonatite intrusives. Earth and Planetary Science Letters, 256(3-4), 433-454.

Tappe, S., Jenner, G.A., Foley, S.F., Heaman, L., Besserer, D., Kjarsgaard, B.A., Ryan, B. (2004). Torngat ultramafic lamprophyres and their relation to the North Atlantic Alkaline Province. Lithos, 76(1-4), 491-518.

Tappe, S., Kjarsgaard, B.A., Kurszlaukis, S., Nowell, G.M., Phillips, D. (2014). Petrology and Nd–Hf isotope geochemistry of the Neoproterozoic Amon kimberlite sills, Baffin Island (Canada): evidence for deep mantle magmatic activity linked to supercontinent cycles. Journal of Petrology, 55(10), 2003-2042.

Tappe, S., Pearson, D.G., Kjarsgaard, B.A., Nowell, G., Dowall, D., (2013). Mantle transition zone input to kimberlite magmatism near a subduction zone: origin of anomalous Nd–Hf isotope systematics at Lac de Gras, Canada. Earth and Planetary Science Letters 371, 235–251.

Tappe, S., Pearson, D.G., Nowell, G., Nielsen, T., Milstead, P., Muehlenbachs, K. (2011). A fresh isotopic look at Greenland kimberlites: cratonic mantle lithosphere imprint on deep source signal. Earth and Planetary Science Letters, 305(1-2), 235-248.

Tappe, S., Smart, K., Torsvik, T., Massuyeau, M., de Wit, M. (2018). Geodynamics of kimberlites on a cooling Earth: Clues to plate tectonic evolution and deep volatile cycles. Earth and Planetary Science Letters, 484, 1-14.

Tollari, N., Barnes, S.J., Cox, R.A., Nabil, H. (2008). Trace element concentrations in apatites from the Sept-Îles Intrusive Suite, Canada—implications for the genesis of nelsonites. Chemical Geology 252:180-190.

Tollo, R.P., Haggerty, S.E. (1987) Nb-Cr-rutile in the Orapa kimberlite, Botswana. Canadian Mineralogist 25(2):251-264

Torsvik, T.H., Burke, K., Steinberger, B., Webb, S.J., Ashwal, L.D. (2010). Diamonds sampled by plumes from the core–mantle boundary. Nature, 466(7304), 352.

Tovey, M., Giuliani, A., Phillips, D., Moss, S. (2020). Controls on the explosive emplacement of diamondiferous kimberlites: New insights from hypabyssal and pyroclastic units in the Diavik mine, Canada. Lithos:105410

Ubide, T., Galé, C., Larrea, P., Arranz, E., Lago, M. (2014) Antecrysts and their effect on rock compositions: the Cretaceous lamprophyre suite in the Catalonian Coastal Ranges (NE Spain). Lithos 206:214-233

van Achterbergh, E., Griffin, W.L., Ryan, C.G., O'Reilly, S.Y., Pearson, N.J., Kivi, K., Doyle, B.J. (2002). Subduction signature for quenched carbonatites from the deep lithosphere. Geology, 30(8), 743-746.

van Straaten, B.I., Kopylova, M.G., Russell, J.K., Scott Smith, B. (2011). A rare occurrence of a crater-filling clastogenic extrusive coherent kimberlite, Victor Northwest (Ontario, Canada). Bulletin of Volcanology, 73(8), 1047-1062.

Veksler, I.V., Keppler, H. (2000). Partitioning of Mg, Ca, and Na between carbonatite melt and hydrous fluid at 0.1–0.2 GPa. Contributions to Mineralogy and Petrology. 138 (1), 27-34.

Veter, M., Foley, S.F., Mertz-Kraus, R., Groschopf, N. (2017). Trace elements in olivine of ultramafic lamprophyres controlled by phlogopite-rich mineral assemblages in the mantle source. Lithos, 292, 81-95.

Wagner, P.A. (1914). The Diamond Fields of Southern Africa, Transvaal Leader, Johannesburg

Watson, E.B. (1980). Apatite and phosphorus in mantle source regions: an experimental study of apatite/melt equilibria at pressures to 25 kbar. Earth and Planetary Science Letters 51:322-335.

Watson, E.B., Green, T.H. (1981). Apatite/liquid partition coefficients for the rare earth elements and strontium. Earth and Planetary Science Letters, 56:405-421.

Webster, J.D., Piccoli, P.M. (2015). Magmatic apatite: A powerful, yet deceptive, mineral. Elements, 11:177-182.

Weiss, Y., Class, C., Goldstein, S.L. Hanyu, T. (2016). Key new pieces of the HIMU puzzle from olivines and diamond inclusions. Nature 537, 666.

White, J.L., Sparks, R.S.J., Bailey, K., Barnett, W.P., Field, M., Windsor, L. (2012). Kimberlite sills and dykes associated with the Wesselton kimberlite pipe, Kimberley, South Africa. South African Journal of Geology, 115(1), 1-32.

Willcox, A., Buisman, I., Sparks, R.S.J., Brown, R.J., Manya, S., Schumacher, J.C., Tuffen, H., (2015). Petrology, geochemistry and low-temperature alteration of lavas and pyroclastic rocks of the kimberlitic Igwisi Hills volcanoes, Tanzania. Chemical Geology 405, 82-101.

Williams, A.J. (1932). The Genesis of Diamond. Ernest Benn Ltd., London (2 volumes).

Wilson, M.R., Kjarsgaard, B.A., Taylor, B. (2007). Stable isotope composition of magmatic and deuteric carbonate phases in hypabyssal kimberlite, Lac de Gras field, Northwest Territories, Canada. Chemical Geology 242:435-454.

Woodhead, J., Hergt, J., Giuliani, A., Maas, R., Phillips, D., Pearson, G., Nowell, G. (2019). Kimberlites reveal 2.5 billion year evolution of a deep isolated mantle reservoir. Nature 573:578-581

Woodhead, J., Hergt, J., Phillips, D., Paton, C. (2009). African kimberlites revisited: in situ Sr-isotope analysis of groundmass perovskite. Lithos, 112, 311-317.

Woolley, A.R., Bergman, S.C., Edgar, A.D., Le Bas, M.J., Mitchell, R.H., Rock, N.M., Scott Scott Smith, B. (1996). Classification of lamprophyres, lamproites, kimberlites, and the kalsilitic, melilitic, and leucitic rocks. The Canadian Mineralogist, 34(2), 175-186.

Wyllie, P.J., Cox, K.G., Biggar, G.M. (1962). The habit of apatite in synthetic systems and igneous rocks. Journal of Petrology 3:238-243.

Wyllie, P.J. (1980). The origin of kimberlite. Journal of Geophysical Research: Solid Earth, 85(B12), 6902-6910.

Yang, Y.H., Wu, F.Y., Wilde, S.A., Liu, X. M., Zhang, Y. B., Xie, L. W., Yang, J.H. (2009). In situ perovskite Sr–Nd isotopic constraints on the petrogenesis of the Ordovician Mengyin kimberlites in the North China Craton. Chemical Geology, 264(1-4), 24-42.

Yaxley, G.M., Kamenetsky, V.S., Nichols, G.T., Maas, R., Belousova, E., Rosenthal, A., Norman, M. (2013). The discovery of kimberlites in Antarctica extends the vast Gondwanan Cretaceous province. Nature communications, 4, 2921.

Zurevinski, S., Mitchell, R.H. (2011). Highly evolved hypabyssal kimberlite sills from Wemindji, Quebec, Canada: insights into the process of flow differentiation in kimberlite magmas. Contributions to Mineralogy and Petrology 161:765-776.